Technical University of Denmark

DTU

Multi-life-stage monitoring system based on fibre bragg grating sensors for more reliable wind turbine rotor blades: Experimental and numerical analysis of deformation and failure in composite materials

Pereira, Gilmar Ferreira; Mikkelsen, Lars Pilgaard; McGugan, Malcolm; Sørensen, Bent F.

DTU Library
Technical Information Center of Denmark

Multi-life-stage monitoring system based on fibre Bragg grating sensors for more reliable wind turbine rotor blades:

Experimental and numerical analysis of deformation and failure in composite materials

Gilmar Ferreira Pereira

Technical University of Denmark,
DTU Wind Energy PhD-0062(EN)
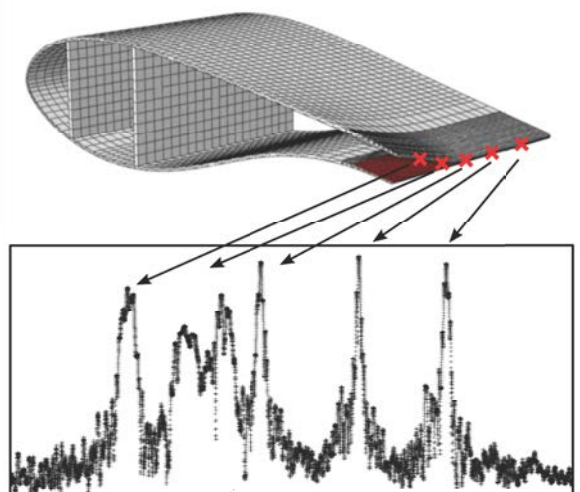
DTU Wind Energy
Department of Wind Energy

Multi-life-stage monitoring system based on fibre Bragg grating sensors for more reliable wind turbine rotor blades: Experimental and numerical analysis of deformation and failure in composite materials

Gilmar Ferreira Pereira

Risø, Denmark 2016

MARIE CURIE ACTIONS

DTU

Prepared by:
Gilmar Ferreira Pereira

Main supervisors:
Lars Pilgaard Mikkelsen, Associate Professor
Technical University of Denmark
Department of Wind Energy, Section of Composite Materials
Mail:lapm@dtu.dk

Malcolm McGugan, Senior Development Engineer
Technical University of Denmark
Department of Wind Energy, Section of Composite Materials
Mail:mamc@dtu.dk

Bent F. Sørensen, Dr.Techn., Head of Section
Technical University of Denmark
Department of Wind Energy, Section of Composite Materials
Mail:bsqr@dtu.dk

Abstract

One of today's greatest global challenges is the need for clean, reliable, and renewable sources of energy, and wind energy has a key role in this process. However, in order to compete with other less "green" sources of energy the cost to produce wind made electricity needs to be reduced. One way to achieve this is by improving the reliability of wind turbine components and optimising operation and maintenance strategies.

This PhD project is part of the European research project MareWint, where the main objective is to develop an innovative approach for coupled multi physics co-simulation, testing, design and optimisation of offshore wind turbines. The MareWint main scientific objective is to optimise the design of offshore wind turbines, maximise reliability, and minimise maintenance costs.

Integrated within the innovative rotor blades work-package, this PhD project is focused on damage analysis and structural health monitoring of wind turbine blades. The work presented sets the required framework to develop a monitoring system based on fibre Bragg gratings (FBG), which can be applied to the different life stages of a wind turbine blade. In this concept, the different measured physical parameters are used to improve the design process, and the implemented sensor are used to control the manufacturing and operation stage of a wind turbine rotor blade. The FBG sensors measurement principle is analysed from a multi-life-stage (design, material testing, manufacturing, and operation) perspective, and supported/validated by numerical models, software tools, signal post-processing, and experimental validation.

The damage in the wind turbine rotor blade is analysed from a material perspective (fibre reinforced polymers) and used as a design property, meaning that damage is accepted in an operational wind turbine as long as it is monitored. Thus, a novel crack/damage detection method using FBG sensors is presented, and software/tools are developed for signal simulation and post-processing. The first part of the thesis is an introduction to the multi-life-stage monitoring system based on FBG sensors and the damage tolerant design of fibre reinforced materials, where the different theory and numerical models used are presented. The second part of the thesis is a compilation of scientific journal papers, in which the use of FBG sensors to monitor the different life-stages of the wind turbine rotor blade is described in more detail.

In Paper P1, a methodology for reliable design and maintenance of wind turbine rotor blades based on a damage tolerance and structural health monitoring approach is presented. Paper P2 presents a novel method to obtain independent strain and temperature measurements using embedded FBG sensors in polymeric tensile tests. In paper P3, a novel method for assessing crack growth in fibre reinforced polymer or structural adhesive bonded structures by combining conventional measured parameters with parameters associated with measurement errors is presented. Paper P4 presents a FBG signal post-processing tool. In paper P5, a software development tool to simulate the FBG signal from a finite element method model is described. Paper P6 fits within the manufacturing stage, describing a residual strain measurement solution based on FBG sensors. In paper P7, the fracture process zone length in double cantilever beam specimens is analysed analytically and numerically.

Resumé

En af vore dages største globale udfordringer er efterspørgslen efter ren, pålidelig, og vedvarende energi. Vindenergi spiller her en central rolle men for bedre at kunne konkurrere med andre mindre "grønne" energikilder skal omkostningerne hertil dog skulle reduceres. En måde at gøre dette på er ved at forbedre holdbarheden af vindmøllekomponenter samt ved at optimere drift og vedligeholdelsen.

Dette ph.d.-projekt er en del af det europæiske forskningsprojekt MareWint, hvis hovedformål er at udvikle en innovativ tilgang til en koblet multifysik simulering, testning, designing og optimering af havvindmøller. MareWints videnskabelige hovedformål er at finde det optimale design af offshore vindmøller, maksimere pålidelighed og minimere vedligeholdelsesomkostningerne.

Ph.d.-projektet er integreret i vindmøllevingearbejdespakken med fokus på skadesanalyse og -overvågning af vindmøllevinger. Det udførte studie sætter rammerne for en udvikling af et vingeskadeskontrolsystem baseret på optiske Fiber Bragg Gratings (FBG) sensorer, som kan anvendes til en detektering af skadesudvikling i løbet af en vindmøllevinges levetid. En detektering som efterfølgende kan bruges til at forbedre selve vingedesignet. Derudover kan de optiske FBG også bruges til at styre selve fremstillingsprocessen af vindmøllevinger samt den efterfølgende drift. Outputtet fra FBG sensorerne analyseres ud fra et multi-life-stadie perspektiv (design, materialetest, fremstilling og drift), og bliver herunder understøttet og valideret af numeriske modeller, software-værktøjer, signalbehandling and eksperimentel validering.

De opståede skader i vindmøllevingen analyseres ud fra et materiale perspektiv (fiberforstærket polymerer) og bruges som en designegenskab, hvilket betyder, at skadesniveauet vil blive accepteret under selve vindmølleoperationen, hvilket kan ske så længe skaden er overvåget. En ny revne/skades-påvisningsmetode ved hjælp af FBG sensorer blevet herved præsenteret hvorunder et stykke software til signalsimulering og efterbehandling er blevet udviklet. Den første del af afhandlingen er en introduktion til dette multi-life-stadie overvågningssystem baseret på FBG sensorer brugt på de skadestolerante fiberforstærkede materialer hvorunder de forskellige teorier og numeriske modeller vil blive præsenteret. Den anden del af afhandlingen er en samling af videnskabelige tidsskriftsartikler, hvor brugen af FBG sensorer til en overvågning af de forskellige stadier af levetiden af en vindmøllevinge vil blive beskrevet mere detaljeret.

Artikel P1 præsenterer en metode til en pålidelig udformning og vedligeholdelse af en vindmøllevinge baseret på et skadestolerant materiale. Artikel P2 præsenterer en ny metode til at opnå uafhængige tøjnings- og temperatur-målinger ved hjælp af indbyggede FBG sensorer i forbindelse med trækprøvning af polymere. I artikel P3, bliver en ny fremgangsmåde foreslået hvor målefejlen fra de optiske FGB fibre bliver brugt til en vurdering af revnevæksten inden i såvel som i limsamlingen mellem fiberforstærket kompositter. Artikel P4 præsenterer et udviklet FBG-signalbehandlingsværktøj. I artikel P5, bliver et udviklet stykke software til brug til at simulere et FBG signal præsenteret. Dette stykke software bygger på en finite element bestemt spændings- og tøjningsfelt. Artikel P6 adressere selve fremstillingsprocessen af fiberforstærkede kompositter hvorunder størkningstøjningerne kan måles ved hjælp af FBG sensorer og relateret til udmattelsesegenskaberne af kompositmaterialet. I artikel P7, bliver længden af skadesområdet i forbindelse med revnevækst i en såkaldt "Double Cantilever Beam" analyseret analytisk og numerisk.

Preface

The thesis was submitted to the Danish Technical University in partial fulfilment of the requirements for obtaining the PhD degree at the Technical University of Denmark, in the PhD-program: Construction, Production, Civil Engineering and Transport. The PhD project was conducted from April 2013 till March 2016 at the Composite and Material Mechanics section of the Department of Wind Energy, supervised by Lars P. Mikkelsen, Malcolm McGugan, and Bent F. Sørensen. The dissertation is organised as a collection of peer-reviewed articles.

This PhD project is part of the European research project MareWint, *new MAterials and REliability in offshore WINd*, where the main objective is to develop an innovative approach for coupled multi-physics co-simulation, testing, design and optimisation of reliable offshore wind turbines. This PhD project deals essentially with modelling and monitoring of damage, applied to the wind turbine rotor blade. The research funding was provided from the FP7-EU research program, Marie-Curie Action ITN, project no. 309395.

<div align="center">Risø, Denmark, May 17, 2016</div>

<div align="right">Gilmar Ferreira Pereira</div>

Acknowledgements

Dedicado ao meu avô António Ferreira,
sem ti nada disto teria sido possível.

Publications

Appended in the thesis

Publications in refereed journals

- M. McGugan, **G. Pereira**, B. F. Sørensen, H. Toftegaard and K. Branner, *Damage Tolerance And Structural Monitoring For Wind Turbine Blades*, Phil. Trans. R. Soc. A, **373 (2015)**, 20140077–20140077. doi:10.1098/rsta.2014.0077;

- **G. Pereira**, L.P. Mikkelsen, M. McGugan, *Crack Detection in Fibre Reinforced Plastic Structures Using Embedded Fibre Bragg Grating Sensors: Theory, Model Development and Experimental Validation*, PLoS ONE, **10 (10)** e0141495.
  doi:10.1371/journal.pone.0141495;

- **G. Pereira**, M. McGugan, L.P. Mikkelsen, *Method for Independent Strain and Temperature Measurement in Polymeric Tensile Test Specimen Using Embedded FBG Sensors*, Polymer Testing, **50 (2016)** 125–134.
  doi:10.1016/j.polymertesting.2016.01.005;

- **G. Pereira**, M. Mcgugan, L.P. Mikkelsen, *FBG SiMul V1.0: Fibre Bragg Grating Signal Simulation Tool for Finite Element Method Models*, **(Submitted to the Journal Software-X, Elsevier)**;

- **G. Pereira**, J. Hüther, L.P. Mikkelsen, P. Brøndsted, *Cure induced strains and fatigue performance of a unidirectional glass fiber reinforced epoxy*, **(Draft version)**;

- **G. Pereira**, B. Sørensen, L.P. Mikkelsen, Double Cantilever Beam Fracture Process Zone Length: Analytical and Numerical Analysis, **(Draft version)**;

Publications in refereed conference proceedings: extended version papers

- **G. Pereira**, L.P. Mikkelsen, M. McGugan, *Fibre Bragg Grating Sensor Signal Post-Processing Algorithm: Crack Growth Monitoring in Fibre Reinforced Plastic Structures*, Proceedings of the 3nd International Conference on Photonics, Optics and Laser Technology, ISBN:978-3-319-30135-8 (Available April 2016);

Not-Appended in the thesis

Publications in refereed conference proceedings

- **G. Pereira**, L.P. Mikkelsen, M. McGugan, *Crack Growth Monitoring by Embedded Optical Fibre Bragg Grating Sensors: Fibre Reinforced Plastic Crack Growing Detection*, Proceedings of OSENS 2015 - Special Session on Optical Sensors at Photooptics 2015. pp. 133-139;

- **G. Pereira**, L.P. Mikkelsen, M. McGugan, *Embedded Fibre Bragg Grating Sensor Response Model: Crack Growing Detection in Fibre Reinforced Plastic Materials*, J. Phys. Conf. Ser. 628 (2015) 012115. doi:10.1088/1742-6596/628/1/012115.

Publications in conference/seminar proceedings

- **G. Pereira**, L.P. Mikkelsen, M. McGugan, *Crack growth monitoring in composite materials using embedded optical Fiber Bragg Grating sensor*, Proceedings of the 5th International Conference on Smart Materials and Nanotechnology in Engineering (SMN) in conjunction with the International Conference on Smart Materials and Structures (Cansmart 2015);

- **G. Pereira**, L.P. Mikkelsen, M. McGugan, *Damage tolerant design and condition monitoring of composite material and bondlines in wind turbine blades: Failure and crack propagation*, Proceedings of EWEA Offshore 2015 Conference. European Wind Energy Association (EWEA);

- **G. Pereira**, L.P. Mikkelsen, M. McGugan, *Damage tolerant design: failure and crack propagation in composites*, Proceedings of 10th EAWE PhD Seminar on Wind Energy in Europe. European Academy of Wind Energy, pp. 1-5;

- B.F. Sørensen, H.L. Toftegaard, M. McGugan, **G. Pereira**, K. Branner, *Very large wind turbine rotor blades require damage tolerance and damage monitoring*, Poster session presented at EWEA Offshore 2015 Conference, Copenhagen, Denmark;

Contents

Nomenclature

Abbreviations

1D	One dimensional	
2D	Two dimensional	
3D	Three dimensional	
CE	Cohesive elements	
CoE	Cost of energy	[\$]
CoI	Cost of installation	[\$]
CoM	Cost of maintenance	[\$]
CoT	Cost of turbine	[\$]
CS	Cohesive surfaces	
CZM	Cohesive zone modelling	
DCB	Double cantilever beam	
FBG	Fibre Bragg grating	
FEM	Finite element method	
FPZL	Fracture process zone length	[m]
FRP	Fibre reinforced polymers	
LEFM	Linear elastic fracture mechanics	
PP	Power Production	[kWh]
RTW	Reference wind turbine	
UD	Unidirectional	
VCCT	Virtual crack closure technique	

Greek symbols

α_f	Optical fibre thermal expansion coefficient	[K^{-1}]
α_h	Host material thermal expansion coefficient	[K^{-1}]
δ_n	Crack face displacement (opening) in the normal direction	[m]
δ_t	Crack face displacement (opening) in the tangential direction	[m]
δn_{eff}	Modulation of the fibre optic core refractive index	[-]
$\overline{\delta n_{eff}}$	Mean induced change in the fibre optic core refractive index	[-]
ε	Uniform strain field magnitude	[-]
θ_c	Critical light angle	[rad]

θ_i	Light incidence angle	[rad]
θ_r	Light refraction angle	[rad]
λ_b	Wavelength of the reflected single peak	[nm]
μ	Shear modulus	[Pa]
ν	Poisson's ratio	[-]
ν_{f12}	Fibre Poisson's ratio	[-]
ν_m	Matrix Poisson's ratio	[-]
ξ	Optical fibre thermo-optic coefficient	[K^{-1}]
η	BK-law fitting parameter	[-]
σ	Stress	[Pa]
σ_n	Cohesive stress in the normal direction	[Pa]
σ_t	Cohesive stress in the normal tangential	[Pa]
$\widehat{\sigma_n}$	Critical cohesive stress in the normal direction	[Pa]
ϕ	Change in the grating period along the length	[-]
Γ	Contour around the crack faces	[-]
Δa	Crack increment length	[m]
$\Delta \lambda$	Wavelength shift of the reflected peak	[nm]
$\Delta \lambda$	Width variation of the reflected peak	[nm]
Λ	Grating nominal period	[nm]
$d\Pi$	Variation of potential energy	[J]
Ψ	Mixed-mode ratio	[-]
$\alpha; \beta; \gamma$	Power-law fitting parameters	[-]

Roman symbols

dA	Created fracture surface	[m^2]
B	DCB specimen width	[m]
E_f	Elastic modulus of the optical fibre	[Pa]
E_{f1}	Elastic modulus of the fibre in the longitudinal direction	[Pa]
E_{f2}	Elastic modulus of the fibre in the transverse direction	[Pa]
E_m	Elastic modulus of the matrix	[Pa]
f	damage criterion	[-]
f_{tol}	damage criterion tolerance	[-]
G	Strain energy release rate	[J/m^2]
G_c	Critical strain energy release rate	[J/m^2]
G_I	Fracture toughness for mode-I fracture	[J/m^2]
G_{II}	Fracture toughness for mode-II fracture	[J/m^2]
G_{III}	Fracture toughness for mode-III fracture	[J/m^2]

G_{12}	Fibre in-plane shear modulus	[Pa]
G_{23}	Fibre transverse shear modulus	[Pa]
G_m	Matrix shear modulus	[Pa]
H	DCB specimen height	[m]
J	J-integral	[J/m^2]
J^{ss}	Steady-state fracture energy	[J/m^2]
J_0	Crack tip fracture energy	[J/m^2]
K_I	Stress intensity factor for mode-I fracture	[MPa m$^{1/2}$]
K_{II}	Stress intensity factor for mode-II fracture	[MPa m$^{1/2}$]
K_{III}	Stress intensity factor for mode-III fracture	[MPa m$^{1/2}$]
M_1	Moment applied to the DCB top beam	[N.m]
M_2	Moment applied to the DCB bottom beam	[N.m]
n_0	Initial refractive index	[-]
n_{core}	Refractive index of the fibre optic core	[-]
$n_{cladding}$	Refractive index of the fibre optic cladding	[-]
n_j	Outwards normal direction to the contour	[-]
p_e	Optical fibre photo-elastic coefficient	[-]
p_{11}	Photo-elastic coefficient of the optical fibre, direction 11	[-]
p_{21}	Photo-elastic coefficient of the optical fibre, direction 21	[-]
S	Curve length along the contour Γ	[mm]
V_f	Fibre volume fraction	[%]
V_m	Matrix volume fraction	[%]
ΔT	Temperature variation	[K]
W	Strain energy density	[-]

Chapter 1

Introduction

This chapter gives a brief introduction to the project scope, the different fields of research, and the main objectives for the thesis.

1.1 Problem Statement

Modern society is moving towards a low-carbon economy, and demands an environmentally responsible energy sector, which means a shift to renewable sources of energy. Adding this to the increasing energy demand, it is estimated that the wind energy sector will have the opportunity to double, or even triple its power production in the next decades [1]. Although, the wind energy sector still has to compete for this market share with other sources of energy, in which the cost of energy (CoE) plays an important role. Lowering the CoE is a central topic shared by all the different industry, government, and research fields.

In a simplified version, the cost to produce energy (CoE in kWhs) during the life-time of a wind turbine is described by equation (1.1),

$$CoE = \frac{CoT + CoI + CoM}{PP} \tag{1.1}$$

where CoT is the wind turbine cost of production, CoI is the cost of installation and transport, CoM is the cost of operation and maintenance, and PP the power produced during the turbine life-time. The cost to produce energy can be then reduced either by increasing the power produced by each individual wind turbine during its life-time (PP), or by decreasing the cost related with the wind turbine production, installation, and maintenance (CoT, CoI, and CoM).

By analysing the wind energy sector in the last decade and the latest research programmes initiatives, a trend is visible in the wind turbine R&D to achieve this common objective of reducing CoT:

- Larger Wind Turbines; the most cost-effective way of increasing the PP is to increase the rotor diameter [2]. This pattern is visible in the size of the state-of-the-art wind turbines installed over recent years, as shown in figure 1.1. Additionally, even if a larger wind turbine is more costly to manufacture (CoT), this cost increase is compensated by the absolute saving when factoring cost of installation (CoI) and the cost of maintenance (CoM) with the power produced (PP).
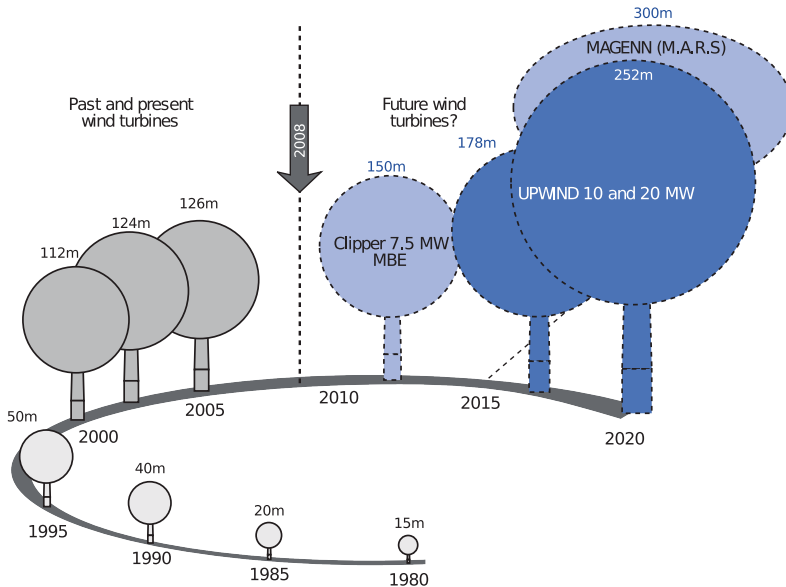
Figure 1.1: Growth in size of commercial wind turbine designs (taken from *The Economics of Wind Energy, a report by the EWEA* [3]).

- More reliable wind turbines, and efficient maintenance plans; other way to increase CoE is by increasing the amount of hours that the wind turbine operates/produces energy. This can be done by increasing the wind turbine reliability and consequently extending its life-time, and also by decreasing its failure rate and maintenance/repair time. When this is achieved, less wind turbines fail, the time to failure increases, and less time is used to repair, which leads to a higher rate of wind turbine availability and consequently reduces the cost per energy output. Additionally, a better maintenance plan and less repair activities leads to a reduction in CoM and consequently lower CoE.

1.2   MareWint Project

This PhD project is part of the European research project MareWint, *new MAterials and REliability in offshore WINd*[1], where the main objective is to develop an innovative approach for coupled multi physics co-simulation, testing, design and optimisation of reliable Offshore Wind Turbines. This project was created to follow the strategic objectives of the industrial initiative of the European Strategic Energy

---

[1]Marie-Curie Action ITN, Nr. 309395, MareWint website: http://www.marewint.eu/

Technology (Set)-Plan[2], to reduce the total cost of energy (CoE) by improving the reliability of wind turbine components and optimising the operation and maintenance strategies.

With a especial focus in the offshore sector, where operation and maintenance represent a high percentage of total cost, MareWint's main scientific concept is to find the optimal design of offshore wind turbine, maximise its reliability, and minimise its maintenance cost. To achieve this, a consortium of 6 universities, 7 research institutes, and 10 private sector enterprises are involved in this research project, and 14 researchers (PhD students) from different multidisciplinary areas are divided into 5 work packages, as shown in figure 1.2. The different work packages are cross-linked and the knowledge from different areas is expected to be integrated into a final global model representing some of the offshore wind turbine hydro-aero-mechanical issues. Thus, the MareWint structure defines the research objectives of this PhD project, as the knowledge developed needs to be integrated with the other work packages and ultimately in the multi-physics model.

1.2.1   Project Reference Wind Turbine: DTU 10MW

The DTU 10MW[3] reference wind turbine [4], was agreed as the common platform for the MareWint project and work packages. This reference wind turbine (RTW) is an open-source/free and publically available model, and it is considered a state-of-the-art design; thus, its geometries, operational constrains, materials, components, etc.,

---

[2]SETIS Website: https://setis.ec.europa.eu/
[3]DTU 10MW reference wind turbine website: http://dtu-10mw-rwt.vindenergi.dtu.dk

MareWint Structure
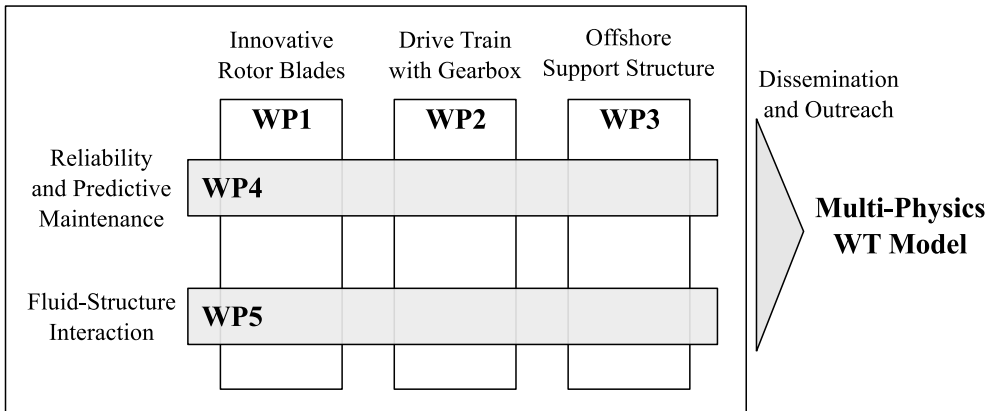
Figure 1.2: MareWint project structure.

were used by all the researches in the different sub-projects as a reference to produce the MareWint multi-physics model concept.

The DTU 10MW RTW was developed by DTU Wind Energy and Vestas Wind Systems, as part of a collaborative research to create the design basis for the next generation of wind turbines, and its design summary is presented in table 1.1.

Table 1.1: DTU 10MW reference wind turbine design summary [4].

Parameter	Value
Rating	10MW
Rotor orientation, configuration	Upwind, 3 blades
Control	Variable speed, collective pitch
Drivetrain	Medium speed, Multiple stage gearbox
Rotor, Hub diameter	178.3m, 5.6m
Hub height	119m
Rated tip speed	90m/s
Pre-bend	3m
Rotor mass	229tons (each blade 41tons)
Nacelle mass	446tons
Tower mass	605tons

As discussed later, this PhD project is focused on the material damaged behaviour, structure reliability analysis, and damage detection methods that can be applied to the rotor blades. Thus, the material properties, the structure/specimens geometry, load configuration, and the location of critical/failure used along this project are defined by this DTU 10MW RTW.

1.2.2   Work Package 1 - Innovative Rotor Blades

This PhD project is integrated with the MareWint work package 1, Innovative Rotor Blades, where the structural and fluid dynamics of the rotor blade are analysed by experimental and numerical methods. Within the work package, two individual projects were developed: the first project (this PhD project) studies the behaviour of the composite material within the rotor blade structure, its damage mechanism and damage detection methods; and, the second project describes the structural behaviour and rotor blade performance by using computational fluid dynamic models. Both project cross-link with other work-packages by providing structural health monitoring tools that can predict the rotor structural performance, and a fluid-structure interaction model to predict the structure response to the varying wind conditions.

1.3   Scientific Objectives within the MareWint Project

The main objective of this PhD project within the MareWint project are:

- damage/defects analysis from a material point of view;

- damage as a design property;

- improve damage detection systems;

- crack/defect detection in wind turbine rotor blade, fibre reinforced polymer;

- structural health monitoring implementation tools (to be used in the global model);

1.3.1   Thesis Structure

The thesis is written as a collection of peer-reviewed papers. In chapter 2, the concept of the multi-life-stage monitoring system based on fibre Bragg gratings is presented, which defines the structure of the thesis and the research topics addressed. Chapter 3 contains the summary of results presented in the paper collection, and its contribution to the PhD project. In appendix A, it is demonstrate that delamination in a rotor blade trailing edge can be analysed, from a material perspective, as a delamination in a double cantilever beam, and the finite element method models used to represent this damage mechanism are explored.

Chapter 2

Wind Turbine Blade Multi-Life-Stage Monitoring System Based on Fibre Bragg Gratings

This chapter presents a short introduction to a new emerging design philosophy for wind turbine rotors, where the structure is designed to operate even in the presence of damage. The requirements of a structural monitoring system to achieve such a concept are described, together with an analysis of good sensor candidates for this function. The selected monitoring system for wind turbine rotor blade, fibre Bragg grating, is then applied to a multi-life-stage monitoring system. Finally, the research activities performed in this PhD project are matched to the structure of the multi-life-stage monitoring system.

2.1 From a Conventional Design to a Damage Tolerance Design

As previously discussed, lowering the cost of energy (CoE) will require larger wind turbines and more reliable components. Thus, changes in the design philosophy will happen as a natural consequence of this process; the traditional design of wind turbine rotor blades and consequently fibre reinforced polymers (FRP) is based on conservative analysis methods, with larger safety factors, where only the linear behaviour of the structure/material is considered. This traditional design philosophy underestimates the material properties and its maximum strength, making it an obsolete approach to design high performance structures, such as large wind turbine rotor blades, with high reliability standards [5–7].

In paper [**P1**], a new methodology for reliability design and maintenance of wind turbine rotor blades is presented. This methodology is based on a damage tolerance and structural health monitoring approach, which enables the structure to operate despite the presence of damage. To accomplish this, the structure is designed with damage tolerant materials with built-in sensors, the damage is detected and charac-

terised by sensors, and models predict the residual life of the structure; then, this information enables decision-making with respect to whether the rotor blade should be repaired or replaced. Thus, "perfect" wind turbine rotor blades are not a requirement any more, and manufacturing defects, handling damage, and in-service damage can be accepted and controlled.

This design methodology can be applied to different wind turbine sub-components or different materials configurations, however in this PhD project the focus was on the FRP delamination mechanisms. During delamination of a FRP material, there is a balance between the energy applied to the structure and the energy consumed by the fracture process. Therefore, the crack will only grow once the energy applied to the structure, per unit of crack advance, is higher than the energy consumed by the crack tip fracture process, per unit of crack advance [8–10].

Two options to design a FRP structure to hold damage without failure are:

- Load design: designing a structure that can sustain an additional load, even if a crack is formed and locally have a reduced load capability; this can be achieved if the material does not have brittle behaviour and it can be altered to a stable and controlled crack growth.

- Damage mechanism design: increasing the fracture resistance and consequently the amount of stable cracks that the structure can hold; in FRP laminates, a rising fracture resistance means that the energy absorbed per unit of crack increases with the increase of the fracture process zone length (R-curve behaviour [8]). The R-curve behaviour can be schematically observed in Fig. 2.1, and it happens when delamination is accompanied by the formation of a fracture process zone, in which intact fibres connect the crack faces behind the crack tip increasing the energy required for a crack to grow (see Fig. 2.2).
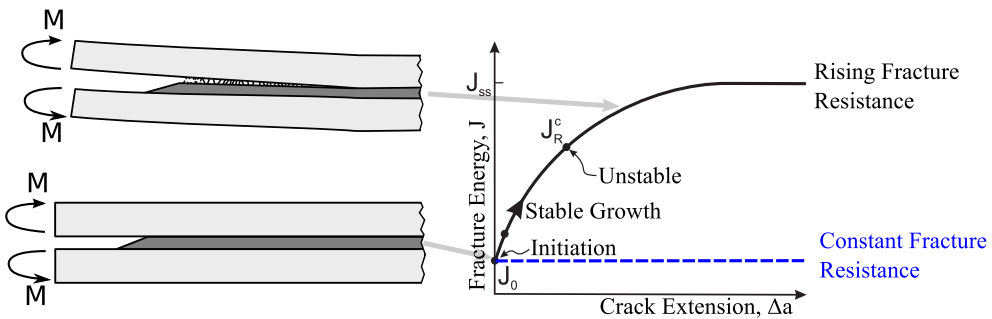
Figure 2.1: Schematics of stable and unstable crack growth due to R-curve behaviour. The crack growth resistance increases from an initial value, J_0, to a steady-state value, J_{ss}.
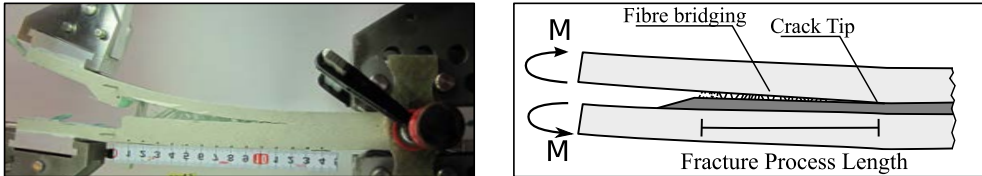
Figure 2.2: Fibre bridging phenomena during delamination in a glass fibre double cantilever beam specimen.

Accepting that a wind turbine rotor blade can operate with a certain amount of damage, requires that each structure must be characterized individually with a unique damage map. Then, once this is achieved, the service life and maintenance plan of each rotor blade can be decided based on their damage state.

2.2   Structural Health Monitoring

A standalone damage tolerance design criterion without a damage monitoring system is not enough for a reliable wind turbine rotor blades design. Due to the wind turbine operational nature and its remote location without easy access, inspection and maintenance activities cannot be made regularly. Therefore, checking if the structure is still inside the damage tolerance limits becomes almost impossible; additionally, it is impossible to predict the aerodynamic load history on a rotor blade for 20-30 years of operation, which makes an accurate and detailed model of its damage behaviour, for that period of time, difficult to produce. Furthermore, each blade will experience its own combination of load history, and its material properties can have some variation as this cannot be accurately controlled during the manufacturing stage.

A structural health monitoring system (damage condition monitoring) integrated in the damage tolerance design gives information about the presence of damage and its severity; then, this information is fed back to the damage tolerance model, where the structure damage state and remaining operational life are evaluated; if a repair action is required, the sensor provides the damage location with a good resolution and a repair plan can be establish. A good structural health monitoring system should be applicable to different life-stages of the wind turbine, as manufacturing, design, operation, emergency situation, etc., in order to measure the maximum information possible and produce the unique damage map of the structure.

In terms of sensing systems, there is a large variety of techniques that have been implemented in the different wind turbine sub-components to prevent failure. Oil debris monitoring can detect early damage in bearing and gear elements [11]; temperature measurements can identify a premature degradation of the different oils, bearings and generator windings [12]; wind turbine performance monitoring is a good indication of the structure efficiency, and it can measure global structural problems

like rotor imbalance [12, 13]; operational modal analysis is a technique that estimates the modal parameters by measuring vibration in the structure [14, 15]. Takoutsing, et al.[16] did an overview of all the different sensing technologies available and implemented in operational/research wind turbines (see Table 2.1).

Table 2.1: Wind turbine failure types in different components and monitoring techniques. Based on table 1 from [16].

Wind Turbine Component	Sub-Component	Type of failure	Sensing Technology
Rotor	Blades	Cracks; Adjustment error; Coating erosion;	Ultrasound; Active thermography; High resolution images; Strain measurements; Visual inspection; Torque measurements; etc.
	Bearings	Spalling; Wear; Defect of bearing shells and rolling elements;	Vibration; Modal analysis; Performance monitoring; Acoustic Emission; Strain measurements; Visual inspection; Torque measurements; etc.
	Shaft	Fatigue; Cracks;	Vibration; Modal analysis; Performance monitoring; Acoustic emission; Strain measurements; Visual inspection; etc.
Drive Train	Main Shaft Bearing	Wear; Vibration;	Vibration; Modal analysis; Strain measurements; Visual inspection; Power signal; Thermography etc.
	Mechanical Brake	Locking position;	Temperature; Visual inspection; Power signal; etc.
	Gearbox	Wearing; Electrical problems; Slip rigs; Winding damage; Rotor asymmetries; Bar break; etc.	Performance monitoring; Temperature; Vibration; Power signal analysis; Electrical effects; etc.
Tower	Tower	Crack formation; Fatigue; Vibration; etc.	Vibrations; Strain measurements; High resolution images;
	Nacelle	Fire; Yaw error; Damage; etc.	Smoke, heat and flame detectors; Strain measurements; etc.

In terms of monitoring systems for delamination/cracks detection in FRP structures, some techniques have been extensively study and applied to wind turbine rotor blades: acoustic emission technique evaluates the energy released during crack propagation [17, 18]; modal analysis method uses inertia sensors to identifying and locate damage in the rotor blade cross section [17]; and, ultrasonic scan measurements are used to detect defects, especially in the layer between the skin laminate and the load carrying main spar [19]. Although, it should be pointed out that most of these techniques can only be applied in controlled environments, as test wind turbines in laboratories or testing facilities, and cannot be applied to an operational wind turbine. Additionally, some of these techniques are not commercially available and have some reliability issues.

The requirements that a structural health monitoring system need to fulfil in order to be considered a good solution for delamination/cracks detection, and support the damage tolerance design of wind turbine rotor blades are:

- commercially available with diverse sensing solutions/configuration, and competitive price;

- can be used in an operational wind turbine;

- can be integrated/embedded into the structure material;

- high resolution and accuracy;

- long-term reliability,

- electromagnetic isolation;

- non-conductive (lighting isolation);

- can be implemented during the manufacturing process;

- can measure different type of parameters, and performed these measurements in different life-stages of the wind turbine;

Based on these requirements, a structural health system based on optical fibres was selected for this PhD project. A detailed description of this type of sensors, and examples of its application to different life-stages of the wind turbine are presented in the next section and in the papers [**P2-P6**].

2.3   Fibre Bragg Grating as a Structural Health Monitoring System for Wind Turbine Rotor Blades

2.3.1   Fibre Optic

A fibre optic is a cylindrical shaped cable, made of a transparent material (usually silica), within which light propagates with a very small optical loss [20, 21]. The glass fibre is typically composed of a core, a cladding, and an external coating (usually polyamide), and its external diameter varies from 100 μm to 250 μm, as shown in Fig. 2.3. The light propagation through the optical fibre can be describe by Snell law

[20, 22], which defines the relation between the reflection and refraction angle of an electromagnetic wave, as described by Eq. (2.1).

$$n_{core}sin(\theta_i) = n_{cladding}sin(\theta_t) \tag{2.1}$$

The parameters n_{core} and $n_{cladding}$ are the refractive index of the fibre optic core and cladding, respectively, and θ_i and θ_r are the light incidence and refraction angle, respectively. The parameter θ_c defines the critical angle that the light is transmitted; in other words, if the light incidence angle is greater than θ_c no light is transmitted and the optical power is lost (see Fig. 2.4).

In a conventional optical fibre, the core refractive index is slightly higher than the cladding, due to the presence of dopants; then, the critical angle can be defined as the incidence angle that corresponds to a reflected angle of $\theta_r = \pi/2$:

$$\theta_c = sin^{-1}\left(\frac{n_{cladding}}{n_{core}}\right) \tag{2.2}$$

Note that for angles $\theta_r < \pi/2$ the light is not reflected back to the core.
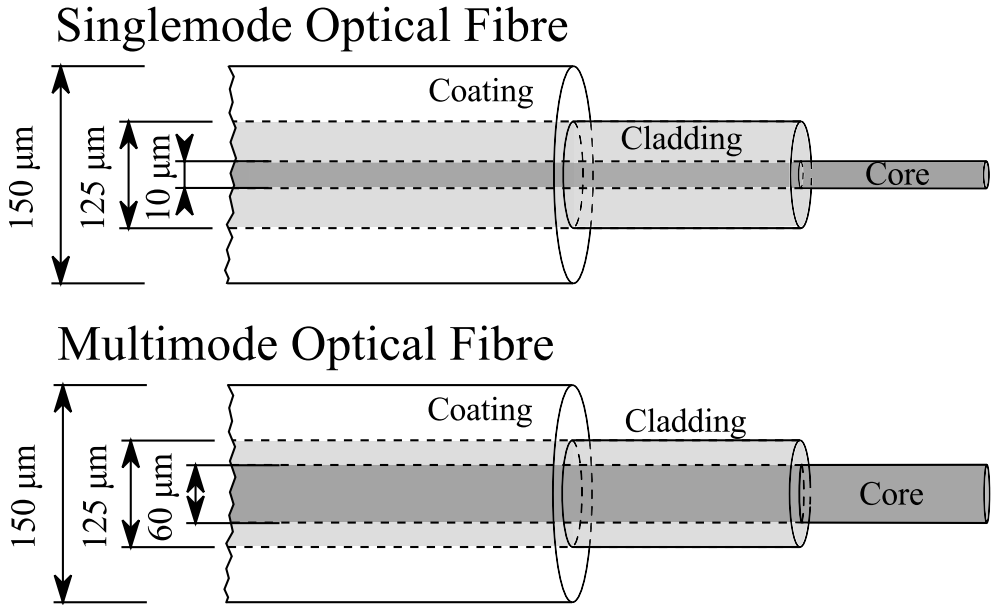
Figure 2.3: Schematic representation of optical fibre dimensions: singlemode and multimode optical fibre.
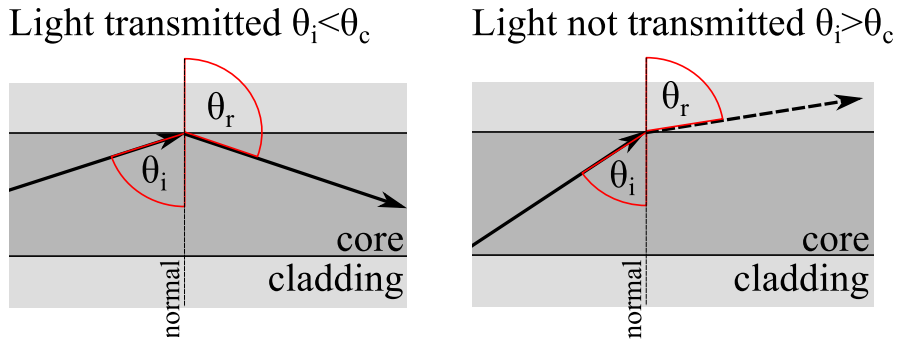
Figure 2.4: Schematic of Snell's law for light propagation in an optical fibre.

In terms of light propagation modes the optical fibre can be divided in two types (see Fig. 2.5):

- Singlemode/Monomode optical fibre; this type of fibre optic has a small core diameter, $\approx 10\mu m$, and the light propagates in a single mode; the main advantage of this type of optical fibre is its low optical attenuation, which makes it the most used technology for sensing applications; (Note: this is the type of optical fibres used during the PhD project)

- Multimode optical fibre; with a larger core diameter, between $30 - 100\mu m$, this type of optical fibre has a higher light-gathering capacity, which allows more waveforms to be transmitted, however with a big attenuation; the main advantage of this type of optical fibre is that requires simple connections and uses lower-cost electronic components.
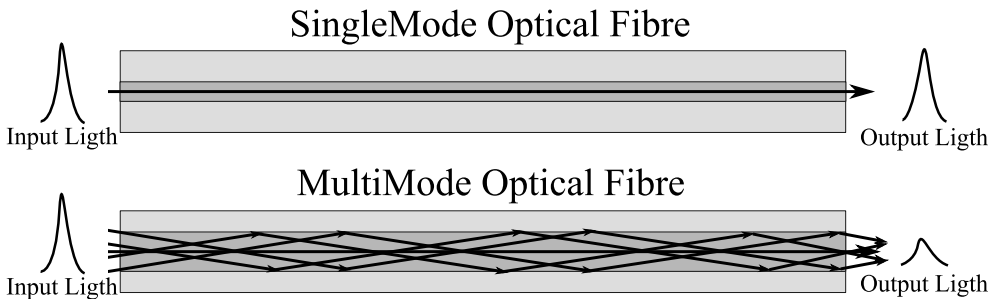
Figure 2.5: Schematic of the different fibre optics's light propagation mode: single-mode and multimode.

Regarding fibre optic sensors, these can be classified based on its [23]:

- Location: intrinsic, when the sensing region is within the fibre structure; or extrinsic, when the light leaves the optical fibre to reach the sensor and then returns to it;

- Operation principles: intensity, phase, frequency, or polarization;

- Application: physical sensor; chemical sensor;

In table 2.2, some sensing solutions that are used for structural health monitoring are presented. In all these sensing solutions, the measured information is encoded as a light (reflected or transmitted) giving this system unique properties, such as immunity to optical/power fluctuation, insulation and immunity to optical/power, long distance measurements, high rate sampling, etc.

Table 2.2: Different type of sensing solutions based on fibre optic.

Type of sensor		Sensing principle
Intrinsic	Local	Intensity-based sensors; Micro-bending sensor; Fabry-Perot interferometer; Michelson interferometer; Bragg gratings;
	Distributed	Raman scattering; Brillouin scattering;
Extrinsic		Optical Coherence Tomography; Encoders; Temperature measurement using a pyrometer;

As observed, there is a large variety of fibre optic based sensors that can be used as a monitoring system for wind turbine rotor blades; however, it is important to select a type of sensor that is commercially available, economically competitive (when compared with other measurement technology's), can measure different type of physical properties, and has a big potential in the wind energy and FRP materials field. Thus, the fibre Bragg grating sensor was selected as the monitoring technology for this PhD project.

2.3.2 Fibre Bragg Grating

A fibre Bragg grating (FBG) is a sensor based on fibre optic technology that was first demonstrated by Hill, et al. [24, 25]. The grating structure is formed by a permanent periodic modulation of the refractive index along a section of an optical fibre, obtained by exposing the optical fibre to an interference pattern of intense ultra-violet light [20–22]. The photo-sensitivity of the silica exposed to the ultra-violet light is increased, so when the optical fibre is illuminated by a broadband light source part of this light is reflected back. The reflected light shape and wavelength depends on the modulation of the fibre optic core refractive index (δn_{eff}).

The δn_{eff} is described by Eq. (2.3),

$$\delta n_{eff}(x) = \overline{\delta n_{eff}}(x) \left\{ 1 + \nu cos \left[\frac{2\pi}{\Lambda} x + \phi(x) \right] \right\} \tag{2.3}$$

where the parameter ν is the fringe visibility, $\phi(x)$ is the change in the grating period along the length, Λ is the grating nominal period, and $\overline{\delta n_{eff}}(x)$ is the mean induced change in the refractive index [26, 27]. The index x denotes the longitudinal direction along the optical fibre. Any combination of these parameters allow the fabrication of a grating, although the two most common types are (see Fig. 2.6):

- homogeneous grating; where the grating has a uniform periodic perturbation in the refractive index of the fibre core ($\phi(x) = 0$), and the reflection spectrum has one narrow peak at the Bragg wavelength [21];

- chirped grating; where the perturbation in the refractive index has a linear variation along the grating's length, which causes a broad reflected spectrum [28];
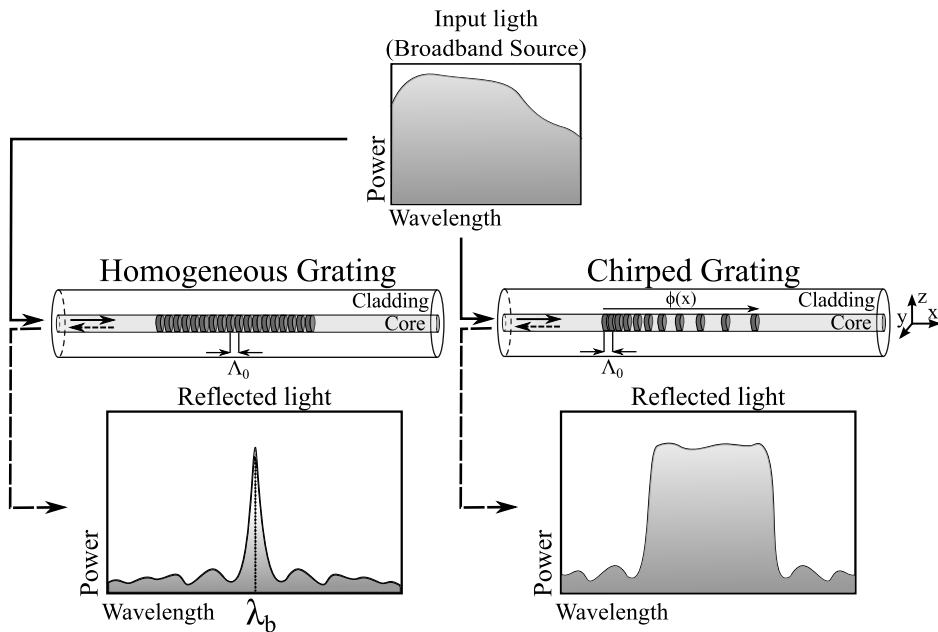
Figure 2.6: Schematic of the light reflection in a homogeneous and chirped grating. The parameter Λ_0 is the grating nominal period in an unstrained state; $\phi(x)$ is the change in the grating period along the length.

Both type of gratings have a similar measurement principle; i.e., any external load or temperature variation affecting the grating region changes the effective index of refraction and/or the period of modulation, which creates a change in the shape and/or wavelength of the reflected light. Then, by tracking this change, it is possible to obtain an indirect measurement of the strain field and temperature variation around the grating region.

The homogeneous grating is the most common type of FBG sensor, and it can be found with a large choice of sensor configurations; also, this type of sensor has been extensively studied, and examples of FBG's applied to monitor different physical parameters within different fields (as aerospace, civil engineering, automotive, and wind energy), can be found in literature [29–32]. The chirped FBG sensor is a more recent technology, and it presents some advantages compared to the homogeneous grating, as it is highly sensitive to non-uniform strain fields. This property gives the sensor the ability to monitor crack propagation in polymers or fibre reinforced polymers with a high resolution [33, 34]. However, the chirped FBG uses a larger bandwidth per grating, fact that reduces its multiplexing capability. Therefore, having fewer sensor per fibre optic line is the trade-off for higher non-uniform strain measurement resolution.

The *MareWint* project partner that provided the FBG sensors (*HBM-Fibersensing*), only produces the homogeneous grating type; thus, only homogeneous FBG were used in this PhD project. However, the FBG's were customized, in length and in its multiplexing configuration, to fit the different tests and applications addressed.

2.3.2.1   Measurement Principle

The spectral response of a homogeneous fibre Bragg grating is a single peak centred at wavelength λ_b, as shown in Fig. 2.6. This can be described by the Bragg condition,

$$\lambda_b = 2n_{eff}\Lambda_0 \tag{2.4}$$

where n_{eff} is the mean effective refractive index at the location of the grating, and Λ_0 is the constant nominal period of the refractive index modulation [21]. Any measured change of the reflected spectrum can be correlated with the strain field or temperature variation in the structure.

Response to uniform uniaxial strain field: when the grating is under a uniform uniaxial strain field, the reflected peak λ_b shifts proportionally to the strain magnitude, as shown in Fig. 2.7a). This strain-wavelength shift relation can be describe by,

$$\Delta\lambda_b = \lambda_b(1 - p_e)\varepsilon \tag{2.5}$$

where the parameter $\Delta\lambda_b$ is the reflected peak wavelength shift, p_e is the optical fibre photo-elastic coefficient, and ε is the uniform uniaxial strain field magnitude [20, 35].
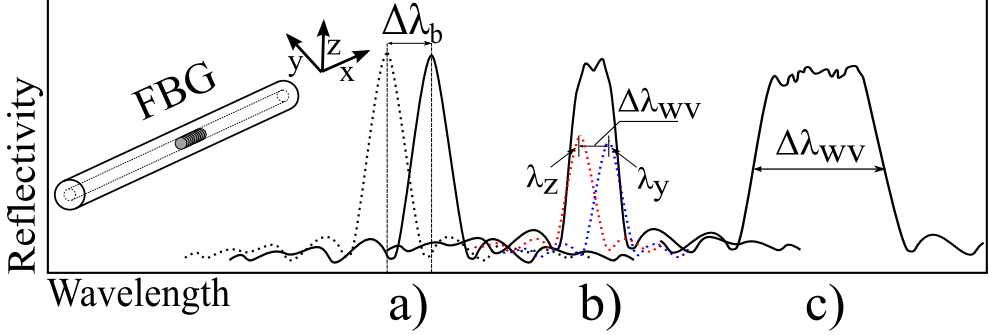
Figure 2.7: Homogeneous fibre Bragg grating response: a) response to uniform uni-
axial strain field, $\Delta\lambda_b$ is the reflected peak wavelength shift; b) response
to transverse stress, $\Delta\lambda_{wv}$ is the width of the peak split, λ_z and λ_y are
the polarized reflect waves; c) response to non-uniform uniaxial strain
field.

Response to transverse stress: a grating under a transverse stress field can ex-
hibit a birefringent behaviour, which can be described by the change of the refractive
index of the two polarized directions, n_{effy} and n_{effz}. This change in the isotropic
optical fibre structure creates a separation of the reflected peak in to two polarized
waves, as shown in Fig. 2.7b). The width of the peak split $\Delta\lambda_{wv}$ can be calculated
by,

$$\Delta\lambda_{wv} = \frac{\Lambda n_o^3}{E_f}[(1 + \nu_f)(p_{12} - p_{11})]|\sigma_z - \sigma_y| \qquad (2.6)$$

where the parameter E_f is the elastic modulus of the optical fibre, ν_f is the Poisson's
ratio, n_0 is the initial refractive index, p_{11} and p_{12} are the photo-elastic coefficients
of the optical fibre, and σ_y and σ_z are the stress acting in the grating transverse
direction [36–38].

Response to non-uniform uniaxial strain field: when the grating is under
a non-uniform strain field (strain gradient), its grating periodicity Λ changes from
uniform to non-uniform, which causes a distortion in the reflected peak [36, 39–41].
Strain evaluation based on a distorted peak can be very challenging, however this
information can be used to quantify other phenomena that can cause this type of
non-uniform strain field, like cracks, defects, etc.

Response to temperature: in a free grating (not embedded), temperature varia-
tion causes the fibre optic to thermally expand, which changes its grating periodicity

Λ, and its refractive index n_{eff}. Thus, the wavelength shift $\Delta\lambda_b$ caused by temperature variation can be described by,

$$\Delta\lambda_b = 2\left(n_{eff}\frac{\partial\Lambda}{\partial T} + \frac{\partial n_{eff}}{\partial T}\Lambda\right)\Delta T = \lambda_b[(1-p_e)\alpha_f + \xi]\Delta T \qquad (2.7)$$

where the parameter ΔT is the temperature change, α_f is the optical fibre thermal expansion coefficient, and ξ is the thermo-optic coefficient [29, 42, 43].

Embedded FBG response to strain and temperature: an embedded FBG sensor presents a strain-temperature cross sensitivity; i.e., the load induced strain, the temperature induced thermal expansion, and the thermal-optic cross dependency generates the same sensor response, a wavelength shift of the reflected peak $\Delta\lambda_b$. Therefore, this temperature-strain cross sensitivity can be problematic for tests/applications where strain and temperature varies simultaneously. The response of an embedded FBG response to strain and temperature is described by Eq. (2.8), where the parameter α_h is the thermal expansion coefficient of the host material.

$$\Delta\lambda_b = \lambda_b[(1-p_e)\varepsilon + ((1-p_e)\alpha_h + \xi)\Delta T] \qquad (2.8)$$

A detailed description of the FBG measurement principle can be found in:

- **[P3] and [P4]**- FBG response to uniform uniaxil strain, non-uniform strain, and transverse stress field; FBG response during crack growth;

- **[P2]**- FBG response to strain and temperature; strain-temperature cross-sensitivity; technique for independent measurement of strain and temperature;

- **[P6]**- FBG response to strain and temperature; strain-temperature cross-sensitivity; cure-induced residual strain measurement;

2.4   "Smart" Rotor Blade Design

As previously discussed, a unique damage mapping of each wind turbine rotor blade is required to support the damage tolerance design and to accurately predict its remaining lifetime. To achieve this, the different life stages of the rotor blade need monitoring, and the measured information integrated into a global multi-life-stage model, a smart rotor blade model.

For a monitoring system based on fibre Bragg gratings some measured parameters at each life stage of the wind turbine rotor blade are:

- **Manufacturing process:** ensuring manufacturing quality level; process/blade certification; initial structure damage map; control cure process; improve manufacturing process; ensure consistency of defects, cracks, voids, dry-spots, etc. within an acceptable tolerance;

- **Transport:** ensuring that critical loads are not achieved; pre-assembly check;

- **Operation:** damage detection; load monitoring; structural stability; active control; vibration; damage mapping;

- **Extreme situation/Emergency stop:** damage assessment; load control;

- **Repair:** damage location; repair certification;

- **Decommissioning:** structural state; decommissioning or refurbishing; final structure damage map;

In a "smart" blade design philosophy (see Fig.2.8), the measured information is fed back to other stages. This allows improvement of each individual stage in the design process, and ultimately increases the structural reliability. For example, data from the operation stage will allow an analysis of the structural performance and a continuous improvement of the structure latest designs (concurrent engineering);
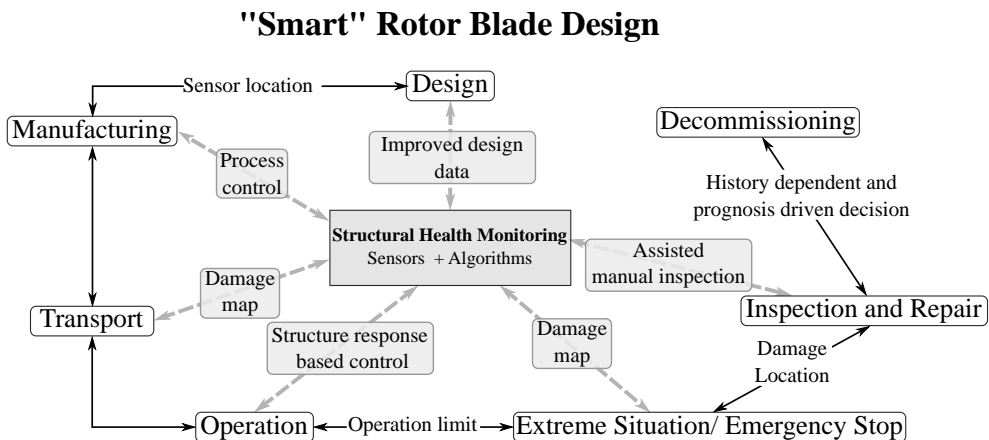
Figure 2.8: Life stages of a wind turbine rotor blade: "Smart" design based on structure health monitoring (SHM).

and, when an extreme load or a change in the material stiffness is detected, caused by damage, the wind turbine operation limit can be readjusted so the structure can operate safely until the next repair action.

However, it is not realistic to jump from the conventional turbine design to this purposed smart wind turbine concept, by simply implementing a FBG in the structure and monitoring different parameters at different life-stages of the structure and expect that this will lead to a structure that is able to operate safely in the presence of damage. The current FBG technology is only half the way through; i.e., the sensor and its different applications have been extensively studied and validated in a controlled environment, however there is a lack of knowledge about its behaviour in real applications, and how to integrate the data into the different stages. Also, there is a visible knowledge and skill gap between the structural design and monitoring design, where tools that can support the implementation of sensors into the design process are lacking.

2.5   Multi-Life-Stage Monitoring System Based on Fibre Bragg Gratings

Thus, this PhD project goals are to address these questions and decrease the gap between structural design and monitoring design, understand and improve measurement of different physical parameters, and to develop tools that allow an easy implementation and signal post-processing. To do this, the FBG technology is applied conceptually to three life stages of the wind turbine rotor blade: design, manufacturing and operation, as shown in Fig. 2.9.

This multi-life-stage concept defines the research activities performed during this PhD project, and consequently the publications content. The different areas addressed are:

- **FBG sensor: from FBG fundamentals to fibre reinforced polymer measurements.**

  As this field is applicable to all life-stages presented in Fig. 2.9, it was important to do a complete overview of the FBG technology and study how this knowledge can be applied to the different life-stages of the rotor blade. The different measurement possibilities are addressed in the different annexed publications, together with solutions for overcoming some sensor limitations, such as temperature-strain cross-sensitivity. The application of the FBG sensor to the material testing procedure, manufacturing process, and operation/damage situation, was analysed with the objective of finding the best implementation solution so different parameters can be monitored according to the relevant life-stage.
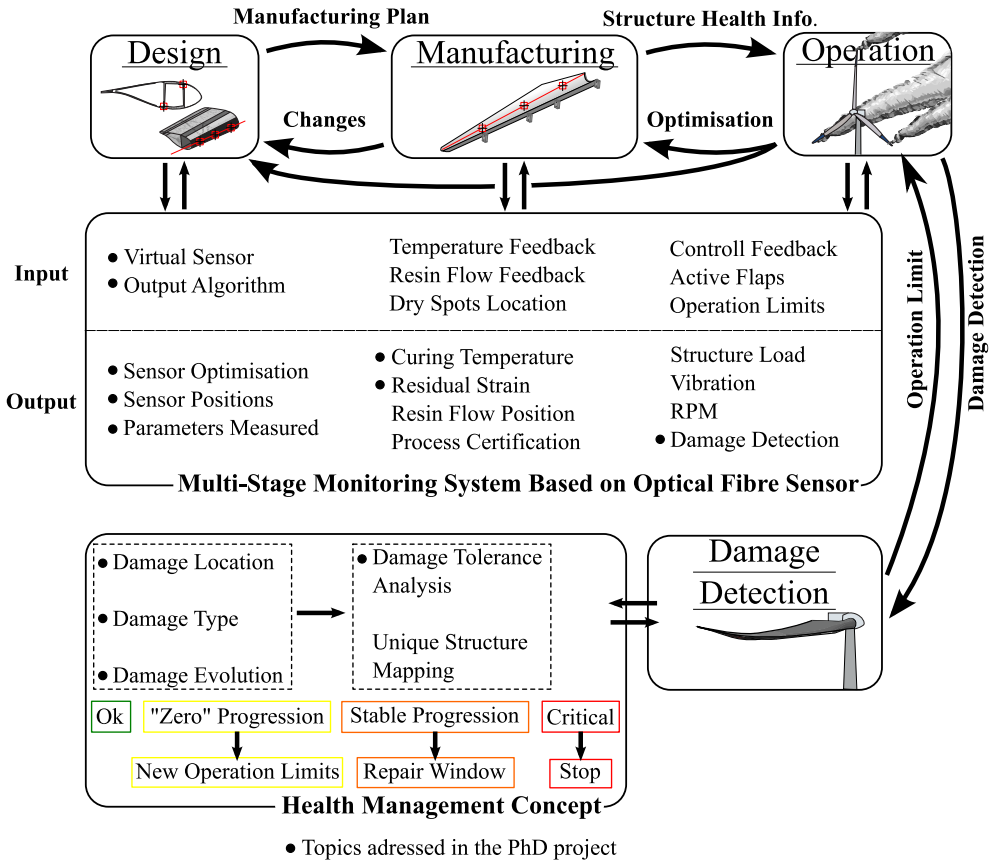
Figure 2.9: Schematic of the multi-life-stage monitoring system based on FBGs.

Topics addressed:

- FBG work principle: uniform strain, non-uniform strain, and transverse stress [**P3, P4**];
- FBG work principle: strain and temperature measurement [**P2, P6**];
- FBG signal post-processing [**P4**];
- FBG signal modulation [**P5**];
- Crack detection by FBG sensors [**P3, P4**];
- Cure-induced residual strain measurement [**P6**];
- Temperature-strain decoupling in tensile fatigue testing [**P2**];

- **Design stage: damage tolerant design and structural health monitoring.**

  At the design stage, and within the damage tolerant and structural health monitoring philosophy, two different topics were studied:

  a) **Damage modelling.** It is important to fully understand the fracture mechanisms that are present during delamination of FRP structures, so this can be connected with the FBG measurement principle, and the minimal crack length that can be detected by the sensor system can be determined. Thus, finite element method (FEM) models of delamination in a double cantilever beam (DCB) specimen and rotor blade trailing edge were developed and analysed. These FEM models were used to optimise the FBG sensors, in terms of location and multiplexing configuration, and also to study the impact of different fracture modes and loading condition on the FBG response.

     Further, FEM models rely on accurate material mechanical properties, such as fracture energy, cohesive behaviour, yield stress, Young's modulus, etc., to simulate the details of the damage mechanism in FRP structures. Thus, the fracture testing procedure by loading DCB specimens with uneven moments, was the other topic analysed within the damage modelling topic; where, the impact of the DCB specimen geometry, fracture properties, and fracture mode in the fracture process was analysed. In addition, this study allowed development of FEM models that are numerically and analytically validated, and that can be used as reference for the following work (as FBG crack detection).

     Topics addressed:

     - Delamination/fracture mechanisms overview [**P3, Appendix A**];
     - 2D/3D FEM model of DCB specimen: numerical and analytical validation [**P3, Appendix A**];
     - Fracture process zone length: geometry and fracture properties dependency [**P7**];

  b) **FBG response simulation.** The FBG sensor response depends on the way that the grating is deformed, i.e., the stress and strain field acting along the grating defines the shape of the reflected spectrum. Thus, FBG simulation becomes important in order to optimize the sensor for a certain application or physical parameter being monitored. As an example, in the crack detection approach using FBG sensors presented in paper [**P3**], FBG simulation was used to support the sensor configuration and location, and to obtain a sensing solution where the measurement capabilities were maximized while maintaining the sensor integrity/reliability (not damaging). Also, these FBG simulations give a prediction of the signal output, which can be used as the reference in the development of a real-time damage monitoring system.

Thus, a software (FBG_SiMul) to virtually simulate the FBG output and support the implementation of the sensors in different structures, which does not require a user with extensive knowledge about FBG sensors, was developed. This software's main objective was to reduce the knowledge/skill gap between structural design and the monitoring system field. Topics addressed:

– FBG signal modulation [**P5**];
– FBG signal output simulation from a FEM model [**P5**];
– User-interface software: FBG spectrum simulation and FBG time response [**P5**];

- **Manufacturing stage: FRP curing monitoring.**

  Within the manufacturing stage, FBG sensors can be used to monitor different parameters, such as the curing temperature, resin flow, presence of dry spots, etc., and eventually to certify the manufacturing process. The information measured can be used to improve the manufacturing process, and to ensure that critical parameters, like residual strain, maximum temperature, load, etc., are within the process limits. Additionally, these sensors, implemented in the manufacturing stage can be used to monitor other parameters in other life stages of the structure; for example, a sensor placed in the blade root to monitor the resin flow during the manufacturing stage can be used later, in the operation stage, to monitoring the loads/ bending moments at that location.

  In this PhD Project, the cure-induced residual strain and its impact on the FRP static and fatigue performance was studied. The main objective was to develop a residual strain measurement solution based on FBG sensors, which could be used to evaluate the impact of different curing parameters (temperature and curing time), on the total amount of epoxy shrinkage and residual strain. This information was used to design an optimum cure cycle, where the residual strain is minimized and the fatigue performance maximized.

  Topics addressed:

  – Multi-parameter measurement [**P2, P6**];
  – Temperature-strain decoupling [**P2, P6**];
  – Residual strain monitoring [**P6**];
  – Influence of residual strain in the FRP static and fatigue performance [**P6**];

- **Operation and Damage Detection stage**

  Within the operation stage, FBG sensors can be used to monitor different structural parameters, as load/ strain levels, vibration, temperature, which can be used to ensure that the structure is within the operation limits. When implemented with an active control system, the FBG sensors can be used to control

the blade pitching in real-time, using the strain measurements from the rotor blade root[1]. However, only damage detection during operation was the focus of this PhD project within the operation stage.

In order to simulate the failure of the trailing edge of the DTU 10 MW reference wind turbine, DCB specimens produced with the same material configuration as the trailing edge were tested in different fracture modes, and the different features of the damage mechanism were analysed using digital image correlation. Thus, specific phenomena caused by the crack, such as non-uniform strain or transverse stress, were correlated with the FBG response, and proved that by tracking this information the sensor response is independent of the loading type, geometry and boundary conditions, and depends only on the presence of damage. Additionally, the DCB FEM models and sensor simulation developed at the design stage were validated experimentally, and the consistency of the results showed that the FBG_SiMul software can predict the sensor output, and it is an excellent tool to design the sensor configuration in an intuitive and reliable way.

Topics addressed:

- Damage detection by FBG sensors [**P3, P4**];
- DCB experimental validation: crack detection with embedded FBG sensors [**P3, P4**];
- FBG_SiMul software: sensor optimization, sensor position and signal simulation [**P3, P4, P5**];
- Trailing edge delamination detection by FBG sensor: FBG_SiMul simulation [**P5**];

---

[1]Prototype system for pitch control: Eleon On-Shore Prototype Wind Turbine, `http://www.fibersensing.com/market/wind/view/pitch-control-16`

Chapter 3

Summary of Results and Concluding Remarks

The *SEVEN PAPERS* [**P1-P7**] and their contribution to this PhD project are briefly presented below. The papers cover all the topics addressed within the multi-life-stage monitoring system based on fibre Bragg grating sensors. Starting from a new design philosophy, based on damage tolerant design and structural health monitoring, where a wind turbine rotor blade can operate even in the presence of damage. Then, this concept is explored using FBG sensors as the selected structural health monitoring technology, and its capability to measure different parameters at different stages, such as crack detection, independent strain-temperature, residual strain, etc., is demonstrated. There is then presented a software (*FBG_SiMul*) developed to simulate the FBG sensor signal response to most of the applications. This software reduces the knowledge/skill required to implement this structural monitoring system in the design process of a wind turbine rotor blade. Within the topics addressed in this PhD, the software was applied to FEM models of the DCB and trailing edge delamination. Collectively, these articles seek to trace the research path required for a viable multi-life-stage monitoring system, which can be applied to a wind turbine rotor blade.

3.1 Summary of Results

Damage tolerance and structural health monitoring, Paper P1

In Paper P1, a methodology for reliable design and maintenance of wind turbine rotor blades based on a damage tolerance an structural health monitoring approach is presented. This design philosophy allows a structure to operate despite the presence of damage. To accomplish this, the structure is designed with damage tolerant materials with built-in sensors; and, the damage detected by the sensors is feedback in to models that predict the residual life of the structure, and then plan the required maintenance/inspection action.

Examples are given on how materials can be tailored to provide higher damage tolerance, and the concept of a damage tolerance index is introduced. Finally, the steps required for a gradual implementation of this proposed design philosophy are presented.

Independent measurement of strain and temperature by embedded FBG sensors, Paper P2

Paper P2 was developed within the FBG measurement fundamentals, and it presents a novel method to obtain independent strain and temperature measurements using embedded FBG sensors in polymeric tensile tests. The temperature and strain cross-sensitivity is an issue for measurements with embedded FBG sensors, especially in long tests, where external variation of temperature can occur. This temperature variation generates a thermal strain that is not taken into account by the measurement system, inducing an error on the strain measurement.

Thus, the fundamental equations that describe the sensor response to temperature and strain are analysed in this article; and, the strain and temperature cross-sensitivity is decoupled by using a novel tensile specimen set-up, composed of two FBGs sensors embedded with a certain angle between them. Equations describing this method, which allows strain and temperature calculation from the FBGs signal, were derived from the general FBG work principal. This multi-parameter measurement method is demonstrated and validated in an epoxy tensile specimen, tested in a unidirectional tensile test machine with a temperature controlled cabinet. Finally, two calibration protocols are suggested, one that is fast to perform, and the other having higher accuracy, obtaining an independent measurement of temperature and strain with an error smaller than 1%.

Crack detection in FRP materials by FBG sensors, Paper P3

Paper P3 fits within the design and operation stage, described in the wind turbine rotor blade multi-life-stage monitoring system. The crack detection by embedded FBG sensors is the central topic addressed in this article, where a novel method is presented for assessing a crack growth event in fibre reinforced polymer or structural adhesive bonded structures by combining conventional measured parameters, such as wavelength shift $\Delta\lambda_b$, with parameters associated with measurement errors. It is demonstrated that specific FBG responses, peak-splinting and peak-width, can be correlated with the presence of damage, and it was shown that this information is independent of the loading, structure geometry, and boundary conditions, and only depends on the proximity of the crack.

To achieve this, three different topics in the article are explored:

- damage mechanisms. Where the delamination/fibre bridging in DCB specimens is analysed for different fracture modes, and the stress distribution along the crack is simulated;

- FBG crack detection principle. Here, the sensor response for different damage situations is characterized (experimentally);

- FBG simulations using DCB FEM models. Both previous topics are merged together into a tool (algorithm) used to predict the sensor output, and where the sensor-structure configuration can be optimized.

This monitoring method was demonstrated and validated using DCB specimens instrumented with an array of 5 FBGs embedded in the material, and tested using an experimental fracture procedure. The strain field in the DCB specimens during the fracture test was monitored with the digital image correlation technique, which was used to link the different fracture features with the sensor response, and consequently validate the FBG detection principle suggest by the authors.

FBG signal post-processing algorithm for crack detection, Paper P4

This paper P4 is a continuation of the work developed in paper P3, with a special focus on the FBG signal post-processing. The digital image correlation measurements, and the correlation between the FBG response and the different fracture/crack features are explored with more detail here. An algorithm for post-processing the FBG output raw signal is presented, which can evaluate the shape of the reflected wave and distinguish between a single peak and a multi-peak. This algorithm gives two more parameters than the conventional FBG measurements (conventional system- wavelength shift; algorithm- number of peaks,wavelength shift, and peak width). The algorithm was demonstrated and validated using DCB specimens instrumented with an array of 5 FBGs embedded in the material and tested using an experimental fracture procedure.

FBG_SiMul: FBG signal simulation software, Paper P5

There is a lack of tools that can support the implementation of FBG sensors into structural health monitoring application, and there is a knowledge gap between the wind turbine rotor blade designer and the fibre optic expert. Thus, in paper P5 a software to simulate the FBG signal from a FEM model was developed. This software is a design tool that can be applied to any kind of structure or application, and it removes the need of an expert user in fibre optic technology. The software FBG_SiMul has a graphical user-interface, meaning that no programming knowledge is required from the user, and parameter manipulation is more intuitive. All the input parameters are pre-checked by the code, meaning that the simulation is robust and does not crash or give calculation errors.

The software uses a modified T-Matrix method to simulate the reflected spectrum based on the stress and strain from a FEM model. The theory and algorithm implementation are presented, and an empirical validation is performed. The software is divided in to 3 main tools: a tool to extract the stress and strain along an optical fibre path from a FEM model; a tool to simulate the reflected spectrum for a specific time increment; and, a tool to simulate the FBG time response. A user-manual is provided together with the software, and a illustrative case is presented, where the FBG sensor is simulated and optimized for crack detection.

Cure induced residual strain measurements by FBG, Paper P6

Paper P6 fits within the manufacturing stage, described in the wind turbine rotor blade multi-life-stage monitoring system, in which a residual strain measurement solution based on FBG sensors is presented. The main goal is to evaluate the impact of different curing parameters (cure of an epoxy system), in the cure induced residual strain, static performance, and fatigue life.

To do this, a new FBG measurement methodology (algorithm) was developed, which allows temperature-strain cross sensitivity decoupling, and gives as output the residual strain, the resin temperature, and curing gelation time. It is demonstrated experimentally that the residual strain strongly depends on the curing temperature and on the reaction exothermic peak, increasing as these two parameters increase. The tensile tests performed showed that the residual strain had no impact on the epoxy and FRP static performance; although, the fatigue test results showed that the FRP fatigue performance is decreased when the curing temperature increases, suggesting that the FRP fatigue performance strongly depends on the amount of cured induced residual strain.

The results achieved have a tremendous importance for the control and optimisation of the cure process of wind turbine rotor blades, and demonstrates that a FBG sensor can be used to minimize the residual strain and ensure that critical parameters, such as residual strain or resin temperature, are within design limits.

Fracture process zone length in DCB specimens: geometric and cohesive-law dependency, Paper P7

This article is a result of the work presented in Appendix-A, and even if it does not fit within the multi-life-stage monitoring system, it has a big impact on the DCB fracture testing, and consequently in the fracture properties used in the FEM models that were developed within this PhD project.

One requirement of the DCB fracture test procedure, where the J-integral is used to evaluate the energy release rate, is that a steady state fracture energy should be obtained; in other words, a fully formed fracture process zone should fit within the specimen length. Thus, the specimen geometry and cohesive law influence on the fracture process zone length (FPZL) is analysed in the article. Analytical equations describing the FPZL for 3D DCB specimens are derived from literature and beam theory, and numerical validation is performed. It is demonstrated that the FPZL is strongly influenced by the specimen geometry, especially in DCB specimens with side-grooves, where the FPZL increases exponentially with the ratio side-groove/specimen width. Also, it is shown that ductile cohesive-law materials have a larger FPZL, which can be critical in fracture mode-II loading. Finally, simplified equations that describe how the FPZL scales with the geometry and fracture properties are developed, these can be used to design the specimen dimension in order to obtain a valid fracture test.

3.2   Contributions and Impact

The work presented sets the required framework to developed a multi-life-stage monitoring system based on fibre Bragg gratings, and how it fits within a damage tolerant design for a wind turbine rotor blade. The work focused on three life stages, design, manufacturing, and operation, and in future should be applied to the reaming life-stages. Nevertheless, it is shown that a structural health monitoring system should be applicable to all design stages and considered an integrated part of the structure, and not only a damage assessment tool. To the author's knowledge, no research papers deal with the integration of FBG sensors at different life stages of the wind turbine, or approach the FBG measurement principles in different fields, as signal simulation, FEM prediction, material testing, etc.

Paper [P1] describes a completely new approach of wind turbine rotor blade design, based on a damage tolerance design, where a wind turbine can operate safely even in a damaged state. The materials and monitoring requirements needed to achieve this are set in this work; and, once accomplished it can give the technological opportunity to enable the future very large wind turbine rotor blades. This article sets the common ground for the remaining articles developed in this PhD project.

In paper [P2] and [P6], the measurement capabilities of FBG sensors in material testing and its strain-temperature coupling issues are explored. The author believes that a FBG sensor, implemented in the manufacturing stage of a wind turbine rotor blade, can control a large variety of parameters during the different life stages of the structure; one application can be to monitor if the material mechanical properties (ex: stiffness) are within the design limits. Thus, it becomes important to use FBG sensors in the material testing procedure, not only to characterize the material but also to understand and calibrate the sensor for that application. Paper [P2] addresses the strain and temperature cross-sensitivity issue of embedded FBG sensors, and a method to obtain independent strain and temperature measurement in polymeric tensile test specimens is presented. This method is specially useful for fatigue testing, where the material self-heating generates a thermal-strain caused by thermal expansion. The main advantage of this method is that it does not required any extra hardware (uses conventional FBGs and conventional interrogators), and is simple and fast to implement.

In Paper [P6], the effect of the curing temperature in the residual strain and material performance is analysed. To the author's knowledge, no research has been made to link the curing profile with these different material properties, or even using FBGs to optimize the curing process. This methodology (algorithm developed) can be directly implemented in the rotor blade manufacturing stage, allowing a real-time residual strain measurement and a controlled curing process.

In paper [P3] and [P4], the crack detection in FRP structure by embedded FBG sensors is addressed. A novel method for crack detection by combining conventional measured parameters with parameters associated with measurement errors is presented. A signal output post-processing algorithm is developed, and the crack detection method is applied to DCB specimens loaded in different fracture modes. The

novelty of this work, is that the sensor measurement principle was analysed from a material and damage mechanism perspective, which allowed us to create a tool that can be used to predict the sensor output, and to optimize the sensor-structure configuration.

The implementation of FBG sensors in monitor application is not a trivial task, as it requires a user/designer with an extensive knowledge about the FBG measurement principle. Inspired by this, in paper [P5] a software that simulates the FBG signal from a FEM model is presented. This software will allow sensor simulation to become part of the design process, where output is simulated and optimised to a structure or application. This will have an immediate impact on the planning, development and implementation of monitoring approaches, as well as promoting further research to include active control elements in the software and real-time data-driven feedback control for smart structures in the future. Equally important is that the software is robust and runs from a user friendly interface, and can be applied to any kind of FEM software, and to the author's knowledge, no tool has been developed to perform such function.

3.3   Future Work

As mentioned previously, this work sets the framework required to obtain a multi-life-stage monitoring system based on FBG sensors; however, due to the short duration of the PhD project, there is more research topics that need to be addressed to achieve such a concept. The sensor can provide useful information in other life-stages of the wind turbine rotor blade, such as repair, transport, etc.; thus, expanding this concept to those stages, and analysing which physical parameters can be monitored by the FBG sensors, is the next step to take into consideration. Furthermore, inside the life-stages addressed, there are more parameters that can be monitored, especially in operation, where the sensor can monitor loads and provide information for active control of the structure.

Measurement reliability and viability studies in an operational wind turbine rotor blade will raise other type of challenges that need to be considered, such as how to install the sensors, sensor replacements/repair, calibration, etc.

Finally, all this FBG-measured information will require decision making algorithms, and action protocols, to deal with possible problems detected. Thus, there is a lot of work to be made in terms of data post-processing/analysis, and integration with other measurement systems.

Bibliography

[1]   G. Corbetta, A. Ho, and I. Pineda, "Wind energy scenarios for 2030," European Wind Energy Association (EWEA), Tech. Rep. August, 2015, pages 1–16.

[2]   T. K. Jacobsen, "Materials technology for large wind turbine rotor blades—limits and challenges," in *32nd Risø International Symposium on Material Science, Composite materials for structural performance: Towards higher limits*, S. Fæster, D. J. Jensen, B. Ralph, and B. Sørensen, Eds., Roskilde, Denmark, September 2011, pages 35–43.

[3]   S. Krohn, P.-E. Morthorst, and S. Awerbuch, "The economics of wind energy," European Wind Energy Association (EWEA), Tech. Rep. March, 2009, pages 1–156.

[4]   C. Bak, F. Zahle, R. Bitsche, A. Yde, L. C. Henriksen, A. Nata-, and M. H. Hansen, "Description of the dtu 10 mw reference wind turbine department of wind energy i-report," DTU Wind Energy, Tech. Rep. July, July 2013, pages 1–138.

[5]   D. F. Braga, S. Tavares, L. F. da Silva, P. Moreira, and P. M. de Castro, "Advanced design for lightweight structures: review and prospects," *Progress in Aerospace Sciences*, volume 69, pages 29–39, August 2014, ISSN: 03760421. DOI: 10.1016/j.paerosci.2014.03.003.

[6]   A. F. Grandt Jr., *Fundamentals of Structural Integrity: Damage Tolerant Design and Nondestructive Evaluation*. Wiley, 2003, ISBN: 0471214590.

[7]   J. Schijve, "Fatigue damage in aircraft structures, not wanted, but tolerated?" *International Journal of Fatigue*, volume 31, number 6, pages 998–1011, Jun. 2009, ISSN: 01421123. DOI: 10.1016/j.ijfatigue.2008.05.016.

[8]   Z. Suo, G. Bao, and B. Fan, "Delamination r-curve phenomena due to damage," *Journal of the Mechanics and Physics of Solids*, volume 40, number 1, pages 1–16, January 1992, ISSN: 00225096. DOI: 10.1016/0022-5096(92)90198-B.

[9]   B. F. Sørensen and T. K. Jacobsen, "Characterizing delamination of fibre composites by mixed mode cohesive laws," *Composites Science and Technology*, volume 69, number 3-4, pages 445–456, March 2009, ISSN: 02663538. DOI: 10.1016/j.compscitech.2008.11.025.

[10]   S. Spearing and A. Evans, "The role of fiber bridging in the delamination resistance of fiber-reinforced composites," *Acta Metallurgica et Materialia*, volume 40, number 9, pages 2191–2199, Sep. 1992, ISSN: 09567151. DOI: `10.1016/0956-7151(92)90137-4`.

[11]   M. P. Barrett and J. Stover, "Understanding oil analysis: how it can improve reliability of wind turbine gearboxes," *Gear Technology*, pages 102–109, November 2013.

[12]   J.-Y. Park, J.-K. Lee, K.-Y. Oh, J.-S. Lee, and B.-J. Kim, "Design of simulator for 3mw wind turbine and its condition monitoring system," in *IMECS 2010- International MultiConference of Engineers and Computer Scientists*, Hong Kong, 2010, ISBN: 978-988-18210-4-1.

[13]   M. R. Wilkinson, F. Spinato, and P. J. Tavner, "Condition monitoring of wind turbine drive trains," in *IEEE International Symposium on Diagnostics for Electric Machines, Power Electronics and Drives, SDEMPED*, Cracow, Poland: IEEE, 2007, pages 388–392.

[14]   E. D. Lorenzo, S. Manzato, B. Peeters, and F. Marulo, "Structural health monitoring techniques applied to operating wind turbines," in *9th International Conference on Structural Dynamics, EURODYN 2014*, A. Cunha, E. Caetano, P. Ribeiro, and G. Müller, Eds., Porto, Portugal, 2014, pages 2255–2262, ISBN: 978-972-752-165-4.

[15]   O. R. Requeson, D. Tcherniak, and G. C. Larsen, "Comparative study of oma applied to experimental and simulated data from an operating vestas v27 wind turbine," in *6th International Operational Modal Analysis Conference*, Spain, 2015.

[16]   P. Takoutsing, R. Wamkeue, M. Ouhrouche, F. Slaoui-Hasnaoui, T. Tameghe, and G. Ekemb, "Wind turbine condition monitoring: state-of-the-art review, new trends, and future challenges," *Energies*, volume 7, number 4, pages 2595–2630, April 2014, ISSN: 1996-1073. DOI: `10.3390/en7042595`.

[17]   M. McGugan, G. Larsen, B. Sørensen, K. Borum, and E. J., *Fundamentals for remote condition monitoring of offshore wind turbines*. Danmarks Tekniske Universitet, Risø Nationallaboratoriet for Bæredygtig Energi, 2008, ISBN: 87-55-03662-7.

[18]   I. Silversides, A. Maslouhi, and G. LaPlante, "Acoustic emission monitoring of interlaminar delamination onset in carbon fibre composites," *Structural Health Monitoring*, volume 12, number 2, pages 126–140, January 2013, ISSN: 1475-9217. DOI: `10.1177/1475921712469994`.

[19]   E. R. Jørgensen, K. K. Borum, M. McGugan, C. L. Thomsen, F. M. Jensen, C. P. Debel, and B. F. Sørensen, *Full scale testing of wind turbine blade to failure - flapwise loading*. Denmark: Risø National Laboratory for Sustainable Energy, 2004, ISBN: 87-550-3183-8.

[20] F. T. S. Yu, *Fiber optic sensors*, First Edit, F. T. YU and S. Yin, Eds. Marcel
      Dekker, 2002, 494 S, ISBN: 9780824744571.

[21] K. Hill and G. Meltz, "Fiber bragg grating technology fundamentals and overview,"
      Journal of lightwave technology, volume 15, number 8, pages 1263–1276, 1997.

[22] J. A. Güemes and J. Sierra-Pérez, "New trends in structural health monitor-
      ing," in, W. Ostachowicz and A. J. Güemes, Eds. Vienna: Springer Vienna,
      2013, ch. Fiber Optics Sensors, pages 265–316, ISBN: 978-3-7091-1390-5. DOI:
      `10.1007/978-3-7091-1390-5_5`.

[23] G. R. G. Shivang and T.Pujal, "Classification of fiber optical sensors," *In-
      ternational Journal of Electronics Communication and Computer Technology
      (IJECCT)*, volume 3, number 4, pages 442–445, 2013.

[24] K. O. Hill, Y. Fujii, D. C. Johnson, and B. S. Kawasaki, "Photosensitivity in
      optical fiber waveguides: application to reflection filter fabrication," *Applied
      Physics Letters*, volume 32, number 10, page 647, August 1978, ISSN: 00036951.
      DOI: `10.1063/1.89881`.

[25] B. S. Kawasaki, K. O. Hill, D. C. Johnson, and Y. Fujii, "Narrow-band bragg
      reflectors in optical fibers," EN, *Optics Letters*, volume 3, number 2, page 66,
      August 1978, ISSN: 0146-9592. DOI: `10.1364/OL.3.000066`.

[26] J. Skaar and O. H. Waagaard, "Design and characterization of finite length
      fiber gratings," *IEEE Journal of Quantum Electron*, volume 39, number 10,
      pages 1238–1245, 2003. DOI: `10.1109/JQE.2003.817581`.

[27] T. Erdogan, "Fiber grating spectra," *Journal of Lightwave Technology*, volume
      15, number 8, pages 1277–1294, 1997, ISSN: 07338724. DOI: `10.1109/50.618322`.

[28] Y. Okabe, R. Tsuji, and N. Takeda, "Application of chirped fiber bragg grating
      sensors for identification of crack locations in composites," *Composites Part A:
      Applied Science and Manufacturing*, volume 35, number 1, pages 59–65, January
      2004, ISSN: 1359835X. DOI: `10.1016/j.compositesa.2003.09.004`.

[29] G. Luyckx, E. Voet, N. Lammens, and J. Degrieck, "Strain measurements of
      composite laminates with embedded fibre bragg gratings: criticism and op-
      portunities for research.," *Sensors (Basel, Switzerland)*, volume 11, number 1,
      pages 384–408, January 2011, ISSN: 1424-8220. DOI: `10.3390/s110100384`.

[30] X.-X. Li, W.-X. Ren, and K.-M. Bi, "Fbg force-testing ring for bridge cable
      force monitoring and temperature compensation," *Sensors and Actuators A:
      Physical*, volume 223, pages 105–113, March 2015, ISSN: 09244247. DOI: `10.
      1016/j.sna.2015.01.003`.

[31] R. Ramly, W. Kuntjoro, and M. K. A. Rahman, "Using embedded fiber bragg
      grating (fbg) sensors in smart aircraft structure materials," *Procedia Engineer-
      ing*, volume 41, pages 600–606, 2012, ISSN: 18777058. DOI: `10.1016/j.proeng.
      2012.07.218`.

[32]   C. Frias, H. Faria, O. Frazão, P. Vieira, and A. Marques, "Manufacturing
       and testing composite overwrapped pressure vessels with embedded sensors,"
       Materials & Design, volume 31, number 8, pages 4016–4022, Sep. 2010, ISSN:
       02613069. DOI: `10.1016/j.matdes.2010.03.022`.

[33]   J. Palaniappan, H. Wang, S. Ogin, A. Thorne, G. Reed, A. Crocombe, Y. Rech,
       and S. Tjin, "Changes in the reflected spectra of embedded chirped fibre bragg
       gratings used to monitor disbonding in bonded composite joints," *Composites
       Science and Technology*, volume 67, number 13, pages 2847–2853, October 2007,
       ISSN: 02663538. DOI: `10.1016/j.compscitech.2007.01.028`.

[34]   J. Palaniappan, S. Ogin, A. Thorne, G. Reed, A. Crocombe, T. Capell, S. Tjin,
       and L. Mohanty, "Disbond growth detection in composite–composite single-lap
       joints using chirped fbg sensors," *Composites Science and Technology*, volume
       68, number 12, pages 2410–2417, Sep. 2008, ISSN: 02663538. DOI: `10.1016/j.
       compscitech.2007.09.020`.

[35]   M. Basu and S. K. Ghorai, "Strain sensing in fiber-reinforced polymer laminates
       using embedded fiber bragg grating sensor," *Fiber and Integrated Optics*, volume
       33, number 4, pages 279–298, August 2014, ISSN: 0146-8030. DOI: `10.1080/
       01468030.2014.906686`.

[36]   L. Sorensen, J. Botsis, T. Gmür, and J. Cugnoni, "Delamination detection and
       characterisation of bridging tractions using long fbg optical sensors," *Com-
       posites Part A: Applied Science and Manufacturing*, volume 38, number 10,
       pages 2087–2096, October 2007, ISSN: 1359835X. DOI: `10.1016/j.compositesa.
       2007.07.009`.

[37]   F. Jülich and J. Roths, "Comparison of transverse load sensitivities of fibre
       bragg gratings in different types of optical fibres," in *Optical Sensing and De-
       tection*, F. Berghmans, A. G. Mignani, and C. A. van Hoof, Eds., volume 7726,
       April 2010, 77261N. DOI: `10.1117/12.854019`.

[38]   F. Bosia, P. Giaccari, J. Botsis, M. Facchini, and H. G. Limberger, "Charac-
       terization of the response of fibre bragg grating sensors subjected to a two-
       dimensional strain field," *Smart Materials and Structures*, volume 925, number
       12, pages 925–934, 2003.

[39]   K. Peters, M. Studer, J. Botsis, A. Iocco, H. Limberger, and R. Salathé, "Embed-
       ded optical fiber bragg grating sensor in a nonuniform strain field: measurements
       and simulations," *Experimental Mechanics*, volume 41, number 1, pages 19–28,
       2001, ISSN: 0014-4851. DOI: `10.1007/BF02323100`.

[40]   L. Sorensen, J. Botsis, T. Gmür, and L. Humbert, "Bridging tractions in mode
       i delamination: measurements and simulations," *Composites Science and Tech-
       nology*, volume 68, number 12, pages 2350–2358, Sep. 2008, ISSN: 02663538. DOI:
       `10.1016/j.compscitech.2007.08.024`.

[41] S. Yashiro, T. Okabe, N. Toyama, and N. Takeda, "Monitoring damage in holed cfrp laminates using embedded chirped fbg sensors," *International Journal of Solids and Structures*, volume 44, number 2, pages 603–613, January 2007, ISSN: 00207683. DOI: 10.1016/j.ijsolstr.2006.05.004.

[42] S. Magne, S. Rougeault, M. Vilela, and P. Ferdinand, "State-of-strain evaluation with fiber bragg grating rosettes: application to discrimination between strain and temperature effects in fiber sensors.," *Applied optics*, volume 36, number 36, pages 9437–9447, 1997, ISSN: 0003-6935. DOI: 10.1364/AO.36.009437.

[43] F. Xie, S. Zhang, Y. Li, and S. B. Lee, "Temperature-compensating multiple fiber bragg grating strain sensors with a metrological grating," *Optics and Lasers in Engineering*, volume 41, number 1, pages 205–216, January 2004, ISSN: 01438166. DOI: 10.1016/S0143-8166(02)00145-8.

Appendix A

Double Cantilever Beam Delamination Modelling:

a representation of a rotor blade trailing edge

The intention of this appendix is to demonstrate that the delamination in a rotor blade trailing edge can be analysed, from a material perspective, as a delamination in a double cantilever beam. To achieve this, the wind turbine rotor blade structure and its main failure types are described, and linked with the failure mechanisms present in the DCB fracture test. Then, different FEM damage modelling techniques that can be applied to the simulation of delamination in DCB specimens are explored, and a DCB FEM model is produced and validated analytically.

Additionally, it is described how the DCB specimen material and geometry (for the FEM models and experiments) were selected; to match the trailing edge of the DTU 10 MW reference wind turbine. Keep in mind that this DCB specimen configuration and FEM model are used in the different topics addressed throughout this PhD project.

A.1 Wind Turbine Rotor Blade Structure

The most common wind turbine configuration is three bladed horizontal axis (HAWT). The blades have a significant contribution to the final structure price, and consequently the cost to produce energy [1, 2], as shown in Fig. A.1. The output power of a wind turbine is related to the rotor length (see Fig. 1.1); thus, it is important to develop new design methodologies, manufacturing processes, and to apply advanced materials in order to design longer structures. On the other hand, the weight of the rotor blade has a big impact on the other components of the wind turbine, i.e., heavier rotor blades require stronger bearings, thicker and heavier towers, deeper foundations, etc. Thus, reducing the amount of material and saving some weight in the rotors will decrease the final price of the wind turbine, and consequently the cost to produce energy.

In terms of design, the wind turbine rotor is composed of a big variety of sub-components that are produced by different processes and combination of materials, and the requirements of these sub-components are based on several structural and aerodynamic considerations. The design of a wind turbine rotor is a multidisciplinary

field with a high level of complexity, and it relies on improvements in structural design, manufacturing processes, and material properties to meet the requirements for longer, light-weight, and stronger rotor blades.

The aerodynamic profile (airfoil shape), formed by two asymmetric shell structures glued together, defines the other shape of the turbine rotor [3–5]. These streamlined shells form the aerodynamic suction and pressure side, which generates the torque moment that is transferred to the load-carrying components. There are two main types of load-carrying configuration designs [5, 6]: a load-carrying laminate in a rectangular hollow beam, also called spar, as shown in Fig. A.2a); or a combination of load-carrying laminate incorporated in the outer shell reinforced with two or three shear webs, as shown in Fig. A.2b);
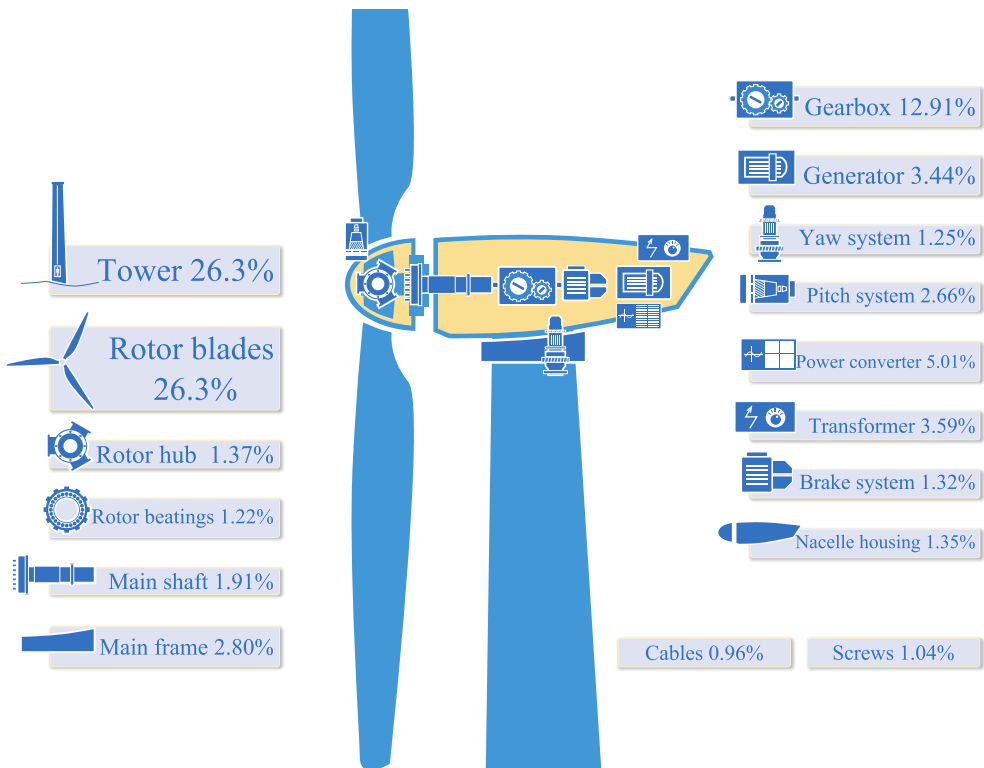
Figure A.1: Cost share of 5 MW wind turbine main components. (Picture modified from figure 1.11 in *The Economics of Wind Energy, a report by the EWEA* [1]).
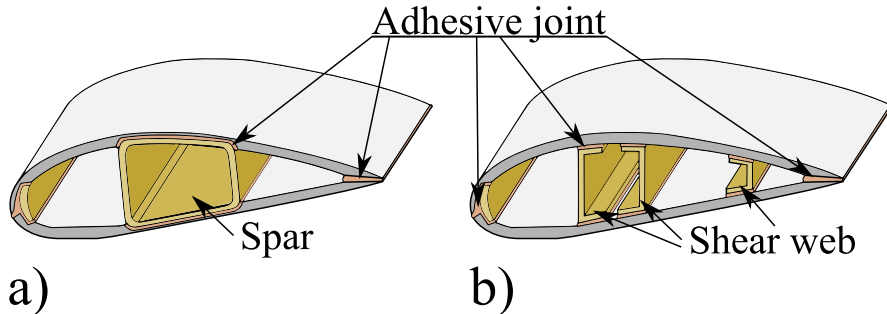
Figure A.2: Schematics of the two main load-carrying configuration design types. a) load-carrying laminate in a rectangular hollow beam, and b) combination of load-carrying laminate incorporated in the outer shell reinforced with two or three shear webs.

The spars/shear webs are the components responsible for carrying the bending moments and restraining the cross section against torsion and buckling deformation. Sandwich cores are assembled between the outer shells at the leading edge, between the spar and outer shell, and between the outer shells, using structural adhesives, which increase the structure's moment of inertia and consequently less material is required [5, 6]. In summary, the main parameters that drive the material selection for wind turbine rotor blades are high stiffness, low density (high stiffness-weight ratio), and long fatigue performance [7]. The most commonly used materials in the modern wind turbine rotor blade are:

- Composite materials:
    - Reinforcements: glass fibre, carbon fibre, natural fibre;
    - Matrix: epoxy, vinylester, polyester, bio-based;
- Sandwich cores: balsa, polyvinyl chloride, Polyethylene terephthalate, polystyrene;
- Structural adhesives: epoxy, vinylester, methyl methacrylate;

A.2   Wind Turbine Rotor Blade Failure

A wind turbine rotor blade can develop various types of damage, as shown in Fig. A.3, which ultimately can lead to its failure. This damage can occur in the component itself, when the materials limit is reached; for example, when the laminate fails by fibre failure in tension, or by delamination (cracking along the laminate plies). Or this damage can occur in the components joints, as failure in the adhesive bonded joints. Of these, delamination of the laminate and failure of the bonded joints are usually the most critical and difficult to predict during the design process [6, 8, 9].
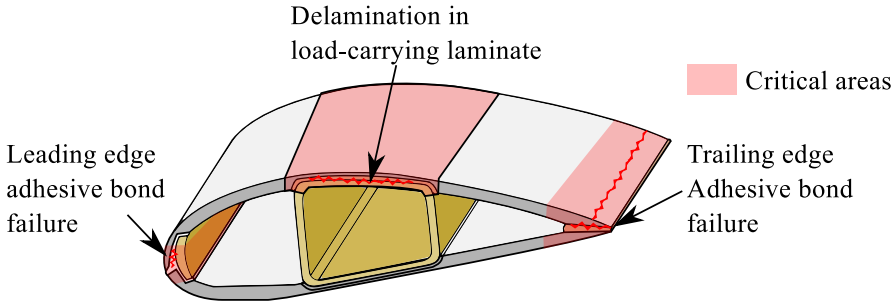
Figure A.3: Schematic representation of the major failures and critical areas in the wind turbine rotor blade.

Ataya and Ahmed [10] found multiple trailing edge damage when they analysed wind turbines that has been operating for more than 17 years (81 blades of 100kW and 18 of 300 kW wind turbines); they found cracks with lengths up to 0.59 m on the blade root and 1.35 m in the trailing edge, and concluded that transverse cracks were mainly concentrated in the high fatigue areas.

For these reasons, this PhD project was focused on these two failure mechanisms, delamination and adhesive bonded failure, at the trailing edge, and its different failure mechanisms were analysed and modelled. Thus, all the specimens, models, and cases developed along the PhD project were based on the trailing edge configuration of the DTU 10 MW reference wind turbine (described in section 1.2.1).

A.2.1   Trailing Edge Failure

Even though the trailing edge failure has been identified as a common cause of rotor blade premature failure, it is still poorly understood, mainly due to its complex geometry and loading conditions, and the lack of models that can represent its complex and multiple damage mechanisms. Haselbach, et al. [11, 12] conducted a comprehensive numerical and experimental investigation of the trailing edge damage, where the effect of geometric non-linear cross section deformation and the formation of trailing-edge waves were studied. In these studies, it was concluded that the trailing-edge components experience not only mode-I fracture, but a mixed mode of fracture conditions, and that delamination can promote local buckling, decreasing the structure resistance.

Thus, despite the promising results from Haselbach the trailing edge damage mechanism is too complex to be analysed by conventional models, and experimental validation requires a full scale test of a wind turbine blade that will be very expensive or even impossible to be make. To overcome this, some authors (and also in this PhD project) approximate the trailing edge with cases already studied and with known solutions, double cantilever beam (DCB) specimens; also, DCB specimens have been

used by several authors for material testing (ex: fracture properties), therefore several test procedures were developed based on this specimen configuration. Eder and Bitsche [8] investigate the fracture energy release of prescribed cracks in the trailing edge, by using DCB specimens as a representation of different trailing edge configurations. In this study, the DCB experimental results were linked with numerical models of the trailing edge failure.

A.3   DCB specimen as a Trailing Edge Representation

Some phenomena observed in the damage process of the trailing edge, at the rotor blade length scale, need to be studied at a smaller scale, as sub-component, laminate, or even at fibre-matrix scale, in order to understand the damage mechanism and its impact on the structure behaviour. For this reason, and from a material point-of-view, the DCB specimen is a good starting point to study the trailing edge failure, as this specimen configuration has been extensively studied and characterized. In Fig. A.4, some DCB configurations used to test delamination and adhesive bonded failure are shown.
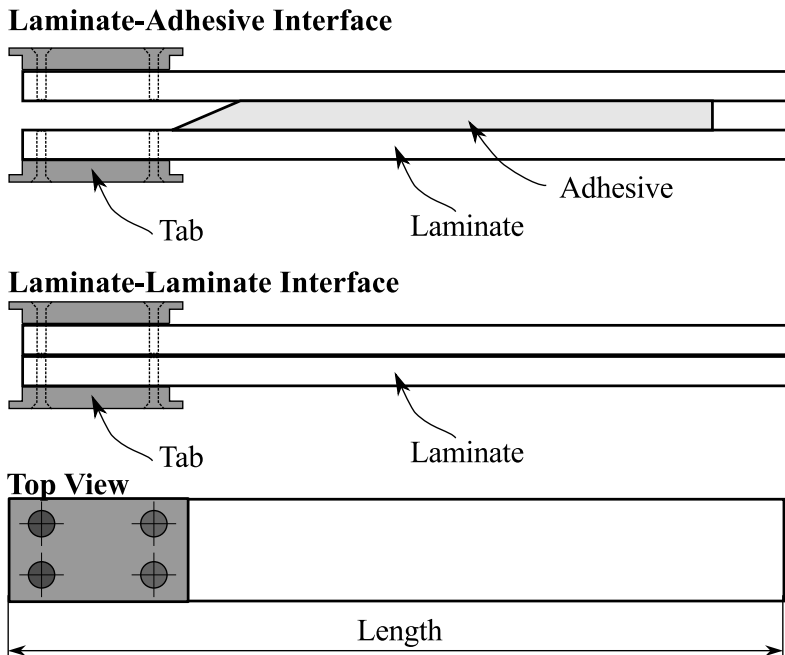
Figure A.4: DCB specimen schematic representation: laminate-adhesive and laminate-laminate failure interface.
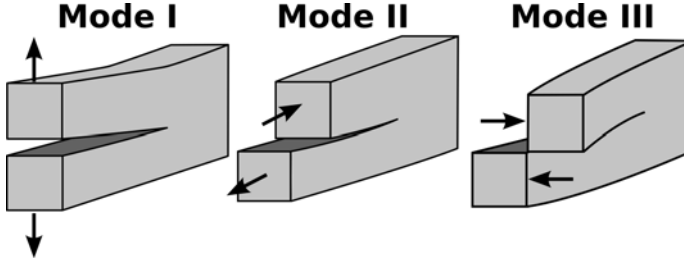
Figure A.5: Schematic representation of the three fundamental fracture modes.

Before describing the numerical modelling and experimental testing of DCB specimens, the fracture mode concept needs to be introduced. There are three fundamentals fracture modes, mode-I, mode-II, and mode-III, (see Fig. A.5) which can be defined by the direction of the stress and opening to the crack plane; mode-I is an opening fracture mode, where the tensile stress and opening are normal to the crack; mode-II is a shear (sliding) mode, where the shear stress and opening are parallel to the crack plane and perpendicular to the crack front; and, mode-III is a tearing mode, where the shear stress and opening are parallel to the crack plane and parallel to the crack front (out-of plane). As the DCB specimen can be loaded with different combination of forces and moments, any combination of these fracture modes can be obtained, also called mixed-mode fracture.

A.3.1 Numerical Modelling

Several authors developed numerical models that can represent the adhesive failure and the delamination mechanisms in DCB specimens. Two distinct approaches have been applied:

a) **Linear elastic fracture mechanics** (LEFM). In LEFM theory, the material behaviour is considered linear and the structure is modelled as a continuously distributed material. The strain energy release rate, G, is the amount of energy consumed per unit area by the crack tip fracture process as the crack advances, and it is described by Eq. (A.1).

$$G = -\frac{d\Pi}{dA} \tag{A.1}$$

The parameter $d\Pi$ represents the variation of the potential energy, and dA is the created fracture surface [13]. Therefore, the fracture toughness (G_c) can be defined as the minimum amount of energy required for a crack to grow,

$$G_c = \frac{dW_s}{dA} = 2w_f \tag{A.2}$$

where W_s is the work required to create new surfaces, and w_f is the fracture energy. LEFM allows the fracture toughness to be evaluated from the stress intensity factors K_i, as described by Eq. A.3.

$$G_c = \frac{K_I^2}{E'} + \frac{K_{II}^2}{E'} + \frac{K_{III}^2}{2\mu} \tag{A.3}$$

The parameter K_I, K_{II} and K_{III} are the stress intensity factors for mode I, II, and III, respectively, μ is the shear modulus, and E' is E (Young's Modulus) for plane stress cases and $E/(1-\nu^2)$ for plain strain cases (ν is the Poisson's ratio). The stress intensity factor is a parameter that scales the magnitude of the singular stress field in the region near the crack tip, and for an isotropic linear elastic material can be defined as:

$$K_I = \lim_{r \to 0} \sqrt{2\pi r}\sigma_{yy}(r,0) \tag{A.4}$$

$$K_{II} = \lim_{r \to 0} \sqrt{2\pi r}\sigma_{yx}(r,0) \tag{A.5}$$

$$K_{III} = \lim_{r \to 0} \sqrt{2\pi r}\sigma_{yz}(r,0) \tag{A.6}$$

Thus, delamination is predicted by LEFM theory when a combination of the stress intensity factors is equal to, or greater than, the fracture toughness. In terms of DCB numerical modelling using LEFM theory, different techniques can be found in literature: virtual crack closure technique (VCCT) [8, 14], virtual crack extension method (VCE) [15], and finite crack extension method [16, 17]. However, these techniques present some limitations. It is not possible to predict the crack initiation, because LEFM requires a crack tip (singularity) to calculate the stress intensity factors; and, progressive and stable crack propagation is difficult to model.

b) **Cohesive Zone Modelling** (CZM). In CZM theory, the fracture process is analysed phenomenologically, and the effect of the material damage initiation, progression and failure is incorporated into the model. The CZM theory was initially develop by Dugdale [18] and Barenblatt [19], and it has been improved/modified to represent different damage mechanism, as FRP delamination and fibre bridging, by other authors [20–22]. A CZM model describes the material stiffness degradation at the damage interface by a traction-separation law, which relates the traction stress at the crack faces with normal and tangential crack opening directions[23]. The traction-separation law can be described as:

$$\sigma_n = \sigma_n(\delta_n) \tag{A.7}$$

$$\sigma_t = \sigma_t(\delta_t) \tag{A.8}$$

where σ_n and σ_t are the cohesive stress in the normal and tangential direction, respectively, and δ_n and δ_t are the crack face displacement also in the normal and tangential direction. Under mixed-mode loading, the coupling effects between the different opening modes need to be considered, which can be handled by different theories available in literature. The two most used mixed-mode coupling theories are the power-law and the BK-law [24, 25]. The power law is defined as,

$$\left(\frac{G_I}{G_{Ic}}\right)^{\alpha} + \left(\frac{G_{II}}{G_{IIc}}\right)^{\beta} + \left(\frac{G_{III}}{G_{IIIc}}\right)^{\gamma} = 1 \qquad (A.9)$$

where the parameters G_{Ic}, G_{IIc}, and G_{IIIc} are the fracture toughness for the three fundamental fracture modes, G_I, G_{II}, and G_{III} are the individual component of energy release rate (for a given time), and α, β, and γ are fitting parameters. Thus, the material is considered damaged when power-law is full-filled (=1).

The BK-law is another failure criterion that, in some cases, can fit the experiments more accurately, which was initially developed by Benzeggagh and Kenane [24], the BK-law is described by Eq. (A.10).

$$G_{Ic} + (G_{IIc} - G_{Ic}) \left(\frac{G_{II} + G_{III}}{G_I + G_{II} + G_{III}}\right)^{\eta} = G_c \qquad (A.10)$$

The parameter η is a parameter found by fitting the BK-law with experimental data. The traction-separation curve, $\sigma_n(\delta_n)$, for mode I is schematically represented in Fig. A.6. The material does not develop permanent deformation/-damage before the stress reaches $\widehat{\sigma_n}$; however, once $\widehat{\sigma_n}$ is reached, the damage is initiated and the cohesive traction decreases with increasing separation. The traction-separation can present different shapes, as linear, bi-linear, exponential, etc., which depends on the material fracture properties; yet, the area under the traction-separation curve represents the material fracture toughness (G_c). In terms of FRP delamination with fibre-bridging behaviour, CZM is a more complete damage modelling approach when compared with LEFM, as it can handle crack initiation and crack growth within the same model. Additionally, a CZM approach is easier to implement, as the simulation is more stable and has fewer convergence issues. However, CZM requires that the user pre-defined the cohesive surfaces or cohesive element, which eventually limits the crack growth to that pre-defined plan/path.
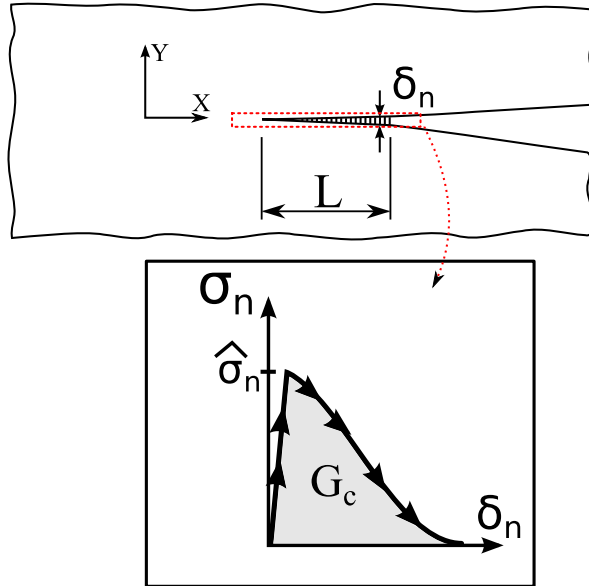
Figure A.6: Schematic representation of a traction-separation curve $(\sigma_n(\delta_n))$ for mode-I fracture; L represents the fracture process zone, $\widehat{\sigma_n}$ is the maximum traction stress that defines damage initiation; the area under the curve represents the fracture energy G_c.

A.4   Experimental Testing

From an experimental point view, the DCB is a common type of test specimen, and it has been extensively used in research and industry to determine the fracture properties of FRP materials and structural adhesives [26–29]. With relevance for this PhD project, a fracture test machine developed by Sørensen[1] [27], allowed testing of the DCB specimens in different fracture modes (mode I, II and mixed mode) with a stable crack growth. This was especially important during the DCB test with embedded FBG sensors, where the test could be paused without reducing the applied load, allowing a correct measurement of the FBG signal for different crack positions.

A.4.1   Determination of Bridging/Cohesive Laws by J-integral

During large-scale bridging, such as found in FRP delamination, LEFM cannot fully represent the damage mechanisms. However, the cohesive-law and consequently the energy release rate can be calculated using the path independent J-integral.

---

[1]fracture test machine located at DTU Wind Energy-composite material section;

Initially developed by Rice [30], the J-integral is defined as:

$$G_c = J = \int_\Gamma W dx_2 - \sigma_{ij} n_j \frac{\partial u_i}{\partial x_1} dS \tag{A.11}$$

where Γ is a contour around the crack faces, u_i indicated the displacement vector, n_j is the outwards normal direction to the contour, W is the strain energy density, and σ_{ij} is the stress tensor. S denotes the curve length along the contour Γ, and the strain energy density can be described by Eq. (A.12).

$$W = \int_0^\varepsilon \sigma_{ij} \varepsilon_{ij} \tag{A.12}$$

Due to its path-independent nature, the J-integral evaluated around the fracture process zone and around the external boundaries is identical ($J_{ext} = J_{loc}$) [31], as shown in Fig. A.7. Therefore, the calculation of the cohesive-law and fracture energy in a DCB specimen can be obtained by integrating the J-integral around the external boundaries.
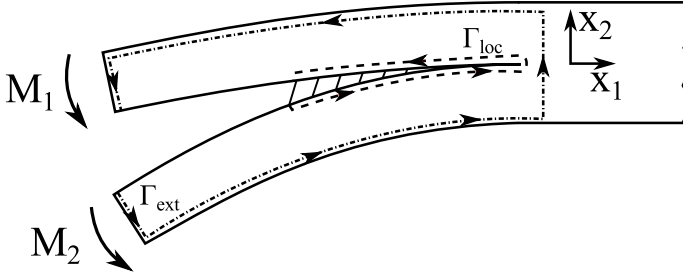
Figure A.7: J-integral path independent integration: J_{loc} and J_{ext} around the fracture process zone.

Sørensen and Kirkegaard [23] developed a generalised mixed-mode J-integral, described by Eq. (A.13), which can be applied despite the shape of the cohesive-law and the interaction of different modes.

$$J = J_{loc} = \int_0^{\delta_n^*} \sigma_n(\delta_n, \delta_t) d\delta_n + \int_0^{\delta_t^*} \sigma_t(\delta_n, \delta_t) d\delta_t + J_0 \tag{A.13}$$

The parameter δ_n^* and δ_t^* represent the end-crack opening/sliding in normal and tangential directions, respectively, and J_0 is the crack tip fracture energy. Then,

the cohesive traction-separation law for any mixed-mode can be determined by Eq. (A.14) and (A.15).

$$\sigma_n(\delta_n^*, \delta_t^*) = \frac{\partial J(\delta_n^*, \delta_t^*)}{\delta_n^*} \tag{A.14}$$

$$\sigma_t(\delta_n^*, \delta_t^*) = \frac{\partial J(\delta_n^*, \delta_t^*)}{\delta_t^*} \tag{A.15}$$

A.4.2   J-integral Measurement in a DCB Specimen

For a symmetric DCB specimen loaded with moments[2] (see Fig. A.8), the J-integral evaluated around the external boundaries is given by [27]:

$$G_c = J = \frac{21(M_1^2 + M_2^2) - 6M_1 M_2}{4B^2 H^3 E'} \ for \ |M_1| < M_2 \tag{A.16}$$

The parameter E' represents the E (Young's Modulus) for plane stress cases and $E/(1-\nu^2)$ for plain strain cases (ν is the Poisson's ratio), M_1 and M_2 are the moments applied to the top and bottom beams, respectively, B is the specimen width, and H is the specimen height. Note that the J-integral is valid for both LEFM problems and large-scale bridging, and for LEFM cases $J = G_c$.

During the DCB fracture testing, the values of M_1, M_2, δ_n^*, and δ_t^* are recorded until a steady crack growth state is achieved. The moments are calculated from the force applied to the test machine's transverse arms (see Fig. P3.20), and the opening is measured from an extensometer and a LVDT mounted at two pins between the two crack faces.
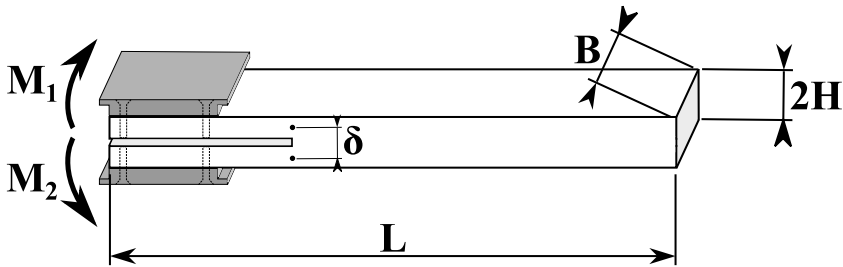
Figure A.8: DCB specimen loaded with moments, M_1 and M_2; L represents the specimen length, δ is the opening, B is the specimen width, and H is the specimen height.

[2]load configuration used in the fracture test machine developed by Sørensen [27];

The J is calculated using Eq. (A.16), and the traction-opening cohesive-law ($\sigma(\delta)$) is obtained by partial derivation J in function of δ_n^*, and δ_t^*, as described in Eq. (A.14) and (A.15).

This procedure can be performed for multiple M_1-M_2 combinations to determine the cohesive-law for pure mode I, pure mode II, or any mixed-mode combination; Ψ defines the mode mixity of the test based on the moments ratio [27]:

$$\Psi = tan^{-1} \left(\frac{\sqrt{3}}{2} \frac{M_1 + M_2}{M_2 - M_1} \right) \; for \; |M_1| < M_2 \tag{A.17}$$

A.5   DCB Specimen Configuration Based on the DTU 10 MW Wind Turbine

The configuration of the DCB specimen used in this PhD project was based on the DTU 10 MW reference wind turbine; i.e., the modelling and experimental properties (material and geometry) of the DCB specimen were based on the properties presented in the report "*Description of the DTU 10 MW reference wind turbine*"[32]. The experimental protocol, specimen manufacturing, and DCB testing is described with more detail in papers [**P3, P4**].
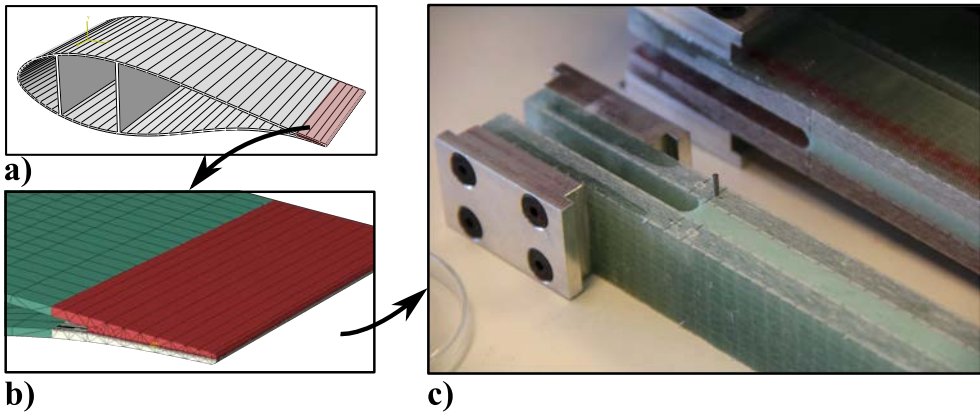
Figure A.9: DCB specimen configuration based on DTU 10 MW wind turbine: a) Wind turbine cross section geometry; b) Trailing edge finite element model; c) DCB specimen produced based on DTU 10 MW configuration.

Laminate Configuration

The laminate configuration of the trailing edge varies along the rotor blade length, as shown in Fig. A.10 and table A.1; however, in order to manufacture DCB specimens that can be tested and validated by models from the literature, constant material properties and standard laminate lay-up are required. In addition, its location in the blade should represent a known critical area, with large deformation or material variation (ex: balsa to no-balsa transition). For these reasons, we select the position at 70 m from the rotor blade root as reference for the geometry and material configuration, as specimens with that geometry and material configuration can be produced and tested in our in-house testing machine; and also, at 60-70 m there is a transition point in sandwich structure making it an interest location, where damage can initiate.

⇒ **Selected laminate configuration (at 70 m):**
2.2 mm Triax/ 2.6 mm UD/ 2.6 mm UD/ 2.2 mm Triax.

Table A.1: Layup configuration of the DTU 10 MW rotor blade trailing edge [32].

X position [m]	Triax [mm]	Uniax [mm]	Balsa [mm]	Uniax [mm]	Triax [mm]
10	7.1	7.2	30.0	7.2	7.1
20	4.2	5.5	70	5.6	4.4
30	2.8	5.1	55.0	5.1	2.9
40	2.6	4.5	30.0	4.5	2.6
50	2.5	3.8	15	3.8	2.5
60	2.3	3.3	5.0	3.2	2.3
70	2.2	2.6	0.0	2.6	2.2
80	2.0	1.9	0.0	2.0	1.9
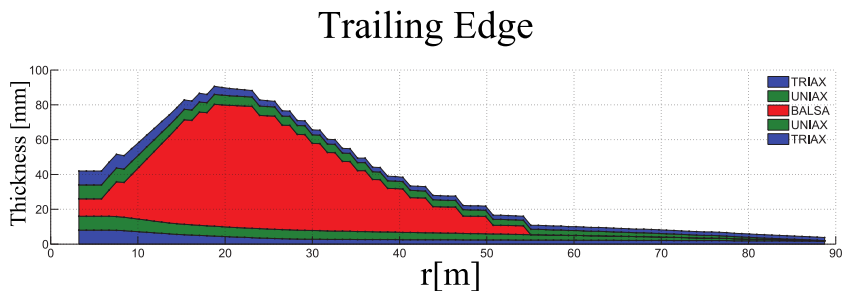
Figure A.10: Trailing edge layup configuration along the rotor blade length (picture from *"Description of the DTU 10 MW reference wind turbine"* [32]).

Theoretical Mechanical Properties of the Laminate

The theoretical mechanical properties of the laminate, implemented in the numerical models, were calculated based on the properties of the constituent materials using micro-mechanics equations and classical laminate theory. The mechanic properties of the constituent materials, epoxy matrix and E-glass fibres, are presented in table A.2.

Table A.2: Mechanical properties of the epoxy matrix and E-Glass Fibre [32, 33].

Property	Epoxy Matrix	E-Glass Fibre
Young's modulus (GPa)	0.35 (E_m)	75 (Longitudinal E_{f1}) 75 (Transverse E_{f1})
Poisson's ratio	1.4815 (ν_m)	0.2 (ν_{f12})
Shear modulus (GPa)	1.4815 ($G_m^{(a)}$)	31.25 (In-plane $G_{f12}^{(b)}$) 31.25 (Transverse $G_{f23}^{(c)}$)

$^{(a)}G_m = E_m/(2(1 + \nu_m))$
$^{(b)}$chosen as $G_{f12} = E_{f1}/(2(1 + \nu_{f12}))$
$^{(c)}$chosen as $G_{f23} = G_{f12}$

The laminate Young's modulus is given by Eq. (A.18), where E_{f1} and E_{f2} are the E-Glass fibre longitudinal and transverse Young's modulus, respectively, E_m is the epoxy matrix Young's modulus, V_f is the fibre volume fraction, and V_m is the matrix volume fraction [32].

$$E_1 = E_{f1}V_f + E_mV_m; \qquad E_2 = \frac{E_m}{1 - \sqrt{V_f}\left(1 - \frac{E_m}{E_{f2}}\right)}; \qquad (A.18)$$

The laminate shear modulus is given by Eq. (A.19), where G_{f12} and G_{f23} are the E-Glass fibre in-plane and transverse shear modulus, G_m is the epoxy matrix shear modulus.

$$G_{12} = \frac{G_m}{1 - \sqrt{V_f}\left(1 - \frac{G_m}{G_{f12}}\right)}; \qquad G_{23} = \frac{G_m}{1 - \sqrt{V_f}\left(1 - \frac{G_m}{G_{f23}}\right)}; \qquad (A.19)$$

Table A.3: Mechanical properties of the theoretical laminate with a fibre volume fraction V_f of 60%.

Property	Laminate	Unit
Fiber volume fraction V_f	0.60	-
Young's modulus in Fiber direction E_1	46.20	GPa
Young's modulus transv. Fiber dir. E_2	11.70	GPa
Young's modulus transv. Fiber dir. E_3	11.70	GPa
In-plane shear modulus dir. G_{12}	4.393	GPa
In-plane shear modulus dir. G_{13}	4.393	GPa
Out-of-plane shear modulus dir. G_{23}	4.393	GPa
In-Plane Poisson's ratio dir. ν_{12}	0.2600	-
In-Plane Poisson's ratio dir. ν_{13}	0.2600	-
Out-of-Plane Poisson's ratio ν_{23}	0.3301	-

The laminate Poisson's ratio is defined by Eq. (A.20),

$$\nu_{12} = \nu_{f12}V_f + \nu_m V_m; \qquad \nu_{23} = \frac{E_2}{2G_{23}}; \qquad \text{(A.20)}$$

where ν_{f12} and ν_m are the E-Glass fibre and epoxy matrix Poisson's ratio, and E_2 and G_{23} are given by Eq. (A.19) and (A.20). Symmetric condition were used to determine the remaining parameters, as shown by Eq. (A.21).

$$E_3 = E_2; \quad G_{13} = G_{12}; \quad \nu_{13} = \nu_{12}; \qquad \text{(A.21)}$$

Thus, the theoretical mechanical properties of the laminate with a fibre volume fraction V_f of 60%, calculated from the equations above, are presented in table A.3. The theoretical elastic properties of the multi-directional plies (Triax and UD) composed by the theoretical laminate, were determined using classic laminate theory, and are presented in table A.4.

Table A.4: Theoretical elastic properties of the multi-directional plies: Unidirectional and Triax laminate.

Property	UD	Triax	Unit
Fiber volume fraction V_f	0.60	0.60	-
0° fibers	95	30	%
90° fibers	5	0	%
+45° fibers	0	35	%
-45° fibers	0	35	%
Young's modulus in Fiber direction E_1	44.3386	23.8299	GPa
Young's modulus transv. Fiber dir. E_2	12.9438	15.05	GPa
Shear modulus G_{12}	4.393	10.544	GPa
Poisson's ratio ν_{12}	0.2325	0.5125	-
Shear modulus $G_{13} = G_{23}$	4.393	4.393	GPa

Structural Adhesive Mechanical Properties

In the DTU 10 MW reference wind turbine report, there is no information about the structural adhesive used in the rotor blade trailing edge. However, as most of the structural adhesives are epoxy based, we used the mechanical properties of an adhesive already tested, and used in our in-house testing lab. This structural adhesive was used in Sørensen, et al.[34], where DCB specimens composed of two laminate plates $[\pm 45, 0_8, \pm 45]$ (similar to our laminate) glued with an epoxy structural adhesive were tested in different fracture modes. The structural adhesive mechanical properties are shown in table A.5.

Table A.5: Epoxy structural adhesive elastic and fracture properties [34].

Property	Adhesive	Unit
Young's modulus	3.0	GPa
Poisson's ratio	0.35	-
Mode-I Fracture		
Peak stress σ_n	2.64	MPa
Critical opening δ_n^0	1.40	mm
Fracture Energy	1.85	kJ/m^2
Mode-II Fracture		
Peak stress σ_t	20.15	MPa
Critical opening δ_n^0	0.37	mm
Fracture energy	3.73	kJ/m^2

DCB Geometry

The DCB geometry and material lay-up used in the modelling and experimental tests
are shown in Fig. A.11. These dimensions were based on the laminate configuration
presented previously, and on the specimen geometric requirements defined by our
in-house fracture test machine.
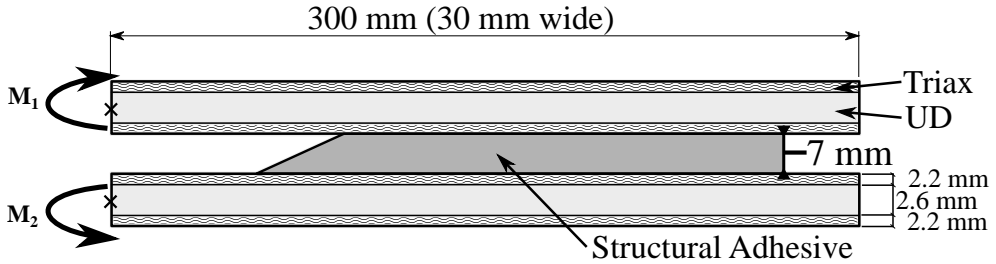
Figure A.11: Double cantilever beam model dimensions and material configuration.

A.6   DCB FEM Model and Validation

The FEM software $ABAQUS^{TM}$ was used to create the numerical models of the DCB
specimen delamination. Three damage tools from $ABAQUS$ were used to simulate the
delamination mechanism, virtual crack closure technique (VCCT), cohesive-elements
(CE), and cohesive-surfaces (CS).

   Even though VCCT cannot represent the non-linear behaviour of the fracture pro-
cess zone (fibre-bridging), this technique has the capability to calculate the energy
release rate for each fracture mode, allowing us to independently evaluate the con-
tribution of each fracture mode. This is especially useful to determine the fracture
mixed-mode ratio (Ψ) in complicated loading configurations. The CE and CS damage
formulation are similar and give identical results, however the CS technique requires
less elements and can be more easily implemented in models with multiple parts.
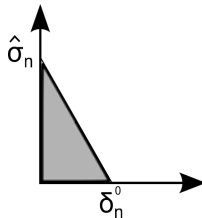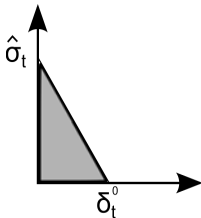
A.6.1   Geometry and Material Definition

Two models with different geometries and material configurations were created:

- **DCB Validation Model:** A simple DCB model was created to validate the accuracy of the different damage techniques, VCCT, CE, and CS, against analytical results. This *DCB validation model* is composed of a symmetric DCB without structural adhesive, where the crack grows in the middle plane; each beam is 8 mm in height, 50 mm in width, and 500 mm in length, and is composed of UD laminate. The cohesive-law that defines the fracture interface between the two beams was selected so the simulation could converge (small values, close to unitary), and its properties are presented in table A.6.

Table A.6: DCB validation model material properties.

UD mechanical properties	
Young's modulus in Fiber direction E_1	44.33 GPa
Young's modulus transv. Fiber dir. E_2	12.94 GPa
Shear modulus G_{12}	4.39 GPa
Poisson's ratio ν_{12}	0.23
Shear modulus $G_{13} = G_{23}$	4.39 GPa

Interface damage properties	
Mode I	**Mode II**

Traction-separation law			
$\hat{\sigma}_n$	1.1 (MPa)	$\hat{\sigma}_t$	11 (MPa)
$\delta_n^0(mm)$	1.1 (mm)	$\delta_t^0(mm)$	0.11 (mm)

Energy criterion			
J_n^{ss}	0.605 kJ/m^2	J_t^{ss}	0.605 kJ/m^2

- **DCB Test Model** (DCB used in the experiments): This model is based on the *DCB Validation Model*, after analytical validation, where its geometry and materials were modified to match the properties of the DCB specimen used in the experiments (described in section A.5).

Note that for both cases analysed, 2D and 3D FEM models were created, as shown in Fig. A.12.
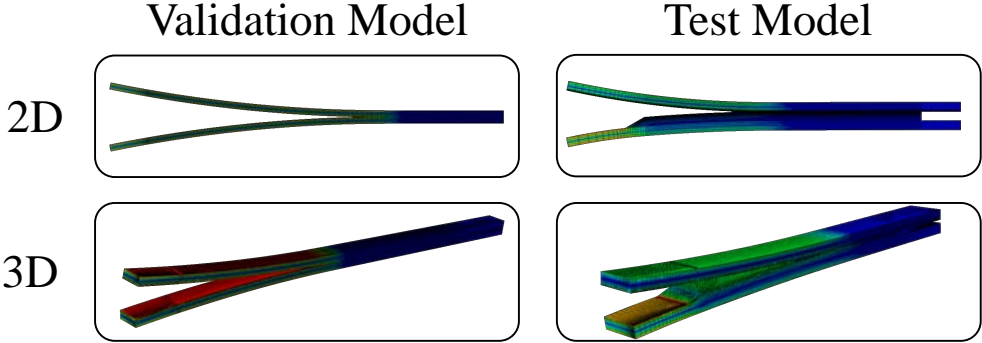
Figure A.12: 2D and 3D DCB FEM models: *DCB Validation Model* and *DCB Test Model*.

A.6.2   Damage Constitutive Response

Cohesive Element and Cohesive Surface

The cohesive elements/surface are modelled to express the cohesive-law (traction-separation), meaning a progressive loss of the cohesion between the two crack faces with the local crack opening δ^*. In an undamaged state, the elements defined as CS/CE follow a linear-elastic behaviour, defined as the penalty stiffness K_n, which relates the nominal stress (σ_n, σ_s, σ_t) to the nominal opening (δ_n, δ_n, δ_t), as shown in Fig. A.13.

ABAQUS can calculate the damage initiation by different criteria, which should be chosen accordingly to the materials behaviour that the user wants to simulate. The *Maximum stress criterion* was used as damage initiation criterion in the *DCB Validation Model*, defined by:

$$f = Max \left\{ \frac{\sigma_n}{N_{max}}; \frac{\sigma_t}{T_{max}}; \frac{\sigma_s}{S_{max}} \right\} = 1 \tag{A.22}$$

and, the *Quadratic stress interaction criterion* was used as damage initiation criterion in the the *DCB Test Model*, defined by:

$$f = \left(\frac{\sigma_n}{N_{max}} \right)^2 + \left(\frac{\sigma_s}{S_{max}} \right)^2 + \left(\frac{\sigma_t}{T_{max}} \right)^2 = 1 \tag{A.23}$$

The parameter f is the damage criterion, and it is fulfilled when it reaches the value $f = 1$. The parameters $\sigma_{n,s,t}$ are the nominal stress in the normal, first shear
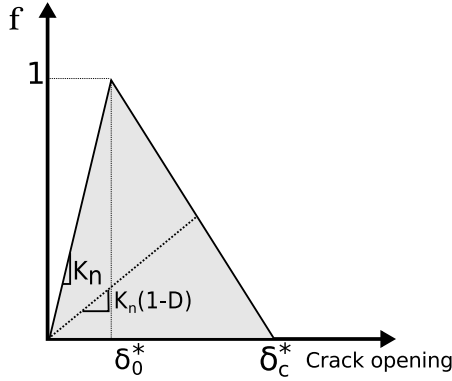
Figure A.13: Constitutive behaviour of the cohesive element or cohesive surface (doi:10.1371/journal.pone.0141495.g009).

and second shear directions, respectively, and N_{max}, S_{max}, and T_{max} are cohesive-law parameters; the parameters δ_0^* and δ_c^* are the crack opening displacement to the local crack plane for damage initiation and critical damage.

When the initiation criterion is fulfilled, a damage evolution law describes the material stiffness degradation. A scalar damage variable, D, ranging from 0 (no damage) to 1 (fully damaged), represents the damage in the cohesive element. Abaqus offers different softening responses: linear, exponential, and tabular; however, only linear softening displacement criterion was used in both models. The linear softening displacement criterion is defined by the opening at damage initiation (δ_0^*) and the opening at failure (δ_c^*). The mixed-mode behaviour was set as mode-independent, meaning that no fracture coupling behaviour is modelled.

Virtual Crack Closure Technique

The VCCT criterion uses LEFM concepts (presented in section A.3.1) to calculate the energy release rate in the different opening modes. For a crack propagating in the direction 1→2→3 (see Fig. A.14), the energy release rates at the node pair 5-2 is calculated as [8]:

$$G_I = \frac{1}{2b\Delta a} F_2 u_2 \tag{A.24}$$

$$G_{II} = \frac{1}{2b\Delta a} F_1 u_1 \tag{A.25}$$

$$G_{III} = \frac{1}{2b\Delta a} F_3 u_3 \tag{A.26}$$

where F_i represents the nodal forces at the crack tip, u_i is the nodal displacements behind the crack tip along direction x_i, b is the element width, and Δa is the crack increment length (= element length). In terms of mixed-mode behaviour, ABAQUS offers different methods, BK-law, power-law, and Reeder-law [35], however only power-law was used to simulate the mixed-mode behaviour.

The nodes at the crack tip (2-5) debond when the fracture criterion, f, reaches the value 1.0 within a given tolerance, f_{tol}, described as follows:

$$f = \frac{G_{equiv}}{G_c} \tag{A.27}$$

$$1 \leq f \leq 1 + f_{tol} \tag{A.28}$$

where G_c is the critical energy release rate, and G_{equiv} is the equivalent energy release calculated by the mixed-mode coupling method.

$$\frac{G_{equiv}}{G_c} = \frac{G_I}{G_{Ic}}^\alpha + \left(\frac{G_{II}}{G_{IIc}}\right)^\beta + \left(\frac{G_{III}}{G_{IIIc}}\right)^\gamma \tag{A.29}$$

The G_{equiv} calculated by the Power-law is described in Eq. (A.29). The parameter G_{Ic}, G_{IIc}, and G_{IIIc} are the fracture toughness for the three fundamental fracture modes, G_I, G_{II}, and G_{III} are the individual components of energy release rate, and α, β, and γ are fitting parameters.
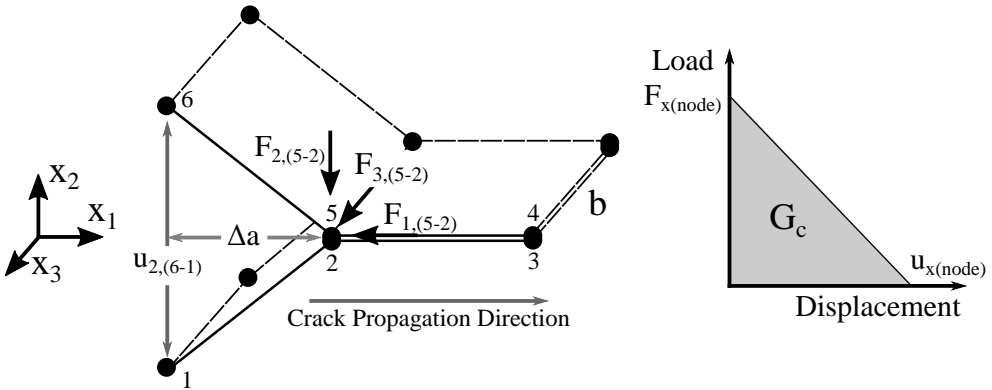
Figure A.14: Schematic representation of the VCCT principle: nodal forces and displacements.

The VCCT assumes a self-similar propagation, meaning that the crack growth does not modify the stress state at the crack tip, and the nodal displacement ahead of the crack tip (node 1-6) is assumed to be equal to the nodal displacement that occurs upon crack extension (node 2-5); however, to fulfill this assumption, a pre-crack is required, which makes the VCCT unable to predict crack initiation [8].

A.6.3   Mesh and Model Convergence

Mesh size is an important issue that needs to be considered in any FEM model, as it can strongly affect the model accuracy and the required computational power. Additionally, in FEM models where the damage is modelled by a CE/CS approach, it is also important to ensure that the fracture process zone is accurately represented.

Some authors [36, 37] suggested a minimum of 10 cohesive elements inside the active fracture process zone, as using too few elements will introduce errors in the crack growth resistance (fracture energy) calculation; however, finer meshes require more computational resources. A mesh sensitivity study was conducted to find the best compromise between the fracture process representation accuracy and the computational power required. A fracture process zone length of 38 mm was obtained for mode-I fracture in the *DCB Test Model*, as shown in Fig. A.15; thus, the minimal element size that can accurately represent the fracture process is 3.8 mm. Despite this, an even smaller element size was selected, 0.5 mm, to represent the stress/strain variation in the fracture process zone with more accuracy, which it is important to obtain high resolution in the FBG simulations. For more details about this, see publication [P3] section P3.4.1.
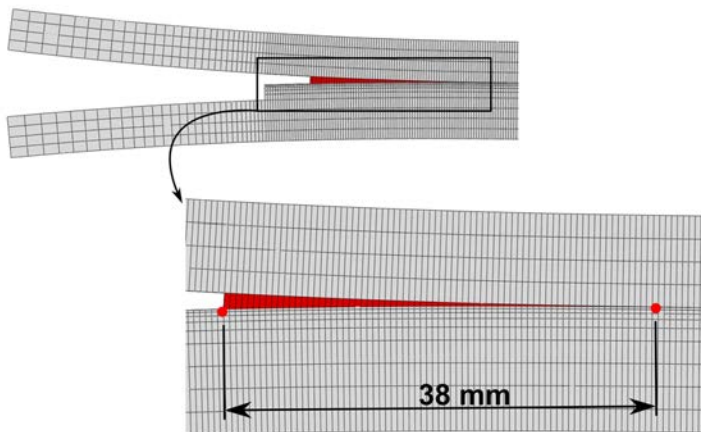
Figure A.15: Fracture process zone length in DCB mode-I fracture; minimum element size used: 3.8 mm.

In terms of numerical errors, the DCB model can present some shear locking behaviour, which is caused by overly stiff elements in bending-loading conditions. Thus, elements with incompatible modes were used to improve the bending behaviour and reduce the shear locking behaviour. The description of the different elements used in the DCB models is presented in table A.7. In all the DCB models non-linear effects were considered (Nlgeom), and the 2D models were developed assuming plane stress conditions.

Table A.7: DCB validation model material properties.

Element Type	2D	3D
FRP Laminate	CPS4I: 4-node bilinear plane stress quadrilateral, incompatible modes;	C3D8I: 8-node linear brick, incompatible modes;
Elastic Adhesive	CPS4I: 4-node bilinear plane stress quadrilateral, incompatible modes;	C3D8I: 8-node linear brick, incompatible modes;
Cohesive Element	COH2D4: 4-node 2D cohesive element;	COH3D8: 8-node 3D cohesive element;

Convergence issues and "heavy" (time consuming) simulations can be an issue found in damage progression simulations based on CS, CE and VCCT. To solve this, Abaqus have a numerical artifice, viscous regularization, which ensures a consistent positive tangent stiffness of the softening material, i.e., when the element is damaged and its stiffness is decreasing, the viscous regularization parameter ensures that the nodes movement is damped and a force equilibrium is found. However, this parameter introduces an extra artificial energy to the system that increases the load required for the crack to grow; thus, this parameter should be as small as possible to decrease this numerical error.

The influence of the viscous regularization parameter in the mode-I fracture energy of the *DCB Validation Model* using cohesive elements (CE) is shown in Fig. A.16. The models with higher viscous regularization have a faster convergence, however this increases the ratio of dissipated visco-energy/internal energy, which induces a numerical error artificially increasing the energy release rate (J); on the positive side, small viscous regularization values give accurate energy release rate simulation, where the energy dissipated by the viscosity regularization is minimal. Although, for viscous regularization values smaller than 1E-7, convergence was not found. A simple way to tune the viscous regularization parameter is by evaluating the ratio of dissipated visco-energy/internal energy, where values $<< 0.1\%$ give a reasonably accurate prediction of the energy release rate in a model that can converge.
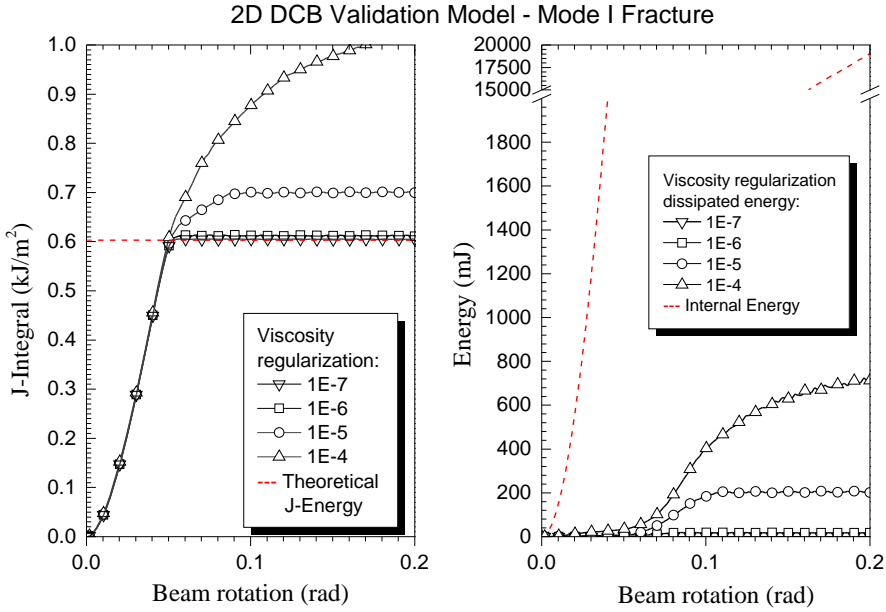
Figure A.16: Influence of the viscous regularization parameter in the fracture energy: Mode I fracture of the *DCB Validation Model* using cohesive elements (CE).

This viscous regularization parameter needs to be tuned for every model; thus, a sensitivity study was performed for the different FEM models, and the final tuned viscous regularization values are shown in table A.8.

**Table A.8:** Tuned viscous regularization parameter for the different DCB models.

Model	2D	3D
DCB Validation Model	1E-6 (VCCT, CE, CS)	5E-6 (VCCT, CE, CS)
DCB Test Model	1E-4 (VCCT, CE, CS)	5E-4 (VCCT, CE, CS)

A.6.4 DCB Model Validation: back calculation of the cohesive-law

As the FEM model represents the fracture testing of a DCB specimen, the J-integral can be measured virtually, similar to a real fracture test, by recording the moments applied to the beams and the crack opening, as shown in Fig. A.17. Then, the J can be calculated by Eq. (A.16), and the cohesive-law obtained should be consistent with the cohesive-law that was set in the FEM model. This back calculation of the cohesive-law is used to validate the different DCB models.

The virtual J-integral, calculated from the 2D DCB models using the three different damage methods (CE, CS, and VCCT), and loaded in mode-I and mode-II is shown in Fig. A.18. In the DCB specimens with CS and CE, the energy release rate (J_{ss}) was accurately predicted for both fracture modes; however, in the DCB modelled with VCCT, the simulated energy release rate was higher than the theoretical.

The VCCT criterion has some numerical issues to simulate growing damage, therefore it uses a tolerance parameter (Eq. (A.27)) which allows higher initiation energy in the nodes subsequent to the crack tip. For the DCB case, the model does not converge if the tolerance parameter is set as $f = 0$; thus, a tolerance value of $f = 0.1$ was used, which matches the energy measured by the VCCT criterion ($J_{SS}^{VCCT} = 0.665$). Further, the DCB modelled with VCCT cannot describe the non-linear behaviour of the damage process nor the damage initiation, which makes this technique not the best approach to model delamination in FRP materials. The only advantage of the VCCT against the CE/CS is that it allows computation of contribution of each mode independently, which is useful to evaluate the mixed-mode ratio in complex loading configurations or non-symmetric specimens.
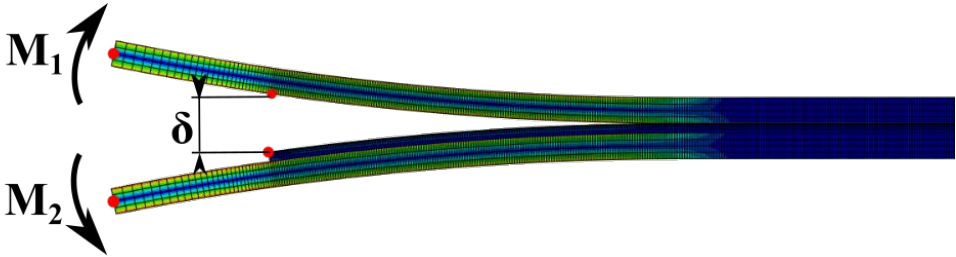
Figure A.17: Virtual measurement of the J-integral in a DCB specimen. FEM model output: bending moments, M_1 and M_2, crack opening δ.
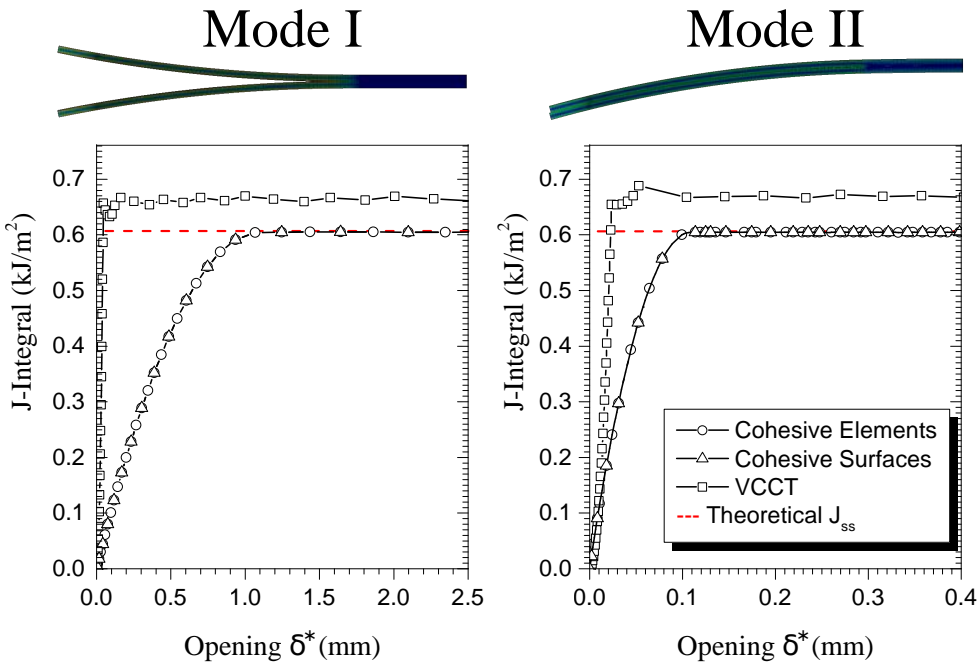
Figure A.18: Virtual measurement of the J-integral in a DCB specimen. FEM
model output: bending moments, M_1 and M_2, crack opening δ.

Finally, the cohesive-law was back calculated by derivation of the J-integral curves,
as described by Eq. (A.14) and (A.15). The original cohesive-law was accurately
obtained, for both fracture modes and CE/CS damage modelling techniques (see Fig.
A.19). These results validate the accuracy of the *DCB Validation Model*, and its
capability to represent the delamination of FRP materials. This validation procedure
was repeated for the 3D cases, and similar results were obtained.
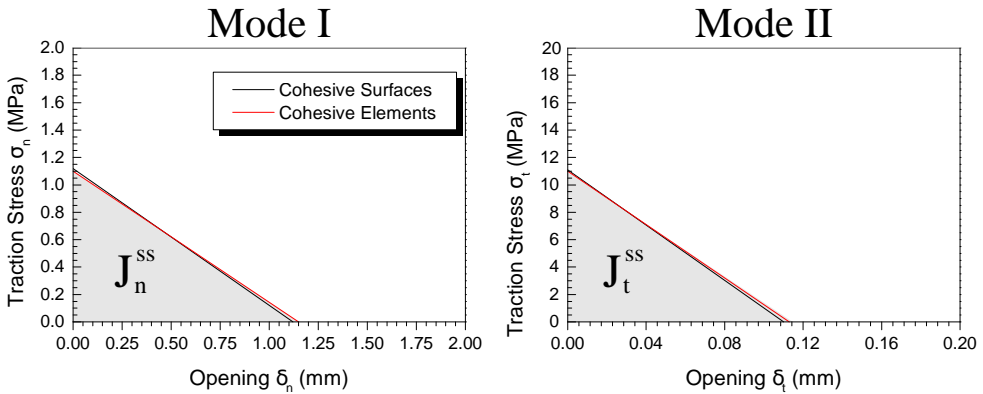
Figure A.19: Mode-I and mode-II traction-opening curves for DCB specimens modelled by CE and CS: back calculated cohesive-law from the virtual J-integral curves.

Appendix A-References

[1] S. Krohn, P.-E. Morthorst, and S. Awerbuch, "The economics of wind energy," European Wind Energy Association (EWEA), Tech. Rep. March, 2009, pages 1–156.

[2] J. G. Mcgowan, R. W. Hyers, K. L. Sullivan, J. F. Manwell, S. V. Nair, B. Mcniff, and B. C. Syrett, "Review a review of materials degradation in utility scale wind turbines," *Energy Materials*, volume 2, number 1, pages 41–64, 2007, ISSN: 1748-9237. DOI: 10.1179/174892407X223902.

[3] *Wind energy explained: Theory, design and application*, 2nd Editio. Wiley, 2009, ISBN: 9780471499725.

[4] P. J. Schubel and R. J. Crossley, "Wind turbine blade design," *Energies*, volume 5, number 12, pages 3425–3449, 2012, ISSN: 1996-1073. DOI: 10.3390/en5093425.

[5] DNV/Risø, "Guidelines for design of wind turbines, second edition," DNV/Risø, Tech. Rep., 2009.

[6] B. Sørensen, J. W. Holmes, P. Brøndsted, and K. Branner, "Blade materials, testing methods and structural design," in *InWind power generation and wind turbine design*, W. Tong, Ed., Kollmorgen Corp., USA: WIT Press, 2010, ch. 13, pages 417–466, ISBN: 978-1-84564-205-1.

[7] P. Brøndsted, H. Lilholt, and A. Lystrup, "Composite materials for wind power turbine blades," *Annual Review of Materials Research*, volume 35, number 1, pages 505–538, 2005, ISSN: 1531-7331. DOI: `10.1146/annurev.matsci.35.100303.110641`.

[8] M. A. Eder and R. D. Bitsche, "Fracture analysis of adhesive joints in wind turbine blades," *Wind Energy*, volume 18, number 6, pages 1007–1022, Jun. 2015, ISSN: 10954244. DOI: `10.1002/we.1744`.

[9] "Defect distribution and reliability assessment of wind turbine blades," *Engineering Structures*, volume 33, number 1, pages 171–180, January 2011, ISSN: 01410296. DOI: `10.1016/j.engstruct.2010.10.002`.

[10] S. Ataya and M. M. Ahmed, "Damages of wind turbine blade trailing edge: forms, location, and root causes," *Engineering Failure Analysis*, volume 20, Jun. 2013, ISSN: 13506307. DOI: `10.1016/j.engfailanal.2013.05.011`.

[11] P. Haselbach, R. Bitsche, and K. Branner, "The effect of delaminations on local buckling in wind turbine blades," *Renewable Energy*, volume 85, pages 295–305, January 2016, ISSN: 09601481. DOI: `10.1016/j.renene.2015.06.053`.

[12] P. U. Haselbach, M. A. Eder, and F. Belloni, "A comprehensive investigation of trailing edge damage in a wind turbine rotor blade," *Wind Energy*, n/a–n/a, January 2016, ISSN: 10954244. DOI: `10.1002/we.1956`.

[13] T. Anderson, *Fracture mechanics : fundamentals and applications*, 3rd edition. CRC, Taylor & Francis, 2005, ISBN: 9780849316562.

[14] M. Shokrieh, H. Rajabpour-Shirazi, M. Heidari-Rarani, and M. Haghpanahi, "Simulation of mode i delamination propagation in multidirectional composites with r-curve effects using vcct method," *Computational Materials Science*, volume 65, pages 66–73, 2012, ISSN: 09270256. DOI: `10.1016/j.commatsci.2012.06.025`.

[15] D. M. Parks, "A stiffness derivative finite element technique for determination of crack tip stress intensity factors," *International Journal of Fracture*, volume 10, number 4, pages 487–502, 1974, ISSN: 0376-9429. DOI: `10.1007/BF00155252`.

[16] P. Cornetti, A. Sapora, and A. Carpinteri, "Short cracks and v-notches: finite fracture mechanics vs. cohesive crack model," *Engineering Fracture Mechanics*, 2016, ISSN: 00137944. DOI: `10.1016/j.engfracmech.2015.12.016`.

[17] A. Turon, "Simulation of delamination in composites under quasi-static and fatigue loading using cohesive zone models," PhD thesis, 2007, page 227, ISBN: 9788469043721.

[18] D. Dugdale, "Yielding of steel sheets containing slits," *Journal of the Mechanics and Physics of Solids*, volume 8, number 2, pages 100–104, 1960, ISSN: 00225096. DOI: `10.1016/0022-5096(60)90013-2`.

[19] G. Barenblatt, *Advances in Applied Mechanics Volume 7*, series Advances in Applied Mechanics. Elsevier, 1962, volume 7, pages 55–129, ISBN: 9780120020072. DOI: `10.1016/S0065-2156(08)70121-2`.

[20] G. Li and C. Li, "Linking bilinear traction law parameters to cohesive zone length for laminated composites and bonded joints," *Advances in aircraft and spacecraft science*, volume 1, number 2, pages 177–196, 2014, ISSN: 2287-528X. DOI: `10.12989/aas.2014.1.2.177`.

[21] B. R. K. Blackman, H. Hadavinia, A. J. Kinloch, and J. G. Williams, "The use of a cohesive zone model to study the fracture of fibre composites and adhesively-bonded joints," *International Journal of Fracture*, volume 119, number 1, pages 25–46, ISSN: 1573-2673. DOI: `10.1023/A:1023998013255`.

[22] T. Jacobsen and B. Sørensen, "Mode i intra-laminar crack growth in composites—modelling of r-curves from measured bridging laws," *Composites Part A: Applied Science and ...*, volume 32, pages 1–11, 2001.

[23] B. F. Sørensen and P. Kirkegaard, "Determination of mixed mode cohesive laws," *Engineering Fracture Mechanics*, volume 73, number 17, pages 2642–2661, 2006, ISSN: 00137944. DOI: `10.1016/j.engfracmech.2006.04.006`.

[24] M. Benzeggagh and M. Kenane, "Measurement of mixed-mode delamination fracture toughness of unidirectional glass/epoxy composites with mixed-mode bending apparatus," *Composites Science and Technology*, volume 56, number 4, pages 439–449, 1996, ISSN: 02663538. DOI: `10.1016/0266-3538(96)00005-X`.

[25] P. P. Camanho, C. G. Davila, M. F. de Moura, and M. F. D. Moura, "Journal of composite materials," *Journal of composite materials*, volume 37, number 16, pages 1415–1438, 2003, ISSN: 00219983. DOI: `10.1177/002199803034505`.

[26] P. Robinson and S. Das, "Mode i dcb testing of composite laminates reinforced with z-direction pins: a simple model for the investigation of data reduction strategies," *Engineering Fracture Mechanics*, volume 71, number 3, pages 345–364, 2004, ISSN: 00137944. DOI: `10.1016/S0013-7944(03)00116-4`.

[27] B. Sørensen, K. Jørgensen, T. Jacobsen, and R. Østergaard, "Dcb-specimen loaded with uneven bending moments," *International Journal of Fracture*, volume 141, number 1-2, pages 163–176, 2006, ISSN: 0376-9429. DOI: `10.1007/s10704-006-0071-x`.

[28] M. Shokrieh and M. Heidari-Rarani, "Effect of stacking sequence on r-curve behavior of glass/epoxy dcb laminates with 0°//0° crack interface," *Materials Science and Engineering: A*, volume 529, pages 265–269, 2011, ISSN: 09215093. DOI: `10.1016/j.msea.2011.09.027`.

[29] B. F. Sørensen and T. K. Jacobsen, "Characterizing delamination of fibre composites by mixed mode cohesive laws," *Composites Science and Technology*, volume 69, number 3-4, pages 445–456, March 2009, ISSN: 02663538. DOI: `10.1016/j.compscitech.2008.11.025`.

[30] J. R. Rice, "A path independent integral and the approximate analysis of strain concentration by notches and cracks," *Journal of Applied Mechanics*, volume 35, number 2, page 379, 1968, ISSN: 00218936. DOI: `10.1115/1.3601206`.

[31] B. Sørensen, *Cohesive laws for assessment of materials failure: Theory, experimental methods and application.* Risø-Technical Univ. of Denmark, Risø National Laboratory for Sustainable Energy. Materials Research Division, 2010, 243 s, ISBN: 9788755038271.

[32] C. Bak, F. Zahle, R. Bitsche, A. Yde, L. C. Henriksen, A. Nata-, and M. H. Hansen, "Description of the dtu 10 mw reference wind turbine department of wind energy i-report," DTU Wind Energy, Tech. Rep. July, July 2013, pages 1–138.

[33] M. J. Hinton, A. S. Kaddour, and P. D. Soden, *Failure Criteria in Fibre Reinforced Polymer Composites.* Elsevier, 2004, ISBN: 0080426999.

[34] B. F. Sørensen, S. Goutianos, and T. K. Jacobsen, "Strength scaling of adhesive joints in polymer–matrix composites," *International Journal of Solids and Structures*, volume 46, number 3-4, pages 741–761, February 2009, ISSN: 00207683. DOI: 10.1016/j.ijsolstr.2008.09.024.

[35] ABAQUS™, *User Manual. Version 6.13, ABAQUS Inc., Pawtucket, Rhode Island, USA.* USA, 2013.

[36] A. Turon, C. Dávila, P. Camanho, and J. Costa, "An engineering solution for mesh size effects in the simulation of delamination using cohesive zone models," *Engineering Fracture Mechanics*, volume 74, number 10, pages 1665–1682, 2007, ISSN: 00137944. DOI: 10.1016/j.engfracmech.2006.08.025.

[37] D. Álvarez, B. Blackman, F. Guild, and A. Kinloch, "Mode i fracture in adhesively-bonded joints: a mesh-size independent modelling approach using cohesive elements," *Engineering Fracture Mechanics*, volume 115, pages 73–95, 2014, ISSN: 00137944. DOI: 10.1016/j.engfracmech.2013.10.005.

Appended Paper P1

Damage Tolerance And Structural Monitoring For Wind Turbine Blades

M. McGugan, **G. Pereira**, B. F. Sørensen, H. Toftegaard and K. Branner

Abstract

The paper proposes a methodology for reliable design and maintenance of wind turbine rotor blades using a condition monitoring approach and a damage tolerance index coupling the material and structure. By improving the understanding of material properties that control damage propagation it will be possible to combine damage tolerant structural design, monitoring systems, inspection techniques and modelling to manage the life cycle of the structures. This will allow an efficient operation of the wind turbine in terms of load alleviation, limited maintenance and repair leading to a more effective exploitation of offshore wind.

P1.1 Introduction

P1.1.1 Offshore wind energy

The potential for Offshore Energy production in Europe is enormous. Industry projection from the European Wind Energy Association (EWEA) is for an increase from 5GW in 2012 to 150GW in 2030 (EWEA, www.ewea.org), and achieving that potential is an important objective of the European Communities. In 2008 the executive body of the European Union issued a communication detailing the Roadmap for Maritime Spatial Planning [1]. This roadmap was intended to balance the requirements of various sectorial interests utilising marine resources, and offshore energy (particularly wind) was anticipated to make very significant increases in the near to medium term.

However, in order to support this growth it is vital to make significant reductions in the Cost of Energy (CoE) of offshore wind, as it was discussed at the most important wind energy conference EWEA 2014 [2]. A radically different approach is needed to design and operate offshore wind turbines. This is what we propose in this paper. The most eye-catching trend for wind energy structural components is the up-scaling history where new turbine designs have consistently provided larger turbines with higher power ratings. The most cost effective way of increasing the power produced (PP) by a wind turbine is to increase the rotor diameter [3], currently prototype rotor blades are exceeding 70 m in length (SSP-technology: 7 MW-83.5 m. blade project). The industry relies on advances in materials technology to deliver cost-effective lightweight structures.

Although larger turbines cost more to manufacture per unit (Cost of Turbine-CoT), this small relative increase is more than compensated for by the absolute saving possible when factoring installation costs (CoI) and the cost of maintenance (CoM) with larger turbine units. These costs are factored against the power produced PP:

$$CoE = (CoT + CoI + CoM)/PP \tag{P1.1}$$

The manual inspection of wind turbines (inconveniently placed on high towers in remote places) involves a certain amount of travel time as equipment and personnel are moved between them; higher Mega Watt turbines help to reduce this cost relative to the power output of the farm. However, economies of up-scaling for the operation of an offshore, multi-MW farm can be challenged as the consequence of a single turbine downtime is more significant, and all personnel operation offshore is more expensive. Therefore, cost reduction by using remote monitoring becomes increasingly attractive as a means to suppress unexpected downtime, and focus limited maintenance and repair operations.

P1.1.2   Multi-physics global model

Some research groups are working on a Multi-physics Global Model [4–8], as represented by the scheme in the Fig. P1.1. A Multi-physics Global Model is defined as a fluid-structural interaction model, that aims to capture and integrate several phenomena; meteorology, aerodynamics, hydrodynamics, aero-elasticity, structural vibration, energy output, control, etc. (For example, the integrated response of the tower pillar to the aerodynamic load on the blades and waves on the foundations). However, this approach will not be achieved until all physical phenomena are fully understood. Wind turbines are a multi-physics problem, and the complexity of the
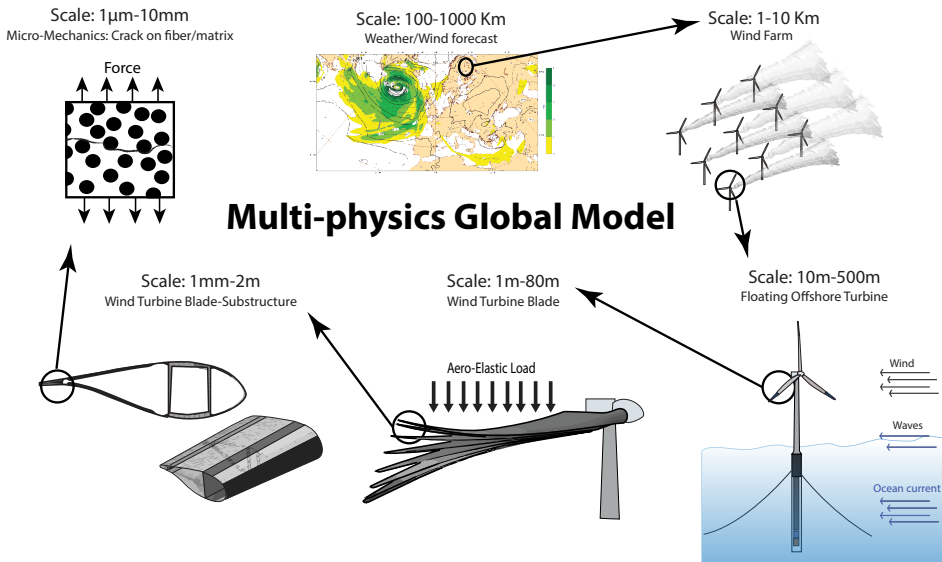

Figure P1.1: Multi-physics Global Model scheme.

structure and loading, and the variability and turbulence of the wind create challenges for the application of such a method. At this time, significant research effort is being made in order to fully research the most complex phenomena at each of the scales presented in Fig. P1.1. Obviously, it is not possible to predict the aero-dynamical load history on a wind turbine rotor blade in details for a 20-years period of time. There are two approaches to address this. One is to make lifetime predictions based on statistics. Another approach, as will be pursued here, involves the use of sensors to detected the conditions of the blades to obtain an updated lifetime prediction.

P1.1.3   Wind Turbine Rotor Blade Structures

A wind turbine rotor blade structure is defined in terms of its outer geometry and inner structural layout. It can be made from different materials and will be subjected to varying loads from wind and varying direction of gravity due to the rotation of the rotor. A typical turbine blade design is based on a load-carrying laminate in a rectangular hollow beam (spar). In another common blade design there is no spar; instead there is a combination of a load-carrying laminate incorporated in the aero shell together with two shear webs [9]. The beam spar and the sandwich face sheets of the aero shell are made from fibre reinforced polymer composite materials, see Fig. P1.2; the sandwich cores are made from polymeric foam or balsa wood; and the blade is assembled with adhesives between the aero shells at the leading edge, between the spar and the aero shell, and between the aero shells at the trailing edge.

At the structural scale, a wind turbine rotor blade can develop various types of damage, such as cracks along adhesive joints (e.g. leading and trailing edges as well as internal bondlines at beam/laminate assemblies). Laminates can fail by cracks parallel to the fibre direction (e.g. splitting cracks and transverse cracks),
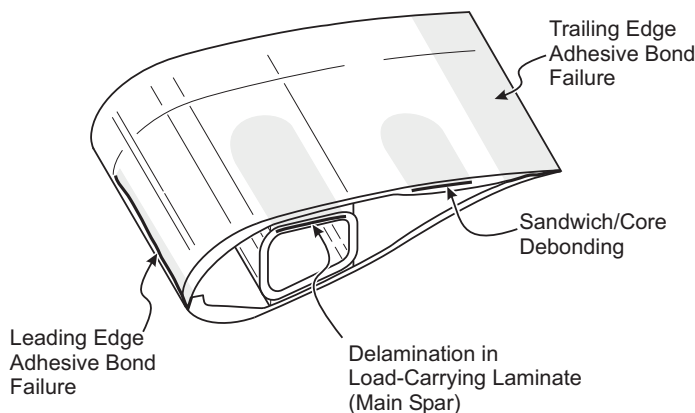
Figure P1.2: Schematics of major failure modes in a part of a wind turbine rotor blade. The shaded areas indicate cracked internal regions.

fibre failure in tension (distributed damage) or compression (localised damage), and by delamination (cracking along the plane between plies). Of these, delamination of laminates and adhesive bonded joints are usually the most critical [9, 10].

P1.1.4   Fibre Reinforced Polymer Composite Materials

Fibre reinforced polymer composite materials consist of two macroscopic phases, a stiff fibre phase (usually glass or carbon) and a polymer matrix (usually polyester or epoxy). One of the advantages of fibre reinforced polymer composites is that the alignment of the fibres can be arranged to suit the required properties of the intended structure. Thus the requirement for a stiff (but light-weight) structure means fibre orientations primarily along the length of the blade and an inherently anisotropic set of material characteristics. A key feature of structures designed using composite material is that the manufacturing process itself will determine certain characteristics of the material, and hence the behaviour of the final structure. All this is to say that when looking to optimise the properties of a wind turbine blade, it is necessary to consider material choice, design approach, and manufacturing process as an integrated issue.

For example, a common processing procedure is to stack layers of the dry reinforcement fibres before infusing with a thermosetting resin to create the finished composite material. This results in a laminated structure with significant stiffening mainly along the length direction of the blade. But the effect on out-of-plane properties and the weak interfaces between layers of the composite material needs to be understood at the material level, if the final structure is to be sound and resistant to any out-of-plane loading.

P1.1.5   Structural Design Philosophies

The design philosophy for fibre reinforced polymer structures was initially based on conservative analysis methods with large safety factors, underestimating the actual material properties, and considering primarily the linear elastic material behaviour. As knowledge about materials and structures increased it has now become possible to safely adopt more advanced design philosophies. This general trend to more advanced structural design is described elsewhere [11]. In wind turbine blade design it is important to take into account different non-linear effect as described in [12]. Failure of a wind turbine blade has a small to minor consequence as the risk for human lives is small, especially offshore since persons are not close to the wind turbines. The optimal target reliability level can therefore be determined by cost benefit analysis, where all the cost during the wind turbines design life is taken into account [13]. Partial safety factors can be calibrated to obtain the desired target reliability level for the structure [14]. And the uncertainties for the material properties for composite materials can be modelled [15]. Probabilistic design methods give a prediction for the risk of failure in average, but give in principle no information for the condition and

risk of failure for a particular blade. However, this information is available within a structural design philosophy based on damage monitoring.

The approach is to use damage tolerant materials and a structural health and prognostic management system as part of a *condition based maintenance* program. It is an axiom of Structural Health Monitoring [16], that detectable changes in response must exist between undamaged and damaged states, thus implying damage tolerance. Damage tolerance (see section P1.3.2 for details) is a property emerging from the particular combination of structure design, loading environment, and material characteristics. Accepting that a distribution of damage types and locations can exist within the blades of an operating offshore wind farm, it follows that each structure must be characterised individually with a unique "damage map" for that structure. Evaluating the severity of the particular combination of damage types requires models that describe the progression parameters for each type under the full range of operating conditions. Only in this way can condition based maintenance be effectively implemented.

P1.2   Vision

Our vision consists of a damage tolerance approach that can be made using conditional inspections and models that describe progression for all known failure types [17, 18]. The future design philosophy will be based on a Structural Health Monitoring approach where sensors integrated during manufacture provide fed back that is used to optimise the entire life-cycle. And this again requires an advance in materials knowledge to implement effectively. The already established concept of composite materials structural design based on an integrated material/structure/manufacturing iteration, should be extended to include an application of the deeper material level (microscopic level) understanding of the damage propagation. So in much the same way as structural load and stiffness requirements are already "tailored" at the material level, optimisation of the material properties can be used to match design objectives related to damage tolerance and reliability for the final structure. All this needs to be achieved in a framework of condition based maintenance, remote monitoring, and prognosis, as presented in Fig. P1.3.

It is important to appreciate that in comparison with aerospace structures, wind turbine rotor blades are unique in the sense that they are made of very large parts, using relative "low cost" composite materials and manufacturing methods. Requiring a very strict quality control and allowing only parts with small manufacturing defect size may lead to a high rate of discarded blade parts. Obviously, this would lead to a higher blade price. An alternative approach, proposed here, is to allow more blades with manufacturing defects to be used in service by ensuring that the defects lead to stable damage, i.e. avoiding unstable blade failure. For a given wind turbine design, the damage evolution will depend on structural details and materials properties that cannot be accurately controlled during manufacturing. Furthermore, each blade on a wind turbine in an off shore wind farm will experience its own, unique combination
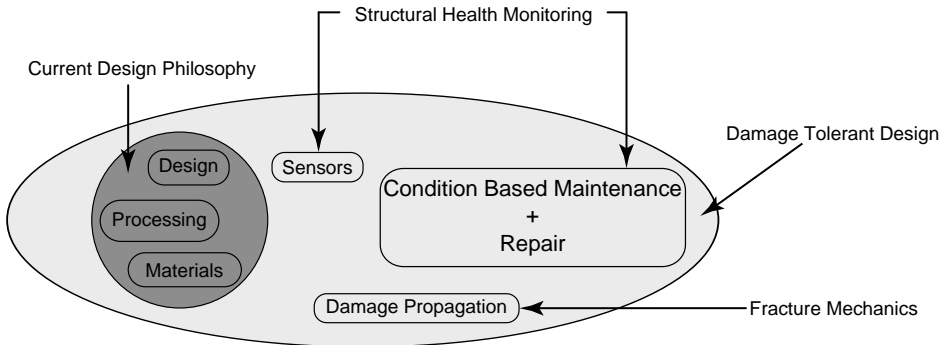
Figure P1.3: Expanded design and manufacturing process including structural
health monitoring.

of load history. Consequently, blades will not undergo identical damage evolution.
One blade may undergo a loading history that leads to more damage in one area,
while another blade, having a different set of manufacturing defects and experiencing
another load history, may develop damage in other areas of the blade.

The key features in the proposed condition based maintenance approach can be
summarised as follows. First, in the design phase, the designer will choose materials
and structural layout that give a high damage tolerance. The designer also will decide
on the type of sensors for damage detection and determines (from structural analysis)
which areas are the most critical and where the sensor should be placed. Next, in
the manufacturing phase, sensors will be placed inside the rotor blade, either as
sensors embedded in laminates or adhesive bond lines or mounted inside the blade
after manufacturing. Sensors surveillance can cover transportation, installation and
in-service operation, and be part of the post-manufacturing control by contributing
to non destructive inspection (NDI) procedures.

For the few blades that will develop serious damage, sensor alarms will be sent from
the off-shore wind turbine to the on-shore surveillance centre, which can then send out
a maintenance team to inspect the blade at the position where the damage is detected.
The team will use non-destructive techniques such as ultrasound scanning,radiography
(x-ray) etc. to identify the damage type, its size and depth. This information will be
used in detailed structural models (e.g. finite element models) of the blade with the
characterised damage to assess the residual fatigue life and residual strength, using
information about fracture data (stress-strain, traction-separation, fatigue data) of
the materials and the anticipated future load history. It will then be possible to assess
the criticality of the damage and decide whether the blade can be used under normal
operation, or whether the aero-loads should be reduced, or the blade repaired on site,
or taken down (replaced with a new blade or repaired on shore).

Such an approach will allow the service life of blades to be decided by their damage
state. There is thus potential for life extension beyond the original planned service

life (typically now 20 years) for healthy blades that do not possess significant damage.

A condition based approach also has the advantage that it is not critical to be able to calculate the aero-loads with high accuracy on all individual rotor blades in an offshore wind turbine park, since the damage evolution can be assessed on basis of the sensor signal. The proposed approach, Fig. P1.4, consists of condition monitoring to detect damage, NDI methods to characterise the damage, and damage and fracture mechanical modelling to predict future damage evolution [19–21], creating the science-based knowledge required to make a decision about what to do.

The proposed new approach has some similarities with the "retirement for cause" approach used in military aircrafts, where the life time of gas turbine engines is determined on the basis of the detection of flaws of a certain detectable size rather than being retired prematurely by the traditional pre-determined life approach [22]. In the following section of the paper, the material properties contributing to structural damage tolerance are presented. These properties are the "levers" that future designs will consciously utilise when engineering reliability from the material level to the structural level. The expanded design and manufacture process showed in Fig. P1.3, will include consideration of the approach for maintenance and repair that is to be adopted for the entire group of structures, and the integrated sensorisation necessary to achieve remote characterisation of the material and structural condition. Finally, the vision is presented of offshore wind farms designed using smart structure technology made possible by this deeper understanding of material behaviour.
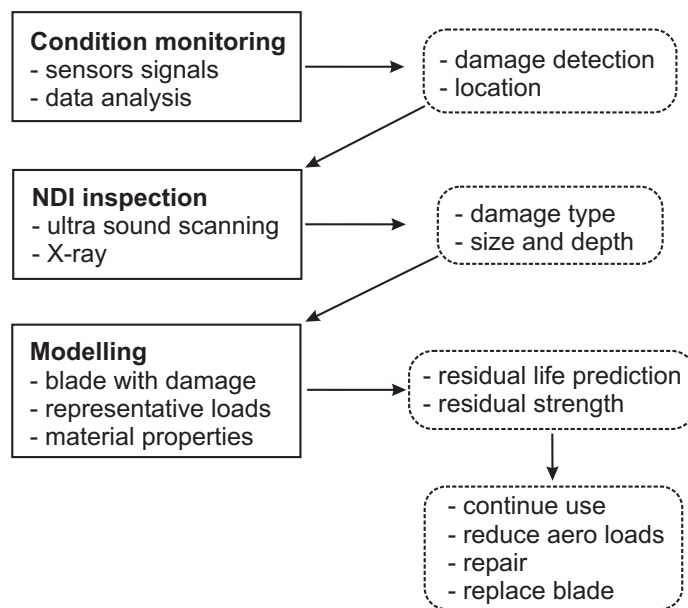
**Figure P1.4:** Condition Monitoring Modelling Approach.

P1.3 Increasing Reliability of Offshore Wind Turbine Blades by Damage Tolerance

P1.3.1 The concepts of distributed and localised damage

The loads on each material point within a rotor blade structure can be characterised mechanically by considering a small volume of the material. On the materials level, the load is characterised in terms of stress σ (defined as load per cross-section area), and deformation is characterised in terms of strain ε (elongation divided by original length). The stress-strain relationship ($\sigma - \varepsilon$) of an undamaged material is in most cases linear (Fig. P1.5a). In a loaded wind turbine rotor blade, distributed damage (e.g., small cracks in the matrix and breakage of fibres in a composite material) can develop in some regions of the blade. The distributed damage may be characterised by the crack area per volume or the number of broken fibres per volume. Damage induces non-linearity in the stress-strain relationship. Therefore, non-linear stress-strain laws must be used to describe the mechanical response of materials experiencing distributed damage (Fig. P1.5a). Distributed damage may over time lead to localised damage. During localisation, the material undergoes weakening in a so-called failure process zone, so that its ability to transfer stress decreases, with increasing local deformation δ (separation). It is then appropriate to describe the material behaviour in terms of a traction-separation law ($\sigma_n - \delta_n$) (see Fig. P1.5b). With increasing separation (corresponding to more localised damage) the traction that the fracture process zone can transmit decreases. When the end-opening of the fracture process zone δ_n^* exceeds a critical value δ_n^0, the traction vanishes completely so that a crack surface forms. The traction-separation law is taken to be a material property, being the same law along the entire fracture process zone. The area under the traction separation curve is the work of the traction, i.e., the fracture resistance.

Owing to the difference in stress levels for different parts of the blade and uneven distribution of the manufacturing defects, the damage state may vary from part to part between undamaged material, distributed damage and localised damage. Depending on the conditions the localised damage may either exhibit stable or unstable crack growth. The damage state can be described by a "damage map" in terms of the location, damage type and size, as well as a parameter indicating how close the damage state is to the critical condition (unstable crack growth).

Offshore wind turbine rotor blades will be subjected to high extreme wind loads (heavy storms) and lower, varying loads from wind changes and rotor rotation. Cyclic loads may induce fatigue damage evolution, i.e., stable crack growth occurring as a very small increase in the crack length during each load cycle. The crack can then become so long that it leads to unstable, fast crack propagation at the maximum cyclic load, potentially leading to structural failure of the rotor blade. The condition for unstable crack growth is thus a key issue. The transition from stable to unstable crack growth can be analysed as crack growth under constant load (the maximum value of the cyclic load). The stability of crack growth will be the focus of the remainder of
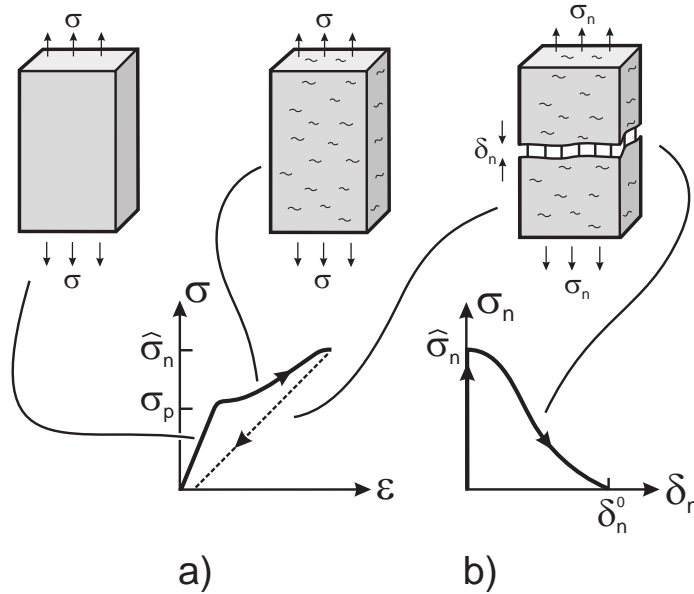
Figure P1.5: The relationship (a) between stress, σ, and strain, ε, is used to characterise deformation of undamaged material (linear stress-strain response) and material with distributed damage (non-linear stress-strain response), while the relationship (b) between stress (traction), σ_n, and separation, δ_n, is appropriate for describing localised damage (fracture). Away from the localised damage the material is unloaded along the dotted part of the stress-strain curve (a).

the section.

P1.3.2   Damage tolerant materials and structures

In the following, we will discuss how materials properties and structural design can be used to achieve enhanced damage tolerance, being the ability to sustain damage without unstable catastrophic failure. In particular, we wish to argue a design philosophy where materials and the structural design are chosen so that each structural detail can be designed to possess a high damage tolerance.

For distributed damage, damage tolerant behaviour is obtained as follows. For undamaged composite materials, the stress-strain behaviour is linear. Damage induces non-linear stress-strain behaviour - the material decreases in stiffness with increasing damage. An undamaged material loaded beyond the linear-elastic limit σ_p will start to develop damage and thus exhibit non-linear stress-strain behaviour up to the failure stress $\hat{\sigma}_n$ (strength). Damage tolerance requires that the materials strength

should be significantly higher than its linear-elastic limit and that the damage can be detected by sensors. It then becomes possible to detect whether the material has been overloaded and to repair or replace the structure while the material still retains a strength above its design stress. Material design can create composite laminates having non-linear stress-strain behaviour even though most fibre types used in composite materials are linear elastic. A non-linear stress-strain behaviour can be obtained by the use of laminates with multiple fibre orientations (enabling some layers to crack at lower strains, denoted "first-ply-failure") or by the use of fibres having different failure strain (hybrid composites).

Localised fracture, such as delamination, can be analysed by fracture mechanics, e.g. by the use of traction-separation laws. With respect to the propagation of a crack, damage tolerance implies that the crack growth should be stable, requiring that the load level for unstable crack growth should be significantly higher than the load level that initiates crack growth. Classic fracture mechanics considers an energy balance between the energy supplied (or released) by the structure and the energy absorbed by the fracture processes at the crack tip. Crack growth will not occur when the energy released by the structure per unit crack advancements is less the energy consumed by the crack tip fracture processes per unit crack advancement.

The energy released per unit cracked area depends on the magnitude of the applied load, the elastic properties and the shape of the structure. If the fracture resistance is constant, the crack growth can be stable (i.e. causing cracking to stop, denoted crack arrest) or unstable depending on how the energy released depends on the load and geometry, i.e., structure properties. The structure should be designed so that it can take the additional load when a crack has formed and the local region carries less load (Fig. P1.5b). It is possible, however, to increase the amount of stable crack growth by designing interfaces that possess increasing fracture resistance with increasing crack extension. Rising fracture resistance, denoted R-curve behaviour, implies that the energy absorbed per unit area of the fracture process zone increases with the crack extension. Typically, the crack growth resistance increases from an initial value to a steady-state value. It follows that the stability of crack growth now depends on the load, geometry (including the initial crack length), and the fracture resistance of the material. Often in composites, delamination is accompanied by the formation of a crack bridging zone, where intact fibres connect the crack faces behind the crack tip. This can lead to a large-scale crack bridging zone, resulting in R-curve behaviour [23]. The bridging law, i.e. the normal traction σ_n as a function of the normal opening $\delta_n, \sigma_n(\delta_n)$, plays a central role in the stability of crack growth, since the R-curve behaviour is related to the traction-separation law. Two conditions for stable crack growth, expressed in terms of the bridging law parameters, are:

$$J_{ext} = J_0 + \int_0^{\delta_n^*} \sigma_n(\delta_n)d\delta_n \quad and \quad \frac{\partial J_{ext}/\partial a}{\partial \delta_n^*/\partial a} \leq \sigma_n(\delta_n^*). \qquad \text{(P1.2)}$$

In (P1.2), J_{ext} is the energy released per unit cracked area, J_0 is the energy at which cracking initiates, σ_n and δ_n are traction and separation (Fig. P1.5b), δ_n^* is

the separation at the end of the crack, and a is the crack length. To obtain stable cracking during an increasing load, these two equations should be fulfilled at all times. The cracking will be unstable when the right hand side inequality is violated.

Equation (P1.2) makes it possible to think intelligently about the damage tolerance of almost any large-scale bridging cracking problem in a structural part of a wind turbine rotor blade. The left hand sides of both equations include all the structural parameters (loads and structural geometry), while the right hand sides depend only on the fracture properties. Thus the initial structure design can be specified to achieve a minimum damage tolerance level throughout the blade. Once the load and geometry of the blades have been fixed, options to modify local stiffening, manufacturing specifications, or material options allow an assessment of which traction-separation law (the right hand side) gives the highest damage tolerance/longest stable crack extension. In this way these relations are very helpful for both the structural designer and the material scientist.

Optimising materials damage tolerance with traction-separation laws

Micromechanical models of crack bridging show that the bridging traction depends on microscale parameters such as the fibre stiffness, the fibre diameter and the fibre/matrix debond energy [23, 24]. It is thus possible to change the traction-separation laws by changing the properties of microscale parameters (this is sometimes called "microstructural optimisation"). For instance, the surface of the fibres can be subjected to chemical or physical treatments before the processing of the composite material.

Crack bridging is only an effective toughening mechanism as long as fibres remain intact. If the fibre/matrix bond is too strong, the fibres break instead of peeling off and create crack bridging. Experimental work has shown that weakening the fibre/matrix interface can lead to more "surviving" fibres, resulting in more fibre bridging [25]. In contrast, for layered structures, e.g., adhesive bonded joints, it has been shown that plasma treatment can increase the fracture resistance of the joint, causing the formation of a parallel crack within the laminate just outside the adhesive layer [26]. Yet another study has shown that simply changing the ply layup, the cracking mechanism changes from the propagation of a single crack to the development of two or three parallel cracks (with two or tree bridging zones), resulting in a doubling or tripling of the fracture resistance [27]. These examples show that materials design can change the damage tolerance of materials significantly.

These observations suggest that fracture mechanics properties of fibre/matrix interfaces as well as the fracture mechanics properties of interfaces between layers in laminates play a central role in the fracture resistance of laminates. Mastering the interface design is thus the key to optimise the fracture resistance. There are many interfaces across the laminate at which delamination cracks can potentially propagate. It is challenging and difficult to design and control the fracture properties of all interfaces. However, the concept of cohesive laws enables us to propose an idea to design/tailor laminates so that cracks will propagate along high-energy absorbing
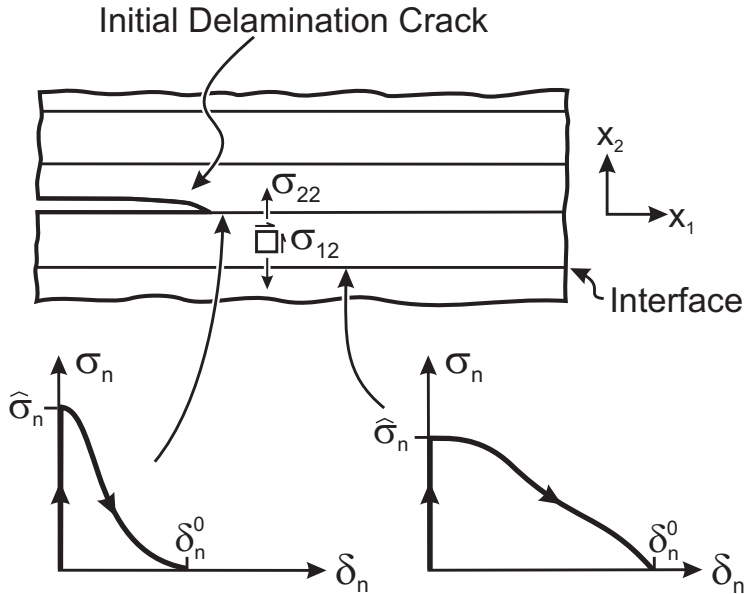
Figure P1.6: Cracking of a laminate having thin plies may shift to the neighbor interface if it has a lowest peak traction value.

interfaces. The idea is that the normal stresses[1] σ_{22} are continuous and do not vary much across a thin layer, so that the normal tractions σ_n is almost the same for two neighbouring interfaces, see Fig. P1.6. Therefore, we postulate that cracking will occur along the interface that possesses the lowest peak traction, $\hat{\sigma}_n$. Thus, it should be possible to design an interface such that it combines a low peak traction and a large work of the cohesive traction (e.g., by having a large critical opening), see Fig. P1.6. Such an interface will then trap the cracking along a high energy-absorbing path and thus impart high damage tolerance. Only a few low-strength, high-toughness interfaces may be needed. The design of interfaces is then reduced to designing and controlling fewer interfaces.

Possible definition of a structural damage tolerance index

It would be useful to have an index that would give a number for the safety margin of offshore wind turbine rotor blades. A practical approach would be to consider various critical parts of the blade individually. Each structural part can then be modelled by numerical modelling, using typical defect or damage sizes (e.g. corresponding to the detection limit of NDI methods) and the relevant cohesive laws. Such progressive

---

[1] For a real applications where craking is mixed mode, the shear stress σ_{12} and the shear traction σ_t should also be considered.

damage analysis should simulate the damage evolution from initiation to unstable growth. Onset of unstable damage growth gives a fracture load (that should exceed the expected service loads) and a change in the compliance of the structural part.

A damage tolerance index would enable the comparison of two designs made of the same material/interface or the same structural design made of two different materials and quantify which combination offers the most damage tolerant behaviour. Such an index D could for instance be a non-dimensional number with the characteristics that $D = 0$ indicates no damage tolerance (always unstable damage evolution or crack growth) while $D \to \infty$ indicates that damage or crack growth is always stable. A damage tolerance index could be defined by the structural compliance at which the cracking becomes unstable, C_c,

$$D = \frac{C_c - C_0}{C_0}, \tag{P1.3}$$

where C_0 is the compliance of the undamaged structural part of the blade. The compliance of a structural part is defined as the deflection of the structural part per unit applied load. A change in compliance due to damage may not be seen for the whole structure but only locally. Furthermore, each structural part may contain one or more competing damage modes for which a damage tolerance index could be calculated.

Different damage modes are likely to have different damage tolerant index values. The structural designer should ensure that all damage types of all structural parts have sufficiently high D values, so that damage evolution can be detected by compliance changes. He can modify the structural design to raise the value of d of the damage mode that has the lowest D values, in order to ease the damage detection by compliance changes. In case the damage type and traction separation laws are such that a sufficiently high compliance change cannot be obtained, the damage detection must rely on sensors that are not based on compliance, e.g. acoustic emission sensors.

Then, the damage tolerance of the entire rotor blade could be assessed in a way similar to the "damage map" mentioned in the Introduction a set of damage tolerance indices. In should be assessed whether unstable damage evolution of a structural part would lead to failure of the entire blade. The damage tolerance of specific material selections and structural designs could then be compared in the design phase.

P1.4   Structural Health Monitoring

A structural health monitoring (SHM) system's main purpose is to give information about the presence of damage in an accurate way, it's location with a good resolution for possible repair/maintenance, the type of damage (that in a complex structure like a wind turbine can be very diverse), the severity of the damage, and finally prognostic information about the remaining operating life [28].

In fact a great deal of sensor information is already available from offshore wind farms concerning the wind conditions, power output, temperatures, gearbox/drive-

train vibrations, and so on; but little or no sensor data specifically for the blades. As modern wind farms have a data handling and transfer framework already in place, an eventual monitoring suite for the blade condition can be designed to be a "module" inside the already existing system. Furthermore, many of these other sources will provide valuable parametric data to the blade sensor outputs.

The current maturity level for state-of-the-art blade damage sensing is very broad, with a great deal of research at the material level on integration/embedding of promising sensors into the composites. This includes fibre optic sensors using fibre Bragg gratings [29] or continuous optical fibre measurement [30], electrically conducting sensors based on conductive polymers and carbon fibres [31], acoustic emission methods using piezoelectric transducer materials for transmission and receiving of stress waves, spatial mapping of filament-matrix interface defects-reflectometry. Closer to application there are various sensor system approaches (including strain gauges [32], structural vibrations [18], and local stress wave [33]) that have been demonstrated as suitable to monitor damage initiation and growth within blades during structural blade testing in commercial or research facilities where support (including hardware control and NDI) is available and the loading conditions are known.

In operation, particularly for long-term remote monitoring, commercial systems exist that can detect ice formation and report changes in vibration response or return strain readings measured around the root section. Although not fulfilling the definition of SHM given above, these systems indicate that issues of robustness, reliability, price competitiveness, and functional operation can be overcome. In order to implement the methodology described in Section P1.2 (Vision), a suite of sensor approaches must be available within the designer 'toolbox' that can be combined and specified to meet the damage tolerance criteria. The resolution for detection of specific types of damage is given by the damage propagation calculations, which in turn calibrates the sensor distribution. However, it is clear that a significant maturation of applied blade sensor technology is required. Monitoring methods are needed from the manufacture process stage to ensure a certain level of quality, controlled cure of matrix material during processing, and improve certification, to produce composite parts in a repeatable and consistent manner with defects such as dry-spots, cracks, delamination and moisture held within acceptable tolerances.

P1.4.1   Traditional design and operation methodology

The traditional design and operation methodology as showed in Fig. P1.7 is no longer optimal for this type of requirements, particularly as blades become larger and more expensive to manufacture, the need for information fed back to maximise their lifetime utilisation increases.

A post manufacture quality assessment using advanced NDI technology can identify defects in the blade. In most cases these are minor, "surface effect" problems that can be corrected easily. In some cases however a major structural repair will be necessary that involves removing material and laying new laminate in place. This operation is best done immediately after production with all manufacturing resources
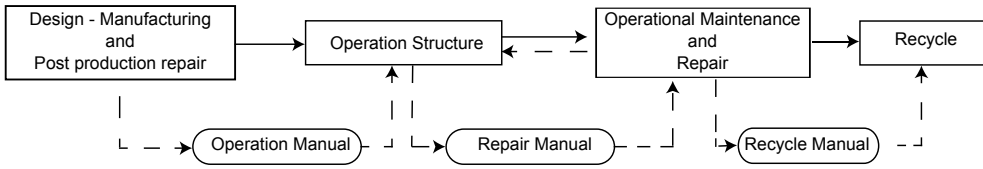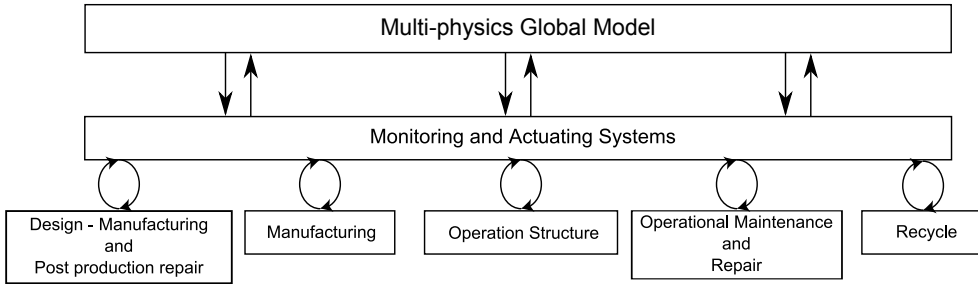
Figure P1.7: Life stages of a turbine: traditional design methodology.

available and results in repairs giving close to the maximum theoretically possible structural strength recovery. The quality of the cured repair should also be inspected before the finished blade leaves the production facility. Once in operation wind turbine blade damage can only be detected by visual inspections (since no sensors are build-in), either by on blade maintenance crews or possibly from examining high-definition images obtained from the ground. Such focused blade inspections are most usually done near the end of product warranty periods. The repair of damage on-site is clearly more challenging than those done in a manufacturing facility. Again the majority of problems identified on operating blades are characterised as "maintenance" and involve correcting hairline surface cracks or pitting/erosion at the leading (or trailing) edge of the blade. In these cases the recovery of a good surface finish is the success criteria for the maintenance effort. But occasionally a major structural repair will be necessary where working conditions are far from optimal; low temperatures, wet conditions, and challenging access issues. The quality of the work will depend heavily on the training level of the technicians, the quality of the materials used, the resources (tools, platforms, tenting, heating, etc.) and the time available to do the repair. Ensuring the effectiveness of repair is also difficult as afterwards the blade surface is again returned to a good finish.

P1.4.2   Smart structure design

In either a post-production repair or an in-situ structural repair the fed back from embedded sensors can improve confidence in the quality and effectiveness of the work undertaken. Furthermore, the smart structure design will help "single-out" blades that return exceptional sensor responses, thus providing an early warning of structural damage in operation, that currently relies on purely visual observations of surface cracking.

The presence of sensors will provide fed back at each stage of the structure life-cycle. For example, the design and manufacture process will become iterative with data from embedded sensors helping to make subtle improvements to the infusion and cure processes as well as making blade manufacture reactive to external effects and thus minimising product variability. In operation data returned from the structure will allow an analysis of the structural performance and a concurrent engineering approach with modified designs for the latest versions of the structure. The main

Figure P1.8: Life Stages of a Turbine: Smart Structure Design.

function of the embedded sensors during operation is early detection of changes in response that could indicate damage present in the material or at interfaces/bondlines. The damage tolerance and structural monitoring methodology described in this paper requires a "damage map" for each structure with an assessment of the blade condition using local and global damage indices. This permits a damage management approach with tools for avoiding (or alleviating) the structural loadings (high wind conditions) that will propagate damage in a particular blade.

All offshore turbines require on-site maintenance, but with detailed structure-specific response history available it becomes possible to make a more efficient application of maintenance tailored to the need of each particular turbine. This is in contrast to the traditional methodology where generic manuals specify the amount of proactive maintenance required. Normally an expensive life assessment program would be required in order to justify any decision to extend the service life of an entire group of structures. But with the approach shown in Fig. P1.8, all the relevant data is already available and near the design end-of-life this database of structure specific histories allows a more informed management decision regarding reinsurance/recommissioning or decommissioning, resale and/or recycle.

P1.5   Discussion

P1.5.1   The path towards condition monitoring based approach

Is not realistic to jump from the conventional turbine to the proposed design and maintenance approach based on condition monitoring since not all tools required are not fully demonstrated and mature. For sensors, for instance, a number of sensors have been tested with satisfactory results in the laboratory or at prototype blade test. However, the durability over many years in hash offshore environment needs to be demonstrated. Concerning NDI methods, many of these have been successfully demonstrated in inspection of blades, both in the laboratory, full scale prototype testing, and in the field. Thus, these methods are demonstrated. Within progres-

sively damage modelling, a lot of progress has been made over the past two decades. However, specific models of blade damages are not yet demonstrated. We think it is possible to bring-in the tools for condition monitoring gradually, by applying them to dedicated problems, where information of damage evolution provide high value. For instance, testing sensors on wind turbine rotor blade during full scale prototype testing is likely to be worth the cost, since more data on damage evolution during the test could lead to the detection of damage originating from a design weakness or pour manufacturing procedures, which could lead to the necessity of many blade repairs if the blade had gone into mass production. Likewise sensors should be used on blades where primary structural parts have been repaired, since the repaired area is likely to act as a site for damage initiation. Installation of few sensors at a critical repair may thus provide very valuable information about the quality of repair, and may allow blades that would otherwise be discarded to be repaired and used.

The condition monitoring modelling approach Fig. P1.4 requires developing the science based knowledge available within sensor application (for detection), NDI (for characterisation), and modelling (for prediction). A plausible order of steps of this gradual implementation of the proposed approach is given below.

Sensors:

- Demonstration of sensors in the laboratory;

- Sensor calibration of output against known damage (location, type, size, depth);

- Sensor durability on subcomponent tests in the lab (long term, cyclic loading);

- Demonstrate sensors during full-scale blade tests;

- Demonstrate sensors on repaired blades in operation;

- Demonstrate sensors on new blades in operation;

Modelling approach (prediction of progressive damage evolution):

- Characterisation of blade materials in terms of traction-separation laws (mixed mode);

- Demonstration of predictability of static and cyclic crack growth on medium size specimens in the lab;

- Development of models for major structural failure modes in rotor blades;

- Formulate guidelines for industrial use of model approach;

Based on the condition monitoring approach, a number of decisions can be made (Fig. P1.4), including the decision to repair a blade. In case the blade is repaired, the repair techniques used should be documented scientifically and the repaired areas

should be checked by NDI methods following the repair to document the quality of the repair. Steps to improve repair techniques are:

- Optimisation of repair techniques in the lab (maximise residual strength and fatigue life);

- Demonstrate repair methods on blade parts in the laboratory;

- Develop and demonstrate NDI methods for quality control;

- Formulation of guidelines for repair approach;

P1.5.2 Towards integration in the Global Model

Sensing and monitoring systems will undoubtedly continue to become cheaper, more robust, and effective. This will increase the amount of monitoring systems in all the blade stages (manufacturing, testing, operation, maintenance, repair, etc.), leading to a better understanding and control of key parameters on the structure performance of the blade. For instance, dedicated sensors will regulate the manufacturing, improving the product quality and dedicated operation sensors will give information about the response of that structure, helping to identify exceptions and improving the limited inspection and maintenance functions.

Better structural models and improved multi-physics global integration will allow for damage management by automatically shutting down a turbine in local conditions likely to progress damage within that particular turbine, and will enable the modification of the operational limits for individual turbines based on their known damage condition enable then to maintain power production. In other words, the smart turbine ability to analyse and adapt to environmental and structural conditions will lead to a more efficient operation of the wind turbine.

P1.6 Summary

In the present paper we have outlined a future approach for the the design and maintenance of wind turbine rotor blades for off-shore farms. This approach is based on the premise that it is not possible to manufacture large "perfect" blades, and that large blades with manufacturing defects or damages are too costly to discard. Furthermore, since manual inspection is very costly for off-shore wind turbines, we propose an approach that can handle blades with manufacturing defects, handling damage and in-service damage to be used. The approach is based on the use of damage tolerant structural design and damage tolerant materials combined with built-in sensors that can detect damage evolution. The concept, which can be termed "condition monitoring and maintenance", consists of detection of damages by sensors, characterisation of damage (type and size) by NDI methods, model predictions of residual life, giving information that enables decision-making with respect to whether a damaged blade should be repaired or replaced. The majority of blades that do not develop significant

damage will not require any manual inspection. Examples are given on how materials can be tailor-made to provide higher damage tolerance. The development of more damage tolerant structures and damage tolerant materials could provide the technological opportunity that enables the future very large wind turbine rotor blades, approaching 100 m in length.

Acknowledgment

References

[1] OWE, *Offshore wind energy: Action needed to deliver on the energy policy objectives for 2020 and beyond, com(2008) 768 final - not published in the official journal*, `http://europa.eu/legislation_summaries/energy/renewable_energy/en0001_en.htm`.

[2] EWEA, *Ewea 2014 day three, rechange, wednesday 12th march, 2014*, `http://www.ewea.org/annual2014/media-and-press/recharge-daily`.

[3] T. Jacobsen, "Materials technology for large wind turbine rotor blades - limits and challenges," *32nd Risø International Symposium on Material Science, Composite materials for structural performance: Towards higher limits*, 2011.

[4] C. Qian, "Multi-scale modelling of fatigue of wind turbine rotor blade composites," PhD thesis, Delft University of Technology, 2013.

[5] O. Bauchau, "Modeling rotorcraft dynamics with finite element multibody procedures," *Mathematical and Computer Modelling*, volume 33, number 10-11, pages 1113–1137, 2001.

[6] C. L. Bottasso, F. Campagnolo, and V. Petrović, "Wind tunnel testing of scaled wind turbine models: beyond aerodynamics," *Journal of Wind Engineering and Industrial Aerodynamics*, volume 127, pages 11–28, April 2014, ISSN: 01676105. DOI: `10.1016/j.jweia.2014.01.009`.

[7] FP7, *Eera-dtoc seventh framework programme- european energy research alliance - design tool for offshore wind farm cluster*, `http://www.eera-dtoc.eu/`.

[8] MAREWINT, *Seventh framework programme (fp7)- new materials and reliability in offshore wind turbines technolog*, `http://www.marewint.eu/`.

[9]   B. Sørensen, J. W. Holmes, P. Brøndsted, and K. Branner, "Blade materials, testing methods and structural design," in *InWind power generation and wind turbine design*, W. Tong, Ed., Kollmorgen Corp., USA: WIT Press, 2010, ch. 13, pages 417–466, ISBN: 978-1-84564-205-1.

[10] H. S. Toft, K. Branner, P. Berring, and J. D. Sørensen, "Defect distribution and reliability assessment of wind turbine blades," *Engineering Structures*, volume 33, number 1, pages 171–180, January 2011, ISSN: 01410296. DOI: `10.1016/j.engstruct.2010.10.002`.

[11] D. F. Braga, S. Tavares, L. F. da Silva, P. Moreira, and P. M. de Castro, "Advanced design for lightweight structures: review and prospects," *Progress in Aerospace Sciences*, volume 69, pages 29–39, August 2014, ISSN: 03760421. DOI: `10.1016/j.paerosci.2014.03.003`.

[12] F. M. Jensen, A. S. Puri, J. P. Dear, K. Branner, and A. Morris, "Investigating the impact of non-linear geometrical effects on wind turbine blades-part 1: current status of design and test methods and future challenges in design optimization," *Wind Energy*, volume 14, number 2, pages 239–254, March 2011, ISSN: 10954244. DOI: `10.1002/we.415`.

[13] J. D. Sørensen, "Framework for risk-based planning of operation and maintenance for offshore wind turbines," *Wind Energy*, volume 12, number 5, pages 493–506, Jul. 2009, ISSN: 10954244. DOI: `10.1002/we.344`.

[14] J. Sørensen, I. Kroon, and M. Faber, "Optimal reliability-based code calibration," *Structural Safety*, volume 15, number 3, pages 197–208, Sep. 1994, ISSN: 01674730. DOI: `10.1016/0167-4730(94)90040-X`.

[15] H. S. Toft, K. Branner, L. Mishnaevsky, and J. D. Sorensen, "Uncertainty modelling and code calibration for composite materials," *Journal of Composite Materials*, volume 47, number 14, pages 1729–1747, Jun. 2012, ISSN: 0021-9983. DOI: `10.1177/0021998312451296`.

[16] C. R. Farrar and K. Worden, "An introduction to structural health monitoring.," *Philosophical transactions. Series A, Mathematical, physical, and engineering sciences*, volume 365, number 1851, pages 303–15, February 2007, ISSN: 1364-503X. DOI: `10.1098/rsta.2006.1928`.

[17] B. Sørensen, L. Lading, P. Sendrup, M. McGugan, C. Debel, O. Kristensen, G. Larsen, A. Hansen, J. Rheinlander, J. Rusborg, and J. Vestergaard, "Fundamentals for remote structural health monitoring of wind turbine blades - a preproject," *Denmark research center Risø*, 2002, ISSN: Risø -R: 1336(EN).

[18] M. McGugan, G. Larsen, B. Sørensen, K. Borum, and J. Engelhardt, "Fundamentals for remote condition monitoring of offshore wind turbines," *Denmark research center Risø*, 2008, ISSN: Risø -R: 1336(EN).

[19] S. Ataya and M. M. Ahmed, "Damages of wind turbine blade trailing edge: forms, location, and root causes," *Engineering Failure Analysis*, volume 35, pages 480–488, December 2013, ISSN: 13506307. DOI: 10.1016/j.engfailanal. 2013.05.011.

[20] P. Takoutsing, R. Wamkeue, M. Ouhrouche, F. Slaoui-Hasnaoui, T. Tameghe, and G. Ekemb, "Wind turbine condition monitoring: state-of-the-art review, new trends, and future challenges," *Energies*, volume 7, number 4, pages 2595–2630, April 2014, ISSN: 1996-1073. DOI: 10.3390/en7042595.

[21] B. Yang and D. Sun, "Testing, inspecting and monitoring technologies for wind turbine blades: a survey," *Renewable and Sustainable Energy Reviews*, volume 22, pages 515–526, Jun. 2013, ISSN: 13640321. DOI: 10.1016/j.rser.2012.12. 056.

[22] S. Suresh, *Fatigue of Materials*. Cambridge University Press, 1991.

[23] S. Spearing and A. Evans, "The role of fiber bridging in the delamination resistance of fiber-reinforced composites," *Acta Metallurgica et Materialia*, volume 40, number 9, pages 2191–2199, Sep. 1992, ISSN: 09567151. DOI: 10.1016/0956-7151(92)90137-4.

[24] B. F. Sørensen, E. K. Gamstedt, R. C. Østergaard, and S. Goutianos, "Micromechanical model of cross-over fibre bridging – prediction of mixed mode bridging laws," *Mechanics of Materials*, volume 40, number 4-5, pages 220–234, April 2008, ISSN: 01676636. DOI: 10.1016/j.mechmat.2007.07.007.

[25] S. Feih, J. Wei, P. Kingshott, and B. Sørensen, "The influence of fibre sizing on the strength and fracture toughness of glass fibre composites," *Composites Part A: Applied Science and Manufacturing*, volume 36, number 2, pages 245–255, February 2005, ISSN: 1359835X. DOI: 10.1016/j.compositesa.2004.06.019.

[26] Y. Kusano, B. F. Sørensen, T. L. Andersen, H. L. Toftegaard, F. Leipold, M. Salewski, Z. Sun, J. Zhu, Z. Li, and M. Alden, "Water-cooled non-thermal gliding arc for adhesion improvement of glass-fibre-reinforced polyester," *Journal of Physics D: Applied Physics*, volume 46, number 13, page 135 203, April 2013, ISSN: 0022-3727. DOI: 10.1088/0022-3727/46/13/135203.

[27] M. Rask and B. Sørensen, "Determination of the j integral for laminated double cantilever beam specimens: the curvature approach," *Engineering Fracture Mechanics*, volume 96, pages 37–48, December 2012, ISSN: 00137944. DOI: 10. 1016/j.engfracmech.2012.06.017.

[28] A. Rytter, "Vibrational based inspection of civil engineering structures," PhD thesis, Aalborg University, Denmark, 1993.

[29] A. Bernasconi, M. Carboni, and L. Comolli, "Monitoring of fatigue crack growth in composite adhesively bonded joints using fiber bragg gratings," *Procedia Engineering*, volume 10, pages 207–212, January 2011, ISSN: 18777058. DOI: 10.1016/j.proeng.2011.04.037.

[30] G. Zhou and L. M. Sim, "Damage detection and assessment in fibre-reinforced composite structures with embedded fibre optic sensors-review," en, *Smart Materials and Structures*, volume 11, number 6, pages 925–939, December 2002, ISSN: 0964-1726. DOI: `10.1088/0964-1726/11/6/314`.

[31] J. W. Cho and J. S. Choi, "Relationship between electrical resistance and strain of carbon fibers upon loading," *Journal of Applied Polymer Science*, volume 77, number 9, pages 2082–2087, August 2000, ISSN: 0021-8995. DOI: `10.1002/1097-4628(20000829)77:9<2082::AID-APP26>3.0.CO;2-W`.

[32] K. Papadopoulos, E. Morfiadakis, T. P. Philippidis, and D. J. Lekou, "Assessment of the strain gauge technique for measurement of wind turbine blade loads," *Wind Energy*, volume 3, number 1, pages 35–65, January 2000, ISSN: 1095-4244. DOI: `10.1002/1099-1824(200001/03)3:1<35::AID-WE30>3.0.CO;2-D`.

[33] J. E.R., B. K.K., M. M., T. C.L., J. F.M., D. C.P., and S. B.F., "Full scale testing of wind turbine blade to failure - flapwise loading," *Denmark research center Risø*, 2004, ISSN: Risø -R: 1392(EN).

Method for Independent Strain and Temperature Measurement in Polymeric Tensile Test Specimen Using Embedded FBG Sensors

Abstract

A novel method to obtain independent strain and temperature measurements using embedded Fibre Bragg Grating (FBG) in polymeric tensile test specimens is presented in this paper. The FBG strain and temperature cross-sensitivity was decoupled using two single mode FBG sensors, which were embedded in the specimen material with a certain angle between them. It is demonstrated that, during temperature variation, both FBG sensors show the same signal response. However, for any applied load the signal response is different, which is caused by the different levels of strain acting in each sensor. Equations to calculate independently the strain and temperature are presented in the article, together with a measurement resolution study. This multi-parameter measurement method was applied to an epoxy tensile specimen, tested in a unidirectional tensile test machine with a temperature controlled cabinet. A full calibration procedure (temperature and strain) was performed to this material-sensor pair, where a calibration error $< 1\%$ was achieved. This was followed by a strain-temperature test case, where multiple two loading/strain stages of $\varepsilon = 0.30\%$ and $\varepsilon = 0.50\%$ were applied during a continuous variation of temperature, from 40^oC to -10^oC. The consistency of the expected theoretical results with the calibration procedure and the experimental validation shows that this proposed method is applicable to measure accurate strain and temperature in polymers during static or fatigue tensile testing. Two different calibration protocols are presented and analysed.

Notation

λ_b	reflected wavelength peak;
λ_b^A	reflected wavelength peak of the FBG_A;
λ_b^B	reflected wavelength peak of the FBG_B;
$\Delta\lambda_b$	wavelength shift;
n_{eff}	effective refractive index for unstrained condition;
Λ_0	nominal period of the refractive index modulation for unstrained condition;
p_e	optical fibre photo-elastic coefficient;
α_h	thermal expansion coefficient of the host material;
ξ	thermo-optic coefficient of the optical fibre;
θ	angle between FBG_A and FBG_B;
ε_1	strain in the longitudinal direction of the optical fibre;
ε_x	strain in the x axis direction of the specimen;
ε_y	strain in the y axis direction of the specimen;
ε_L	specimen strain caused by the uniaxial loading;
T	specimen temperature (K);
ΔT	specimen temperature variation;
E	Young's modulus of the host material;
ν_{12}	Poisson's ratio of the host material;
$\varepsilon_L^{resolution}$	method strain resolution;
$\varepsilon_{hardware}^{resolution}$	signal acquisition hardware resolution;

P2.1   Introduction

Improving measurement techniques to obtain more accurate strain measurements is a central research topic in the material characterization field. Specifically in the polymeric materials field, some authors have developed new methods to perform strain measurement, and improved current techniques to obtain more accurate and reliable strain measurement. Zike et al.[1], have developed a procedure to correct the gauge factor for strain gauges used in polymer composite testing. Jerabek et al.[2] and Crupi et al.[3] have developed digital image correlation techniques to evaluate the strain during shear and static/fatigue tensile testing.

Fibre Optic Bragg grating (FBG) sensors are considered a promising alternative to the conventional strain measurement techniques. Due to its small diameter, 125 μm, it is possible to embed the sensor in the specimen without compromising the material resistance. Additionally, the fact that the FBG is embedded improves the strain transfer between the host material and the sensor, increasing the measurement accuracy. The FBG measured information is encoded as a light resonance wavelength, giving this system unique properties, such as immunity to optical/power fluctuation, insulation and immunity to electromagnetic fields [4]. However, strain and temperature cross-sensitivity, limited measuring range, expensive hardware and difficulties in handling the sensors are some of the drawbacks of this technology.

Strain and temperature cross-sensitivity is especially problematic for long tests, where external variation of temperature can occur. On the other hand, during dynamic tests, such as fatigue testing, the material self-heating can generate a strain caused by thermal expansion. A simple solution to decouple the strain from the temperature measurement is by embedding two gratings in the material, one of which is isolated with a glass or a metallic sleeve [5, 6]. However, the sleeve used to isolate the grating will increase the sensor diameter, which becomes more intrusive to the material and can lead to a decrease in the measured mechanical strengths. Moreover, the optical fibre needs to be cut to introduce the sleeve, which makes having several gratings in the same fibre optic (multiplexing) impossible. Other authors propose an indirect measurement method that can be used for simultaneous measurement of the bending force and temperature. This is done by drilling a hole in the material, near the grating location, which will create a change in the width of the standardised sum of the transmission spectra, and consequently a decoupling of strain from the temperature [7]. However, as this technique requires a hole to be drilled near the grating, the material strength is reduced, compromising the results of the material testing. Within the optical fibre sensors field, new techniques and sensors have been developed for multi-parameter measurement, such as a dual grating in the same location using a standard FBG and a Long Period Grating (LPG) [8], chirped FBG and Fabry-Perot [9], different FBG sensor diameter [10], FBG with a thermochromic material [11]. However, these techniques require more advanced and costly technology, skilled operators, and some cases are not commercial available. In this article, a simple approach for multi-parameter measurement is presented, where the strain and temperature can be measured independently in a tensile test specimen using commer-

cially available technology. This method can be used in static testing, but it was developed especially for fatigue/dynamic testing where the specimen can experience temperature variation.

The article is divided into four sections: *FBG Working Principle*, where the sensor response to strain and temperature is shown; *Strain and Temperature Independent Measurement Method*, the independent strain and temperature method is discussed, and its impact to the measurement resolution is studied; *Experimental Procedure and Validation*, the calibration procedure is performed, and the strain and temperature are independently measured in a tensile specimen under thermal and strain loading; and *Proposed Calibration Protocol*, where two different measurement protocols, with or without calibration, are presented and analysed.

P2.2   Fibre Bragg Grating Working Principle

A Fibre Bragg Grating is formed by a permanent periodic modulation of the refractive index along a section of an optical fibre [12]. This is made by exposing the optical fibre to an interference pattern of intense ultraviolet light, which will increase the photosensitivity of the silica. Then, when the optical fibre is illuminated by a broadband light source, a narrow wavelength band is reflected back, as showed in Fig. P2.1.
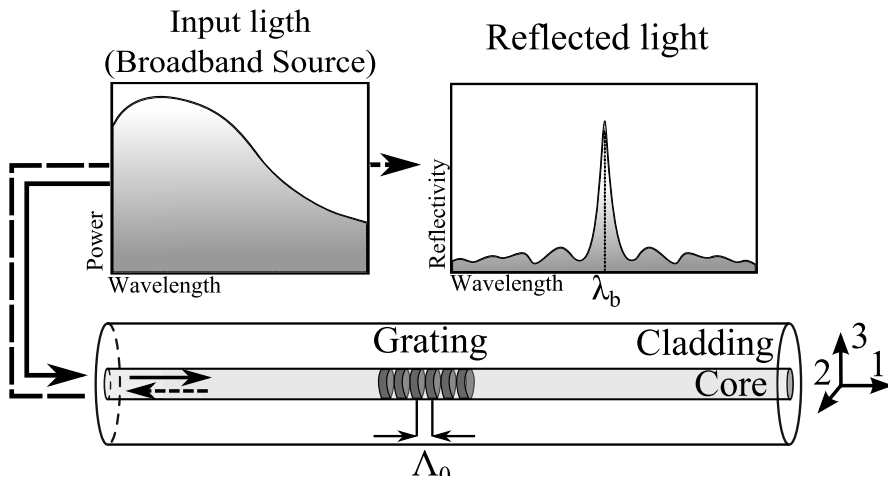
Figure P2.1: Fibre Bragg Grating working principle: spectral response of a homogeneous FBG. The parameter λ_b is the wavelength of the reflected peak, and Λ_0 is the constant nominal period of the refractive index modulation.

The spectral response of a homogeneous FBG is a single peak centred at the wavelength λ_b, described by the Bragg condition Eq. (P2.1),

$$\lambda_b = 2n_{eff}\Lambda_0 \qquad\qquad \text{(P2.1)}$$

where the parameter n_{eff} is the effective refractive index at the location of the grating, and Λ_0 is the constant nominal period of the refractive index modulation [13]. Any external load or temperature variation affecting the grating region will change the effective index of refraction and/or the period of modulation, which will create a shift in the wavelength reflected peak. Tracking this wavelength peak shift is the sensing principle of the FBG sensor, giving an indirect measurement of strain and/or temperature in the structure.

P2.2.1   Embedded FBG Response to Strain and Temperature Variation

If perfect strain transfer between the embedded FBG sensor and the host material is assumed. The wavelength shift $(\Delta\lambda_b)$ caused by the load induced strain in the longitudinal direction of the optical fibre (ε_1), and temperature change (ΔT), is given by Eq. (P2.2).

$$\frac{\Delta\lambda_b}{\lambda_b} = (1 - p_e)\varepsilon_1 + (1 - p_e)\alpha_h\Delta T + \xi\Delta T \qquad\qquad \text{(P2.2)}$$

The parameter p_e is the optical fibre photo-elastic coefficient, α_h is the thermal expansion coefficients of the host material and ξ is the thermo-optic coefficient [14]. The effect of the optical fibre to the overall specimen stiffness is very small, because the FBG cross section $<<$ specimen cross section. Thus, it can be assumed that the FBG measurements represent the true material behaviour and the FBG thermal expansion contribution to Eq. (P2.2) can be neglected.

P2.3   Strain and Temperature Independent Measurement Method

Multi-parameter measurement is an important topic within the fibre measurement field, allowing parameter discrimination in situations where cross-sensitivity is a critical issue. In the following section a technique to perform independent strain and temperature measurements in a polymeric tensile specimen with embedded optical fibres is presented.
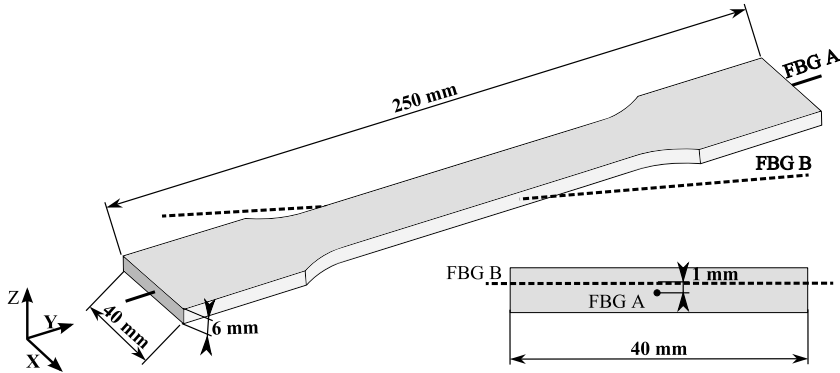
Figure P2.2: FBG sensors configuration for independent strain and temperature measurement. The FBG sensors are placed parallel to the *xy* plan, being the FBG-A in the middle-plan and the FBG-B *1 mm* ahead.

P2.3.1   Strain and Temperature Cross-sensitivity Decoupling

For a single FBG sensor configuration, it is impossible to measure independently the temperature and strain variation if both happen at the same time. By analysing Eq. (P2.2), the load induced strain (ε_1), the temperature induced strain/ thermal expansion ($\alpha_h \Delta T$) and the thermal-optic dependency ($\xi \Delta T$) creates the same sensor response, a wavelength shift of the reflected peak $\Delta \lambda_b$. Thus, it is impossible to determine each phenomenon contribution to the wavelength shift. To overcome this problem, the authors propose a new sensor configuration during tensile testing, as presented in Fig. P2.2.

The tensile specimen is instrumented with a pair of embedded FBG sensors, aligned in different directions; one FBG sensor is aligned with the loading direction (FBG-A), and the other is tilted with a certain angle (θ). With this configuration, the FBG sensors will have a distinct response to temperature variation and to strain, as shown schematically in Fig. P2.3.

Assuming that the specimen material has isotropic thermal expansion, i.e. it expands or contracts with the same magnitude in all directions, both sensors will experience the same deformation under temperature variation; however, when the specimen is loaded (direction *y* and FBG A), the sensors will have a different response from each other. This is caused by the different level of strain that is acting along each sensor longitudinal direction. While the FBG-A will measure the maximum strain caused by the load, the FBG-B will measure a smaller strain that is dependent on the angle θ and the specimen Poisson's ratio. Herewith, by knowing the angle (θ) between the FBG-B and the loading direction, and the difference in the sensors response it is possible to calculate directly the specimen strain by extracting the temperature effect.
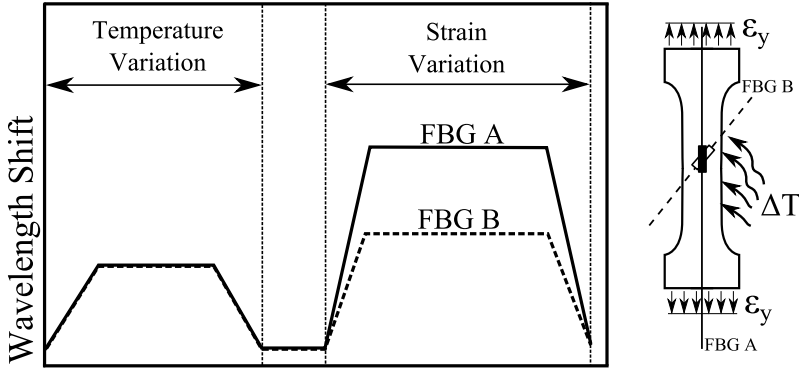
Figure P2.3: Schematic representation of the FBG sensors signal response under strain (ε_y) or temperature variation (ΔT). The solid line represents the FBG-A wavelength shift, and the dashed line the FBG-B wavelength shift.

P2.3.2   Strain-angle relationship between the FBG sensors

As previously mentioned, the magnitude of strain measured by each sensor will depend on the angle between the FBG sensors. Considering the directions shown in Fig. P2.4, the transformation matrix from xy coordinate system to $x'y'$ coordinate system is given by the Eq. (P2.3).

$$[T]_{xy \to x'y'} = \begin{bmatrix} cos(\theta) & -sin(\theta) \\ sin(\theta) & cos(\theta) \end{bmatrix} \tag{P2.3}$$

The parameter θ is the angle between the two coordinate systems (FBG sensors longitudinal direction). The strain tensor in the xy coordinate system is described by Eq. (P2.4), where ε_x and ε_y are the strain components in the direction x and y. As this measurement method was developed for unidirectional tensile tests, the shear strain component does not contribute ($\gamma_{xy} = 0$).

$$[\varepsilon]_{xy} = \begin{bmatrix} \varepsilon_x & 0 \\ 0 & \varepsilon_y \end{bmatrix} \tag{P2.4}$$

The strain tensor in the $x'y'$ coordinate system can be calculated by the Eq. (P2.5).

$$[\varepsilon']_{x'y'} = [T][\varepsilon][T]^T \tag{P2.5}$$
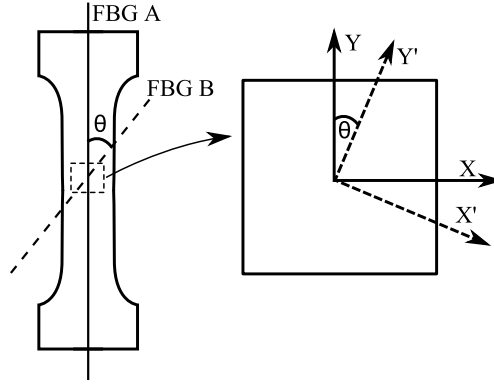
Figure P2.4: Coordinate system transformation from FBG-A to FBG-B. The parameter θ is the angle formed between the FBG sensors.

Finally, the strain in the longitudinal direction of the optical fibre (sensor measurement direction) for any given angle is given by Eq. (P2.6).

$$\varepsilon_\theta = \varepsilon_y cos(\theta)^2 + \varepsilon_x sin(\theta)^2 \tag{P2.6}$$

P2.3.3 Temperature Measurement ($\varepsilon_L = 0$)

Both FBG sensors will measure the same wavelength shift during any temperature variation. Thus, if we consider that no load/strain is applied to the specimen during temperature variation, the wavelength shift measured by the FBG can be described by Eq. (P2.7).

$$\frac{\Delta\lambda_b^A}{\lambda_b^A} = \frac{\Delta\lambda_b^B}{\lambda_b^B} = [(1 - p_e)\alpha_h + \xi]\Delta T \tag{P2.7}$$

However, Eq. (P2.7) only remains valid if the temperature in the two FBG sensors is the same, which is true if the gratings are close enough to each other.

P2.3.4 Strain Measurement ($\Delta T = 0$)

For the specimen configuration presented in Fig. P2.2, loaded in the specimen y direction, the parameter ε_L represents the strain caused by the loading the specimen. Thus, the strain in the xy coordinate system can be described by Eq. (P2.8),

$$\varepsilon_y = \varepsilon_L \ ; \ \varepsilon_x = -\nu_{12}\varepsilon_L \tag{P2.8}$$

where the strain ε_y is equal to the strain caused by the loading and ε_x is caused by the Poisson's effect. Therefore, the wavelength shift measured by each FBG sensor can be obtained by combining Eqs. (P2.6), (P2.8) and (P2.2).

$$\frac{\Delta\lambda_b^A}{\lambda_b^A} = (1 - p_e)\varepsilon_L \tag{P2.9}$$

$$\frac{\Delta\lambda_b^B}{\lambda_b^B} = (1 - p_e)(cos(\theta)^2 - \nu_{12}sin(\theta)^2)\varepsilon_L \tag{P2.10}$$

P2.3.5   Strain and Temperature Independent Measurement Method

For a simultaneous strain and temperature variation, the wavelength shift measured by each grating are shown in Eqs. (P2.11) and (P2.12).

$$\frac{\Delta\lambda_b^A}{\lambda_b^A} = (1 - p_e)\varepsilon_L + [(1 - p_e)\alpha_h + \xi]\Delta T \tag{P2.11}$$

$$\frac{\Delta\lambda_b^B}{\lambda_b^B} = (1 - p_e)(cos(\theta)^2 - \nu_{12}sin(\theta)^2)\varepsilon_L + [(1 - p_e)\alpha_h + \xi]\Delta T \tag{P2.12}$$

As can be observed, the effect of temperature as a wavelength shift is identical in both FBG sensors. Therefore, the difference between the two responses is caused by the strain in the specimen (ε_L) without the temperature effect, as demonstrated by Eq. (P2.13).

$$\varepsilon_L = \left(\frac{\Delta\lambda_b^A}{\lambda_b^A} - \frac{\Delta\lambda_b^B}{\lambda_b^B}\right) = \frac{1}{(1 - p_e)(cos(\theta)^2 - \nu_{12}sin(\theta)^2)} \tag{P2.13}$$

Finally, the temperature change (ΔT) can be calculated by subtracting the strain contribution to the wavelength shift measured. Reorganizing Eq. (P2.14), the temperature variation is given by:

$$\Delta T = \frac{\frac{\Delta\lambda_b^A}{\lambda_b^A} - (1 + p_e)\varepsilon_L}{(1 - p_e)\alpha_h + \xi} \tag{P2.14}$$

P2.3.6   Measurement Resolution

The strain resolution of this method strongly depends on the angle between the FBG sensors (θ) and the material Poisson's ratio, as demonstrated in Eq. (P2.15). The parameter $\varepsilon_{Hardware}^{resolution}$ is the resolution given by the signal acquisition hardware, typically around $1\mu\varepsilon$.
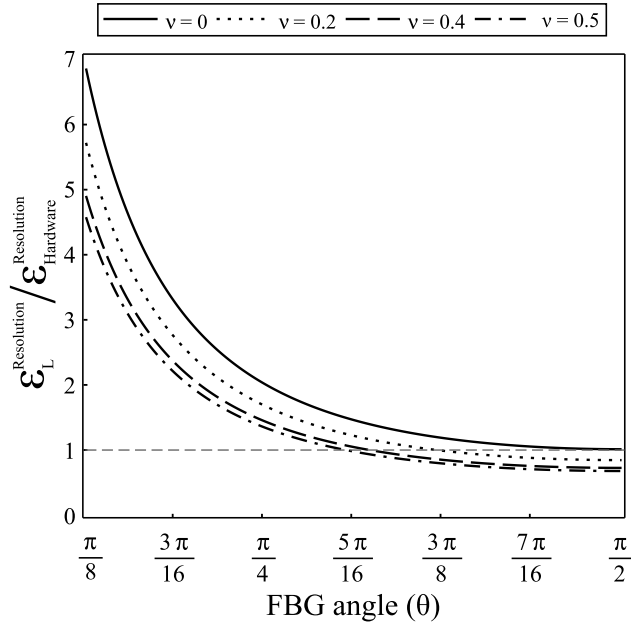
Figure P2.5: Strain resolution for different FBG angles (θ) and Poisson's ratio (ν_{12}). The different lines represent different Poisson's ratios (ν_{12}).

$$\varepsilon_L^{resolution} = \varepsilon_{Hardware}^{resolution} \frac{1}{(1 - cos(\theta)^2 - \nu_{12} sin(\theta)^2)} \tag{P2.15}$$

The angle between FBG sensors (θ) has a big impact on the strain resolution, as shown in Fig. P2.5. For an angle θ around 90°, the resolution is actually improved, benefiting from the Poisson's effect. However, for some cases, the FBG sensors angle is limited by the tensile specimen width ($specimen_{width} > FBG_{length} sin(\theta)$).

P2.4   Experimental Procedure and Validation

Two tensile test specimens were manufactured with the dimensions presented in Figure 2 using an epoxy system based on *Araldite LY 1564* and *Aradur 3486*. Two uncoated single mode FBG sensors, with a grating length of 10 mm, were embedded in each specimen; both gratings were placed parallel to the *xy* plan, being the FBG-A in the middle plan and the FBG-B 1 mm ahead. The FBG-A was aligned with the load/y direction, and the FBG-B was aligned with an angle θ of 37.5^o. The test was performed in a tensile testing machine, *Instron 8802*, where the head displacement
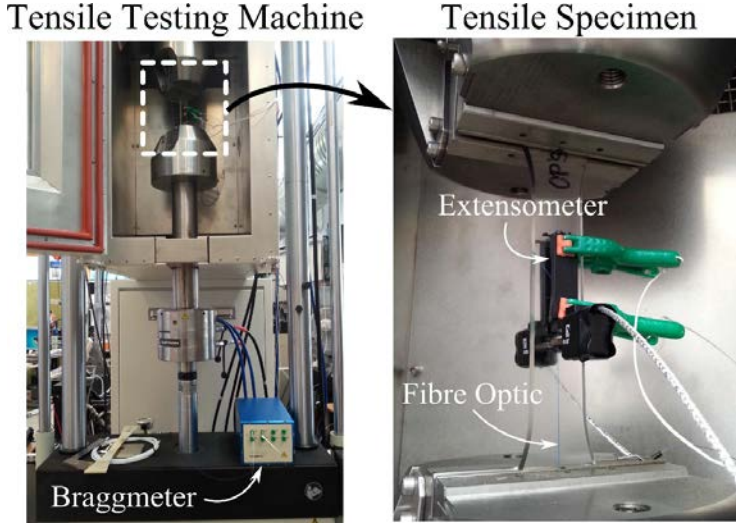
Figure P2.6: Experimental set-up apparatus. Epoxy tensile specimen with two embedded FBG sensors and two side mounted extensometers.

speed was set to 0.02 mm/s. A tensile testing cabinet from Weiss was used to perform a controlled temperature variation testing. Two side mounted extensometers were used to monitor the specimen strain and to calibrate the FBG sensors, as shown in Fig. P2.6. The FBG sensor signal was acquired using a *FS2200-Industrial BraggMeter* supplied by *FiberSensing$^T M$*, and synchronized with the strain measured by the extensometers. The optical fibre parameters, material properties and specimen geometry used are presented in Table P2.1.

Table P2.1: Optical fibre parameters, material properties, and specimen geometry.

Specimen Geometry			
Thickness	5 mm	Width	25 mm
FBG angle (θ)	37.5^o		
Epoxy Properties (Manufacture Data Sheet)			
Young's modulus (E)	3.3 GPa	Poisson's ratio (ν_{12})	0.35
Thermal expansion coefficient (α_h) [15]	8.3E-5 ε/K		
Fibre Optic Parameters			
Photo-elastic coefficient (p_e) [13]	0.22	Thermo-optic coefficient (ξ) [13]	8.3E-6
Wavelength peak FBG-A (λ_b^A)	1566.65 nm	Wavelength peak FBG-B (λ_b^B)	1553.75 nm

P2.4.1 Measurement Calibration

A calibration procedure was performed to determine accurately the material and fibre optic parameters, and to minimize any measurement errors.

The calibration procedure was divided in two parts:

- Strain calibration: calibration of the photo-elastic coefficient (p_e), using the strain measured by the surface mounted extensometers;

- Temperature calibration: calibration of the thermo-optic coefficient (ξ) and the host material thermal expansion coefficient (α_h), by a controlled variation of temperature in the environmental chamber;

Strain Calibration

To perform the strain calibration three loading/strain stages of 0.15, 0.30, and 0.50 $\varepsilon(\%)$ at a constant temperature were applied. The strain measured by the extensometers and the temperature from the environmental chamber are shown in Fig. P2.7a). The wavelength shift $\Delta\lambda_b$ response of each sensor is different, as can be observed in Fig. P2.7b), which proves the authors' statement that the sensors have different responses during loading.

The strain without thermal effect was calculated using Eq. (P2.13), and good agreement between the applied strain and FBG measured strain was found, as shown in Fig. P2.8. This material-geometry pair was calibrated for strain measurement with a maximum error of 0.9%. The calibrated parameters are presented in Table P2.2.
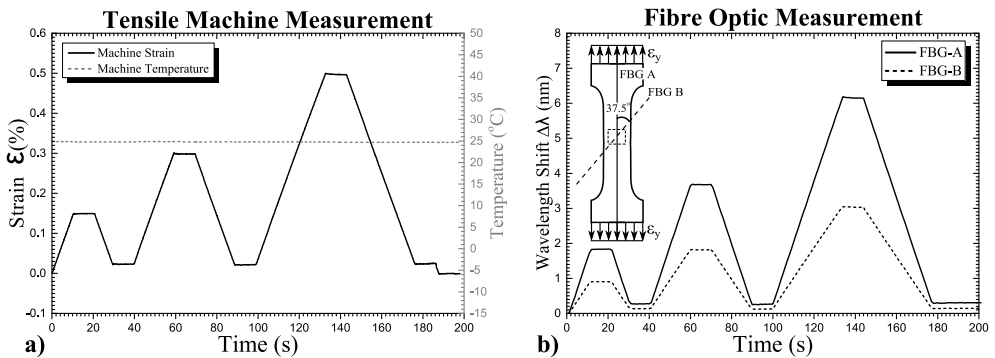
Figure P2.7: Strain calibration procedure; a) Machine measurement of temperature and strain; b) FBG wavelength shift $\Delta\lambda_b$.
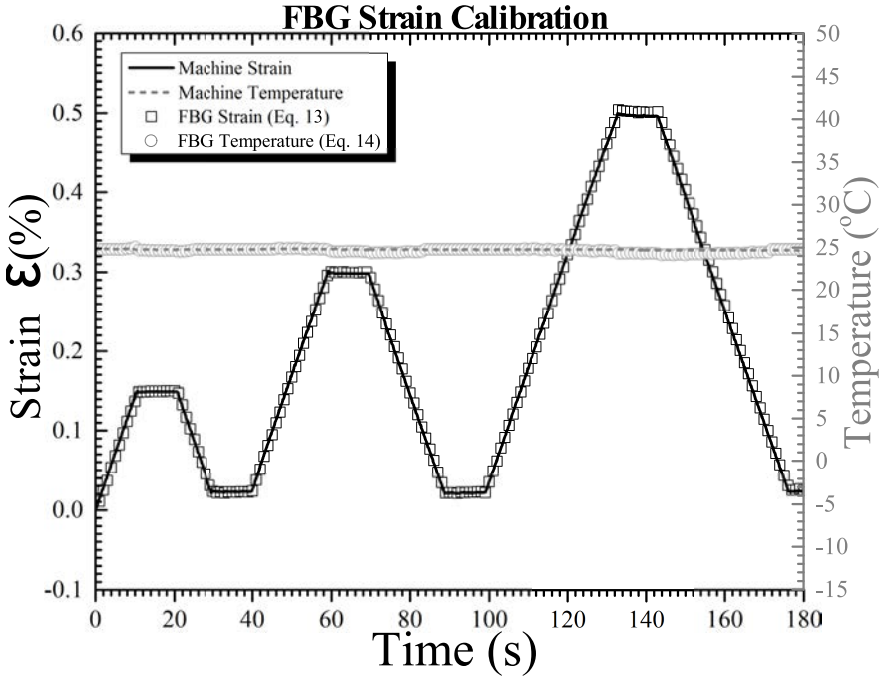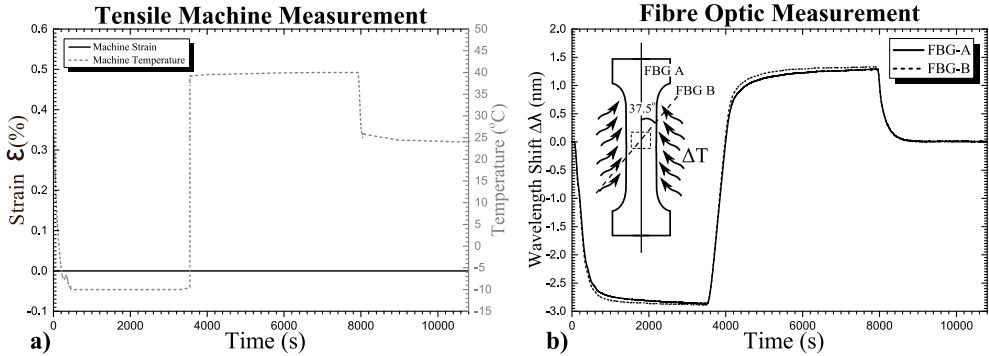
Figure P2.8: Strain and temperature measured independently by the FBG sensors. The lines show the strain and temperature measured by the machine, and the symbols the strain and temperature obtained by the developed method using the FBG sensors measurement.

Table P2.2: FBG strain calibration: calibrated parameters.

Calibrated Parameters	
Photo-elastic coefficient (p_e)	0.21 ± 0.05
Poisson's ratio (ν_{12})	0.35 ± 0.07
Calibration Error ($\varepsilon_{machine} - \varepsilon_{FBG}/\varepsilon_{machine}$)	0.9 %

Temperature Calibration

To perform the temperature calibration, three temperatures stages (25^oC, -10^oC and 40^oC) controlled by the environmental chamber were applied. No load or displacement constrains were applied to the specimens, which allows them to expand or contract freely. The temperature was kept constant for 60 min at each stage to ensure a complete temperature homogenisation in the specimen and, consequently, in the FBG sensors.
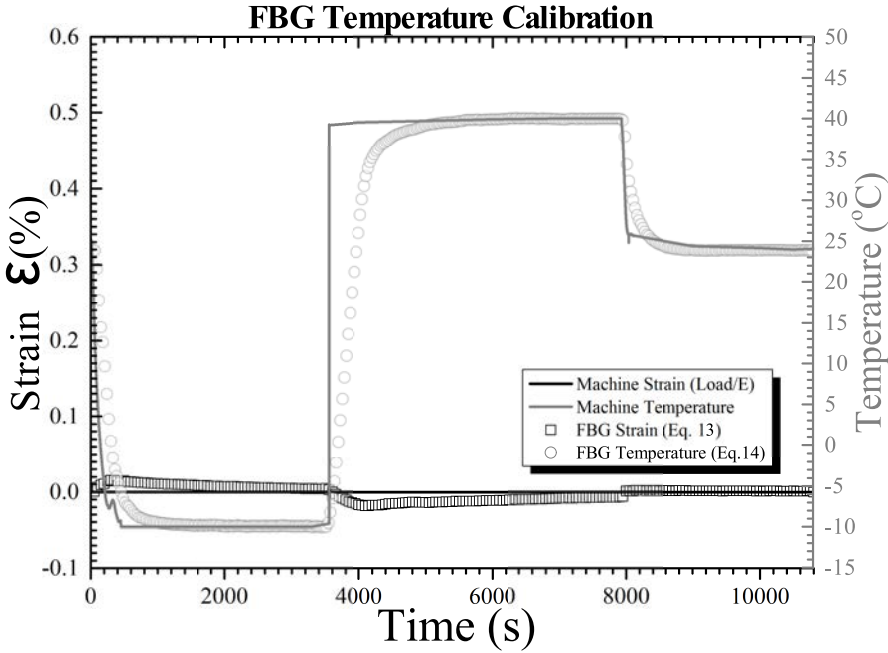
Figure P2.9: Temperature calibration procedure; a) Machine measurement of temperature and strain; b) FBG wavelength shift $\Delta\lambda_b$.

The strain measured by the extensometers and the temperature from the environmental chamber are shown in Fig. P2.9a). As previously described, both FGB sensors have the same response to temperature variation, as can be observed in Fig. P2.9b). However, a small difference in the sensor response is observed every time the temperature changes. This is because FBG-B is closer to the specimen surface, which makes it experience the temperature change first.

The strain without thermal effect and temperature were calculated using Eqs. (P2.13) and (P2.14), as shown in Fig. P2.10. Good agreement between the predicted and measured temperature was found. However, the small difference in the sensor response observed in Fig. P2.9b) caused an error in the strain measurement, which disappears once the temperature homogenised inside the specimen. Thus, the distance between the sensors can be problematic for the strain measurement accuracy and it should be as small as possible to minimize this effect. The temperature calibrated parameters are presented in Table P2.3.

Table P2.3: FBG temperature calibration: calibrated parameters.

| Calibrated Parameters	
Thermo-optic coefficient (ξ)	8.3E-6
Thermal expansion coefficient (α_h)	6.31 $\pm$0.03E-5
Calibration Error ($T_{machine} - T_{FBG}/T_{machine}$)	0.05 %

Figure P2.10: Strain and temperature measured independently by the FBG sensors during temperature calibration. The lines show the strain and temperature measured by the machine, and the symbols the strain and temperature obtained by the developed method using the FBG sensors measurement.

Simultaneous Strain and Temperature Measurement

As a final test, a continuous variation of temperature from -10°C to 40°C was applied to the specimen and, at the same time, the specimen was cyclically loaded with two strain stages of $\varepsilon= 0.30\%$ and $\varepsilon= 0.50\%$, as shown in Fig. P2.11a). However, in order to compare both measured strains without the thermal effect, the machine strain was converted using the load applied by the tensile machine ($\varepsilon_{noThermal} = F/(A_{section}E)$); $E = 4.4GPa$).

The wavelength shift $\Delta\lambda_b$ of each FBG sensor can be observed in Fig. P2.11b) and, as expected, the signal global behaviour follows the specimen temperature variation in both sensors, and the difference in the sensor response $[(\Delta\lambda_b^A/\Delta\lambda_b^A)-(\Delta\lambda_b^B/\Delta\lambda_b^B)]$ increases as the strain in the specimen increases.

The strain and temperature measured independently by the FBG sensors during the tensile test are shown in Fig. P2.12. The strain in the specimen caused by the loading without the thermal expansion effect was successfully measured with a
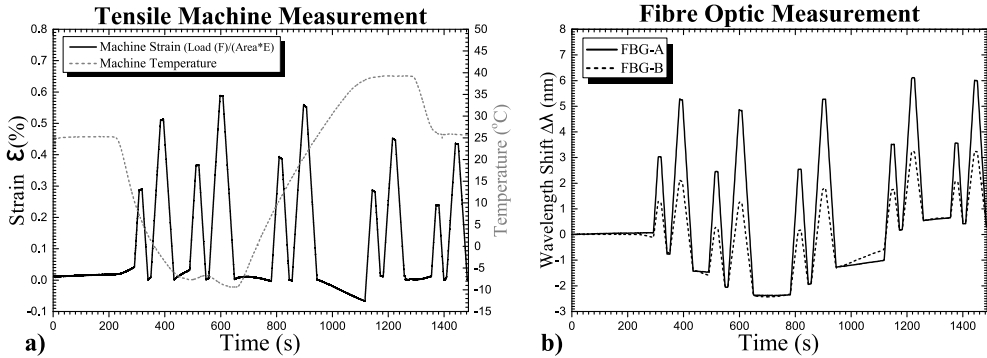
Figure P2.11: Simultaneous strain and temperature measurement; a) Machine measurement of temperature and strain; b) FBG wavelength shift $\Delta\lambda_b$.

maximum error of 2.4%. This measurement error can be justified by the mismatch in temperatures acting in each sensor, as this error is only observed during large temperature variation. This problem can be solved by minimizing the distance between sensors. Nevertheless, the error value achieved is acceptable, and in common tests or application this magnitude of temperature variation will not happen. The observed difference between the two measured temperatures is caused by fact that the machine temperature is measured in the environmental chamber, and the FBG temperature is measured inside the specimen. Therefore, the specimen needs more time to homogenise its temperature, creating a delay in the measurement.

In summary, these results showed that by using this method it is always possible to determine the strain without the thermal effect within a reasonably low error, even for a complicated temperature-loading case.

P2.5   Proposed Calibration Protocol

A calibration procedure is required before any measurement can be made. The two calibration options are:

- Full calibration or using already calibrated parameters; this is the most accurate method but it is time consuming;

- Strain/partial calibration; it is faster to perform but the temperature cannot be measured;
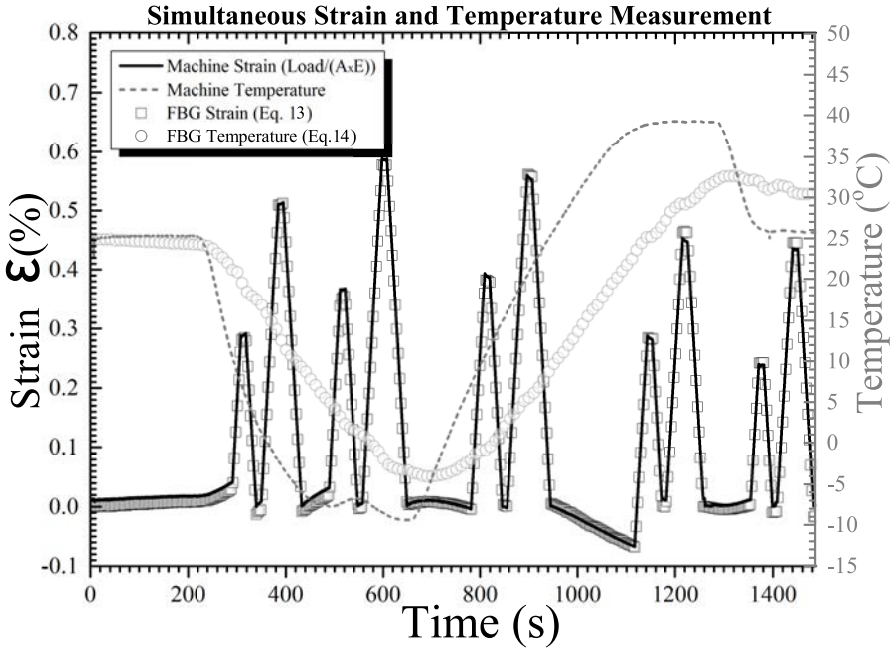
Figure P2.12: Strain and temperature measured independently by the FBG sensors during a tensile test with simultaneous temperature and strain variation. The lines show the strain and temperature measured by the machine, and the symbols the strain and temperature obtained by the developed method using the FBG sensors measurement.

P2.5.1 Measurement with Full Calibration

The full calibration procedure allows more parameters to be measured; it is possible to measure the specimen strain and temperate independently, and also to measure the material Poisson's ratio (ν_{12}) and thermal expansion coefficient (α_h). The full calibration procedure requires the following steps:

(a) Strain calibration:

  1. Load/Unload the specimen and maintain the temperature constant during the test;

  2. Measure the wavelength shift from both FBGs, $\Delta\lambda_b^A$ and $\Delta\lambda_b^B$;

  3. Measure the specimen strain using the surface mounted extensometers; this strain is considered the reference strain ($\varepsilon_{ref} = \varepsilon_{extensometer}$);

  4. Calibrate the photo-elastic coefficient (p_e) using Eq. (P2.16);

$$\frac{\Delta\lambda_b^A}{\lambda_b^A} = (1 - p_e)\varepsilon_{ref} \tag{P2.16}$$

5. Calibrate the Poisson's ratio (ν_{12}) using the Eq. (P2.17); Use the calibrated p_e value;

$$\varepsilon_{ref} = \left(\frac{\Delta\lambda_b^A}{\lambda_b^A} - \frac{\Delta\lambda_b^B}{\lambda_b^B}\right) \frac{1}{(1 - p_e)(1 - cos(\theta)^2 - \nu_{12}sin(\theta)^2)} \tag{P2.17}$$

(b) Temperature calibration:

1. Apply a controlled variation of temperature, ensuring that no load or any displacement constrains are applied to the specimen;

2. Measure the wavelength shift from both FBGs, $\Delta\lambda_b^A$ and $\Delta\lambda_b^B$;

3. Measure the chamber temperature variation; This temperature is considered the reference value ($\Delta T_{chamber} = \Delta T_{ref}$);

4. Calibrate the thermo-optic coefficient (ξ) and the host material thermal expansion coefficient (α_h) using the Eq. (P2.18); Use the calibrated p_e value;

$$\frac{\Delta\lambda_b^A}{\lambda_b^A} = \frac{\Delta\lambda_b^B}{\lambda_b^B} = [(1 - p_e)\alpha_h + \xi]\Delta T_{ref} \tag{P2.18}$$

5. This material-sensor calibrated parameters: ν_{12}; p_e; ξ; α_h;

P2.5.2   Measurement with strain/partial calibration

If the thermal expansion coefficient (α_h) is unknown and the full calibration was not performed, the temperature of the specimen cannot be measured by the developed method. However, it is still possible to measure the strain without the thermal effect by executing a strain/partial calibration. This calibration method is faster to execute and it does not requires surface mounted extensometers or an environmental chamber, which makes it a good calibration alternative (for measurements where the temperature is not a requirement). The strain/partial calibration procedure requires the following steps:

(a) Strain/partial calibration:

1. Load/Unload the specimen and maintain the temperature constant during the test;

2. Measure the wavelength shift from both FBGs, $\Delta\lambda_b^A$ and $\Delta\lambda_b^B$;

3. The strain measured by the FBG-A is considered the reference strain ($\varepsilon_{ref} = \Delta\lambda_b^A/(\lambda_b^A[1 - p_e])$);

4. Assume the parameter p_e as the value provided by the manufacture (in this case p_e=0.22);

5. Calibrate the Poisson's ratio (ν_{12}) using Eq. (P2.17);

(b) Execute the tensile test, and calculate the strain without the thermal expansion effect using Eq. (P2.13) and the calibrated Poisson's ratio.

A comparison between the two calibration methods, full calibration and strain/-partial calibration, is presented in Appendix P2-A.

P2.6   Summary and Conclusions

The FBG sensors have a strain and temperature cross-sensitivity, making them inaccurate for tests where the temperature can change. A temperature variation in the specimen will create an additional strain, caused by the thermal expansion. A simple measurement method to decouple this cross-sensitivity, enabling independent and accurate measurement of strain and temperature, was developed in this article. This technique was developed especially for polymeric tensile test specimens, and it can be accomplished by using two single mode FBG sensors embedded in the material.

Equations describing this method, which allows strain and temperature calculation from the FBGs signal, were derived from the general FBG work principle. It was demonstrated that, during temperature variation, both sensors will measure the same amount of wavelength shift $\Delta\lambda_b$, caused by the material thermal expansion. However, during loading, the sensor response will have a different evolution, which gives information about the strain in the material. Moreover, the angle between FBG sensors (θ) has a big impact on the strain resolution. For an angle θ around 90°, the resolution is actually improved, benefiting from the Poisson's effect.

Two different calibration protocols were presented; one, fast that allows measuring the strain without the thermal effect, sacrificing temperature measurement and accuracy; other, more time consuming but that allows accurate measurement of strain and temperature. Nevertheless, the authors suggest that for each material-sensor configuration the full calibration procedure should be performed, in order to tune the parameters used by the method.

This multi-parameter measurement method was applied to an epoxy tensile specimen. The full calibration protocol was performed and achieved a calibration error smaller than 1%. Then, multiple two loading/strain stages of ε= 0.30% and ε= 0.50% during a continuous variation of temperature, from 40^oC to -10 ^{o}C, were applied to the specimen. The consistency of the expected/theoretical results with the calibration procedure, and the experimental validation, suggests that this proposed method is applicable to measure accurate strain and temperature in a wide range of polymer materials during tensile testing, being specially promising for polymer fatigue test specimens.

P2.7 Acknowledgements

References

[1] S. Zike and L. P. Mikkelsen, "Correction of gauge factor for strain gauges used in polymer composite testing," *Experimental Mechanics*, volume 54, number 3, pages 393–403, 2013, ISSN: 0014-4851. DOI: 10.1007/s11340-013-9813-7.

[2] M. Jerabek, Z. Major, and R. Lang, "Strain determination of polymeric materials using digital image correlation," *Polymer Testing*, volume 29, number 3, pages 407–416, May 2010, ISSN: 01429418. DOI: 10.1016/j.polymertesting.2010.01.005.

[3] V. Crupi, E. Guglielmino, G. Risitano, and F. Tavilla, "Experimental analyses of sfrp material under static and fatigue loading by means of thermographic and dic techniques," *Composites Part B: Engineering*, volume 77, pages 268–277, August 2015, ISSN: 13598368. DOI: 10.1016/j.compositesb.2015.03.052.

[4] F. T. S. Yu, *Fiber optic sensors*, First Edit, F. T. YU and S. Yin, Eds. Marcel Dekker, 2002, 494 S, ISBN: 9780824744571.

[5] D. W. Jung, I. B. Kwon, and N. S. Choi, "Application of a temperature-compensating fbg sensor to strain measurement," *Advanced Materials Research*, volume 26-28, pages 1089–1092, 2007, ISSN: 1662-8985. DOI: 10.4028/www.scientific.net/AMR.26-28.1089.

[6] Z. Zhou and J. Ou, "Techniques of temperature compensation for fbg strain sensors used in long-term structural monitoring," *Proceeding of Asian Pascifc Fundamental Problems of Opto- and Microelectronics (APCOM 2004)*, number Apcom, pages 465–471, 2004, ISSN: 0277786X. DOI: 10.1117/12.634047.

[7] P. Kisała, "Method of simultaneous measurement of bending forces and temperature using bragg gratings," in *Proc. SPIE-Optical Sensors 2015*, F. Baldini, J. Homola, and R. A. Lieberman, Eds., volume 9506, May 2015, page 950 627. DOI: 10.1117/12.2179009.

[8] E. Marin and Y. Ouerdane, "Dual-fibre bragg grating sensor for simultaneous temperature and strain sensing of composite materials manufacturing," in *7th European Workshop on Structural Health Monitoring*, V. Le Cam, L. Mevel, and Schoefs, Eds., 2014, pages 946–953.

[9]   Y. J. Rao, S. F. Yuan, X. K. Zeng, D. K. Lian, Y. Zhu, Y. P. Wang, S. L. Huang, T. Y. Liu, G. F. Fernando, L. Zhang, and I. Bennion, "Simultaneous strain and temperature measurement of advanced 3-d braided composite materials using an improved efpi / fbg system," *Optics and Laser in Engineering*, volume 38, pages 557–566, 2002, ISSN: 01438166. DOI: 10.1016/S0143-8166(02)00014-3.

[10] S. James, M. Dockney, and R. Tatam, "Simultaneous independent temperature and strain measurement using in-fibre bragg grating sensors," *Electronics Letters*, volume 32, number 12, page 1133, 1996, ISSN: 00135194. DOI: 10.1049/el: 19960732.

[11] C. Fernández-Valdivielso, I. Matías, and F. Arregui, "Simultaneous measurement of strain and temperature using a fiber bragg grating and a thermochromic material," *Sensors and Actuators A: Physical*, volume 101, number 1-2, pages 107–116, Sep. 2002, ISSN: 09244247. DOI: 10.1016/S0924-4247(02)00188-7.

[12] K. Hill and G. Meltz, "Fiber bragg grating technology fundamentals and overview," *Journal of lightwave technology*, volume 15, number 8, pages 1263–1276, 1997.

[13] W. W. Morey, G. Meltz, and W. H. Glenn, "Fiber optic bragg grating sensors," in *Proc. SPIE, Fiber Optic and Laser Sensors VII*, R. P. DePaula and E. Udd, Eds., volume 1169, February 1990, pages 98–107. DOI: 10.1117/12.963022.

[14] S. Magne, S. Rougeault, M. Vilela, and P. Ferdinand, "State-of-strain evaluation with fiber bragg grating rosettes: application to discrimination between strain and temperature effects in fiber sensors.," *Applied optics*, volume 36, number 36, pages 9437–9447, 1997, ISSN: 0003-6935. DOI: 10.1364/AO.36.009437.

[15] T. Kosaka, K. Osaka, and Y. Sawada, "Evaluation of residual strain of fibres in matrix resin during cure process by optical fibre sensors," in *ICCM17- 17TH INTERNATIONAL CONFERENCE ON COMPOSITE MATERIALS*, 2009.

P2 Appendix-A: Comparison Between The Two Calibration Methods: Full And Strain/Partial Calibration

In this appendix the two calibration methods, full and strain/partial calibration, are compared. To simulate the case where only the strain/partial calibration was performed, only the FBG data measured during tests is considered (without included the strain measured by the surface mounted extensometers).

The parameters obtained after preforming the calibration protocols are shown in Table P2.4.

Table P2.4: Calibrated and assumed parameters used. Comparison between the two calibration methods, full and strain/partial calibration.

Parameters	Full Cal.	Strain/Partial Cal.
Photo-elastic coefficient (p_e)	0.21±0.05	0.22 (given by manufacturer)
Poisson's ratio (ν_{12})	0.35±0.07	0.35±0.04
Thermo-optic coefficient (ξ)	8.3E-6	8.3E-6 (given by manuf.)
Thermal expansion coefficient (α_h)	6.1±0.03E-5	Not possible to obtain

The comparison between the strain and temperature measured by the two methods are shown in Fig. P2.13 and the maximum strain measurement error obtained is presented in Table P2.5. The measurement where full calibration was performed shows a lower strain measurement error, but it requires a more time consuming procedure. On the other hand, the measurement where only strain/partial calibration was performed shows an error slightly larger; however it does not allow any temperature measurement. In any case, both options will give accurate measurement of strain without the thermal effect.

Table P2.5: Maximum strain measurement error obtained during the test: Comparison between the two calibration methods.

	Full Calibration	Strain/Partial Calibration
Maximum Strain error	2.4%	3.7%
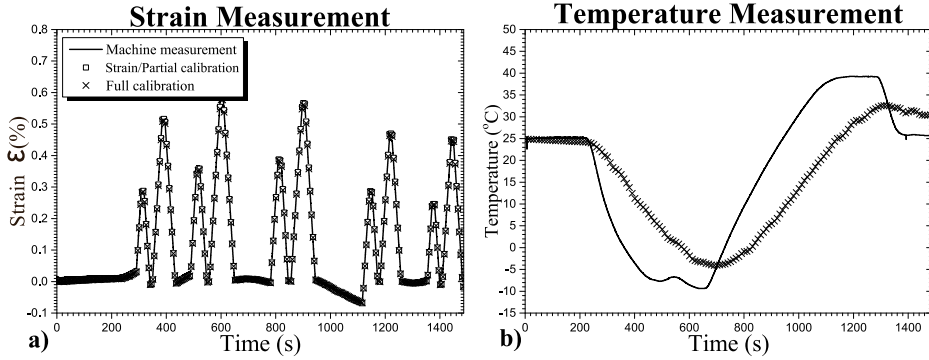
Figure P2.13: Strain and temperature measured independently by the FBG sensors during a tensile test with simultaneous temperature and strain variation: Comparison between the two calibration methods, full and strain/partial calibration. The line represents the control strain and temperature measured by the machine, the cross symbol the strain and temperature measured by the full calibration method, and the square symbol the strain measured by the strain/partial calibration method.

Appended Paper P3

Crack Detection in Fibre Reinforced Plastic Structures Using Embedded Fibre Bragg Grating Sensors

G. Pereira, L.P. Mikkelsen, M. McGugan

Abstract

In a fibre-reinforced polymer (FRP) structure designed using the emerging *damage tolerance* and *structural health monitoring* philosophy, sensors and models that describe crack propagation will enable a structure to operate despite the presence of damage by fully exploiting the material's mechanical properties. When applying this concept to different structures, sensor systems and damage types, a combination of damage mechanics, monitoring technology, and modelling is required. The primary objective of this article is to demonstrate such a combination. This article is divided in three main topics: the damage mechanism (delamination of FRP), the structural health monitoring technology (fibre Bragg gratings to detect delamination), and the finite element method model of the structure that incorporates these concepts into a final and integrated damage-monitoring concept. A novel method for assessing a crack growth/damage event in fibre-reinforced polymer or structural adhesive-bonded structures using embedded fibre Bragg grating (FBG) sensors is presented by combining conventional measured parameters, such as wavelength shift, with parameters associated with measurement errors, typically ignored by the end-user. Conjointly, a novel model for sensor output prediction (virtual sensor) was developed using this FBG sensor crack monitoring concept and implemented in a finite element method code. The monitoring method was demonstrated and validated using glass fibre double cantilever beam specimens instrumented with an array of FBG sensors embedded in the material and tested using an experimental fracture procedure. The digital image correlation technique was used to validate the model prediction by correlating the specific sensor response caused by the crack with the developed model.

P3.1   Introduction

P3.1.1   Damage Tolerant Design and Structural Health Monitoring in Fibre-Reinforced Polymer Material Structures

Fibre-reinforced polymer materials (FRP, often referred to as composite materials) have been extensively used in aerospace, automotive, naval, wind energy and civil engineering applications, mostly due to their high stiffness/weight ratio. A fibre-reinforced polymer composite material consists of two distinct macroscopic phases: a stiff phase (generally glass or carbon) and a polymer matrix. One of the advantages of FRP material is their ability to be tailored for a specific application; this enables an enhancement and a high level of customisation of their mechanical properties. Thus, in a FRP structure, it is possible to align the reinforcement in the directions where higher stiffness is required, which makes the structure lighter compared with the structure of a conventional material [1].

Currently, the higher demand for more cost-effective, light-weight FRP structures is pushing advances in material technology and design philosophy. In this way, the design philosophy of FRP structures that is based on conservative analysis methods,

with large safety factors, underestimation of the material properties, and considering only the linear behaviour of the materials, is becoming obsolete. A shift in the design philosophy has been discussed by several authors [2, 3], where the concept of damage tolerance is suggested as an energy concept based on a particular combination of structural design, loading environment, and material characteristics, which will enable the structure to operate despite the presence of damage. However, a standalone damage tolerance approach will not be achieved until all physical phenomena present in the FRP field are fully understood. The solution starts by accepting the presence of damage and its unpredictability, tracking this damage using a structural health monitoring approach, where sensors integrated during manufacturing will provide information about the presence of damage in an accurate way, its location, the type of damage and the remaining operating life of the structure.

P3.1.2   Article Objectives

The main objective of this article is to provide a better understanding of the different fields that need to be addressed to design a structure using a *damage tolerance* and *structural health monitoring* philosophy, as well as a methodology that can follow this concept to different structures, sensor systems and damage types.

To achieve this goal, it is necessary to explore three different fields in more detail; thus, the following key concepts are linked and fully described.

- Damage mechanism: delamination in FRP as a damage tolerance property of the structure. Fracture mechanism and stress distributions along the crack/damage area.

- Structural health monitoring technology: embedded fibre Bragg gratings to detect and track cracks/delamination in FRP structures. FBG working principle.

- Finite element method (FEM) model of the structure: incorporation of the damage mechanism with the structural health monitoring technology to a final and integrated *damage-monitoring concept*. Virtual FBG: FEM sensor output model for FRP delamination.
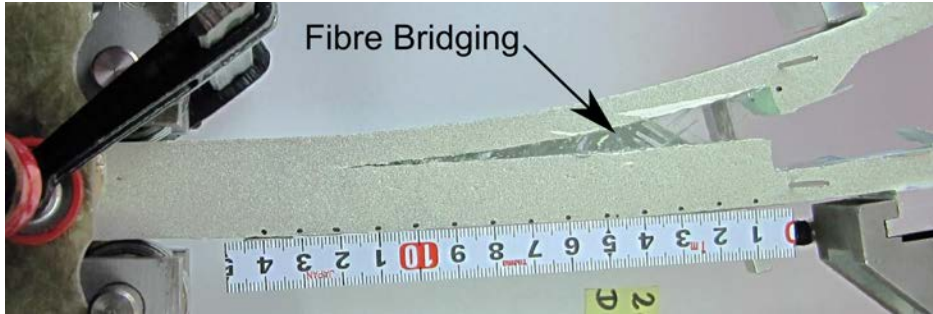
Figure P3.1: Fibre bridging phenomenon during delamination in a glass fibre specimen.

P3.2   Delamination as a Damage Tolerant Mechanism

Interface fracture resulting from crack growth along interfaces in laminated structures is called delamination, and it can be considered as the most widespread cause of life reduction and one of the most important failure mechanisms in FRP structures. Delamination can be analysed through fracture mechanics; thus, damage tolerance implies that the crack growth is stable and that the energy required for unstable crack growth (catastrophic event) is higher than the energy level required to initiate the crack. This damage tolerant mechanism can be defined as a crack bridging phenomenon, i.e., the delamination is accompanied by the formation of a fracture process zone, in which intact fibres connect the crack faces behind the crack tip, as shown in Fig. P3.1, which increases the energy required for a crack to grow.

This large-scale crack bridging zone cannot be addressed by linear elastic fracture mechanics (LEFM). Rather, a cohesive model can be used to describe the fracture process zone [4]. The cohesive law $\sigma_n(\delta_n)$ can be briefly described as a normal traction, σ_n, as function of the normal opening, δ_n, in the active cohesive zone [5].

P3.2.1   Stress Distribution in the Crack/Damage Area

To successfully detect the growth of a crack in an FRP material, the measurement technique should track specific fracture features that only occur in the vicinity of a crack. Thus, the stress distribution around the crack tip in an FRP specimen was analysed. This allowed the different measured parameters to be linked with all the different fracture features.

The fracture process zone (FPZ) is a region near the crack tip where the material strength is locally reduced. The stress distribution in the FPZ can be divided into two distinct contributions: the crack tip singularity at the front of the FPZ and the crack bridging at the FPZ wake. Near the crack tip, the singularity dominated the
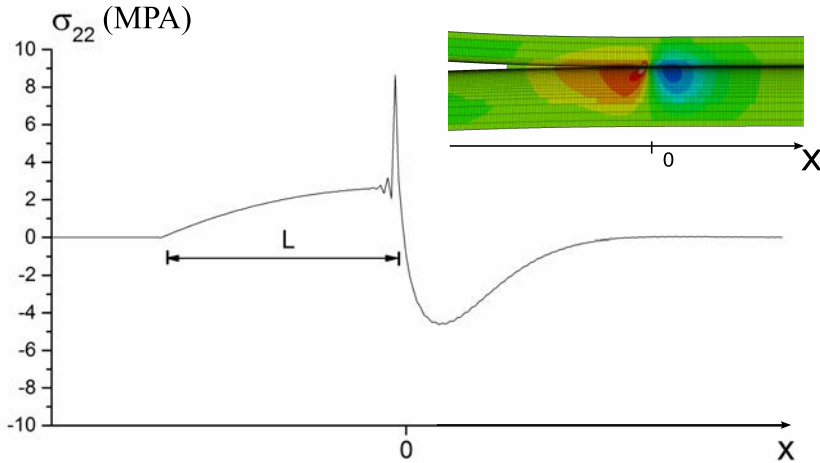
Figure P3.2: Finite element method simulation: stress σ_{22} distribution at the fracture process zone (FPZ) for Mode I fracture.

zone (K-dominant). The stress field closely approached the singular stress field of LEFM, indicating that the stress tends to infinity, creating a high stress gradient area, as shown in Figs. P3.2 and P3.3a).

Considering the crack tip where the material is developing damage at $x = 0$, in the fracture process zone given by $-L < x < 0$, the material is damaged, and its ability to transfer stress is decreased, as described by the cohesive law. This FPZ is characterised by a positive stress zone, as shown in Figs. P3.2 and P3.3b), which is balanced by a compression zone ahead of the crack tip ($x > 0$). The size of the compression zone will depend on the cohesive law and the material parameters [4].

P3.3   Structural Health Monitoring

Accepting damage and incorporating it as part of the design process will require full control over the structural integrity. A structural health monitoring system's main purpose is to provide information about the presence of damage in an accurate way, its location with good resolution, and the prognosis for the remaining life of the structure. Some techniques have already been implemented to detect cracks and monitor their growth, such as acoustic emission [6], where ultrasonic stress waves generated by crack growth are detected; vibration [7], by measuring the change in the specific damping capacity; modal analysis [8], by monitoring the natural frequencies
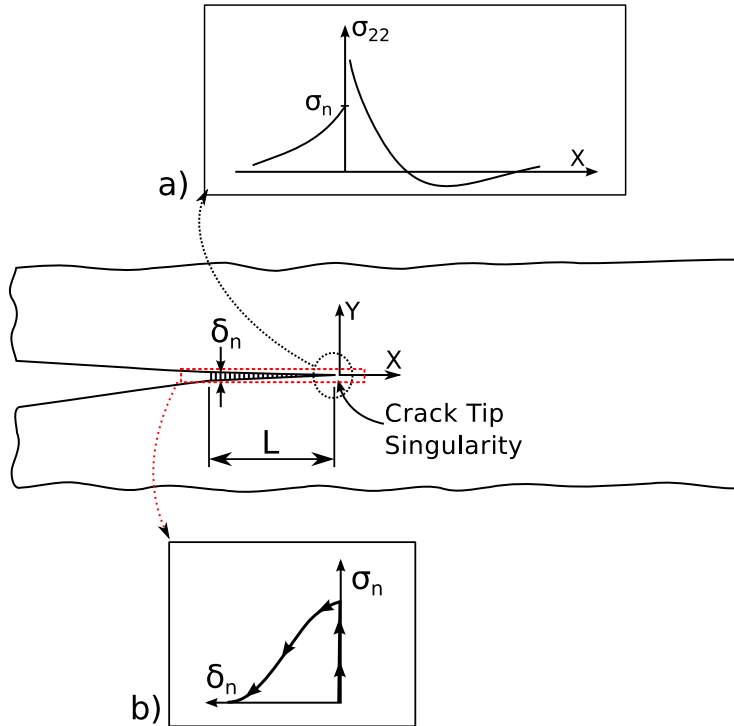
Figure P3.3: Illustration of bridging zone stress distribution. (a) Crack tip singular
stress field and (b) schematic of a bridging law: relationship between
the normal stress, σ_n, and separation, δ_n, across the FPZ.

and mode shapes; piezoelectric actuators/sensors; and wavelet analysis [9] based on
the energy variation in the structural dynamics. However, applying these techniques
in operational structures presents some difficulties due to technical limitations, the
need for manual inspections performed by qualified operators, expensive hardware,
and so forth.

P3.3.1   Fibre Optic Sensors as Structural Health Monitoring Technology

Fibre optic sensors, such fibre Bragg gratings (FBG), have the ability to perform
damage/failure monitoring during the operation of a structure without compromis-
ing its performance and structural resistance. The small size of an FBG, a diameter
of 125 μm, makes it virtually non-intrusive when embedded in the material. Addi-
tionally, FBG sensors have high resolution, multiple measurement points per fibre
capability (multiplexing), immunity to electromagnetic fields, chemical inertness, im-

munity to optical power fluctuations, and long-term stability. These characteristics make embedded FBGs a very promising technology for tracking cracks in composite materials.

Knowing that an embedded FBG sensor will be under the influence of different fracture phenomena during a crack growth event, such as a crack bridging zone, where intact fibres connect the crack faces and a stress concentration zone near the crack tip that influences the stress distribution (stress gradient), being able to identify and measure these specific phenomena is the key factor for determining the presence of damage and its growth in a structure. In the next section, FBG sensor responses for three different stress/strain states that occur during crack growth are presented.

P3.3.2 Fibre Bragg Grating Sensor

A fibre Bragg grating is formed by a permanent periodic modulation of the refractive index along a section of an optical fibre grating by exposing the optical fibre to an interference pattern of intense ultra-violet light [10]. The photosensitivity of the silica exposed to the ultra-violet light is increased; thus, when the optical fibre is illuminated by a broadband light source, the grating diffraction properties are such that only a very narrow wavelength band is reflected back, as shown in Fig. P3.4.

In a free state, without strain and at a constant temperature, the spectral response of a homogeneous FBG is a single peak centred at wavelength λ_b, with a certain bandwidth $\overline{\lambda_0}$ (distance between the two first minima), as shown in Fig. P3.4. The wavelength λ_b is described by the Bragg condition,

$$\lambda_b = 2n_{eff,0}\Lambda_0 \tag{P3.1}$$

where $n_{eff,0}$ is the mean effective refractive index at the location of the grating, the index 0 denotes unstrained conditions (initial state), and Λ_0 is the constant nominal period of the refractive index modulation [11]. The bandwidth is given by

$$\frac{\overline{\lambda_0}}{\lambda_b} = \frac{1}{n_{eff,0}}\sqrt{(\xi\overline{\delta n_{eff,0}})^2 + (\lambda_b/L)^2} \tag{P3.2}$$

where L is the gauge length, $\overline{\delta n_{eff,0}}$ is the mean induced change in $n_{eff,0}$, and ξ is the amplitude of the induced index change [12]. An external load or temperature variation will change the effective index of refraction and/or the period of modulation; this will create a shift of the wavelength reflected peak from its original value.
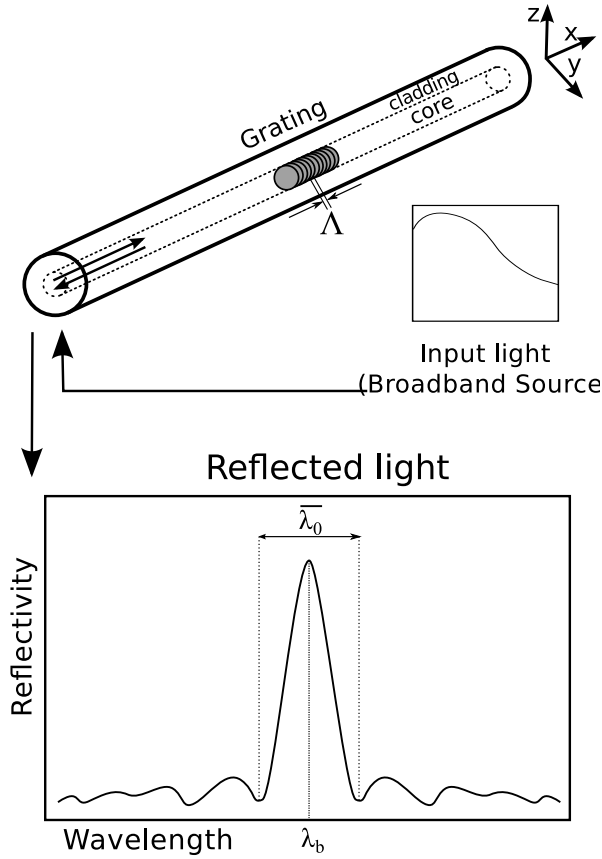
Figure P3.4: Fibre Bragg grating response in a free state.

In the following sections, the temperature is assumed to be constant and to have no effect on the sensor response.

Response to Uniform Axial Strain

The sensor response to a uniform axial strain is schematically shown in Fig. P3.5. Assuming a uniform strain ε_{xx} along the grating length, the wavelength shift $\Delta\lambda_b$ in the sensor response is described by equation (P3.3)[13].

$$\frac{\Delta\lambda_b}{\lambda_b} = (1 - p_e)\varepsilon_{xx} \tag{P3.3}$$

The parameter p_e is a photo-elastic coefficients.
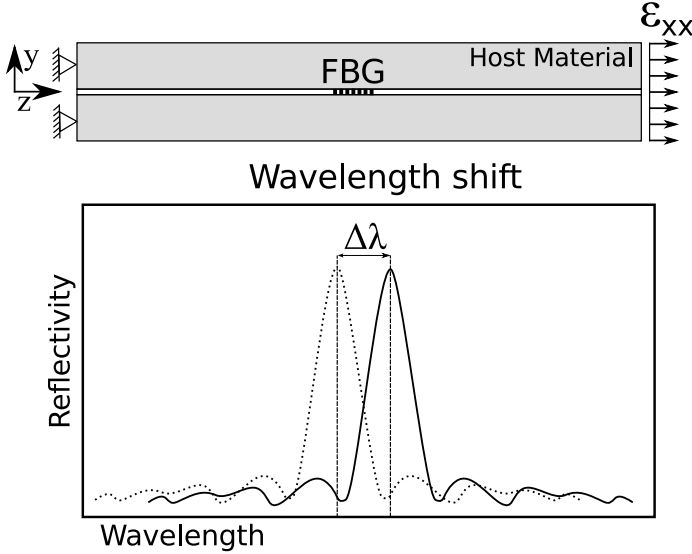
Figure P3.5: Embedded FBG response to a uniform variation of strain and/or temperature.

Response to Transverse Deformation: Birefringence Effect

An optical fibre can exhibit birefringent behaviour, which is defined by the change in the refractive index n_{eff} of the two directions n_{effy} and n_{effz} when the grating is subjected to a transverse force [14–17]. The change in the refractive index of the two directions n_{effy} and n_{effz} is given by equations (P3.4) and (P3.5).

$$\Delta n_{effz} = -\frac{n_0^3}{2E_f}\{(p_{11} - 2\nu_f p_{12})\sigma_z + [(1 - \nu_f)p_{12} - \nu_f p_{11}](\sigma_y + \sigma_x)\} \quad \text{(P3.4)}$$

$$\Delta n_{effy} = -\frac{n_0^3}{2E_f}\{(p_{11} - 2\nu_f p_{12})\sigma_y + [(1 - \nu_f)p_{12} - \nu_f p_{11}](\sigma_z + \sigma_x)\} \quad \text{(P3.5)}$$

The parameter E_f is the elastic modulus of the optical fibre, ν_f is Poisson's ratio, n_0 is the initial refractive index, and p_{11} and p_{12} are the photo-elastic coefficients of the optical fibre.

With this, when a transverse stress is applied to the grating, a separation of the reflected Bragg peak occurs (peak splitting), as presented in Fig. P3.6. The width variation of the reflected peak due to transverse deformation [15] $\Delta\lambda'_{WV} = |\lambda_z - \lambda_y|$ can be calculated using equations (P3.1), (P3.4) and (P3.5).
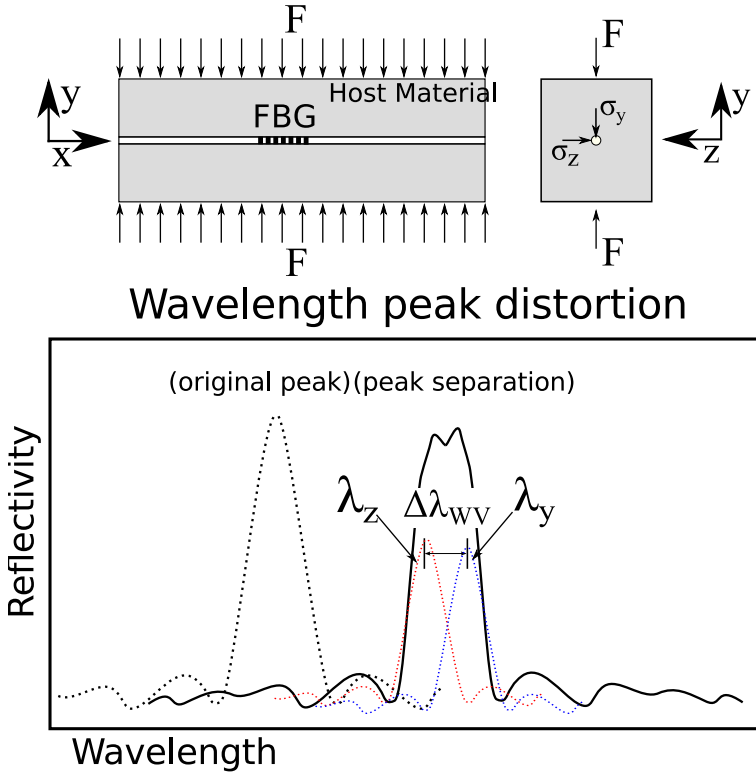
Figure P3.6: FBG response under a transverse force: Birefringent effect.

$$\Delta\lambda'_{WV} = 2\Lambda|\Delta n_{effz} - \Delta n_{effy}| \tag{P3.6}$$

$$= \frac{\Lambda n_o^3}{E_f}[(1+\nu_f)(p_{12} - p_{11})]|\sigma_z - \sigma_y| \tag{P3.7}$$

Response to Non-uniform Strain

A crack or defect in the material can create a stress concentration/gradient, which leads to an abrupt variation in strain. If the FBG sensor is inside this strain gradient zone, the grating will experience a non-uniform deformation, causing a sensor response that is significantly more complicated compared to a uniform case [14, 18]. The non-uniform strain along the sensor length will change the periodicity of the grating pattern. In this way, the grating pattern is modified from a *uniform* to a *chirped* configuration [19, 20], as shown in the Fig. P3.7.

Free State FBG

FBG under non-uniform strain
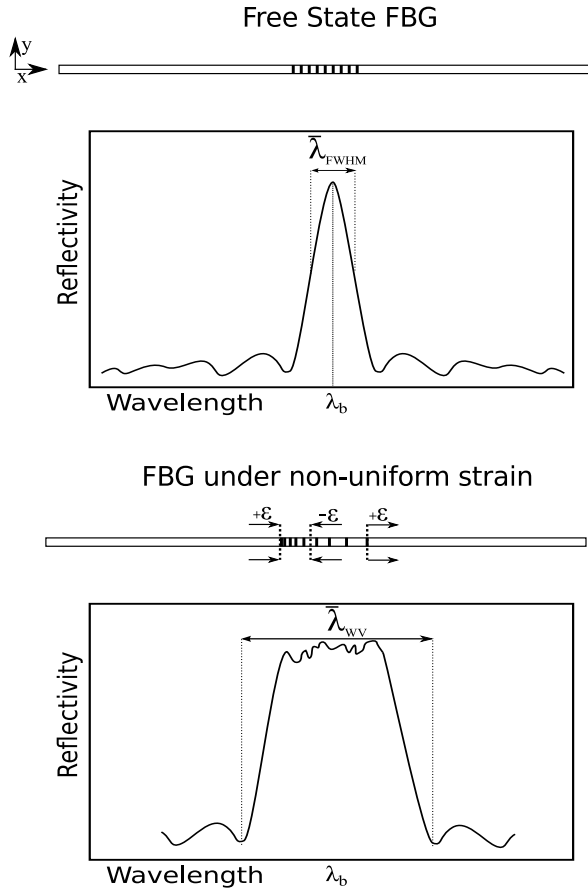
Figure P3.7: FBG response under a non-uniform strain.

As demonstrated by Peters [12], in a non-uniform grating, the applied strain will induce a change in both the grating period and the mean index. These two effects can be superimposed by applying an effective strain of "$(1 - p_e)\varepsilon_{xx}(x)$", where $\varepsilon_{xx}(x)$ is the strain variation along the x direction. Thus, it is possible to rewrite the grating period from (P3.1) as [12].

$$\Lambda(x) = \Lambda_0[1 + (1 - p_e)\varepsilon_{xx}(x)] \qquad (P3.8)$$

The effective mode index along the x direction $\delta n_{eff}(x)$ can be calculated by [12].

$$\delta n_{eff}(x) = \left(1 + \xi cos\left[\frac{2\pi}{\Lambda_o[1 + (1 - p_e)\varepsilon_{xx}(x)]}z\right]\right) \qquad (P3.9)$$

In a real crack growth situation, the strain variation along the grating $\varepsilon_{xx}(x)$ (non-uniform strain) can be difficult to predict/simulate due to its strong non-linearity. The authors propose a simple method for evaluating the contribution of the non-uniform strain to the width variation of the reflected peak by subtracting the bandwidth of the grating in a free state $\overline{\lambda_0}$ from the bandwidth $\overline{\lambda_{WV}}$ of the grating under a linear variation of strain calculated using the maximum $\varepsilon_{xx}^{max}(x)$ and minimum $\varepsilon_{xx}^{min}(x)$ strains along the grating length.

The bandwidth of an FBG in a free state can be calculated using an approximate expression that provides the full-width at half-maximum (FWHM) bandwidth [21],

$$\overline{\lambda_0} \approx \overline{\lambda_{FWHM}} = \lambda_b s \left[\left(\frac{\delta n_{eff}}{2 n_{core}} \right)^2 + \left(\frac{\Lambda}{L} \right)^2 \right]^{1/2} \tag{P3.10}$$

where $s \approx 1$ for strong gratings with high reflectivity, and $s \approx 0.5$ for weak gratings, n_{core} is the unexposed core refractive index.

The width variation of the reflected peak resulting from the non-uniform strain effect can be approximated using the maximum and minimum strain values along the grating, $\varepsilon_{xx}^{max}(x)$ and $\varepsilon_{xx}^{min}(x)$, respectively. The maximum grating period Λ_{max} and minimum grating period Λ_{min} can be calculated using equation (P3.8), and the width variation of the reflected peak resulting from non-uniform strain $\Delta\lambda_{WV}''$ is obtained by combining equations (P3.8) and (P3.1).

$$\Delta\lambda_{WV}'' = [2 n_{eff} \Lambda_{max} - 2 n_{eff} \Lambda_{min}] - \overline{\lambda_{FWHM}} \tag{P3.11}$$

P3.3.3 FBG Response During Crack Growth

The FBG responses under different stages of crack growth are shown in Fig. P3.8.

P3.8(a) - No crack is present and a uniform strain, ε_{xx}, builds up around the grating area as the structure is loaded. The FBG response is a uniform wavelength shift in the reflected peak, $\Delta\lambda$.

P3.8(b) - A crack has initiated and is approaching the grating area. A compressive strain transverse to the FBG, ε_{yy}, forms ahead of the crack tip. Compressive strain changes the FBG response creating a splitting (and hence a widening) of the reflected peak, $\Delta\lambda_{WV}'$.

P3.8(c) - Progression of the crack causes a non-uniform strain field around the crack tip to reach the grating area. This modifies the FBG response by significantly increasing the width of the reflected peak, $\Delta\lambda_{WV}''$.

P3.8(d) - The crack has passed the FBG sensor, and the FBG response has returned to its original shape. Only uniform strain acts on the grating, resulting in a uniform shift of the FBG reflected peak, $\Delta\lambda$.
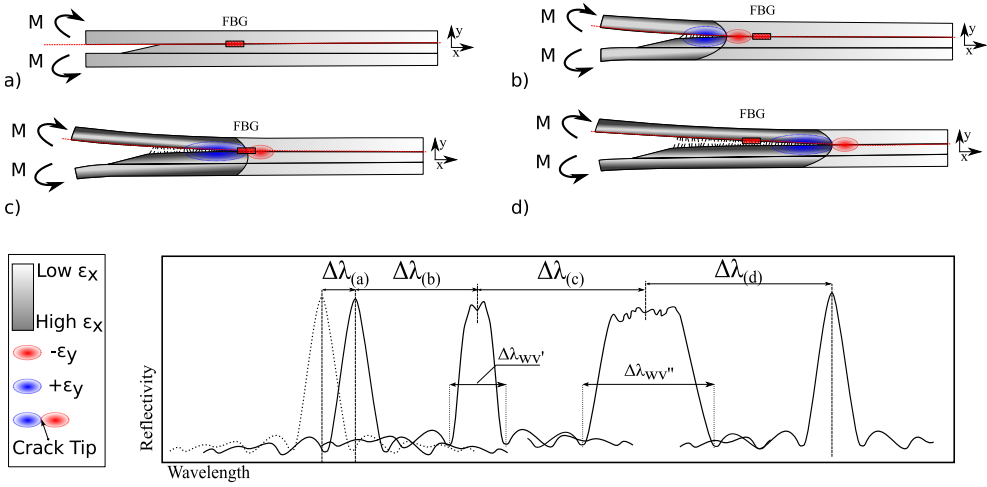
Figure P3.8: Different stages of the FBG response under a crack growth event.

P3.4   Finite Element Method Model

P3.4.1   Delamination Model

To analyse the delamination problem and to link it with the structural health monitoring technique, a finite element method (FEM) model of a double cantilever beam (DCB) specimen was developed using the commercial software ABAQUS™. This specimen geometry, DCB, was chosen because it is commonly used in fracture testing of composite materials, and later in this article, it will be used for experimental validation. The model was developed assuming plane stress conditions (plane stress elements), and the delamination/fibre bridging was modelled using 4-node cohesive elements along the delamination plane [22, 23].

This method assumes that one or more interface elements (cohesive elements) can be predefined to hold the delamination phenomenon, allowing the introduction of a discontinuity in the displacement field. The cohesive elements are modelled to express the cohesive law (traction-separation), meaning a progressive loss of the cohesion between the two crack faces with the local crack opening δ. The crack was modelled to occur between the interface of the adhesive and the glass fibre arm beam. A cohesive element with a small thickness (0.5% of the adhesive layer thickness) was used to model only the interface between the two materials and to avoid neglecting the elastic contribution of the adhesive to the DCB global behaviour. In an undamaged state, the cohesive element follows a linear-elastic behaviour, defined as the penalty stiffness K_n, which relates the nominal stress (traction vector- $\sigma_n, \sigma_s, \sigma_t$) to the nominal strains $(\delta_n, \delta_s, \delta_t)$, as presented in Fig. P3.9.
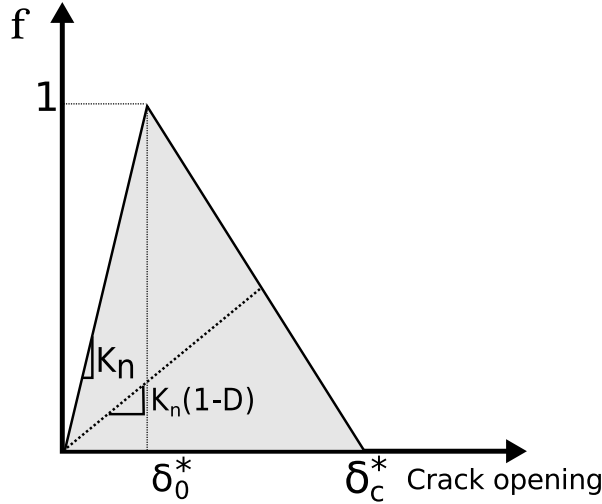
Figure P3.9: Constitutive behaviour of the cohesive element.

The damage initiation was calculated using a quadratic stress criterion presented in equation (P3.12) [24].

$$f = \left(\frac{\sigma_n}{N_{max}}\right)^2 + \left(\frac{\sigma_s}{S_{max}}\right)^2 + \left(\frac{\sigma_t}{T_{max}}\right)^2 = 1 \qquad (P3.12)$$

The parameter f is the damage criterion, and it is fulfilled when it reaches the value $f = 1$. The parameters $\sigma_{n,s,t}$ are the nominal stress in the normal, first shear and second shear directions, respectively, and N_{max}, S_{max}, and T_{max} are cohesive law parameters; these parameters are determined experimentally. The parameters δ_0^* and δ_c^* are the crack opening displacement to the local crack plane for damage initiation and critical damage. For mixed mode loading, δ_0^* and δ_c^* were calculated using the law of Pythagoras.

$$\delta_0^* = \sqrt{\delta_{0,n}^2 + \delta_{0,s}^2} \; ; \; \delta_c^* = \sqrt{\delta_{c,n}^2 + \delta_{c,s}^2} \qquad (P3.13)$$

When the initiation criterion is reached, a damage evolution law will describe the material stiffness degradation. A scalar damage variable, D, ranging from 0 (no damage) to 1 (fully damaged), represents the damage in the cohesive element. A linear softening displacement criterion was used, given by δ_0, which is the opening at damage initiation, and δ_c, which is the opening at failure. In terms of mixed mode behaviour, a linear relation between Modes I and II was implemented.
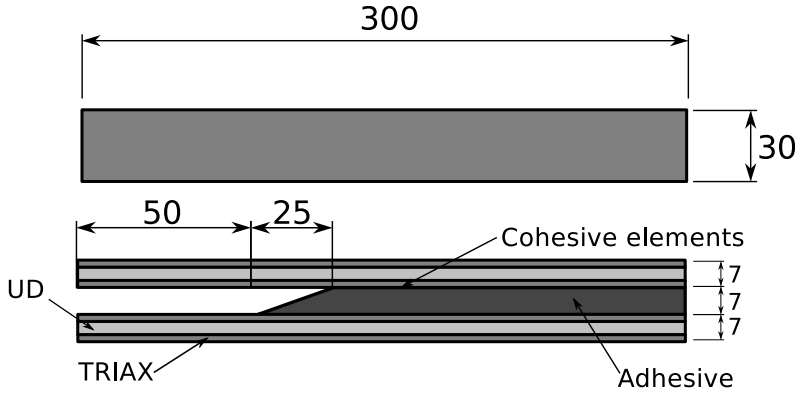
Figure P3.10: Double cantilever beam geometry dimensions.

Description of the Delamination FEM Model

The dimensions of the DCB specimen are shown in Fig. P3.10, and the material properties implemented in the FEM model are presented in Table P3.1.

The beams were modelled using a combination of two different laminates: unidirectional glass fibre (UD) and triaxial glass fibre (Triax). Moments were applied to the extremities of the beams, as shown in Fig. P3.11. Three different loading combinations were used: pure mode I-opening fracture, by applying identical moments to the DCB arms; pure mode II-shear fracture, by applying symmetric moments to the DCB arms; and mixed mode-opening and shear fracture, by applying a moment to one arm and leaving the other arm free.

Table P3.1: Double cantilever beam material properties.

Composite Material		Adhesive
Triaxial Fabric (Composite)	Uniaxial Fabric (Composite)	Elastic
$E_1 = 44.3$ GPa	$E_1 = 23.8$ GPa	$E = 4.56$ GPa
$E_2 = E_3 = 12.9$ GPa	$E_2 = E_3 = 15.05$ GPa	$\nu = 0.35$
$\nu_{12} = \nu_{13} = \nu_{23} = 0.23$	$\nu_{12} = \nu_{13} = \nu_{23} = 0.513$	
$G_{12} = G_{13} = G_{23} = 4393$GPa	$G_{12} = G_{13} = G_{23} = 4.393$GPa	

Interface (Cohesive Law)		
Penalty Stiffness	Damage (Quadratic stress)	Damage Evolution
$K = 4.2\,E12$ Pa;	$\sigma_n = 2.64$ MPa (Mode I)	$\delta_{c1} = 1.4$ (Mode I)
	$\sigma_t = 22.15$ MPa (Mode II)	$\delta_{c2} = 0.37$ (Mode II)

Figure P3.11: FEM simulation of different fracture modes in a DCB specimen.

A minimum of 10 cohesive elements inside the active fracture process zone is suggested by some authors [25, 26]. Using too few elements will introduce error in the crack growth resistance (fracture energy) calculation; however, finer meshes require more computational resources. Moreover, the mesh should be sufficiently fine to accurately represent the cohesive zone and the stress/strain variation along the grating length. An example of a coarse mesh is shown in Fig. P3.12. The stress and strain are not correctly represented along the grating length, leading to an inaccurate prediction of the sensor output.

A mesh resolution and result convergence study was conducted, as presented in Table P3.2. The maximum stress σ_y that is possible to measure along the sensor length (*10 mm*) and the maximum strain variation $\Delta\varepsilon_{xx}$ at the crack tip were analysed. Based on this analysis, a cohesive element size of 0.5 *mm* was selected, which meets the minimum element number requirement and provides a good stress and strain resolution along the sensor length.
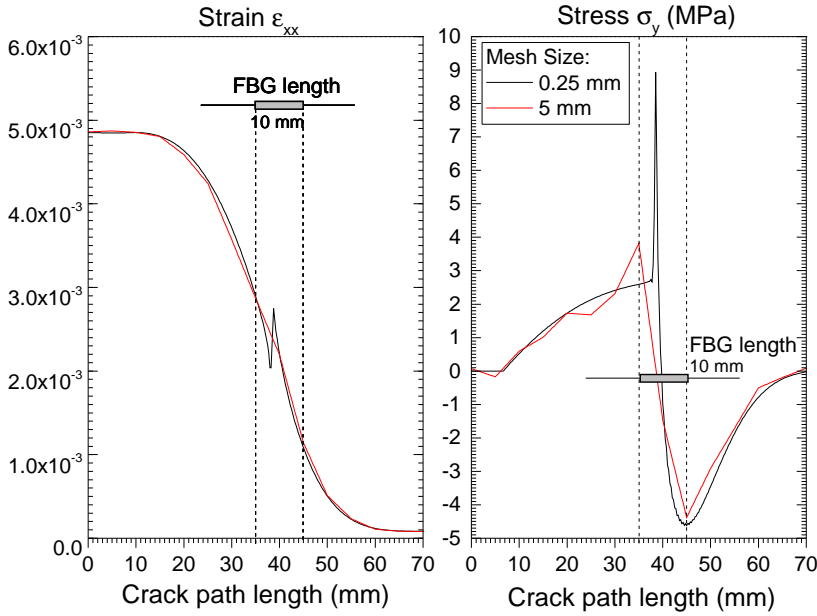
Figure P3.12: Mesh resolution study: cohesive zone and the stress/strain variation along the grating length.

Table P3.2: Mesh resolution and result convergence study.

Element size(mm)	Mode I		Mode II	
	Max σ_y(MPa)	Max $\Delta\varepsilon_{xx}$(%)	Max σ_y(MPa)	Max $\Delta\varepsilon_{xx}$(%)
5.0	3.81	0	1.29	0
3.8	3.78	0	2.36	0.012
1.0	6.27	0.2	5.55	0.022
0.5	7.84	0.7	10.13	0.82
0.25	7.88	0.71	10.67	0.87

P3.4.2   FBG Response Model: Crack Detection/Prediction

One of the goals of this article is to develop a numerical model for predicting the FBG output in a general crack growth situation, thus making it possible to use this *material-structure-sensor* model as a design tool, and to study the application of this monitoring technology in different composite material structures/locations.

To accomplish this goal, an algorithm was developed using *Python* and incorporated into the FEM model, as shown in Fig. P3.13. The algorithm was developed as a post-processing tool that uses the stress σ and strain ε state at the grating positions as input. In the first step, the algorithm synchronises the stress, the strain, and the crack tip position with the virtual grating positions. Then, the algorithm computes the wavelength shift $\Delta\lambda$ and width variation of the reflected peak $\Delta\lambda_{WV}$ versus the crack position for each virtual grating using the equations developed in this article.
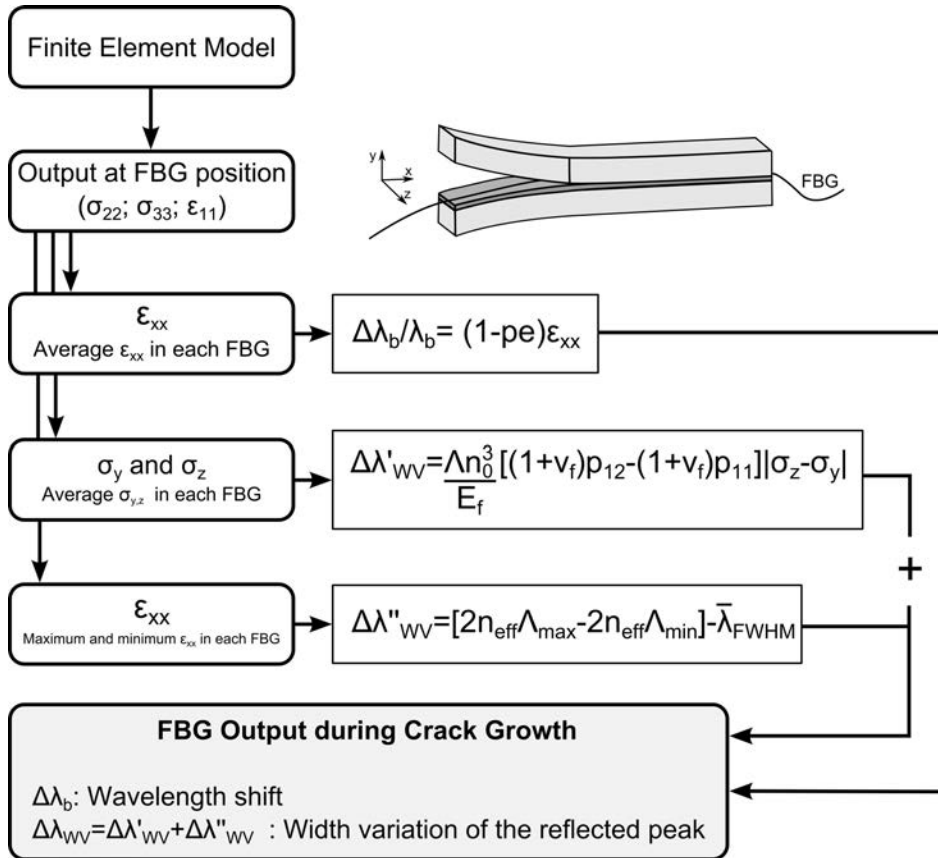
Figure P3.13: Algorithm applied to the FEM model to obtain the FBG output prediction.

Some assumptions were made to compute the contribution of each fracture phenomenon to the sensor response. In a real application, the grating has a finite length, generally 8-10 mm; however, the FEM technique discretised the grating into finite parts or elements. Thus, to compute the wavelength shift $\Delta\lambda_b$, which only depends on the global state of strain ε_{xx} around the grating, the average strain ε_x in the elements at the position of the virtual grating was used. Similarly, to compute the width variation of the reflected peak due to the compressive strain $\Delta\lambda'_{WV}$, the average stress in the transverse direction σ_y and $\sigma_z$ at the virtual grating position was used. To compute the non-uniform strain contribution to the reflected peak width variation $\Delta\lambda''_{WV}$, a linear strain variation was assumed, using the maximum and minimum strain values along the elements in the virtual grating position. In reality, the strain distribution follows a polynomial curve, which depends on the material, geometry and crack shape. However, this approximation can be considered good due to the small size of the sensor. The final width variation $\Delta\lambda_{WV}$ value is obtained by simply adding both contributions: the non-uniform strain ($\Delta\lambda''_{WV}$) and the transverse stress ($\Delta\lambda'_{WV}$). The *Python* script used to calculate the sensor response from the FEM model is shown in Supporting information (**P3-S1 File**).

Description of the Sensor Response FEM Model

In the FEM model, pure mode I, pure mode II and mixed mode were simulated to represent different crack growth conditions. An FBG array of 5 gratings was defined as virtual measurement points, each with a *10 mm* length and spaced *10 mm* from each other. The first grating was placed 10 mm from the beginning of the adhesive, as shown in Fig. P3.14. The FBG array was placed between the interface of the composite material and the structural adhesive. Table P3.3 lists the parameters of the optical fibre used to implement the algorithm.

Table P3.3: Fibre Bragg Grating Parameters.

Parameters:	
λ_b- Initial wavelength	From manufacturer (Ex:1528.81;1541.31; 1554.25;1567.12;1580.24 (nm))
L- FBG length	10 (mm)
$n_{eff,0}$- Initial refractive Index	1.45
p_e- Photo-elastic coefficient	0.215
p_{11}- Photo-elastic coefficient [20]	0.121
p_{12}- Photo-elastic coefficient [20]	0.270
E_f- Elastic modulus of FBG	75 GPa
ν_f- Poisson's ratio of FBG	0.17
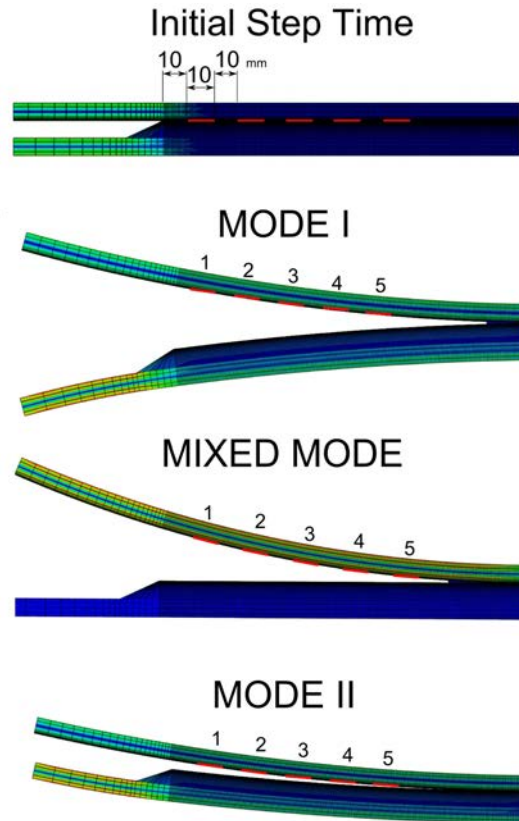
Figure P3.14: FBG measurement point in the FEM model.

P3.5   Numerical Simulation of the FBG Sensor Output During Crack Growth

In Fig. P3.15, the numerical simulation of the FBG output response for a crack growing in a DCB specimen is shown.

The plots in the left column represent the wavelength shift $\Delta\lambda_b$ caused by the longitudinal strain ε_{xx}. The plots in the right column represent the width variation of the reflected peak $\Delta\lambda_{WV}$ caused by the fracture/damage phenomenon near the grating. Different fracture modes were addressed, namely, Mode I, Mixed Mode and Mode II in the first, second and third plot rows, respectively. The wavelength shift $\Delta\lambda_b$ and the width variation of the reflected peak $\Delta\lambda_{WV}$ vs. crack tip position (CTP) were plotted in all figures. At each abscissa point (CTP), the output values of the 5
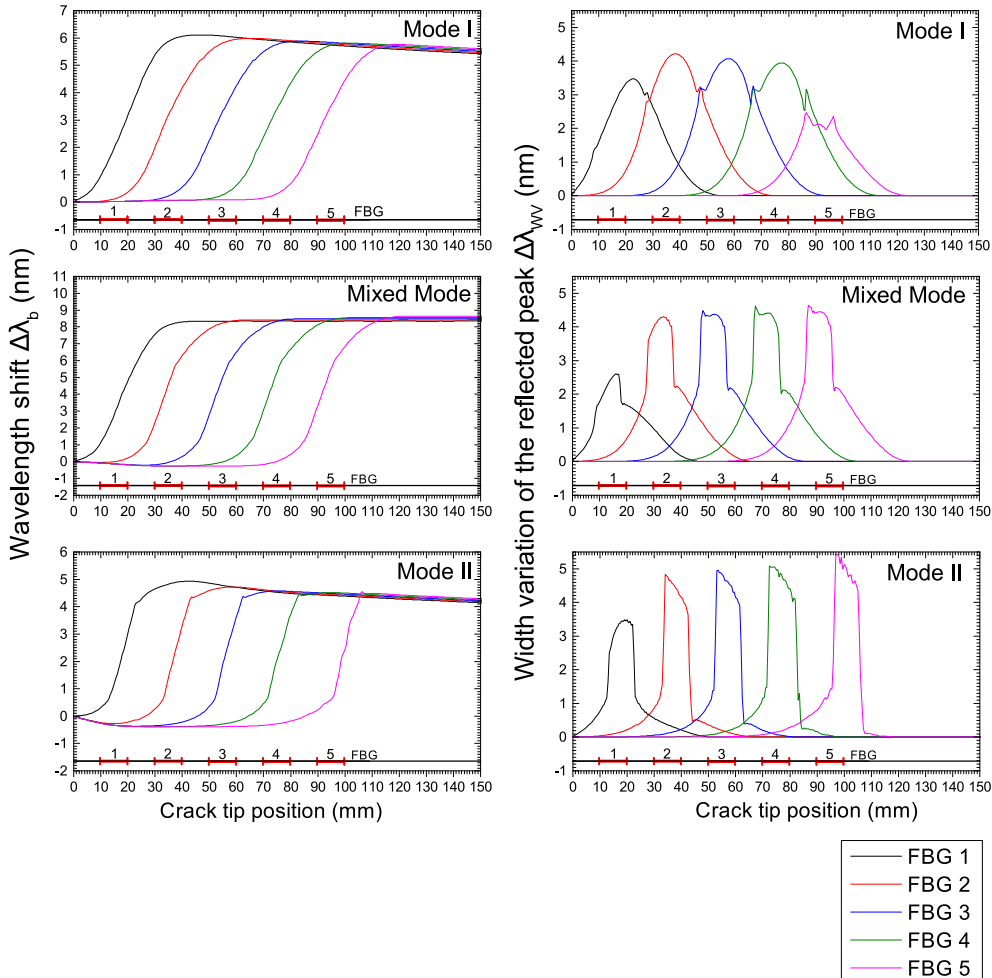
Figure P3.15: FBG sensor output simulation under crack growth: Mode I, II and mixed Mode fracture.

FBG sensors in that specific crack position are presented. A jump in the wavelength shift $\Delta\lambda_b$ was observed when the crack passed the position of the grating. The damage/crack changes the local compliance of the material and load distribution, making the area that surrounds the sensor less stiff and more deformed; therefore, an increase in the strain was measured. However, it is possible to observe some differences in the evolution (shape) of the wavelength shift $\Delta\lambda$ because the position of the sensor and the crack related to the applied moments is different.
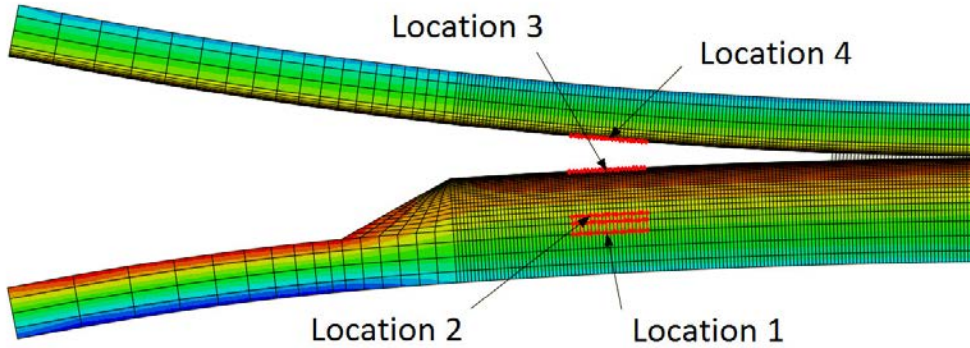
Figure P3.16: FBG sensor position analysis scheme.

The model predicted that a variation in the width of the reflected peak $\Delta\lambda_{WV}$ will occur when the crack is near the grating, in which the original peak width is restored after the crack passes the grating. The width variation response in all cases showed the same evolution pattern, exhibiting a loading- and geometry-independent behaviour. The magnitude of the differences of the $\Delta\lambda_{WV}$ in mode II is related to the fracture material properties, i.e., the fracture resistance in mode II is higher than that in mode I. This means that the stress distribution during crack growth in mode II is different, creating a higher strain variation. The differences observed in the $\Delta\lambda_{WV}$ response for the FBG *5* in Mode I, FBG *1* in Mode II, and FBG *1* in Mixed Mode are due to the effect of the model boundary conditions.

As previously discussed, this *material-structure-sensor* can be used as a tool for studying the application of this monitoring technology in different locations or structures. A grating position analysis scheme is presented in Fig. P3.16. Four positions were analysed: bottom composite laminate, bottom adhesive-composite interface, top adhesive-composite interface, and top composite laminate for Mode I and Mode II fractures. The sensor response for each position is shown in Fig. P3.17. As expected, in Mode I fracture (Fig.P3.17a)), the gratings located closer to the crack tip measure higher magnitude values. However, placing the sensor close to the crack can be technically difficult or even increase the probability of damaging the sensor during crack growth.
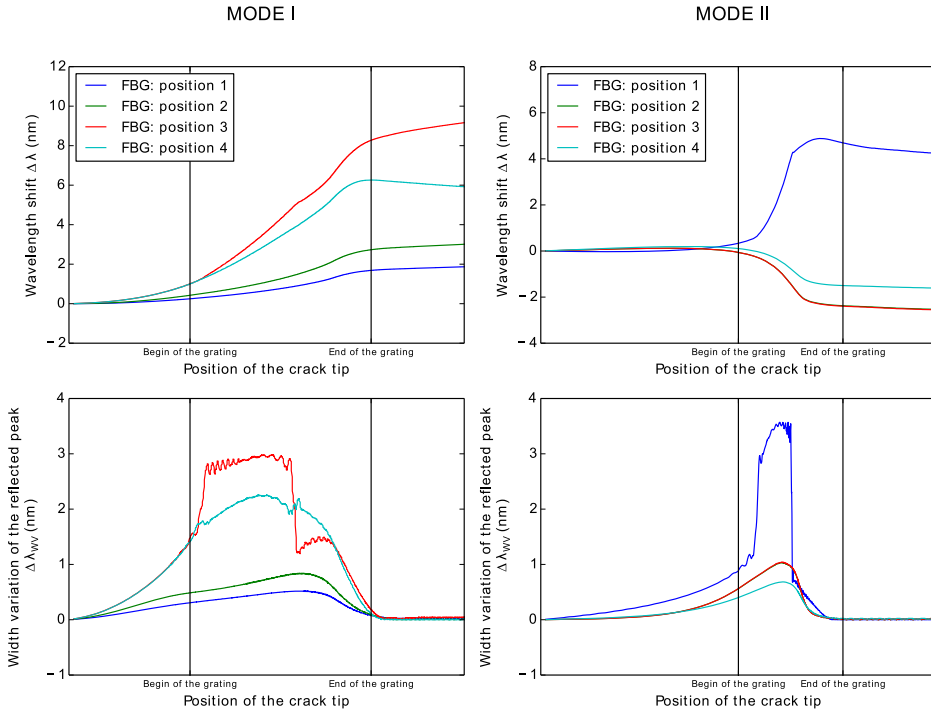
Figure P3.17: FBG sensor position analysis. a)Sensor output for Mode I fracture; b)Sensor output for Mode II fracture.

This analysis revealed that the sensor in position 2 (interface) can confidently detect damage because the common resolution of measurement equipment is approximately 0.01 nm and ensure the structural integrity of the sensor by increasing the distance from the crack surface. In Mode II fracture (Fig. P3.17b)), the sensor in position 1 showed a greater magnitude of $\Delta\lambda_b$ and $\Delta\lambda_{WV}$. This result is because at position 1, the sensor is more distant from the bending neutral-axis, consequently deforming more, $\varepsilon_{xx} \to \Delta\lambda_b$, and experiencing a larger amount of non-uniform strain, $\varepsilon_{xx}(x) \to \Delta\lambda_{WV}$.

Note that the sensor output $\Delta\lambda_{WV}$ showed a variation in the signal that depends on the location of the crack and the loading type. However, for the width variation of the reflected peak $\Delta\lambda_{WV}$, the sensor showed the same behaviour for different fracture modes, presenting a loading-independent behaviour. This makes $\Delta\lambda_{WV}$ **a key parameter for detecting cracks** in composite material structures.

P3.6 Model Experimental Validation

P3.6.1 Material and Experimental Procedure

To measure the FBG sensor response under a crack/delamination situation, double cantilever beam specimens with embedded fibre Bragg grating sensors were subjected to a controlled fracture progression. A special effort was made to identify specific fracture features, such as compression stress and non-uniform fields, during the crack growth.

P3.6.1.1 Loading and Fracture Modes

The three different combinations of forces that can cause a crack to grow are presented in Fig. P3.18. Mode I crack: opening mode, by tensile stress normal to the plane of the crack. Mode II crack: shear mode, by shear stress acting parallel to the plane of the crack and perpendicular to the crack front. Mode III: tearing mode, by shear stress acting parallel to the plane of the crack and parallel to the crack front.

Nominal mode mixity or phase angle, ψ_{nom}, is a parameter that defines the ratio of Mode I and Mode II [27],

$$\psi_{nom} = tan^{-1}\left(\frac{K_{II}}{K_I}\right) \tag{P3.14}$$

where K_{II} and K_I are the mode II and mode I stress intensity factors, respectively.
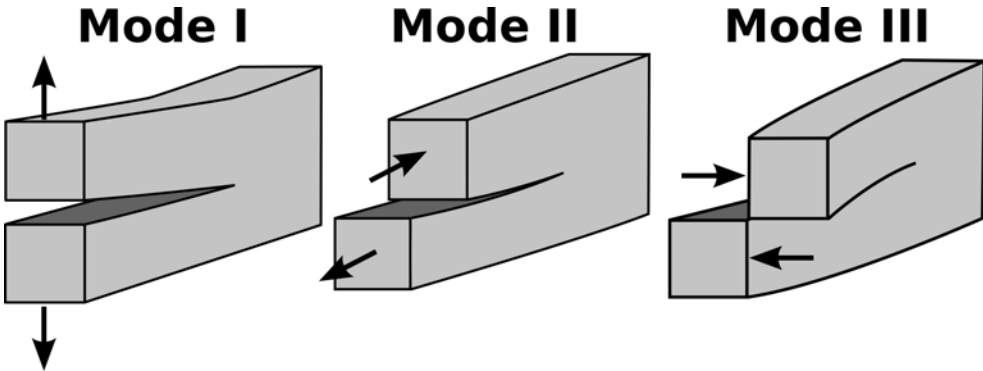
Figure P3.18: Scheme of the three modes of loading that can be applied to a crack.
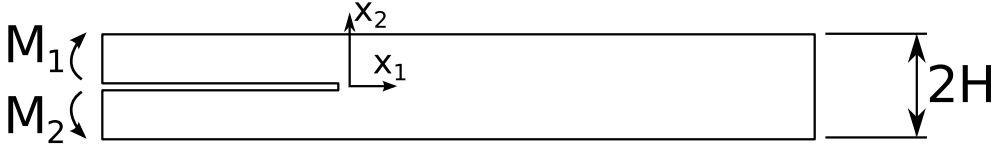
Figure P3.19: Homogeneous mixed mode specimen scheme.

For a homogeneous specimen without considering the adhesive layer, as shown in Fig. P3.19, the parameter ψ_{nom} can be defined as [28],

$$\psi_{nom} = tan^{-1}\left(\frac{\sqrt{3}}{2}\frac{M_1 + M_2}{M_1 + M_2}\right) \qquad (P3.15)$$

where M_1 and M_2 are the moments applied to the top and bottom arms, respectively. The mixed mode ratio ψ_{nom} can be defined by the ratio of the moments applied to the DCB arms (M_1/M_2). For pure Mode I (opening fracture $\psi_{nom} = 0°$), when the moments are the same and applied in opposite directions, $M_1 > M_2$ and $\| M_1 \| = \| M_2 \|$, and for pure Mode II (shearing fracture $\psi_{nom} = 90°$), when the moments are the same and applied in the same direction, $M_1 = M_2$.

The three different fracture modes used to conduct the experiments were as follows: pure Mode I, opening fracture $\psi_{nom} = 0°$; pure Mode II, shear fracture $\psi_{nom} = 90°$; and mixed mode I/II, with a phase angle of $\psi_{nom} = 68°$. The experiments were conducted with a constant displacement rate of the lower beam of the test machine of 2.5 mm/min [29].

P3.6.1.2   Fracture Testing Procedure

To correctly evaluate the different stages in the FBG response, a stable and controlled crack growth is required. However, the standard test methods used to characterise the macroscale fracture energy provide an unstable crack growth, particularly in Mode II loading. To overcome this, the fracture test machine developed by Sørensen [29], shown in Fig. P3.20, was used. In this testing apparatus, the loading is applied through moments, providing a stable crack growth in the range of mode I to Mode II. Moreover, this testing apparatus allows the test to be stopped without decreasing the applied load, making it possible to perform measurements in a process that simulates continuous crack growth conditions.

To perform the loading, wires apply an equal transverse force to the transverse arms, which are attached to the DCB beams. The position where the wires are connected to the transverse arms defines the moments applied to each DCB beam, meaning that different wire positions will provide different loading types, from pure Mode I to pure Mode II. The force in the wires is measured by two load cells. One extensometer and two LVDTs (linear variable differential transformers) measure the crack face opening and sliding in the DCB specimen.
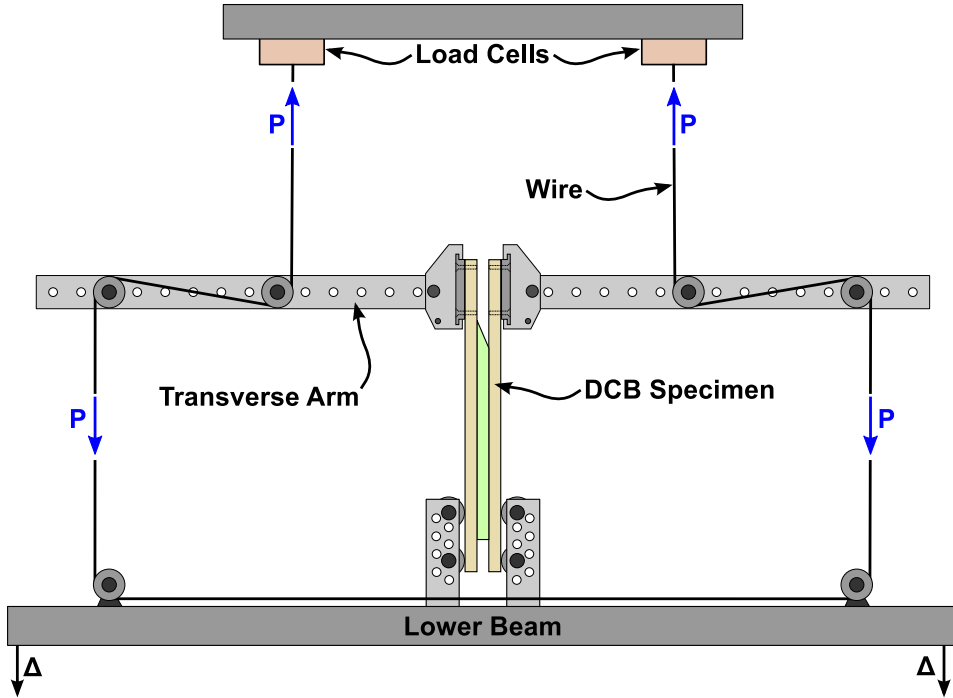
Figure P3.20: Schematic illustration of the double cantilever beam test set-up.

P3.6.1.3   DCB Specimen Manufacturing

Two plates with dimensions of 700×1000 mm and a thickness of approximately 7 mm were produced using multiaxial glass fibre. Ten layers of fabric per plate were used, consisting of two triaxial fabrics (Saertex Triax S32E4590) as skin layers and eight unidirectional central layers (Saertex S35EU910). The layup stacking of the laminates was $[90/+45/-45/0_4/0_4/+45/-45/90]$, and the backing of the unidirectional layers was facing outwards, away from the central plane. The plates were made by hand lay-up of dry fibre fabric, followed by epoxy impregnation (Momentive-Epikote/Epikure-100:30) by vacuum infusion at 50°C for 5 hours and post-curing at 80°C for 3 hours. The plates were glued using a commercial structural adhesive (Momentive-Epikote/Epikure MGS BPR 135G/137G), and 7 mm spacers were used to obtain a well-defined specimen thickness and geometry. A thin slip foil was placed on the edge of the structural adhesive to act as a pre-crack and ease crack initiation.

An array of 5 uncoated single-mode FBG sensors (5 gratings in one optical fibre), with a length of 10 mm, were embedded in the interface of the laminate plate with the structural adhesive. The gratings in the array were spaced 10 mm from each other, and the first grating was positioned 10 mm from the edge of the adhesive.
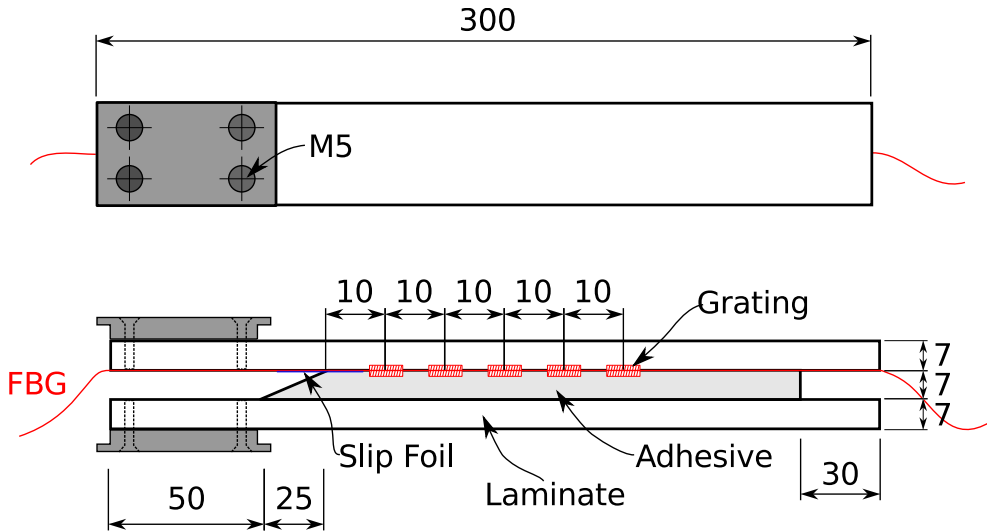
Figure P3.21: Sketch of the specimen geometry and FBG sensor position.

Five specimens, 30 mm in width, were cut from the sandwich plates. Steel parts were fixed to each beam by 4 steel screws (M5) by an epoxy adhesive (Scotch-Weld DP 460 from 3M, hardened at 40°C for two hours). The DCB dimensions, different components, and fibre grating locations are shown in Fig. P3.21.

P3.6.2   Measurement Technology

P3.6.2.1   Digital Image Correlation Technique

The digital image correlation (DIC) technique was used during the DCB fracture testing to determine the presence of specific phenomena caused by the crack, such as non-uniform strain or transverse stress, and correlate it with the FBG sensor output. The DIC technique is a non-contact optical method that can correlate the deformation/strain in a material by tracking changes in a random pattern on the specimen.

A pattern was painted on the side surface of the DCB specimen, as shown in Fig. P3.22, and ARAMIS[TM] V6.3 software was used to calculate the strains in each measurement. To perform the measurements, ARAMIS recognises the surface pattern in the unloaded specimen and allocates coordinates to the image pixels. Then, ARAMIS compares the pattern in the loaded specimen picture and, by tracking the changes, calculates the displacement and consequently the strain distribution in the specimen face. The facet parameters used for strain calculation were 60×60 pixel
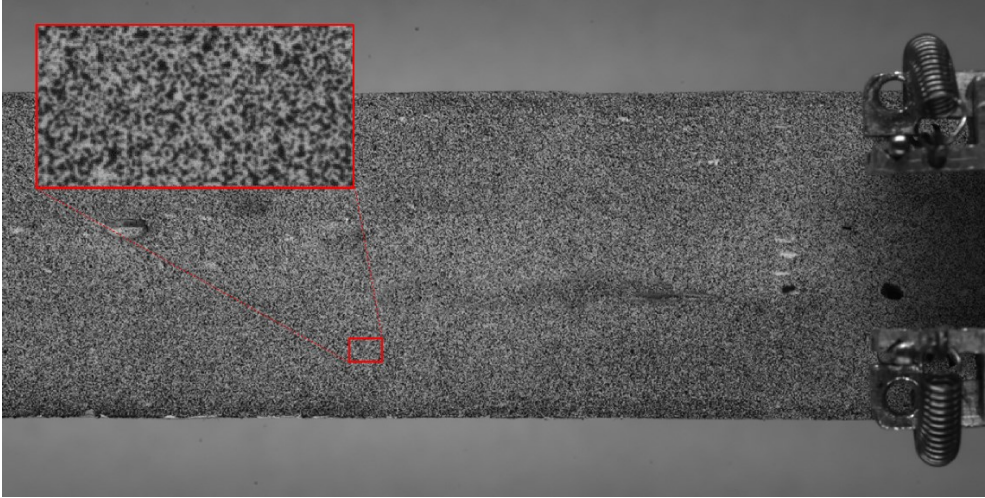
Figure P3.22: DIC pattern painted on the side surface of the DCB specimen.

facets with a facet step of 15 pixels, which corresponds to a 45 pixel overlapping area [30].

P3.6.2.2 Fibre Bragg Grating Optical Spectral Analyser System

The FBG sensor was connected to an optical spectral analyser (OSA) *FS2200- Industrial BraggMeter* from FiberSensing[TM] [31]. Each measurement performed by the OSA is a file with 20000 points, corresponding to the reflected light spectrum for the bandwidth from 1500 to 1600 nm. To manage this amount of data, an algorithm using *Python* was developed that computes from the reflected spectrum the wavelength shift $\Delta\lambda_b$ and the increase in width of the reflected peak $\Delta\lambda_{WV}$. Similar to the DIC technique, the algorithm uses the first reflected optical spectrum, measured in the unloaded specimen, to calculate the variation in the wavelength shift and increase in reflected peak width for each measurement (see Fig. P3.23).

To calculate the wavelength shift $\Delta\lambda_b$, the algorithm detects the maximum reflected optical power of each grating and then computes $\Delta\lambda_b$ in relation to the original reflected peak. If the reflected peak is distorted or shows a split shape, the algorithm interpolates $\Delta\lambda_b$ between the maximum points in the grating bandwidth and the last maximum peak before the split occurred. To calculate the width of the reflected peak λ_{WV}, the algorithm determines the maximum and minimum reflected optical power for each grating and measures the peak width at half maximum optical power $((maximum + minimal)/2)$. It then computes the width variation of the reflected peak $\Delta\lambda_{WV}$ relative to the original reflected peak width.
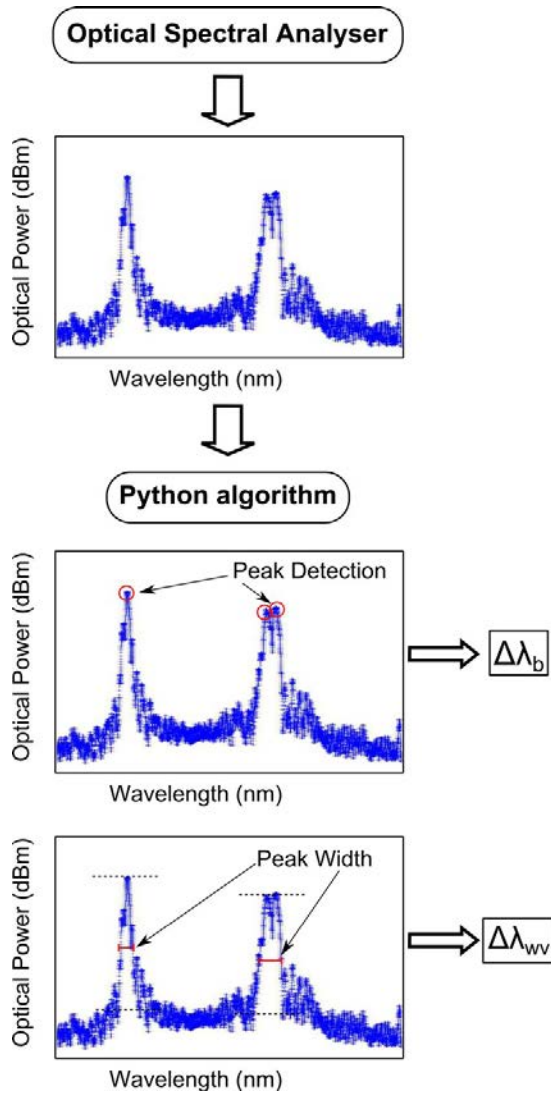
Figure P3.23: Algorithm for calculating the wavelength shift $\Delta\lambda_b$ and the width variation of the reflected peak $\Delta\lambda_{WV}$ from the reflected optical spectrum.
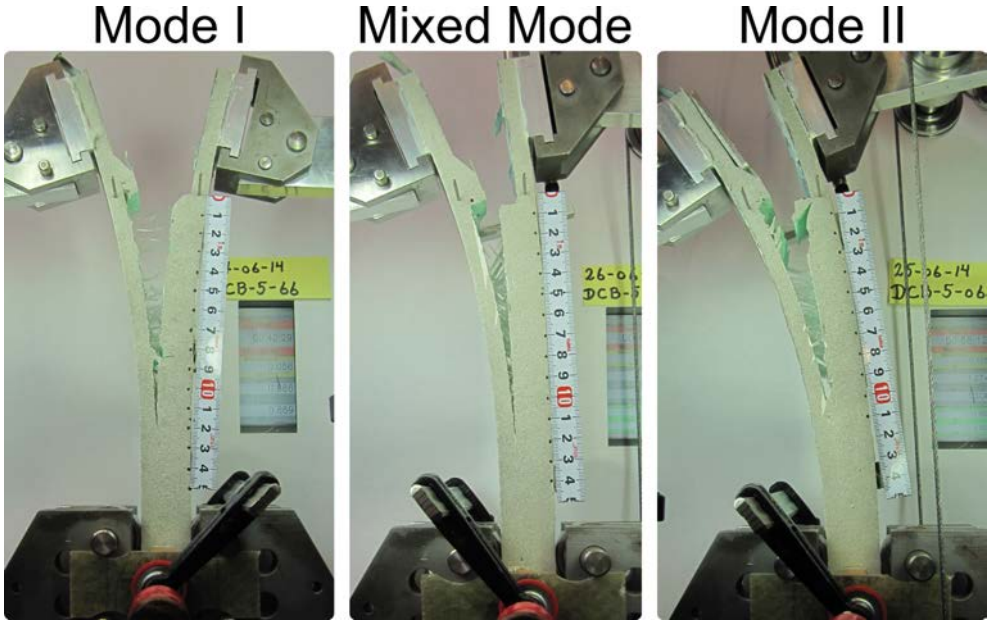
Figure P3.24: Fracture modes addressed in the DCB testing.

P3.7 Experimental Results and Discussion

Three DCB specimens loaded with different fracture modes, namely, Mode I ($\psi_{nom} = 0°$), Mode II ($\psi_{nom} = 90°$), and Mixed Mode ($\psi_{nom} = 68°$), are shown in Fig. P3.24. The type of fracture mode performed for each DCB specimen is described in Table P3.4.

Table P3.4: Fracture Modes Tested.

DCB specimen	1	2	3	4	5
Fracture Mode	I/II	I	I	I	II
	I				I/II
	II				I

In specimens 1 and 5, an initial fracture test was performed until the crack reached the middle of the FBG array. Then, the test was restarted with a different fracture mode to simulate a change in the loading conditions and evaluate the ability of the sensors to measure a crack independent of the loading configuration.
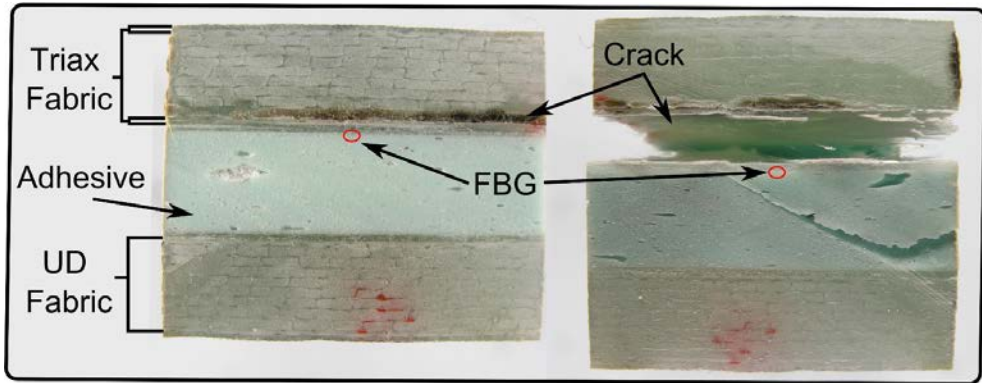
Figure P3.25:   Crack face in the DCB specimen.

A critical issue found when using FBG sensors embedded in the FRP material is the possibility of damaging the sensor. If the crack changes it path direction and crosses the optical fibre, this will cut the signal, losing all the gratings ahead of that point. To avoid this situation, crack initiation between the triaxial laminate and the unidirectional laminate was promoted by using a thin slip foil, as shown in Fig. P3.25. Thus, the FBG sensor was *0.3-0.4 mm* away from the crack face, protected from any damage, as long as the crack did not change direction. As planned, the crack followed the predicted path for the Mode II and mixed mode testing. However, the crack did change direction during the test of specimens 2, 3 and 4 under Mode I, losing some of the gratings during the propagation of the crack. Nevertheless, sufficient data was acquired during these tests, allowing the validation of the structure-material-sensor model in mode I fracture.

The FBG response and DIC strain measurements during crack growth in a DCB specimen are shown in Fig. P3.26. The reflected peak of the Bragg grating that is situated closer to the adhesive edge corresponds to FBG 5, with an original reflected peak of $\lambda_b = 1580$ nm. All the different crack features/phenomena that can change the shape of the reflected peak were identified and correlated with a specific FBG response. The left row pictures are DIC measurements, where the top shows the negative component of strain in the y direction, ε_y ("compression" strain), and the bottom shows the strain in the x direction, ε_x.

The blue spot in the top DIC measurements is the compression field ε_y formed ahead of the crack tip. The colour gradient in the bottom DIC measurements is the indication of longitudinal variation of strain that moves with the crack tip.

By analysing the three figures, it is possible to identify all the different stages in the sensor response during crack growth, as described previously. In Fig. P3.26a), before the crack reaches the proximity of the grating, the material accumulates uniform strain. This induces a uniform wavelength shift in the sensor response, from $\lambda_{b,0} =$
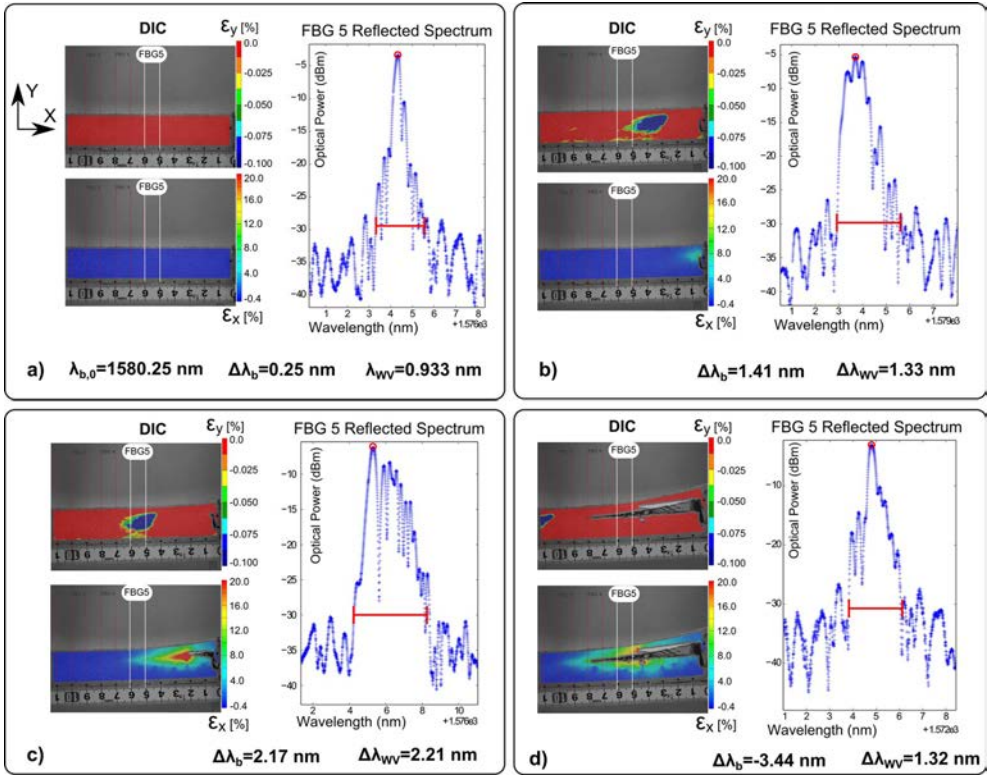
Figure P3.26: FBG sensor output during crack growth in Mode II. a) Before crack initiation; b) crack growth: compression field at grating position; c) crack growth: non-uniform strain at grating position; and d) crack growth and passing all grating length.

1580.00 nm to $\lambda_b = 1580.25$ nm. Next, the compression field formed ahead of the crack tip reaches the grating area. This modified the shape of the reflected peak to a split peak shape, with a peak width increase of $\Delta\lambda_{WV} = 1.33$ nm, as shown in Fig. P3.26b). Additionally, an increase in the wavelength shift, $\Delta\lambda_b = 1.41$ nm, was measured, which was caused by the loading increase that consequently increased the strain in the specimen. If the crack continues to grow, the grating will gradually experience the influence of the crack singularity (region dominated by stress concentration), which creates a non-uniform strain distribution around the sensor length. This non-uniform strain will create a change in the reflected peak shape, where multiple reflected peaks appear and the peak width increases $\Delta\lambda_{WV} = 2.21$ nm, as shown in Fig. P3.26c). Following the previous stages, an increase in the

wavelength shift was measured, $\Delta\lambda_b = 2.17\ nm$, which was caused by the continuous load increase. Finally, after the crack passed the grating full length, the reflected peak width decreased, $\Delta\lambda_{WV} = 1.32\ nm$, and the shape of the reflected peak gradually recovered its original shape, as shown in Fig. P3.26d). However, the wavelength shift continued to vary, $\Delta\lambda_{WV} = -3.44\ nm$, following the increase of load and strain in the specimen.

Due to the large quantity of data saved during the fracture tests, it is impossible to present all the results in this article. However, to provide the reader with a better understanding of the crack detection technique, three movies from the three fracture modes tested **(S1 Video, S2 Video and S3 Video)** are presented in the *Supporting Information in the article*[1]. In each movie is shown the reflected spectrum from the FBG array, a picture of the specimen during the test, and the DIC results, synchronised with the wavelength shift $\Delta\lambda_b$ and peak width variation $\Delta\lambda_{WV}$ measured during the test.
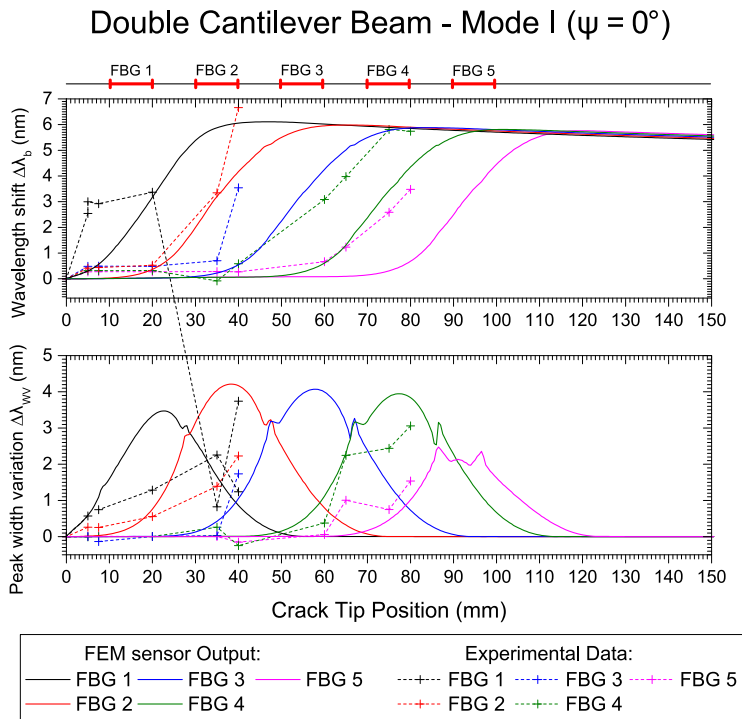
Figure P3.27: Embedded FBG sensor output in a DCB specimen under Mode I fracture testing: numerical and experimental results.

The Mode I, Mode II and Mixed Mode fracture testing experimental results are compared with the numerical simulation in Figs. P3.27, P3.28 and P3.29. The wavelength shift $\Delta\lambda$ and width variation of the reflected peak $\Delta\lambda_{WV}$ were computed from the measured reflected spectrum given by the OSA of the Braggmeter using the developed algorithm. The crack tip position was calculated using the DIC technique.
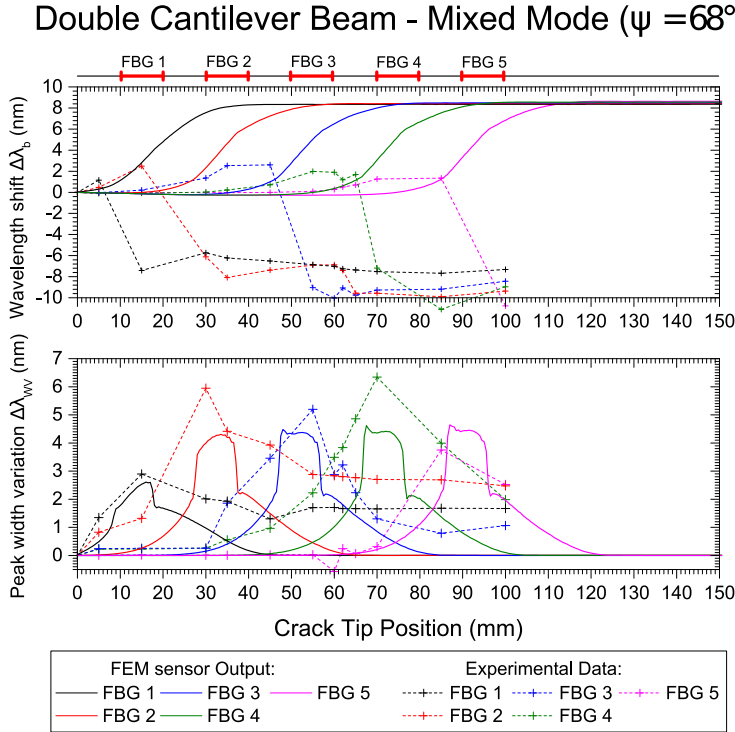
Figure P3.28: Embedded FBG sensor output in a DCB specimen under Mixed Mode fracture testing: numerical and experimental results.

Note that the goal of this technique is to detect cracks, not to quantify stress or strain. Thus, the magnitude of the measured values can vary, but the information obtained that is used to determine the presence of the crack is accurate. With this, a good agreement between the experiments and simulation was found.

The wavelength shift, $\Delta\lambda_b$, difference between the experimental results and the numerical prediction is due to the loading and geometric dependency of this parameter; i.e., small variations in the position of the sensor or a different crack growing path can vary the measured strain. For the Mode II and Mixed Mode cases, the path of the crack shifts during the test, changing the position of the grating from the top crack face to the bottom face, as shown in Fig. P3.25. This causes a change in the measured strain, $\Delta\lambda_b$), from positive to negative. However, in terms of absolute
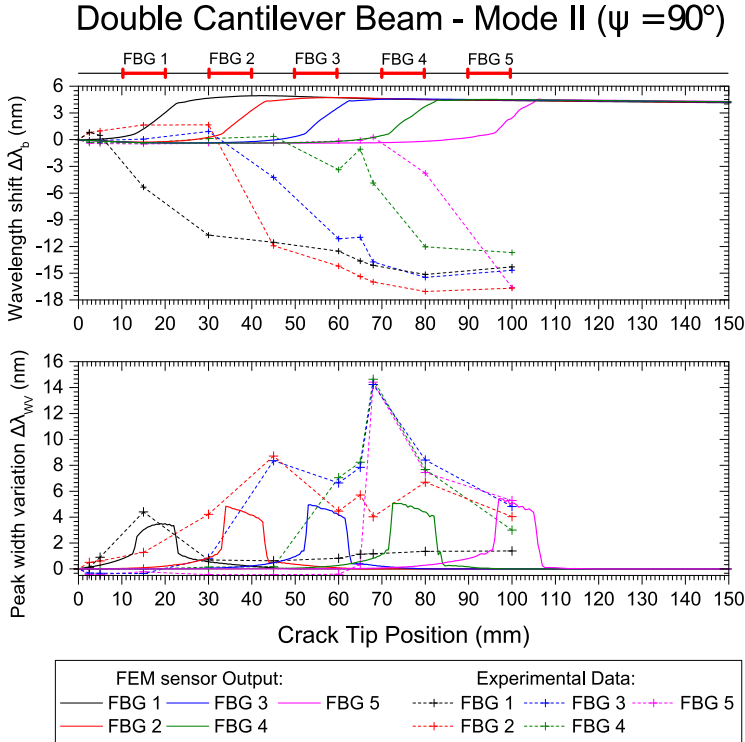
Figure P3.29: Embedded FBG sensor output in a DCB specimen under Mode II fracture testing: numerical and experimental results.

values, both cases exhibited the predicted behaviour.

As previously discussed, the main advantage of this monitoring technique is the use of two different FBG output parameters, $\Delta\lambda_b$ and $\Delta\lambda_{WV}$, to determine the presence of the crack and to track its growth. The wavelength shift, $\Delta\lambda_b$, is a parameter related to the strain level in the structure, but it is dependent on the loading and geometry configuration. This can be observed in mode I loading, where an increase of $\Delta\lambda_b$ is observed, and in Mode II/Mixed, where a decrease in $\Delta\lambda_b$ occurs. However, the rapid increase in the magnitude of $\Delta\lambda_b$ is caused by a damage event that reduces the stiffness of the structure. In contrast, the width variation of the reflected peak, $\Delta\lambda_{WV}$, is a parameter that only depends on the presence of a crack, independent of geometry and loading type. The width of the reflected peak, $\Delta\lambda_{WV}$, increases when the crack is near the grating area, being low in magnitude before and after the crack passes. In summary, these two parameters are a good indicator of the presence of cracks, and a structural health monitoring system based on FBG sensor technology needs to evaluate both variables to accurately detect such damage.

As an example of this crack detection methodology, refer to Fig. P3.28, when the crack tip is at 50 mm (beginning of FBG3). The value of $\Delta\lambda_b$ is larger for FBG1 and FBG2; the FBG3 $\Delta\lambda_b$ value is starting to increase; and the FBG4 and FBG5 $\Delta\lambda_b$ values are still low. This indicates that the compliance of the material is changing in location 3. However, the value of $\Delta\lambda_{WV}$ is higher for FBG3 and FBG4, and it is lower for FBG1, FBG2, and FBG5. This result indicates that these two locations, 3 and 4, are experiencing specific fracture features ahead of the crack tip (compression and non-uniform strain). Using this information, we can confidently predict the crack position, which has already passed positions 1 and 2 and is located at position 3.

P3.8   Summary and Conclusions

Inspired by the change in the "conventional" structure design philosophy to a damage tolerant structural design, through the use of damage tolerant materials combined with structural health monitoring techniques, an approach to detect damage in structures composed of composite materials and structural adhesive was outlined in this paper. This concept will eventually lead to a condition monitoring-maintenance, which consists of the detection of damage by sensors, characterisation of damage (type and size), and model predictions of residual life that will enable decision-making with respect to whether a structure should be repaired or replaced.

The ability of fibre Bragg gratings embedded in composite materials to detect and track cracks/delamination by identifying the response of a sensor to a specific fracture/damage phenomena was demonstrated. Three different mechanisms that can change the sensor output, namely, longitudinal strain ε_{xx}, transversal stress $\sigma_{y,z}$ and non-uniform strain $\varepsilon_{xx}(x)$, were described and linked with the different damage mechanisms that occur during a crack growth event. These different measurement concepts were incorporated into a finite element model of a delamination of a double cantilever beam to simulate the sensor output under different conditions. Using this technique, it becomes possible to extract information from the sensor output that is independent of the loading type, structure geometry and boundary conditions, depending only on the proximity of the crack and the material properties.

The *material-structure-sensor* model can be used as a design tool for applying this monitoring technology in different composite material structures, predicting the sensor output, and determining the optimised sensor-structure configuration. As per the authors' vision, this *material-structure-sensor* model concept will make it possible to design structures in composite materials that can operate safely, even when in damaged conditions.

Acknowledgments

References

[1] R. Jones, *Mechanics of composite materials*, Second. Taylor & Francis, 1999, 519 s, ISBN: 156032712x, 9781560327127.

[2] D. Braga, S. Tavares, L. da Silva, P. Moreira, and P. de Castro, "Advanced design for lightweight structures: review and prospects," *Progress in Aerospace Sciences*, volume 69, page 29, April 2014, ISSN: 03760421. DOI: `10.1016/j.paerosci.2014.03.003`.

[3] M. McGugan, G. Pereira, B. F. Sørensen, H. Toftegaard, and K. Branner, "Damage tolerance and structural monitoring for wind turbine blades," *Philosophical Transactions of the Royal Society of London A: Mathematical, Physical and Engineering Sciences*, volume 373, number 2035, 2015, ISSN: 1364-503X. DOI: `10.1098/rsta.2014.0077`.

[4] B. Sørensen, *Cohesive laws for assessment of materials failure: Theory, experimental methods and application.* Risø-Technical Univ. of Denmark, Risø National Laboratory for Sustainable Energy. Materials Research Division, 2010, 243 s, ISBN: 9788755038271.

[5] B. F. Sørensen, "Cohesive law and notch sensitivity of adhesive joints," *Acta Materialia*, volume 50, number 5, pages 1053–1061, 2002, ISSN: 13596454. DOI: `10.1016/S1359-6454(01)00404-9`.

[6] I. Silversides, A. Maslouhi, and G. Laplante, "Interlaminar fracture characterization in composite materials by using acoustic emission," in *5th International Symposium on NDT in Aerospace*, Singapore, November 2013.

[7] C. Kyriazoglou, B. Le Page, and F. Guild, "Vibration damping for crack detection in composite laminates," *Composites Part A: Applied Science and Manufacturing*, volume 35, number 7-8, pages 945–953, Jul. 2004, ISSN: 1359835X. DOI: `10.1016/j.compositesa.2004.01.003`.

[8] H. Hu, B.-T. Wang, C.-H. Lee, and J.-S. Su, "Damage detection of surface cracks in composite laminates using modal analysis and strain energy method," *Composite Structures*, volume 74, number 4, pages 399–405, August 2006, ISSN: 02638223. DOI: `10.1016/j.compstruct.2005.04.020`.

[9] Y. Yan and L. Yam, "Online detection of crack damage in composite plates using embedded piezoelectric actuators/sensors and wavelet analysis," *Composite Structures*, volume 58, number 1, pages 29–38, 2002, ISSN: 02638223. DOI: `10.1016/S0263-8223(02)00043-0`.

[10] K. Hill and G. Meltz, "Fiber bragg grating technology fundamentals and overview," *Journal of Lightwave Technology*, volume 15, number 8, pages 1263–1276, 1997.

[11] R. Kashyap, *Fiber Bragg Gratings*, Second. Academic Press, 1999, ISBN: 15575837. DOI: `doi:10.1016/B978-012400560-0/50005-1`.

[12] K. Peters, M. Studer, J. Botsis, A. Iocco, H. Limberger, and R. Salath, "Embedded optical fiber bragg grating sensor in a nonuniform strain field: measurements and simulations," *Experimental Mechanics*, volume 41, number 1, pages 19–28, 2001.

[13] I. B. Lin Zhang W. Zhang, *In-Fiber Grating Optic Sensor, Fiber Optic Sensors*, Second, C. Press, Ed. CRC Press, 2008. DOI: `doi:10.1201/9781420053661.ch4`.

[14] L. Sørensen, J. Botsis, T. Gmür, and J. Cugnoni, "Delamination detection and characterisation of bridging tractions using long fbg optical sensors," *Composites Part A: Applied Science and Manufacturing*, volume 38, number 10, pages 2087–2096, October 2007, ISSN: 1359835X. DOI: `10.1016/j.compositesa.2007.07.009`.

[15] W. Zhang, W. Chen, Y. Shu, X. Lei, and X. Liu, "Effects of bonding layer on the available strain measuring range of fiber bragg gratings," *Applied Optics*, volume 53, number 5, page 885, February 2014, ISSN: 0003-6935. DOI: `10.1364/AO.53.000885`.

[16] F. Jülich and J. Roths, "Comparison of transverse load sensitivities of fibre bragg gratings in different types of optical fibres.," in *Proc. of SPIE: Optical Sensing and Detection*, volume 7726, April 2010, 77261N. DOI: `10.1117/12.854019`.

[17] F. Bosia, P. Giaccari, J. Botsis, M. Facchini, and H. G. Limberger, "Characterization of the response of fibre bragg grating sensors subjected to a two-dimensional strain field," *Smart Materials and Structures*, volume 925, number 12, pages 925–934, 2003.

[18] L. Sørensen, J. Botsis, T. Gmür, and L. Humbert, "Bridging tractions in mode i delamination: measurements and simulations," *Composites Science and Technology*, volume 68, number 12, pages 2350–2358, Sep. 2008, ISSN: 02663538. DOI: `10.1016/j.compscitech.2007.08.024`.

[19] S. Yashiro, T. Okabe, N. Toyama, and N. Takeda, "Monitoring damage in holed cfrp laminates using embedded chirped fbg sensors," *International Journal of Solids and Structures*, volume 44, number 2, pages 603–613, January 2007, ISSN: 00207683. DOI: `10.1016/j.ijsolstr.2006.05.004`.

[20]   X. Zhang, J. Max, and X. Jiang, "Experimental investigation on optical spectral deformation of embedded fbg sensors," *Proceedings of SPIE - the International Society for Optical Engineering, Photonics Packaging, Integration, and Interconnects VII*, volume 6478, 2007.

[21]   I. Bennion, J. Williams, L. Zhang, K. Sugden, and N. Doran, "Uv-written in-fibre bragg gratings," *Optical and Quantum Electronics*, volume 28, pages 93–135, 1996.

[22]   G. Alfano and M. A. Crisÿeld, "Finite element interface models for the delamination analysis of laminated composites: mechanical and computational issues," *International Journal for Numerical Methods in Engineering*, volume 50, number 7, pages 1701–1736, 2001.

[23]   V. N. Burlayenko and T. Sadowski, "Fe modeling of delamination growth in interlaminar fracture specimens," *Budownictwo i Architektura*, volume 2, pages 95–109, 2008.

[24]   ABAQUS™, *User Manual. Version 6.13, ABAQUS Inc., Pawtucket, Rhode Island, USA*. USA, 2013.

[25]   A. Turon, C. Dávila, P. Camanho, and J. Costa, "An engineering solution for mesh size effects in the simulation of delamination using cohesive zone models," *Engineering Fracture Mechanics*, volume 74, number 10, pages 1665–1682, 2007, ISSN: 00137944. DOI: `10.1016/j.engfracmech.2006.08.025`.

[26]   D. Álvarez, B. Blackman, F. Guild, and A. Kinloch, "Mode i fracture in adhesively-bonded joints: a mesh-size independent modelling approach using cohesive elements," *Engineering Fracture Mechanics*, volume 115, pages 73–95, 2014, ISSN: 00137944. DOI: `10.1016/j.engfracmech.2013.10.005`.

[27]   J. Rice, "Elastic fracture mechanics concepts for interfacial cracks," *Journal of Applied Mechanics*, volume 55, number 1, pages 98–103, 1988.

[28]   B. F. Sørensen, S. Goutianos, and T. K. Jacobsen, "Strength scaling of adhesive joints in polymer–matrix composites," *International Journal of Solids and Structures*, volume 46, number 3-4, pages 741–761, February 2009, ISSN: 00207683. DOI: `10.1016/j.ijsolstr.2008.09.024`.

[29]   B. Sørensen, K. Jørgensen, T. Jacobsen, and R. Østergaard, "Dcb-specimen loaded with uneven bending moments," English, *International Journal of Fracture*, volume 141, number 1-2, pages 163–176, 2006, ISSN: 0376-9429. DOI: `10.1007/s10704-006-0071-x`.

[30]   ARAMIS™, *User Manual. Version 6.3, GOM optical measuring Techniques, Mittelweg 7-8, D-38106 Braunschweig, Germany*. Germany, 2011.

[31]   FiberSensing™, *User Manual FS2200- Industrial BraggMeter v.1.3, FiberSensing - Advanced Monitoring Systems,Rua Vasconcelos Costa, 277,4470-640 Maia - Portugal*. Portugal, 2012.

Appendix P3-S1: *Python* script to calculate the FBG sensor response from the FEM model

```python
"""
Created by Gilmar Pereira---Contact email: gfpe@dtu.dk

This code is used as Abaqus Post-processing tool to predict the
FBG sensor output during crack Growth for a 2D Case.
"""
#Packages
import numpy as np
import scipy as sp
import sympy
import matplotlib.pyplot as plt
import math


"""
The code starts by loading the report files given by Abaqus.
Export 2 different files(sigma_22 and epsilon_11), using the path
    tool,
along the fiber optic position. This script will work for a 2D case.
For a 3D case, add a third file with the stress in the transverse
direction (sigma_33).
"""
#Load file sigma_22
filess22='filename_s22.txt'
#Load file epsilon_11
fileLE11='filename_E11.txt'
"""Script Input"""
#Size of elements (mm)
se=0.5
#Length of the grating(mm)
lg=10
#Number of gratings
ng=5
#Space between gratings(mm)
sbg=10
#Number of elements per grating
neg=lg*se

"""Optical Fiber input Parameters"""
#Original wavelength
LFBG=[1528.813*10**(-9),1541.317*10**(-9),1554.252*10**(-9),
        1567.121*10**(-9),1580.246*10**(-9)]


```

```python
42  #PhotoElastic Parameter
43  pe=0.215
44  #Initial refractive index
45  n0=1.45
46  #Optical fiber young's module
47  Ef=75*10**3
48  #Poisson's coefficient of the optical fiber
49  vf=0.17
50  #Directional refractive index parameters.
51  p11=0.121
52  p12=0.270
53  # Inital Grating period calculation
54  igp=[x/(2*n0) for x in LFBG]
55
56  """----------------------------------------------------------------
57  Loading Data: FBGX-Y; x- is the FBG number,
58  Y is the element number- starting from 0 to neg."""
59  names =('x',)
60  formats=('f8',)
61  for x in np.arange(ng,0,-1):
62      FBGref= 'FBG'+str(x)
63      for i in np.arange(neg,0,-1):
64          names= names + (FBGref+'-'+str(i),)
65          formats=formats+ ('f8',)
66  dtypes = {'names' : names,'formats': formats}
67  #Loading file
68  s22=np.loadtxt(filess22, dtype=dtypes,skiprows=5)
69  LE11=np.loadtxt(fileLE11, dtype=dtypes,skiprows=5)
70  """----------------------------------------------------------------
71  Calculation of the Wavelength shift - uniform strain contribution,
72  wlv: wavelength variation: average of the strain in the length
73  of the grating """
74  LEaverage={}
75  for b in range(1,ng+1):
76      LEaverage['FBG'+str(b)]= []
77  for a in range(0,size(LE11)):
78      for f in range(1,ng+1):
79          temp=0
80          temp2=0
81          FBGname= 'FBG'+str(f)
82          for l in range(1,neg+1):
83              sensorname=FBGname+'-'+str(l)
84              temp=temp+ LE11[sensorname][a]
85          temp2=temp/neg
86          LEaverage[FBGname].append(temp2)
87
88
```

```python
 89  # Wavelength shift calculation (Units of wavelength in nm)
 90  WaveShift={}
 91  for b in range(1,ng+1):
 92      Fbgname= 'FBG'+str(b)
 93      WaveShift[Fbgname]=[x*LFBG[b-1]*(1-pe)*10**9 for x in
 94                          LEaverage[Fbgname]]
 95  """------------------------------------------------------------
 96  Reflected Peak Width Variation calculation: Transversal Stress
 97  Using an average of the transverse stress values. """
 98  s22average={}
 99  for b in range(1,ng+1):
100      s22average['FBG'+str(b)]= []
101  for a in range(0,size(s22)):
102      for f in range(1,ng+1):
103          temp=0
104          temp2=0
105          FBGname= 'FBG'+str(f)
106          for l in range(1,neg+1):
107              sensorname=FBGname+'-'+str(l)
108              temp=temp+ s22[sensorname][a]
109          temp2=temp/neg
110          s22average[FBGname].append(temp2)
111  # Peak Width Variation calculation
112  #Equation fixed component
113  fce=(((1+vf)*p12-(1+vf)*p11)*n0**3)/Ef
114
115  Wavegap={}
116  for b in range(1,ng+1):
117      Fbgname= 'FBG'+str(b)
118      #Units of the wavelength in nm (*10**9)
119      Wavegap[Fbgname]=[abs(abs(x)*fce*igp[b-1]*10**9) for x in
120              s22average[Fbgname]]
121  """------------------------------------------------------------
122  Reflected Peak Width Variation calculation: Non-uniform strain
123  Using maximum and minimum strain along the grating. """
124  graperiodmax={}
125  graperiodmin={}
126  Wavegap2={}
127  for b in range(1,ng+1):
128      graperiodmax['FBG'+str(b)]= []
129      graperiodmin['FBG'+str(b)]= []
130      Wavegap2['FBG'+str(b)]= []
131  for a in range(0,size(LE11)):
132      for f in range(1,ng+1):
133          maxim= None
134          minm= None
135          FBGname= 'FBG'+str(f)
```

```python
136            for l in range(1,neg+1):
137                sensorname=FBGname+'-'+str(l)
138                if LE11[sensorname][a]>maxim or maxim== None:
139                    maxim=LE11[sensorname][a]
140                if LE11[sensorname][a]<minm or minm== None:
141                    minm=LE11[sensorname][a]
142            graperiodmax[FBGname].append(igp[f-1]*(1+(1-pe)*maxim))
143            graperiodmin[FBGname].append(igp[f-1]*(1+(1-pe)*minm))
144            #Units of wavelength in nm (*10**9)
145            Wavegap2[FBGname].append(2*n0*(graperiodmax[FBGname][a]
146                -graperiodmin[FBGname][a])*10**9)
147 """------------------------------------------------------------
148 Writing file with Results """
149 file = open("Name_of_the_file.txt", "w")
150 file.write("Step increment\t")
151 for b in range(1,ng+1):
152     file.write("Wavelength Shift (nm)- FBG" + str(b)+'\t')
153 for c in range(1,ng+1):
154     file.write("Peak Splitting (nm)- FBG" + str(c)+'\t')
155 file.write('\n')
156
157 for a in range(0,size(LE11)):
158     file.write('%5f \t' %(LE11['x'][a]))
159     for b in range(1,ng+1):
160         Fbgname= 'FBG'+str(b)
161         file.write('%5f \t' %(WaveShift[Fbgname][a]))
162     for b in range(1,ng+1):
163         Fbgname= 'FBG'+str(b)
164         file.write('%5f \t' %(Wavegap[Fbgname][a]
165             +Wavegap2[Fbgname][a]))
166     file.write('\n')
167 file.close()
```

.

Fibre Bragg Grating Sensor Signal Post-Processing Algorithm

This is an extended version paper of a short list of selected papers from the 3nd International Conference on Photonics, Optics and Laser Technology. This paper was selected as result from a double blind peer-reviewed.

Springer Proceedings in Physics

© 2016

Photoptics 2015
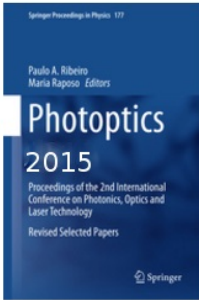
Proceedings of the **3rd** International Conference on Photonics, Optics and Laser Technology Revised Selected Papers

Editors: **Ribeiro**, Paulo A., **Raposo**, Maria (Eds.)

The paper is in Press, due: June, 2016;

Abstract

A novel method to assess a crack growing/damage event in fibre reinforced plastic, using conventional single mode Fibre Bragg Grating sensors embedded in the host material is presented in this article. Three different damage mechanisms that can change the sensor output, longitudinal strain ε_{xx}, transversal stress $\sigma_{yy,zz}$, and non-uniform strain $\varepsilon_{xx}(xx)$, were identified. These damage mechanisms were identified during the experimental testing and linked with the sensor output using a digital image correlation technique. A dedicated algorithm to extract information from the reflected spectrum that enables crack detection was developed. Double Cantilever Beams specimens made with glass fibre and bonded with structural adhesive, were instrumented with a Fibre Bragg Grating array embedded in the host material, and tested using an experimental fracture procedure. This method was successfully validated in three different loading conditions, where were obtained very promising results that enable crack growth monitoring.

P4.1   Introduction

P4.1.1   Fibre Reinforced Polymer Materials

Fibre Reinforced Polymer (FRP) materials, or as often called composite materials, have been extensively used in aerospace, automotive, naval, civil engineering and wind energy applications. The main difference with FRP materials compared to metals is that they have an isotropic behaviour, which means that it shows different mechanical properties in different directions. These FRP materials consist of two macroscopic phases, a stiff fibre phase usually glass or carbon fibre, and a polymer matrix usually polyester or epoxy. The main advantage of this material is its capability to be tailored for a specific application, enabling an enhancement, and a high level of customization of mechanical properties, such as light-weight, thermal expansion, chemical/corrosion resistance, fatigue behaviour, etc [1].

P4.1.2   FRP Failure and Damage Mechanism

Many structures made of FRP material, such as aerospace structures, ships, air-crafts and wind turbine blades, are constructed using multi-directional laminates that are bonded together using structural adhesives. Therefore, the most common failures in this type of structures are delamination, by crack growth along interfaces between layers inside the laminates, or adhesive joint failure, by cracking along the interface of the laminate and structural adhesive, as shown in Fig. P4.1.

In both failure situations a fibre crack bridging is often created, where intact fibres connect the crack faces behind the crack tip, as shown in Fig. P4.2. This fibre crack bridging creates an extra resistance that the crack has to overcome to grow, meaning that the energy required for the crack to grow is higher than that the energy
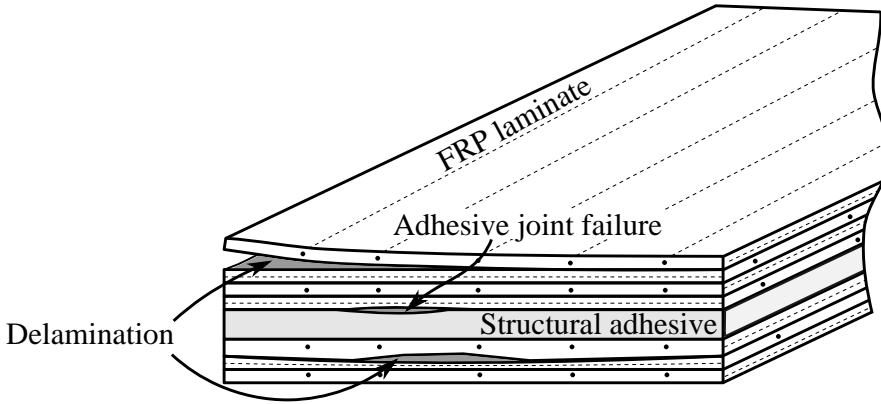
Figure P4.1: Most common type of failure in FRP laminate structures: delamination and adhesive joint failure.

required to initiate it. However, this damage mechanism can't be analysed by classic linear elastic fracture mechanics. Instead, a cohesive law can be used to describe the fracture mechanism, as described by some authors [2, 3]. The cohesive law, $\sigma(\delta)$, is a traction-separation relation that represents the stress transmitted between crack faces in the active cohesive zone (active fracture process zone).

To develop a monitoring system capable of detecting cracks/delamination, the stress distribution around the crack and the active cohesive zone needs to be analysed. A Finite Element Method Model (FEM) that simulates the delamination of a FRP structure bonded with structural adhesive was developed, based on the material/structure tested in this study.

The stress distribution along the active fracture process zone is shown in Fig. P4.3, and can be divided in two distinct contributions:

- near the crack tip ($x = 0$), where the material strength was reduced, and due to the proximity with the stress singularity (crack tip) the stress tends to infinite, creating a high stress gradient region;

- in the fibre bridging zone ($x < 0$), the fibres connecting the crack faces behind the crack tip will act like cables, forcing the faces to close, which creates a traction stress in that area. However, to maintain a force equilibrium, a compression field is formed ahead the crack tip;

These two crack/fracture phenomena, stress gradient and compression field, will move as the crack grows.
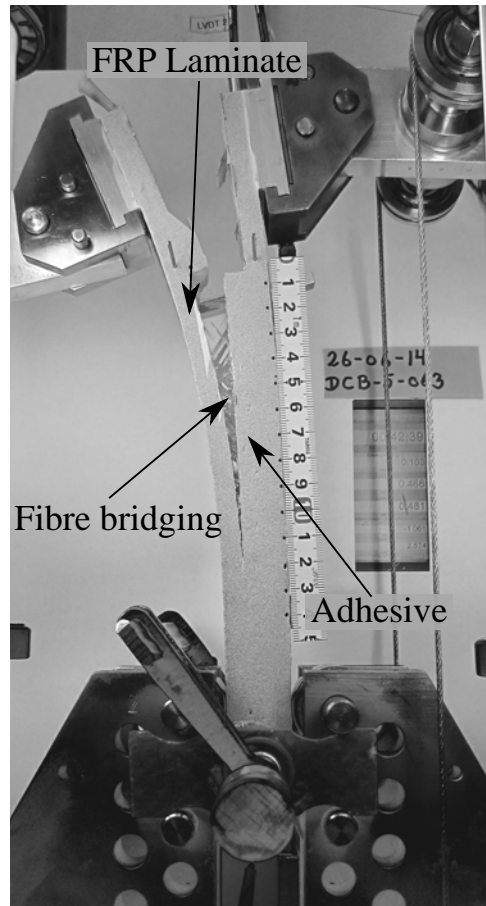
Figure P4.2: Fibre bridging phenomenon during adhesive joint failure of a FRP specimen.

P4.1.3   Crack/Delamination Detection in Fibre Reinforced Polymer Materials

Sensing technology has been implemented in FRP materials to track delamination. Acoustic emission [4] that measures the stress waves generated by the crack front growing, vibration [5] that detects changes in the specific damping capacity of the structure, modal analysis [6] by monitoring the material natural frequencies and mode shapes, piezo-electric actuators/sensors and wavelet analysis [7] based on the energy variation of the structural dynamic. However, these measurement systems have several limitations, among these the need for qualified operators, expensive hardware and impractical to use under operation. Also, to detect delamination in FRP materials
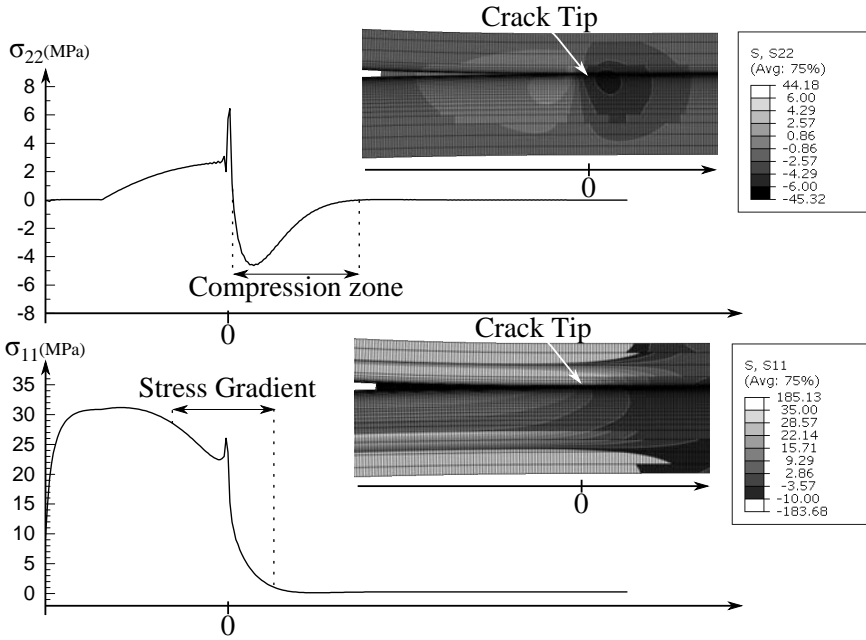
Figure P4.3: Finite element method simulation: Stress σ_{11} and σ_{22} distribution along the crack surface.

the sensor must be embedded in the laminate layers or in the interface between the FRP and the structural adhesive.

Fibre Bragg Gratings (FBG) have the capability to be embedded in the FRP material, even in an operational structure, without compromising its structural resistance. This is due to the FBG reduced size, with a diameter of $125\,\mu m$ it is virtual nonintrusive to the material. Also, FBG sensors present other interesting features, such high resolution, multiplexing capability, immunity to electromagnetic fields, chemical inertness and long term stability.

P4.1.4   Crack/Delamination Detection by Embedded Fibre Bragg Gratings

During a crack/delamination event different fracture features will be present near the crack tip, as such as a stress gradient and a compression field. Thus, being able to identify and measure this specific phenomena with a FBG sensor is a key factor to correctly determine the presence of damage and it growth.

Different FBG response stages under a crack growth event are presented in Fig. P4.4. First, before the crack reaches the proximity of the grating, Fig. P4.4a), the material will build up uniform strain (considering structure loading or geometric
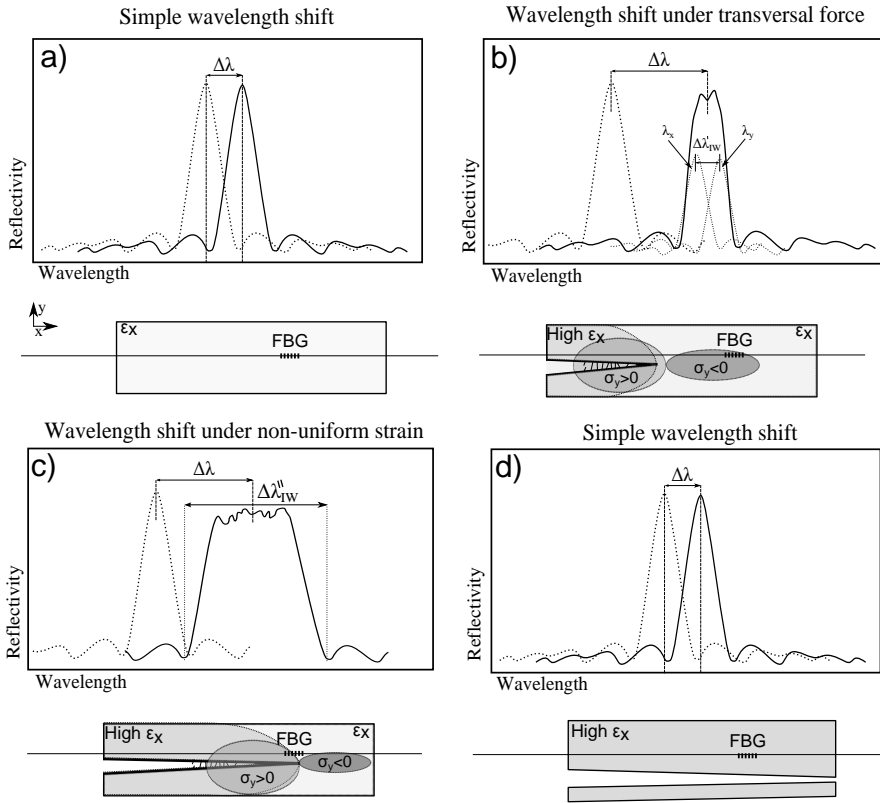
Figure P4.4: Different stages of the FBG response under a crack growth event.

singularities distant enough from the grating), which will make a uniform wavelength shift in the FBG reflected peak. Next, the compression field formed ahead the crack tip due to the the fibre bridging will reach the grating area, creating a splitting of the FGB reflected wave, as shown in Fig. P4.4b). Then, when the grating is near the influence of the crack singularity, the non-uniform strain field will change the shape of the reflected peak increasing the width of the reflected wave, as shown in Fig. P4.4c). At last, after the crack passes the FBG sensor, the shape of the reflected wave will return to it original shape, and the sensor response will be again a simple wavelength shift, because at this stage only uniform strains will be acting in the FBG, as shown in Fig. P4.4d).
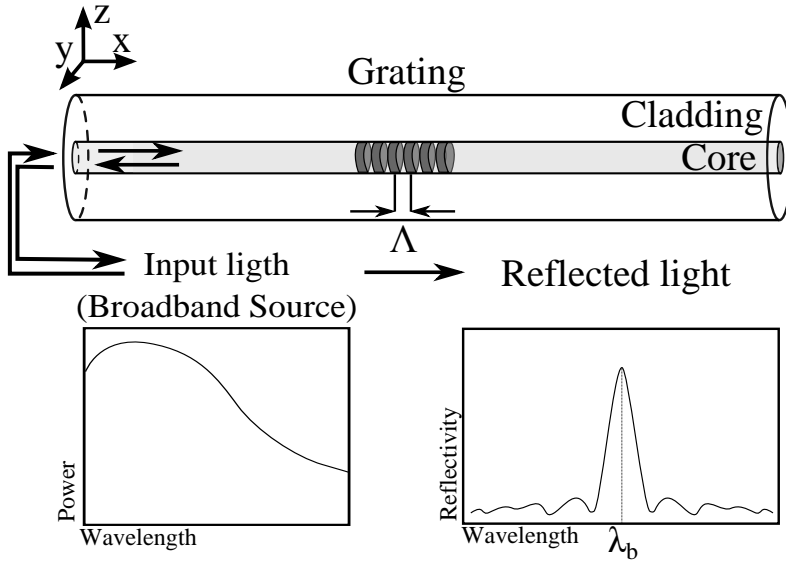
Figure P4.5: Fibre Bragg grating response working principle.

P4.2 Fibre Bragg Grating Working Principle

A Fibre Bragg Grating (FBG) is formed by a permanent periodic modulation of the refractive index along a section of an optical fibre, by exposing the optical fibre to an interference pattern of intense ultra-violet light [8]. The photosensitivity of the silica exposed to the ultra-violet light is increased, so when the optical fibre is illuminated by a broadband light source a very narrow wavelength band is reflected back. The spectral response of a homogeneous FBG is a single peak centred at the wavelength λ_b, as shown in Fig. P4.5. The wavelength λ_b is described by the Bragg condition,

$$\lambda_B = 2n_{eff,0}\Lambda_{,0} \tag{P4.1}$$

where n_0 is the mean effective refractive index at the location of the grating, the index 0 denotes unstrained conditions (initial state). The parameter n_{eff} is the effective refractive index and Λ is the constant nominal period of the refractive index modulation [9].

P4.2.1 Fibre Bragg Grating Response to Uniform Variation of Strain and/or Temperature

The wavelength shift $\Delta\lambda_b$ of an embedded FBG under a uniform variation of strain ε_{xx}, and temperature ΔT is given by the Eq. (P4.2),

$$\frac{\Delta\lambda_b}{\lambda_b} = (1 - p_e)\varepsilon_{xx} + [(1 - p_e)(\alpha_s - \alpha_f) + \xi]\Delta T \tag{P4.2}$$

where p_e is a photoelastic coefficients, α_s and α_f are the thermal expansion coefficients of the host material and the optical fibre, respectively, and ξ is the thermo-optic coefficient.

P4.2.2 Fibre Bragg Grating Response Under Transverse Force: Birefringent Effect

An optical fibre can present a birefringent behaviour, defined by the change of the refractive index n_{eff} in the two directions n_{effy} and n_{effx}, when the grating is subjected to a transverse force. The variation of the refractive index in the two directions n_{effy} and n_{effz} is given by the Eq. (P4.3) and (P4.4) [10–13].

$$\Delta n_x = -\frac{n_0^3}{2E_f}\{(p_{11} - 2\nu_f p_{12})\sigma_z + [(1 - \nu_f)p_{12} - \nu_f p_{11}](\sigma_y + \sigma_x)\} \tag{P4.3}$$

$$\Delta n_y = -\frac{n_0^3}{2E_f}\{(p_{11} - 2\nu_f p_{12})\sigma_y + [(1 - \nu_f)p_{12} - \nu_f p_{11}](\sigma_x + \sigma_z)\} \tag{P4.4}$$

$\sigma_{y,z}$ is the transverse stress, E_f is the elastic modulus of the optical fibre, ν_f is the Poisson's ration, n_0 is the initial refractive index, p_{11} and p_{12} are the photo-elastic coefficients of the optical fibre.

Rewriting the Eq. (P4.3) and (P4.4), it is possible to determine the increase in the width of the reflected wave, $\Delta\lambda'_{IW} = \|\lambda_x - \lambda_y\|$, caused only by a transverse stress.

$$\begin{aligned}\Delta\lambda'_{IW} &= 2\Lambda|\Delta n_{effz} - \Delta n_{effx}| \\ &= \frac{\Lambda n_o^3}{E_f}[(1 + \nu_f)p_{12} - (1 + \nu_f)p_{11}]|\sigma_z - \sigma_y|\end{aligned} \tag{P4.5}$$

P4.2.3 Fibre Bragg Grating Response Under Non-Uniform Strain

When an FBG sensor is near a defect, a crack, a material change or a geometric variation, this can create a stress concentration that will lead to an abrupt variation of strain. This non-uniform strain, or strain gradient, can change the periodicity of

the grating along the sensor length, modifying the grating pattern configuration from "uniform" to "chirped" [14, 15].

As demonstrated by Peters [16], in a uniform grating the applied strain will induce a change in both grating period and the mean index. These two effects can be superimposed by applying an effective strain of "$(1-p_e)\varepsilon_{xx}(x)$", similar the first part of Eq. (P4.2) but taking into account the strain variation along the x direction. Then it is possible to rewrite the grating period as:

$$\Lambda(z) = \Lambda_0[1 + (1 - pe) \times \varepsilon_{xx}(x)] \tag{P4.6}$$

Where the parameter Λ_0 is the grating period with zero strain. The non-uniform strain effect can be approximated by using the maximum and minimum strain values along the grating. So, the maximum grating period Λ_{max} and minimum Λ_{min} can be calculated using the Eq. (P4.6). Thus, an approximated increase of the width of the reflected wave due to a non-uniform strain, $\Delta\lambda_{IW}^{''}$, is given by combining Eqs. (P4.6) and (P4.1).

$$\Delta\lambda_{IW}^{''} = 2n_{eff}\Lambda_{max} - 2n_{eff}\Lambda_{min} \tag{P4.7}$$

P4.3   Crack Detection Algorithm

Conventional signal processing software, provided by the FBG measurement system manufactures, were developed for simple and reliable strain and temperature measurements. This is made by tracking only the wavelength shift of the reflected wave maximum optical power. However, this software has several limitations for crack detection. It isn't possible to evaluate the shape of the reflected wave or distinguish between a single peak from a multi-peak, which are key features for a reliable crack detection method. Thus, a dedicated algorithm was developed to detect and evaluate the different stages of the FBG response during a crack growth event, as presented in Fig. P4.4.

The FBG signal acquision system used in this work, *FS2200 Industrial BraggMeter* from *FiberSensing^{TM}*, measures the reflected light coming from the optical fibre every second (*1 Hz*), where it is outputted the reflected power amplitude for the bandwidth *1500-1600 nm* as a *20 000* points file. The algorithm developed computes this raw data at this level, allowing us to extract more information per sensor.

All the different reflected wave spectrum features that the algorithm will detect are schematically shown in Fig. P4.6. The *Grating Band* is a parameter, inputed by the user, which will define the bandwidth boundaries where the algorithm will make the measurements considering only one FBG sensor in that interval. This will allow us to detect multi-peaks and connect them with a single FBG sensor, as well as the moment that the peak splitting occurred. The *Peak Height* is the maximum optical power of the reflected wave inside each *Grating Band*. The *Height Threshold* is a percentage of the *Peak Height*, defined by the user, used to determine the number of peaks in each FBG, and consequently determine the correspondent wavelength
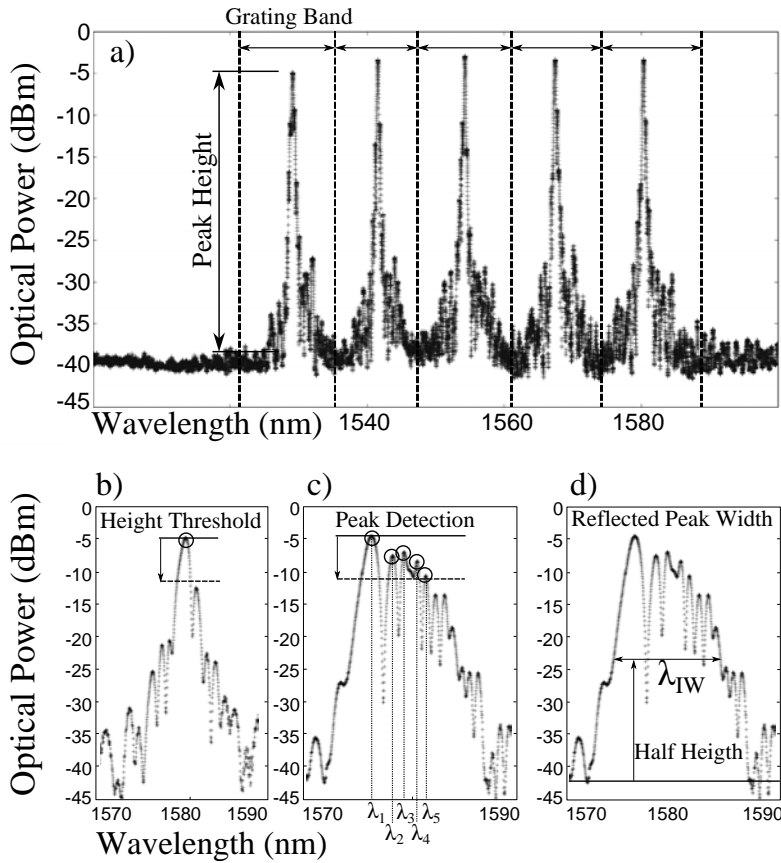
Figure P4.6: Crack Detection Algorithm: reflected spectrum features detected.

$\lambda_{1,2,...}$ for a single peak or multi-peak FBG. The *Peak Width*, λ_{IW}, is the width of the reflected wave that is calculated at half of the peak height for each FBG.

The algorithm is schematically shown in Fig. P4.7. Initially, the user will define the number of FBG sensors per optical fibre, and assign to each one a *grating band*. The user will define the *height threshold* and register the initial wavelength of each FBG in a free-state (unstrained). During operation and every second (1Hz), the algorithm will perform a measurement inside each grating band defined. The maximum height of the reflected wave will be calculated, and the number of peaks detected inside the defined height threshold together with the correspondent wavelength. At this point, the algorithm will output the number of peaks and the wavelength shift, assigned to each grating. Finally, the algorithm will measure the width of the reflected wave at half height.

In summary, every second for each FBG, the algorithm measures the number of peaks (NP), the wavelength shift ($\Delta\lambda$) using the wavelength measured in a free-state as reference, and the peak wave ($\Delta\lambda_{IW}$).
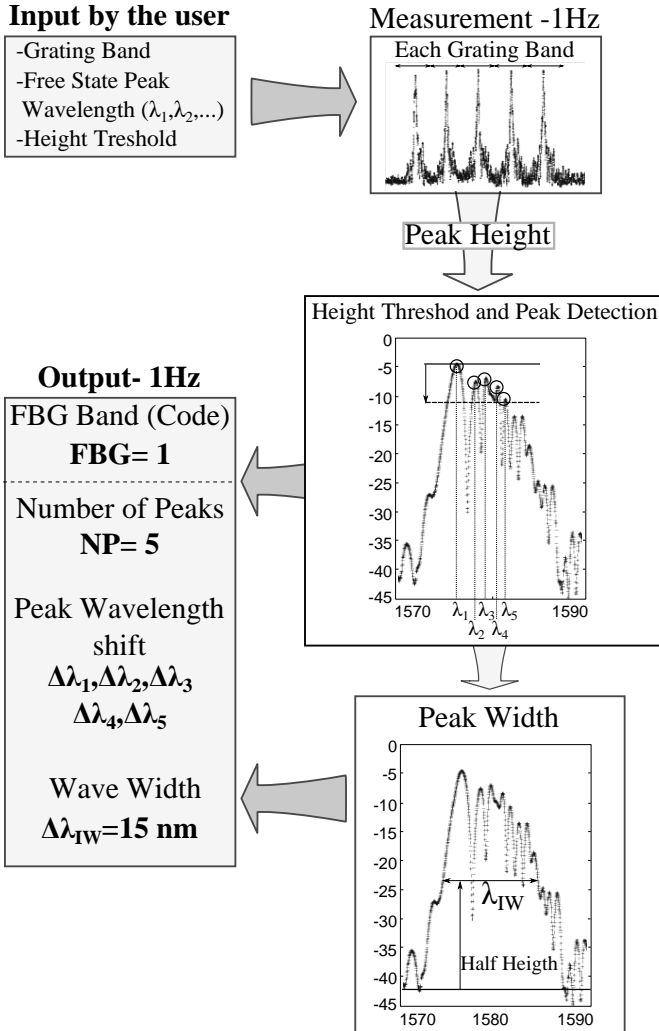
Figure P4.7: Schematic of the sensor output algorithm for crack detection.

P4.4   Material and Experimental Procedure

In order to measure all the different features of the damage mechanism and to relate them with the FBG response, experiments were conducted on Double Cantilever Beams (DCB) with embedded FBG sensors, subjected to a fracture testing procedure.

P4.4.1   Material and Testing Procedure

To correctly evaluate the different stages in the FBG response, a stable and controlled crack growth is required. Eight (8) DCB specimens were tested in a fracture test machine commonly used to determine material fracture properties, developed by *Sørensen* [17]. The DCB specimens were loaded in different conditions at 1 mm/min, ranging pure Mode I (tensile loading) to pure Mode II (shear loading), in order to simulate the different crack/delamination situations. This testing technique allows stable crack growth that makes it possible to correctly evaluate the FBG response at different stages.

The DCB specimens were manufactured using two composite material arms, glued by a commercial epoxy structural adhesive, Epikote MGS BPR 135G/Epikote MGS BPH137G. The geometry of the DCB specimen is presented in Fig. P4.8. To manufacture the DCB arms two plates of $700 \times 1000mm$, and approximately 7 mm of thickness, were produced using multiaxial glass fibre. Ten layers of fabric per plate were used, consisting of two triaxial fabrics, Saertex Triax S32E4590, as skin layers,
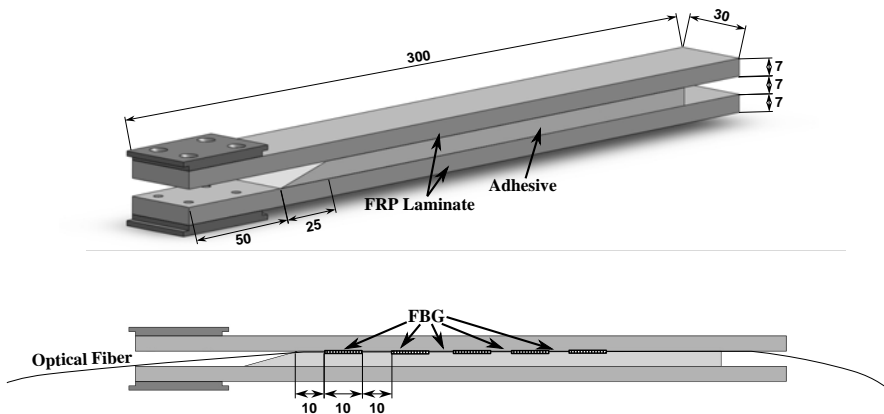
Figure P4.8: DCB specimen geometry and FBG array Configuration.

and eight unidirectional central layers, Saertex S35EU910. The layup stacking of the laminates was : $[90/ + 45/ - 45/0_4/0_4/ + 45/ - 45/90]$, and the backing of the unidirectional layers was facing out-wards, away from the central plane. The plates were made by hand-lay up of dry fibre fabric followed by epoxy impregnation, Momentive-Epikote/Epikure-100:30, by vacuum infusion at 50°C for 5 hours, and post-cured at 80°C for 3 hours. The plates were glued using a commercial structural adhesive, Momentive-Epikote/Epikure MGS BPR 135G/137G, and 7 mm spacers were used to give a well defined specimen thickness and geometry. A thin slip foil was placed in the edge of the structural adhesive, to act as a pre-crack and ease crack initiation. An array of 5 uncoated single mode FBG sensors (5 gratings in one optical fibre), with 10 mm of length, were embedded in the interface of the laminate plate with the structural adhesive. The gratings array were spaced 10 mm from each other, and the first grating was positioned 10 mm from the edge of the adhesive.

Digital image correlation (DIC) technique was applied to the specimens, in order to determine the presence of specific phenomenon caused by the crack and to correlate it with the FBG output. Digital image correlation is an optical method that by tracking changes in a random pattern in the specimen, can correlate this information with deformation/strain in the material. A pattern was painted on the side surface of the DCB specimen and ARAMIS™software was used to calculated the strains from each measurement. All the measurements from the *BraggMeter* and *Aramis* were synchronized with the crack growth.

P4.5   FBG Response to Crack Growth: Experimental Results

Fig. P4.9 shows some measurements from a five FBG array embedded in a DCB specimen under a Mode II fracture testing. The reflected peak at 1580 nm, furthest to the right, corresponds to the grating closest to the crack tip, and consequently the peak at 1530 nm corresponds to the most distant. The table shows the algorithm output for each measurement, where is possible to observe, as the crack propagates, changes in the shape of the reflected wave ($\Delta\lambda_{IW}$), in the number of peaks per FBG (NP), and in the wavelength shift($\Delta\lambda$).

As mentioned before and observed here, the crack proximity to the FBG will make a change in the shape of the reflected peak, thus evaluating and tracking this change will permit an accurate determination of the crack. The shape of the *FBG 5* reflected wave during Mode II crack growth, and the strain distribution in the DCB surface given by the DIC technique are presented in Fig. P4.10. It can be observed that during propagation of the crack, different damage features can change the shape of the reflected wave. In the left column are the DIC measurement of ε_y, where the red area is a compressive stress/strain created ahead the crack tip. As mentioned, the compression stress causes a birefringent effect in the FBG, making a peak separation and an increasing of the reflected wave width, as can be observed in Fig. P4.4.
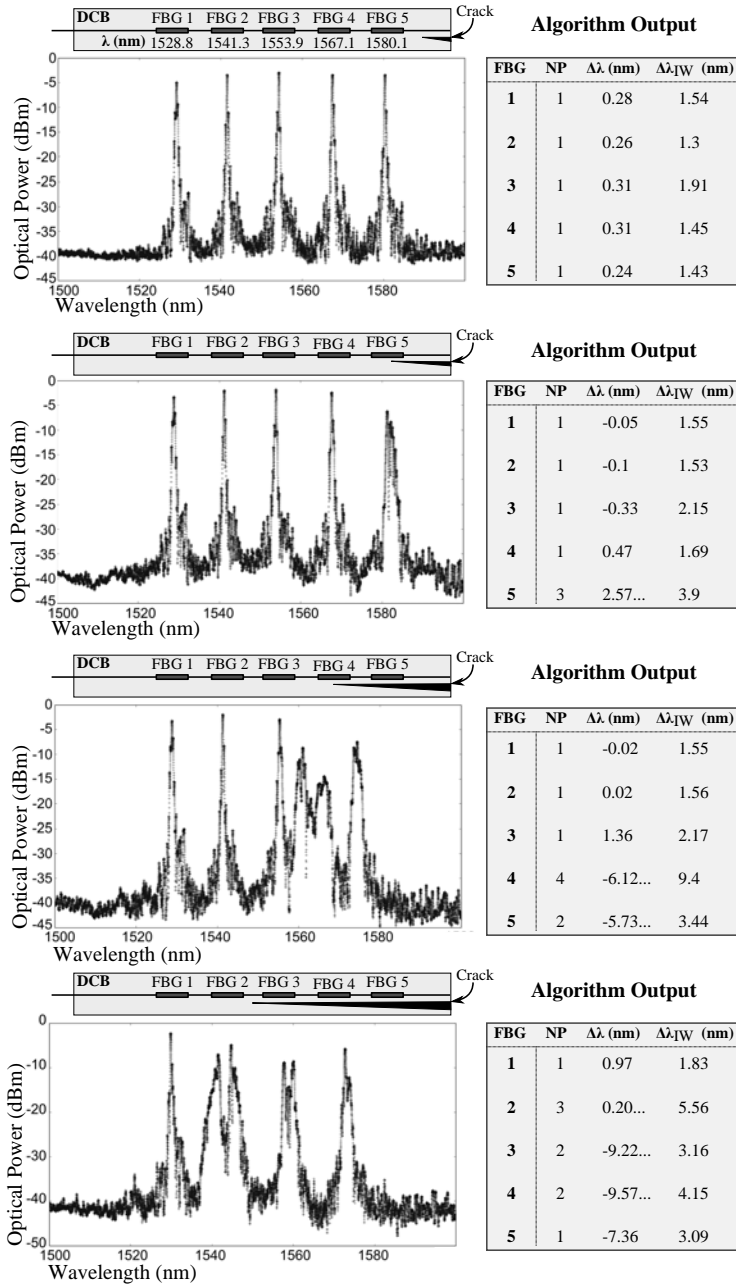
Figure P4.9: FBG array output under Mode II crack growing.

In the center column DIC measurement of ε_x are represented, where the gradient of colours represents variation of strain, indication of non-uniform strain acting in the FBG length, and consequently the change in the reflected wave.

As described in section P4.1.4, it is possible to identify the different stages of the crack growth from the sensor response, and therefore detect crack growth. Before the crack reaches the proximity of the grating, the material builds up uniform strain, that induces a uniform wavelength shift in the sensor response. Next, the compression field formed ahead of the crack tip reaches the grating area, this creates a peak splitting/increase of the width. Then, when the grating is near the influence of the crack singularity, the non-uniform strain field creates a change in the shape of the reflected wave. Finally, after the crack passes the FBG sensor the shape of the reflected peak gradually recovers its original shape.
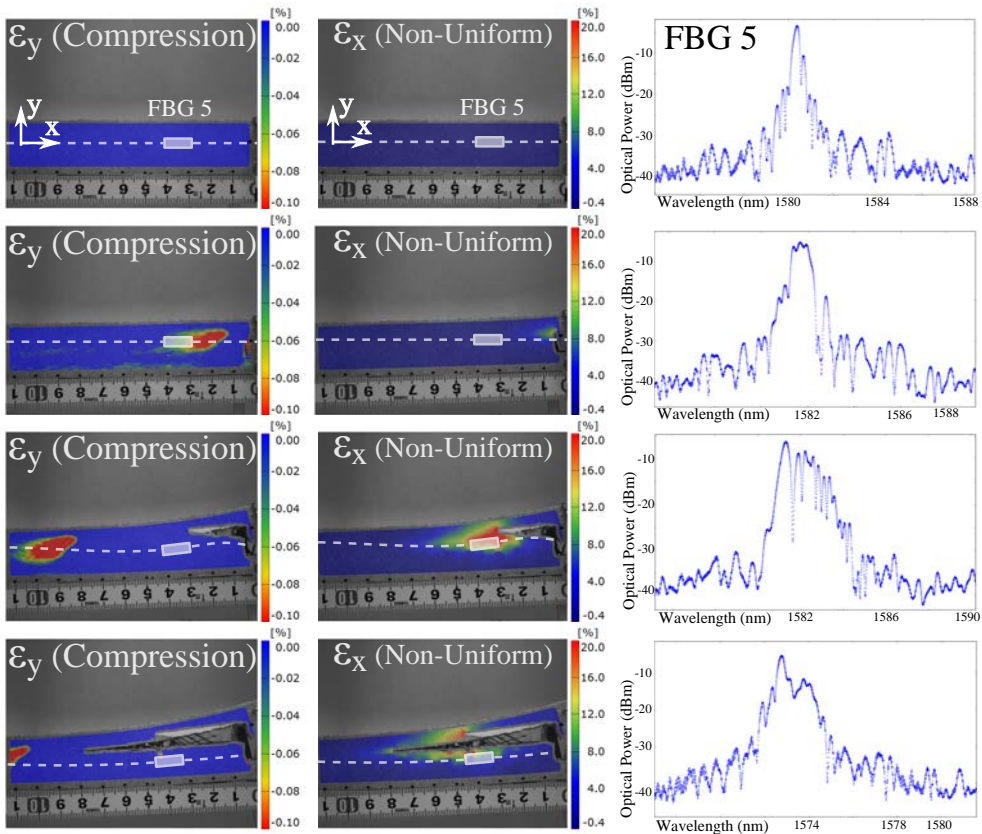
Figure P4.10: Stages of the FBG output during crack growth: DIC measurement and FBG spectrum.

P4.6   Discussion of Results

The wavelength shift $\Delta\lambda$, the wave width $\Delta\lambda_{IW}$, and the number of peaks per FBG, computed using the algorithm developed in this article, are presented in Fig. P4.11, P4.12 and P4.13, for three different loading conditions. Each symbol represents each FBG in the sensor array, FBG5 being the sensor closest to the adhesive edge (initiation of the crack), and FBG1 the sensor most distant. The crack growth in the order: FBG $5 \rightarrow 4 \rightarrow 3 \rightarrow 2 \rightarrow 1$. During Mode I loading, three FBG sensors were lost during the test, because the crack path crossed the fibre optic cutting the connection with the measurement equipment. However, the system was capable to record the growth of the crack.

The wavelength shift $\Delta\lambda$, is a direct indication of strain ε_x along the specimen. By analysing the graphs, it was observed that the magnitude of the $\Delta\lambda$, measured by each FBG, increases after the crack passes the grating area. This is because the structure loses compliance and it becomes easier to deform the material surrounding the FBG sensor.
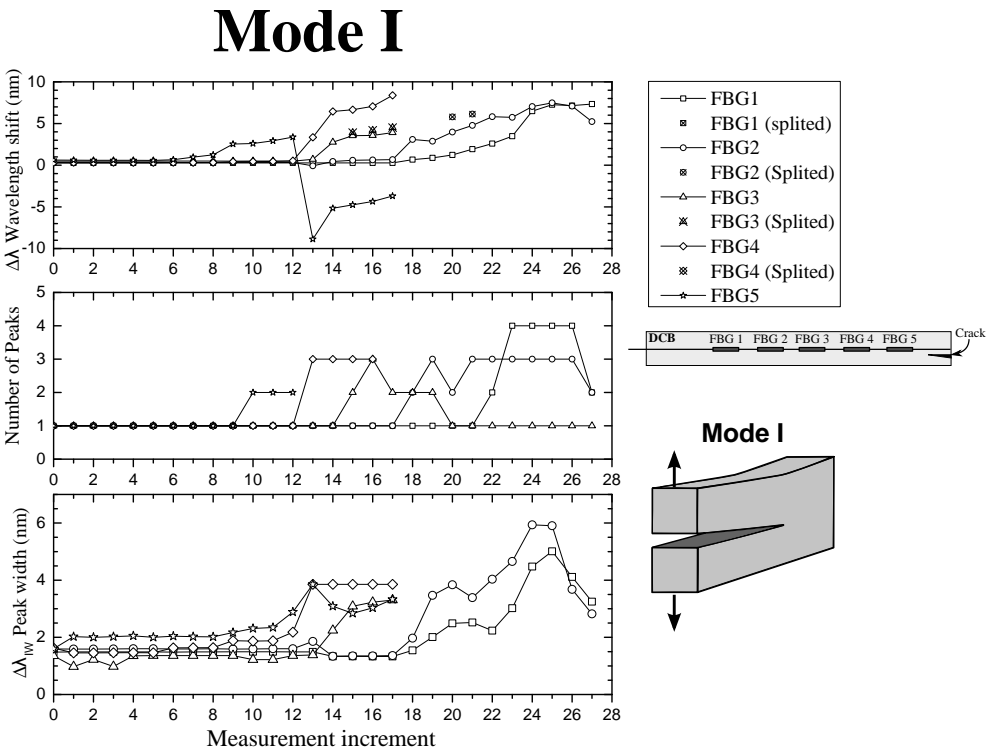
Figure P4.11: FBG sensor array output: mode-I crack growth.

However, the evolution of the wavelength shift $\Delta\lambda$ is different for the three loading types. For Mode I, the location where the fibre optic was embedded is under traction loading, therefore a positive $\Delta\lambda$ was measured. For Mode II and Mixed Mode, the location is under compression loading, resulting in a negative $\Delta\lambda$ value. Bases on this, it can be concluded that an abrupt change of $\Delta\lambda$ is an indication that the structure is losing compliance, probably due to crack growth.

The number of peaks and the reflected wave width $\Delta\lambda_{IW}$, are a direct indication of the presence of the crack. By analysing the graphs, it is observed that these values increase when the crack is near the FBG sensor, in all loading cases, returning to its original values after the crack passes. Thus, we can conclude that the wavelength shift is dependent on the loading type, but the increase in the width and number of peaks is related to the presence of a crack. Using this information it is possible to track the crack independently of the loading conditions or geometry of the specimen.
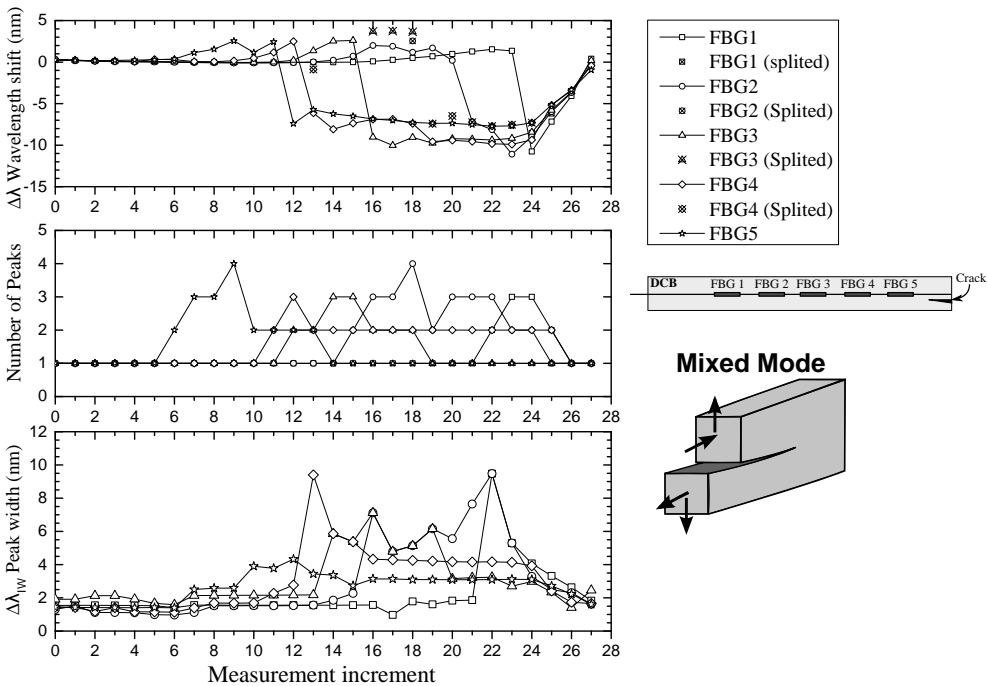
Figure P4.12: FBG sensor array output: mixed-mode crack growth.
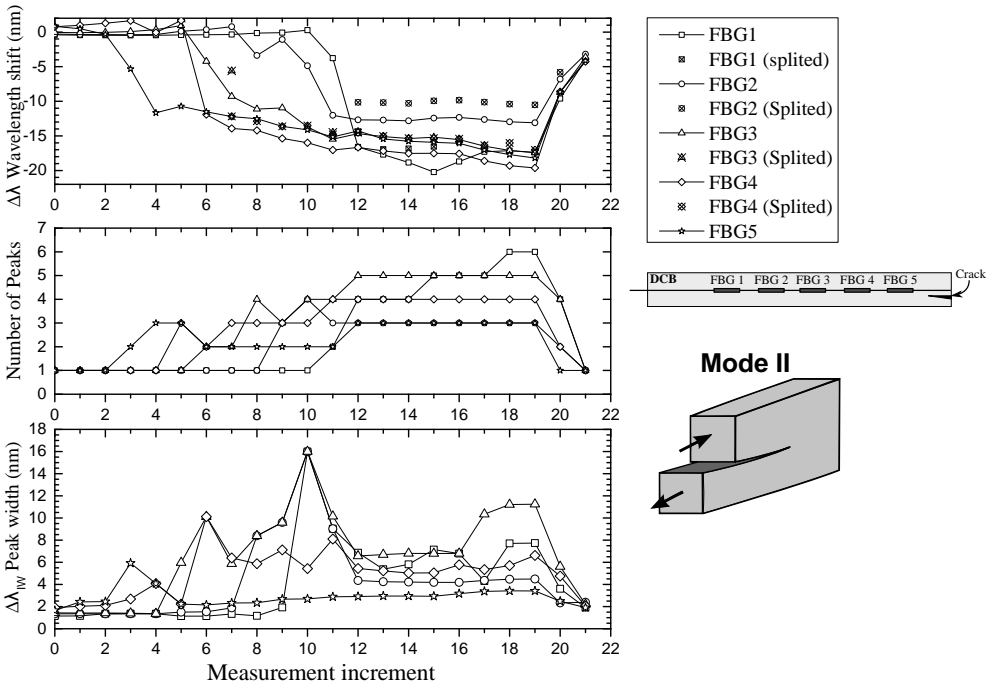
Figure P4.13: FBG sensor array output: mode-II crack growth.

P4.7   Conclusions

In this article, the capability of Fibre Bragg Gratings embedded in composite material to detect and track cracks/delamination was demonstrated. Three different damage mechanisms that can change the sensor output, longitudinal strain ε_{xx}, transversal stress $\sigma_{yy,zz}$ and non-uniform strain $\varepsilon_{xx}(xx)$, were identified. By the use of digital image correlation technique, these damage mechanisms were identified during the experimental testing and linked with the sensor output. Thus, it is possible to extract information from the sensor that is independent of the loading type, geometry and boundary conditions, and only depends on the proximity of the crack.

A dedicated algorithm was developed to extract more information from the reflected spectrum when compared to conventional FBG signal processing software. The algorithm presented is a tool to detect and evaluate all the different stages in the FBG response during a crack growth event. This technique was successfully validated in three different loading conditions, and very promising results were obtained that enables crack growth monitoring.

The authors vision is that this monitoring method can be implemented into operational structures, enabling the design of structures in fibre reinforced materials that can operate safely, even when in damaged condition.

Acknowledgements

References

[1]   R. Jones, *Mechanics of composite materials*. Taylor & Francis, 1999, 519 s, ISBN: 156032712x, 9781560327127.

[2]   B. Sørensen, *Cohesive laws for assessment of materials failure: Theory, experimental methods and application*. Risø DTU, 2010, 243 s, ISBN: 9788755038271.

[3]   Z. Suo, G. Bao, and B. Fan, "Delamination r-curve phenomena due to damage," *Journal of the Mechanics and Physics of Solids*, volume 40, number 1, pages 1–16, January 1992, ISSN: 00225096. DOI: 10.1016/0022-5096(92)90198-B.

[4]   I. Silversides, A. Maslouhi, and G. Laplante, "Interlaminar fracture characterization in composite materials by using acoustic emission 2 . experimental procedures and fem modeling," number November, pages 13–15, 2013.

[5]   C. Kyriazoglou and F. Guild, "Vibration damping for crack detection in composite laminates," *Composites Part A: Applied Science and Manufacturing*, volume 35, number 7-8, pages 945–953, 2004, ISSN: 1359835X. DOI: 10.1016/j.compositesa.2004.01.003.

[6]   H. Hu, C. L. B. Wang, and J. Su, "Damage detection of surface cracks in composite laminates using modal analysis and strain energy method," *Composite Structures*, volume 74, number 4, pages 399–405, August 2006, ISSN: 02638223. DOI: 10.1016/j.compstruct.2005.04.020.

[7]   Y. Yan and L. Yam, "Online detection of crack damage in composite plates using embedded piezoelectric actuators/sensors and wavelet analysis," *Composite Structures*, volume 58, number 1, pages 29–38, October 2002, ISSN: 02638223. DOI: 10.1016/S0263-8223(02)00043-0.

[8]   K. Hill and G. Meltz, "Fiber bragg grating technology fundamentals and overview," *Journal of lightwave technology*, volume 15, number 8, pages 1263–1276, 1997.

[9]   W. Morey, G. Meltz, and W. Glenn, "Fiber optic bragg grating sensors," *OE/-FIBERS'89*, 1990.

[10] L. Sørensen, J. Botsis, T. Gmür, and J. Cugnoni, "Delamination detection and characterisation of bridging tractions using long fbg optical sensors," *Composites Part A: Applied Science and Manufacturing*, volume 38, number 10, pages 2087–2096, October 2007, ISSN: 1359835X. DOI: `10.1016/j.compositesa.2007.07.009`.

[11] W. Zhang, W. Chen, Y. Shu, X. Lei, and X. Liu, "Effects of bonding layer on the available strain measuring range of fiber bragg gratings," *Applied Optics*, volume 53, number 5, page 885, 2014, ISSN: 0003-6935. DOI: `10.1364/AO.53.000885`.

[12] F. Jülich and J. Roths, "Comparison of transverse load sensitivities of fibre bragg gratings in different types of optical fibres.," volume 7726, F. Berghmans, A. G. Mignani, and C. A. van Hoof, Eds., pages, 2010. DOI: `10.1117/12.854019`.

[13] F. Bosia, P. Giaccari, J. Botsis, M. Facchini, and H. Limberger, "Characterization of the response of fibre bragg grating sensors subjected to a two-dimensional strain field," *Smart Materials and Structures*, volume 925, number 12, pages 925–934, 2003.

[14] S. Yashiro, T. Okabe, N. Toyama, and N. Takeda, "Monitoring damage in holed cfrp laminates using embedded chirped fbg sensors," *International Journal of Solids and Structures*, volume 44, number 2, pages 603–613, January 2007, ISSN: 00207683. DOI: `10.1016/j.ijsolstr.2006.05.004`.

[15] X. Zhang, J. Max, and X. Jiang, "Experimental investigation on optical spectral deformation of embedded fbg sensors," *SPIE, Photonics Packaging, Integration, and Interconnects VII*, volume 6478, 2007.

[16] K. Peters, M. Studer, J. Botsis, A. Iocco, H. Limberger, and R. Salath, "Embedded optical fiber bragg grating sensor in a nonuniform strain field : measurements and simulations," pages 19–28,

[17] B. Sørensen, K. Jørgensen, T. Jacobsen, and R. C. Østergaard, "Dcb-specimen loaded with uneven bending moments," *International Journal of Fracture*, volume 141, number 1-2, pages 163–176, Sep. 2006, ISSN: 0376-9429. DOI: `10.1007/s10704-006-0071-x`.

FBG_SiMul V1.0: Fibre Bragg Grating Signal Simulation Tool for Finite Element Method Models

G. Pereira, M. McGugan, L.P. Mikkelsen, *FBG_SiMul V1.0: Fibre Bragg Grating Signal Simulation Tool for Finite Element Method Models, SoftwareX,* **Submitted**, *(2016)*

Code metadata

Current code version	1.0
Permanent link to code/repository	`https://github.com/GilmarPereira/FBG_SiMul.git`
Legal Code License	GNU GPL-3
Computing platform/ Operating System	Windows
Installation requirements & dependencies for the standalone file	None
Installation requirements & dependencies for the python file	Python 2.7.5: numpy, matplotlib, math
Link to user-manual	`https://github.com/GilmarPereira/FBG_SiMul/blob/master/Standalone_Version/Software_Documentation.pdf`

In FBG_SiMul user-manual (see link above), it is presented and detailed all the software functionalities, however due to its size only a section is attached to the end of this paper, where a tutorial/demonstration case is presented.

Abstract

FBG_SiMul V1.0 is a tool to study and design the implementation of fibre Bragg grating (FBG) sensors into any arbitrary loaded structure or application. The software removes the need of an expert in fibre optics technology, which makes the sensor signal simulation of a structural health monitoring solution based on FBG sensors more comprehensible. The software uses a modified T-Matrix method to simulate the FBG reflected spectrum, based on the stress and strain from a finite element method model. The article describes the theory and algorithm implementation, followed by an empirical validation.

P5.1   Introduction

More demanding structural applications and new design philosophies are increasingly motivating engineers and researchers to implement sensors into structures and to develop new structural health monitoring (SHM) solutions [1, 2]. This opportunity is driven by new low-cost sensors and transducers, new electronics and new manufacturing techniques. In particular, the cost of fibre Bragg grating (FBG) sensors has dropped over the last few years and robust fibre-optic monitoring systems suitable for SHM have become commercial off the shelf hardware.

However, the sustainment of structures using these permanent on-board health monitoring systems is a complex and multi-disciplinary technological field that requires a holistic approach that cannot be addressed solely by advances in the various technology platforms on which the SHM is constructed. What is required is twofold; that the next generation of research scientists and engineers are specifically trained with the skills, research experience, and multi-disciplinary background to adopt the new structural sustainment concepts. And that tools are available that enable the demanding task of integrating, supporting, and maintaining an innovative holistic health management system and to propel its application in the aerospace, wind energy, and other industries.

The FBG_SiMul software described here is an example of the type of tool that will allow sensor simulation to become part of the design process, where output is simulated and optimised to a structure. This will have an immediate impact on the planning, development and implementation of SHM as well as provoking further research and development to include active control elements in the software and real-time data-driven fed back control for smart structures in the future. Equally important is that the software is robust and runs from a user friendly interface. This ensures its uptake both within and outside the modelling and sensor communities as it provides an opportunity for non-experts to simulate the signals and support their sensor implementation plans; whether for a one-off full-scale structural test, or a series of mechanical test specimens [3].

P5.2   Problems and Background

The shape and response of the FBG reflected spectrum (measured signal) depends on the way that the grating is deformed, i.e., the stress and strain field acting along the grating will define the signal response. The FBG response simulation based on the stress and strain state from a finite element method (FEM) model was only recently addressed. *Hu*, et al.[4] developed a Matlab code to simulate the FBG response under non-uniform strain fields caused by the transverse cracking in cross-ply laminates; and in a similar work, *Hasson* el al.[5] developed a Matlab code to simulate the FBG response for mode-I delamination detection. However, the code developed by both authors is limited either by the type of FEM model or by the type of sensor response analysed; and, in both cases the code/algorithm for the signal simulation code is not provided.

Thus, FBG_SiMul was developed to tackle this gap in the FBG simulation field, where the FBG response is simulated independently of the structure, loading, or application type. As the software removes the need of a fibre optic expert user, the FBG sensor response of a structural health monitoring solution becomes more intuitive.

P5.2.1   Fibre Bragg Grating Signal Response

A FBG sensor is formed by a permanent periodic modulation of the refractive index along its core. When the optical fibre is illuminated by a broadband light source a narrow wavelength band is reflected back, as shown in Fig. P5.1.

Any external force/load acting in the grating region will change the effective index and/or the period of modulation, which will create a shift in the wavelength and/or modify the shape of the reflected peak. However, different stress and strain fields acting in the FBG sensor create different signal responses [3, 6–9] (see Fig. P5.1); a
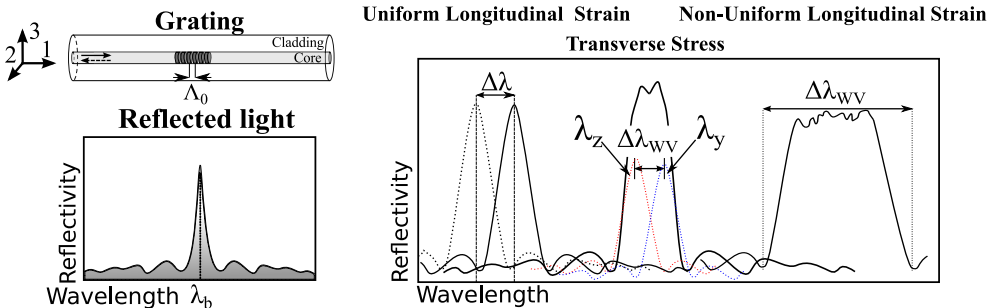
Figure P5.1: Fibre Bragg grating response for uniform strain, transverse stress and non-uniform strain.

longitudinal uniform strain field creates a wavelength shift in the reflected peak ($\Delta\lambda$), but its shape remains unchanged; a longitudinal uniform and non-uniform strain field, acting along the grating, causes an increase in the reflected peak width ($\Delta\lambda_{WV}$) and a wavelength shift ($\Delta\lambda$); a transverse stress field, acting along the grating, causes a separation of the reflected Bragg peak due to the optical fibre birefringent behaviour, which can be described by an increase in the reflected peak width ($\Delta\lambda_{WV}$) and a wavelength shift ($\Delta\lambda$).

P5.2.2   Spectrum Simulation: Transfer-Matrix Method

The transfer-matrix method was originally developed to simulate the reflected spectrum of FBG sensors under a uniform strain field by *Yamada* and *Sakuda* [10]; later, this theory was modified to simulate the reflected spectrum of FBG sensors under other types of strain field or different FBG configurations [11–14]. The modified T-Matrix method, developed by Peters, et al. [15], consists of dividing the waveguides (grating periodic pattern) into short segments, and in each segment the grating is assumed to be periodic. This assumption allows each segment to be handled as a uniform grating and its signal to be simulated by the original *Yamada* T-Matrix method. Then, when the grating is deformed, the grating period (Λ) in each increment is calculated using the average strain acting in that increment; and, the total reflected signal is reconstructed by combining the signal contribution from all increments.

P5.2.3   From a Finite Element Method Model to Spectrum Simulation

In a FEM model the structure domain is divided in small sections called elements, which contain stress and strain information that describes the structural behaviour. In the T-Matrix method the grating is divided into short segments, and the simulated signal from each segment is added to the total reflected signal. Thus, it is possible to simulate the FBG reflected spectrum based on a FEM model, by matching the number of short segments used by the T-Matrix method with the number of elements in the FEM model, as shown in Fig. P5.2.

Then, the stress and strain from each FEM element is used by FBG_SiMul to simulate the sensor signal, using a modified T-Matrix method. The different theory and algorithm structure implemented in the software are presented in appendix A-*Spectrum Simulation Theory and Algorithm.*
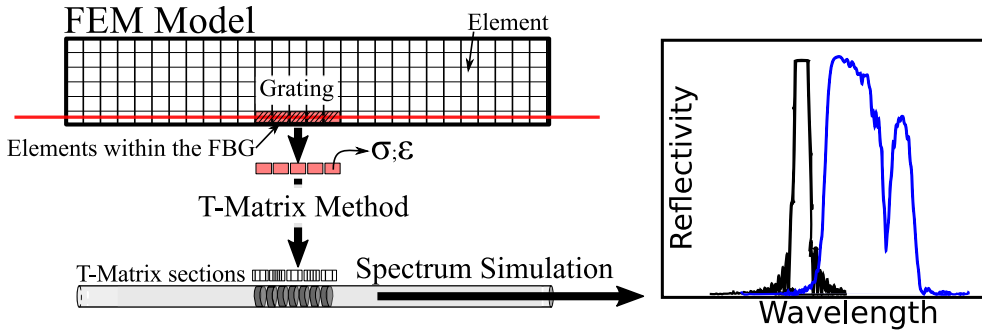
Figure P5.2: Schematic representation of the algorithm implemented in the FBG_SiMul software: from a FEM model to FBG spectrum simulation.

P5.3   Software Description

FBG_SiMul was developed with a graphical user-interface, no programming knowledge is required to perform FBG simulation; all the input parameters are pre-checked by the software, meaning that the simulation is robust and the code does not crash. However, the source code (python) is provided and it can be re-used or changed to fit any purpose. The software is provided in two formats: a standalone file, in *.exe* format, which does not require installation or any dedicated software; and, in Python format, which can be modified but requires a python compiler.

A user-manual is provided together with the software. In this documentation, the user can find information about the code structure, the type of functions/algorithms implemented, the software input/output and different functionalities, and a software tutorial case.

P5.3.1   Software Conceptual Structure

The FBG_SiMul conceptual structure is shown in Fig. P5.3. First, the software extracts the stress and strain along a predefined path in a FEM model, and save it as a .txt file. This can be made for a specific/single time increment, or for multiple time increments (ex: dynamic models, time dependent behaviour). Next, the software identifies the elements that are inside of each FBG, and creates a local variable per FBG sensor containing all information needed to simulate the FBG response, as the number of elements per grating, and the stress and strain field. Finally, two simulation options are given to the user: reflected spectrum simulation for a specific time increment, to evaluate the shape of the reflected signal; and, FBG time response, to simulate the sensor response for multiple time increments.

FBG_SiMul Conceptual Structure
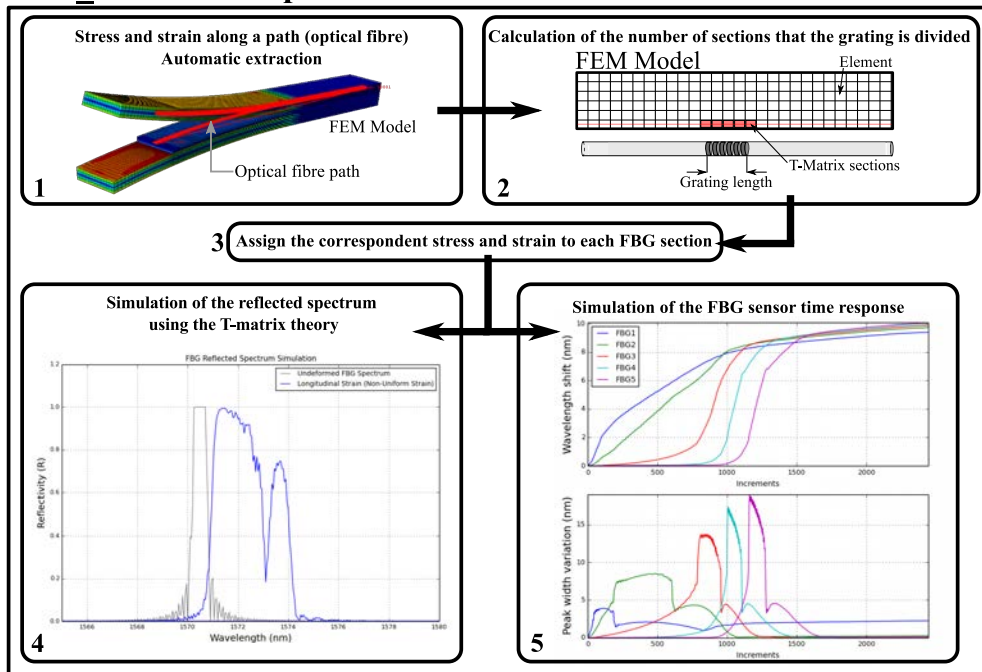
Figure P5.3: FBG_SiMul conceptual structure. FBG spectrum simulation from a finite element method.

P5.3.2   Software Functionalities

The software is divided between 4 tabs according to functionality:

- **Tab 1- Software:** Software front page, where the user can find information about all the different tabs and their functionalities, open the user manual, or learn more about the software copyright and author;

- **Tab 2- Extract Stress/Strain along Optical Fibre (Abaqus):** Tool to automatically extract the stress and strain along a pre-defined path in a FEM model. The output is a .txt file containing the stress and strain distribution along a FBG path for a specific time increment. Tool options: multiple FBG paths; coordinate system rotation; single or multiple time increment;

    Note: this tool was developed for *Abaqus* FEM models. Nevertheless, the user can simulate the FBG response using a different FEM software by extracting the

files manually, and ensuring that the files have the required format, as described in the user-manual.

- **Tab 3- FBG Spectrum Simulation (Specific Step Increment):** FBG reflected spectrum simulation for a specific time increment. Here, the user can study the FBG spectrum response, plan the sensor location, optimise the sensor wavelength, check available bandwidth, evaluate signal distortion or measurement errors, and so forth. The tab output is the FBG reflected spectrum, and it can be saved as an image or as a .txt file. Tool options: different SI units, mm or m; type of simulation, as longitudinal uniform strain, longitudinal non-uniform strain or transverse stress; user-defined optical fibre parameters; number of FBG sensors per fibre; FBG length; user-defined FBG array configuration; plot configuration;

- **Tab 4- FBG Signal variation (Time Response):** FBG signal response for multiple time increments. Here, the user can study the wavelength shift variation($\Delta\lambda_{WV}$) and the peak width variation ($\Delta\lambda$) along the selected time increments, compare the sensor response for multiple FBG paths, plan the sensor location, and so forth. The tab output is the $\Delta\lambda_{WV}$ and $\Delta\lambda$ along the selected time increments, and it can be saved as an image or as a .txt file. Tool options: different SI units, mm or m; user-defined optical fibre parameters; number of FBG sensors per fibre; FBG length; user-defined FBG array configuration; plot configuration;

P5.4   Software Empirical Validation

To validate the software algorithm, 3 input files representing known cases of uniform strain, non-uniform strain and transverse stress were created. The wavelength shift, $\Delta\lambda_{WV}$, and the peak width variation, $\Delta\lambda$, for the 3 cases were calculated using the analytical equations (Eq. (3), (7), and (11)) developed by Pereira, et al. [3]. Each input file contains the stress and strain along a 10 mm grating, discretised in 20 segments.

Theoretical Benchmark cases:

- Uniform strain: grating under 1.0 $\varepsilon(\%)$ longitudinal strain. Default parameters: $p_e = 0.215$ and $\lambda_b = 1550\,nm$;

- Non-uniform strain: half grating under 1.0 $\varepsilon(\%)$ and the other half under 0.5 $\varepsilon(\%)$ longitudinal strain. Default parameters:$p_e = 0.215$, $\lambda_b = 1550\,nm$, $n_{eff} = 1.46$ and $\Lambda_0 = 530.82$;

- Transverse stress: grating under a compressive stress of $100 MPa$ in the z direction. Default parameters: $p_{11} = 0.121$, $p_{12} = 0.270$, $E = 70\,GPa$, $\nu = 0.17$, $\lambda_b = 1550\,nm$, $n_{eff} = 1.46$ and $\Lambda_0 = 530.82$;
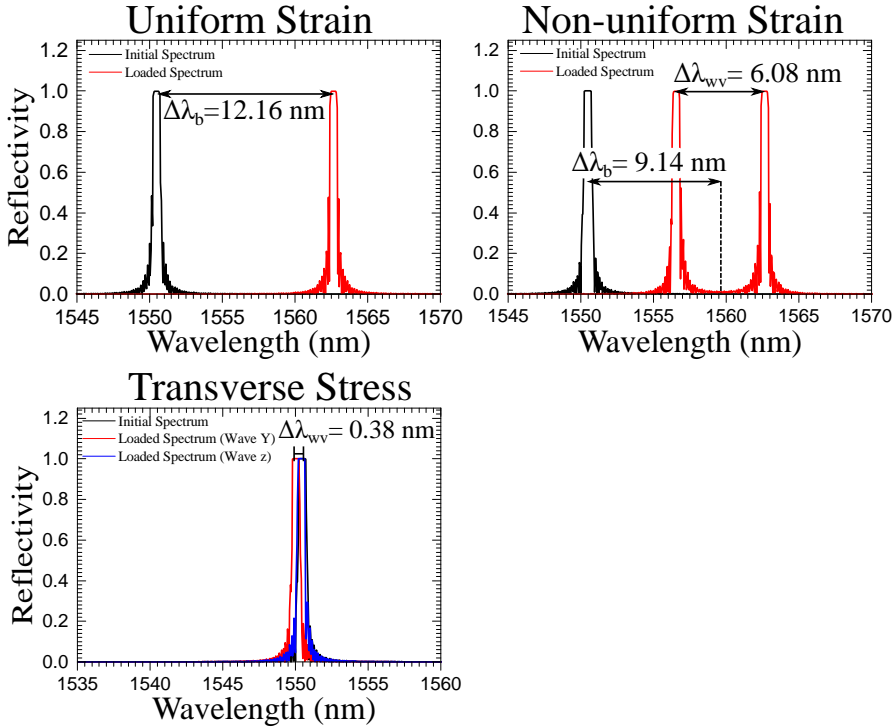
Figure P5.4: FBG_SiMul simulation results. Simulated test cases: uniform strain, non-uniform strain, and transverse stress.

The three empirical test cases were simulated with good accuracy by the FBG_SiMul software, as shown in Fig. P5.4 and table P5.1. Thus, it can be concluded that the software can represent the FBG response for different type of strain/stress fields.

Table P5.1: Software empirical validation: comparison between theoretical and FBG_SiMul simulation for three known cases.

Test Cases	(nm)	Theoretical Results	FBG_SiMul Simulation
Uniform Strain	$\Delta\lambda$	12.16	12.16
	$\Delta\lambda_{WV}$	0	0
Non-Uniform Strain	$\Delta\lambda$	9.15	9.14
	$\Delta\lambda_{WV}$	6.07	6.08
Transverse Stress	$\Delta\lambda$	0	0
	$\Delta\lambda_{WV}$	0.38	0.38
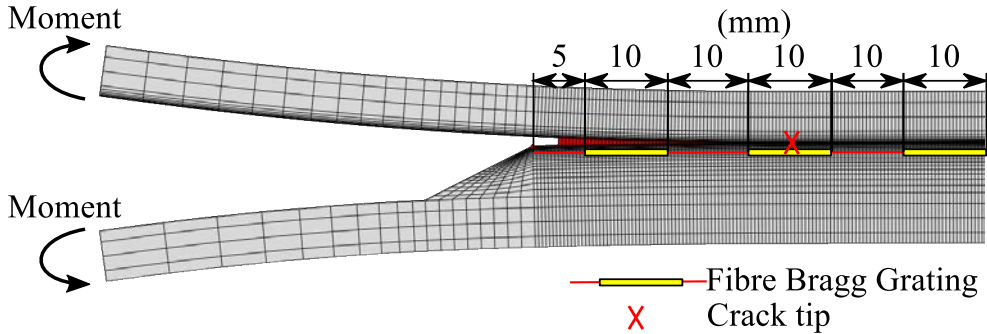
Figure P5.5: FBG array configuration in the DCB specimen.

P5.5   Illustrative Example

In this section, FBG_SiMul was used to simulate and design a delamination/crack monitoring solution based on FBG sensors. A double cantilever beam (DCB) FEM model, based on the work presented by Pereira, et al. in [3], was used to represent the delamination phenomenon. The complete FEM model description and a simulation tutorial can be found in the FBG_SiMul user-manual.

   The simulated virtual FBG array was composed of 5 gratings, spaced by 10 mm (see Fig. P5.5), and its path was a 0.03 mm line parallel with the delamination plane. Then, the FBG array spectrum response in the presence of a crack was simulated using the FBG_SiMul tab 3; and, the FBG signal response during the delamination process was simulated using the FBG_SiMul tab 4.

P5.5.1   FBG Spectrum Simulation

The reflected spectrum was simulated for a specific time increment using the FBG_SiMul tab 3-FBG Spectrum Simulation, where the crack tip was situated 36 mm from the beginning of the optical fibre, which corresponds to the middle of the second grating.

   A screen-shoot of the FBG_SiMul plot/output window is shown in Fig. P5.6, where the deformed reflected spectrum (red curves) can be compared with the original reflected spectrum (grey curves). It can be observed that the two first FBGs measure a high amount of wavelength shift ($\Delta\lambda$) and peak width variation ($\Delta\lambda_{WV}$), as a result of the presence of the crack.
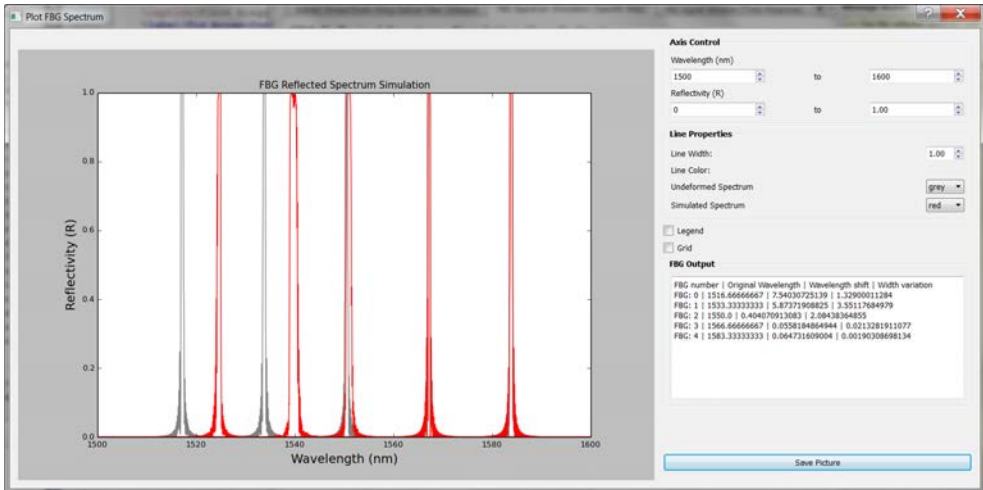
Figure P5.6: FBG_SiMul plot window: FBG reflected spectrum simulation for the non-uniform strain contribution. The five peaks are the reflected spectrum of the five FBG sensors, where the grey curves represent the unstrained state and the red curves the deformed state.

P5.5.2   FBG Time Response Simulation

The FBG response was simulated using the FBG_SiMul tab 4-FBG Signal Variation. Multiple time increments represent the delamination of the DCB specimen from an undamaged to a fully damage state. A screen-shoot of the FBG_SiMul plot/output window is shown in Fig. P5.7, where the top plot represents the wavelength shift($\Delta\lambda_{WV}$), and the bottom plot represents the peak width variation ($\Delta\lambda$). This simulation shows an increase of the $\Delta\lambda$ as the crack passes the position of the grating, caused by change in the material compliance and load distribution; and, an increase of the $\Delta\lambda_{WV}$ when the crack is near the grating, caused by a non-uniform strain field generated at the crack tip.
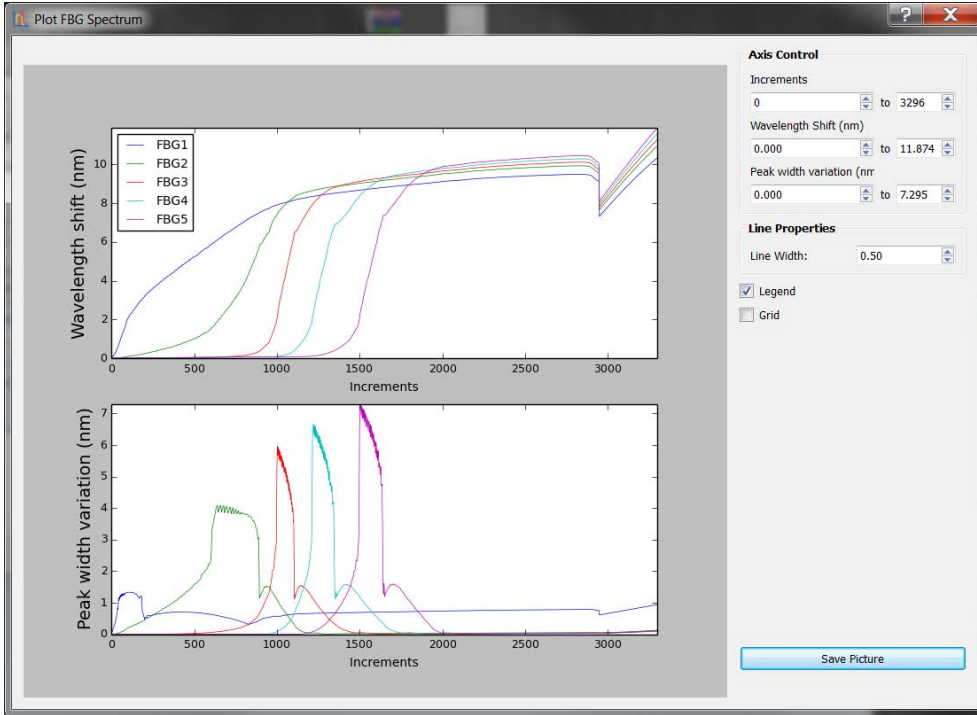
Figure P5.7: FBG_SiMul plot window: FBG time response simulation.

P5.6   Conclusions

FBG_SiMul provides the user with a tool to study and design structural health monitoring solutions based on FBG sensors. The software is divided in to 3 main tools: a tool to extract the stress and strain along an optical fibre path from a FEM model; a tool to simulate the reflected spectrum for a specific time increment; and a tool to simulate the FBG time response.

The software uses a modified version of the T-Matrix method to simulate the FBG signal from a FEM model. Thus, it can simulate the FBG response independently of the type of structure, loading or application. Also, the software removes the need for a fibre optic expert to plan and design monitoring solutions. The user interacts with the software through a user-interface, meaning that no programming knowledge is required, making parameter manipulation more intuitive to the user. Also, the input data is pre-checked by the software, meaning that the simulation is robust and does not crash or give calculation errors.

Acknowledgement

References

[1] D. F. Braga, S. Tavares, L. F. da Silva, P. Moreira, and P. M. de Castro, "Advanced design for lightweight structures: review and prospects," *Progress in Aerospace Sciences*, volume 69, pages 29–39, 2014, ISSN: 03760421. DOI: 10.1016/j.paerosci.2014.03.003.

[2] P. Takoutsing, R. Wamkeue, M. Ouhrouche, F. Slaoui-Hasnaoui, T. Tameghe, and G. Ekemb, "Wind turbine condition monitoring: state-of-the-art review, new trends, and future challenges," *Energies*, volume 7, number 4, pages 2595–2630, 2014, ISSN: 1996-1073. DOI: 10.3390/en7042595.

[3] G. F. Pereira, L. P. Mikkelsen, and M. McGugan, "Crack detection in fibre reinforced plastic structures using embedded fibre bragg grating sensors: theory, model development and experimental validation.," *PloS one*, volume 10, number 10, e0141495, 2015, ISSN: 1932-6203. DOI: 10.1371/journal.pone.0141495.

[4] H. Hu, S. Li, J. Wang, Y. Wang, and L. Zu, "Fbg-based real-time evaluation of transverse cracking in cross-ply laminates," *Composite Structures*, volume 138, pages 151–160, 2016, ISSN: 02638223. DOI: 10.1016/j.compstruct.2015.11.037.

[5] O. Hassoon, M. Tarfoui, and a. E. Malk, "Numerical simulation of fiber bragg grating spectrum for mode- delamination detection," *International Journal of Mechanical, Aerospace, Industrial and Mechatronics Engineering*, volume 9, number 1, pages 144–149, 2015.

[6] L. Bjerkan, K. Johannessen, and X. Guo, "Measurements of bragg grating birefringence due to transverse compressive forces," in *Proc. 12th Int. Conf. of Optical Fiber Sensors*, volume 16, 1997, pages 60–63.

[7] F. Jülich and J. Roths, "Comparison of transverse load sensitivities of fibre bragg gratings in different types of optical fibres," in *Optical Sensing and Detection*, F. Berghmans, A. G. Mignani, and C. A. van Hoof, Eds., volume 7726, 2010, 77261N. DOI: 10.1117/12.854019.

[8] L. Sorensen, J. Botsis, T. Gmür, and J. Cugnoni, "Delamination detection and characterisation of bridging tractions using long fbg optical sensors," *Composites Part A: Applied Science and Manufacturing*, volume 38, number 10, pages 2087–2096, October 2007, ISSN: 1359835X. DOI: 10.1016/j.compositesa.2007.07.009.

[9]   S. Stutz, J. Cugnoni, and J. Botsis, "Crack – fiber sensor interaction and characterization of the bridging tractions in mode i delamination," *Engineering Fracture Mechanics*, volume 78, number 6, pages 890–900, 2011, ISSN: 00137944. DOI: `10.1016/j.engfracmech.2011.01.014`.

[10] M. Yamada and K. Sakuda, "Analysis of almost-periodic distributed feedback slab waveguides via a fundamental matrix approach.," *Applied optics*, volume 26, number 16, pages 3474–3478, 1987, ISSN: 0003-6935. DOI: `10.1364/AO.26.003474`.

[11] K. Peters, M. Studer, J. Botsis, A. Iocco, H. Limberger, and R. Salathé, "Embedded optical fiber bragg grating sensor in a nonuniform strain field: measurements and simulations," *Experimental Mechanics*, volume 41, number 1, pages 19–28, 2001, ISSN: 0014-4851. DOI: `10.1007/BF02323100`.

[12] H.-Y. Ling, K.-T. Lau, W. Jin, and K.-C. Chan, "Characterization of dynamic strain measurement using reflection spectrum from a fiber bragg grating," *Optics Communications*, volume 270, number 1, pages 25–30, 2007, ISSN: 00304018. DOI: `10.1016/j.optcom.2006.08.032`.

[13] Y. Chen, J. Li, Y. Yang, M. Chen, J. Li, and H. Luo, "Numerical modeling and design of mid-infrared fbg with high reflectivity," *Optik - International Journal for Light and Electron Optics*, volume 124, number 16, pages 2565–2568, 2013, ISSN: 00304026. DOI: `10.1016/j.ijleo.2012.07.016`.

[14] A. Ikhlef, R. Hedara, and M. Chikh-bled, "Uniform fiber bragg grating modeling and simulation used matrix transfer method," *IJCSI International Journal of Computer Science*, volume 9, number 1, pages 368–374, 2012, ISSN: 1694-0784.

[15] K. Peters, M. Studer, J. Botsis, A. Iocco, H. Limberger, and R. Salathé, "Embedded optical fiber bragg grating sensor in a nonuniform strain field: measurements and simulations," *Experimental Mechanics*, volume 41, number 1, pages 19–28, 2001, ISSN: 0014-4851. DOI: `10.1007/BF02323100`.

P5 Appendix-A: Spectrum Simulation Theory and Algorithm

In a free state, without strain and at a constant temperature, the spectral response of a homogeneous FBG is a single peak centred at wavelength λ_b, which can be described by the Bragg condition.

$$\lambda_b = 2n_{eff}\Lambda_0 \tag{P5.1}$$

The parameter n_{eff} is the mean effective refractive index at the location of the grating, Λ_0 is the constant nominal period of the refractive index modulation, and the index 0 denotes unstrained conditions (initial state).

The change in the grating period due to a uniform strain field is described in Eq. (P5.2),

$$\Lambda(x) = \Lambda_0[1 + (1 - p_e)\varepsilon_{FBG}(x)] \tag{P5.2}$$

where the parameter p_e is the photo-elastic coefficient, and $\varepsilon_{FBG}(x)$ is the strain variation along the optical fibre direction [11]. The variation of the index of refraction δn_{eff} of the optical fibre is described by Eq. (P5.3),

$$\delta n_{eff}(x) = \overline{\delta n_{eff}} \left\{ 1 + \nu cos \left[\frac{2\pi}{\Lambda_0}x + \phi(x) \right] \right\} \tag{P5.3}$$

where ν is the fringe visibility, $\phi(x)$ is the change in the grating period along the length, and $\overline{\delta n_{eff}}$ is the mean induced change in the refractive index [11].

By the couple-mode theory, the first order differential equations describing the propagation mode through the grating x direction are given by Eq. (P5.4) and (P5.5).

$$\frac{dR(x)}{dx} = i\widehat{\sigma}R(x) + i\kappa S(x) \tag{P5.4}$$

$$\frac{dS(x)}{dx} = i\widehat{\sigma}S(x) + i\kappa R(x) \tag{P5.5}$$

The parameter $R(x)$ and $S(x)$ are the amplitudes of the forward and backward propagation modes, respectively, $\widehat{\sigma}$ is the self-coupling coefficient as function of the propagation wavelength λ, and κ is the coupling coefficient between the two propagation modes [11–13].

The self-coupling coefficient $\widehat{\sigma}$ for a uniform grating ($\phi(x) = 0$) in function of the propagation wavelength λ is described in Eq. (P5.6), where the parameter λ_b is the FBG reflected wavelength in an unstrained state defined by the Eq. (P5.1).

$$\widehat{\sigma} = 2\pi n_{eff} \left(\frac{1}{\lambda} - \frac{1}{\lambda_b} \right) + \frac{2\pi}{\lambda}\overline{\delta n_{eff}} \tag{P5.6}$$

The coupling coefficient between the two propagation modes κ is defined by Eq. (P5.7), where the parameter m is the striate visibility that is ≈ 1 for the conventional single mode FBG [12, 13].

$$\kappa = \frac{\pi}{\lambda} m \overline{\delta n_{eff}} \tag{P5.7}$$

Spectrum reconstruction

The optical response matrix of the ith (each segment) uniform grating can be described by the coupled mode theory [4, 12]. By considering the FBG length (L) divided in n short segments, then the $\Delta x = L/n$ is the length of each segment. Note that n is constrained by the grating period [12], as described by Eq. (P5.8).

$$n \leq \frac{2n_{eff}}{\lambda_b} L \tag{P5.8}$$

For the FBG length limits, $-L/2 \leq x \leq L/2$, and the boundary conditions, $R(-L/2) = 1$ and $S(L/2) = 0$, the solution of the coupling mode of Eq. (P5.5) and (P5.5) can be expressed as:

$$\begin{bmatrix} R(x_{i+1}) \\ S(x_{i+1}) \end{bmatrix} = F_{x_i, x_{i+1}} \begin{bmatrix} R(x_i) \\ S(x_i) \end{bmatrix} \tag{P5.9}$$

where $R(z_i)$ and $S(z_i)$ are the input light wave travelling in the positive and negative directions, respectively, and $R(z_{i+1})$ and $S(z_{i+1})$ are the output waves in the positive and negative directions, respectively. Thus, the TTM matrix $F_{x_i, x_{i+1}}$ for each segment (Δx) of the grating can be calculated using the Eq. (P5.10) and (P5.11).

$$F_{x_i, x_{i+1}} = \begin{bmatrix} S_{11} & S_{12} \\ S_{21} & S_{22} \end{bmatrix} \tag{P5.10}$$

$$\begin{cases} S_{11} = cosh(\gamma_B \Delta x) - i\frac{\widehat{\sigma}}{\gamma_B} sinh(\gamma_B \Delta x) \\ S_{12} = -i\frac{\kappa}{\gamma_B} sinh(\gamma_B \Delta x) \\ S_{21} = i\frac{\kappa}{\gamma_B} sinh(\gamma_B \Delta x) \\ S_{22} = cosh(\gamma_B \Delta x) + i\frac{\widehat{\sigma}}{\gamma_B} sinh(\gamma_B \Delta x) \\ \gamma_B = \sqrt{\kappa^2 - \widehat{\sigma}^2} \end{cases} \tag{P5.11}$$

Finally, the grating total response matrix F is obtained by multiplication of each segment response matrix, as described in Eq. (P5.12).
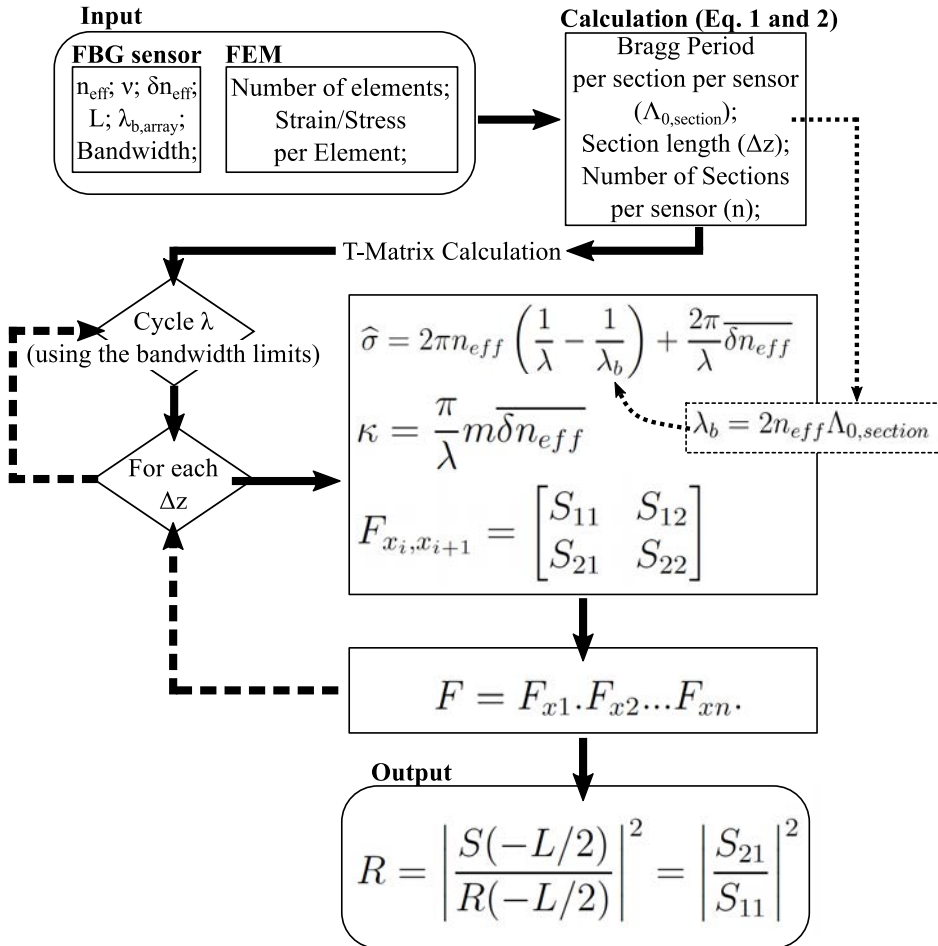
$$F = F_{x1}.F_{x2}...F_{xn}. \tag{P5.12}$$

And, the reflectance of the grating can be described by the Eq. (P5.13).

$$R = \left| \frac{S(-L/2)}{R(-L/2)} \right|^2 = \left| \frac{S_{21}}{S_{11}} \right|^2 \tag{P5.13}$$

FBG_SiMul spectrum simulation algorithm structure

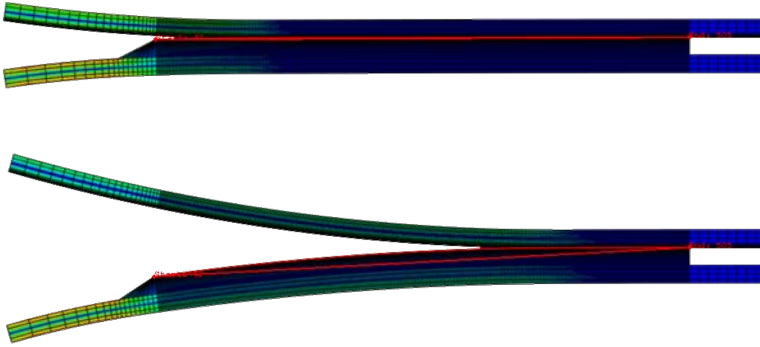The structure of the spectrum simulation algorithm implemented in the FBG_SiMul is shown in Fig. P5.8.

Figure P5.8: FBG_SiMul spectrum simulation algorithm structure.

P5 Annex: Software Example/Tutorial- Delamination of a Double Cantilever Beam

Delamination of DCB

Figure P5.9: Delamination of a Double Cantilever Beam.

In this section, the software FBG_SiMul is applied to a FEM model of delamination of a Double Cantilever Beam (DCB). Two "virtual" FBG sensor lines with an array of 5 gratings are simulated using two distinct paths.

Objectives/tasks:

- Stress/strain along two different paths;

- FBG spectrum simulation for different array configurations; FBG optimization for crack detection;

- Time response simulation during the crack growth process;

Note: The FEM model, and the input files are provided and can be found in the "InputData_Test.rar" file.

1. FEM Model

A complete description of the DCB model used can be found in Pereira, et al.[1]. The 2D Model was developed using Abaqus FEM software, and its .CAE file can be found in the FBG_SiMul webpage. It was assumed a plane stress condition, and the delamination was modelled using 4-node cohesive elements along the delamination plane. The cohesive elements were modelled to express the cohesive law, meaning a progressive loss of the cohesion between the two crack faces with the local crack opening. The crack was modelled to occur between the adhesive and the glass fibre arm beam interface, and a cohesive element size of 0.5 mm was selected. The damage initiation was calculated using a quadratic stress criterion.
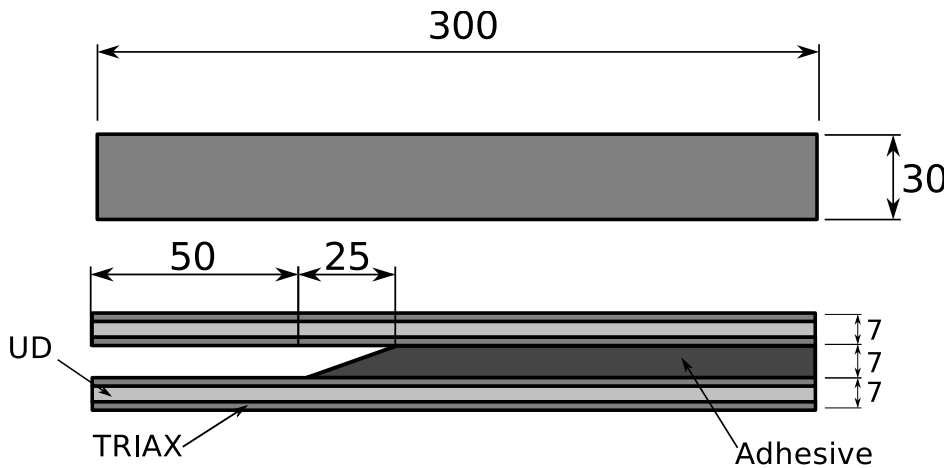
Figure P5.10: Double cantilever beam specimen dimensions. Picture taken from (doi:10.1371/journal.pone.0141495.g010).

The dimensions of the DCB specimen are shown in Fig. P5.10, and its material properties are presented in table P5.2. Note that the geometry and material properties were implemented in SI (mm) units.

The specimen beams were modelled by considering a combination of two different laminates: unidirectional glass fibre (UD) and triaxial glass fibre (Triax). Moments were applied to the extremities of the beams to create a pure mode-I opening/delamination.

---

[1] G.F. Pereira, L.P. Mikkelsen, M. McGugan, Crack Detection in Fibre Reinforced Plastic Structures Using Embedded Fibre Bragg Grating Sensors: Theory, Model Development and Experimental Validation., PLoS One. 10 (2015) e0141495. doi:10.1371/journal.pone.0141495.

Table P5.2: Double cantilever beam material properties.

Composite Material		Adhesive
Triaxial Fabric (Composite)	Uniaxial Fabric (Composite)	Elastic
$E_1 = 44.3$ GPa	$E_1 = 23.8$ GPa	$E = 4.56$ GPa
$E_2 = E_3 = 12.9$ GPa	$E_2 = E_3 = 15.05$ GPa	$\nu = 0.35$
$\nu_{12} = \nu_{13} = \nu_{23} = 0.23$	$\nu_{12} = \nu_{13} = \nu_{23} = 0.513$	
$G_{12} = G_{13} = G_{23} = 4393$GPa	$G_{12} = G_{13} = G_{23} = 4.393$GPa	

Interface (Cohesive Law)		
Penalty Stiffness	Damage (Quadratic stress)	Damage Evolution
$K = 4.2\ E12$ Pa;	$\sigma_n = 2.64$ MPa (Mode I)	$\delta_{c1} = 1.4$ (Mode I)
	$\sigma_t = 22.15$ MPa (Mode II)	$\delta_{c2} = 0.37$ (Mode II)

2. FBG Paths

Two different fibre paths will be simulated from the FEM model: one path is 0.03 mm parallel from the crack delamination plane; and the second path is 4.4 mm parallel from the crack, as shown in Fig. P5.11.
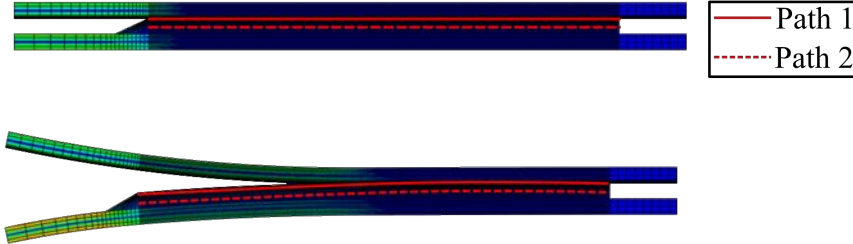
Figure P5.11: Virtual FBG paths.

The coordinates that define the crack plane and the two fibre paths are presented in table P5.3.

Table P5.3: Path points coordinates.

	Initial point coordinates (mm)	Final point coordinates (mm)
Crack	-25 , 7.572 , 0	185 , 7.572 , 0
Path-1	-25 , 7.539 , 0	185 , 7.539 , 0
Path-2	-25 , 3.161 , 0	185 , 3.161 , 0

3. Stress/strain along the paths (Tab 2)

Now, we will extract the stress and strain files using the two fibre paths. To do this, we will use the tab 2- *Extract Stress/Strain along Optical Fiber (Abaqus)*.

Stress/strain along the paths tutorial (Tab 2):

1. Station (1): Select the .odb file- MI_05.odb.

2. Station (2): Because the DCB model and the optical fibre longitudinal direction are aligned with the x axis, there is no need to rotate the coordinate system (see Fig. P5.12). Default option is selected.
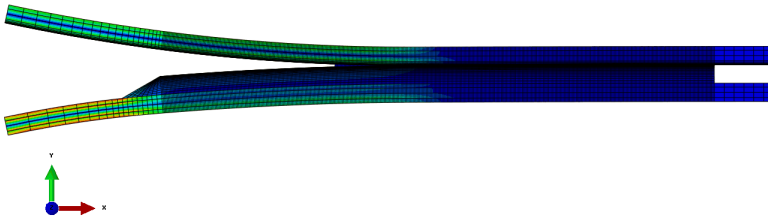

Figure P5.12: FEM axis direction.

3. Station (3): Insert the optical fibre coordinates for the two fibre paths using the values presented in table P5.3.
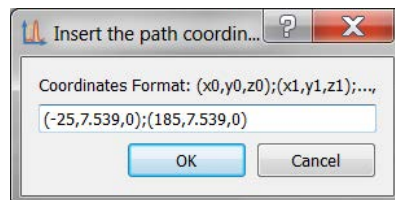
Figure P5.13: Dialogue window to insert the path coordinates: Path-1.
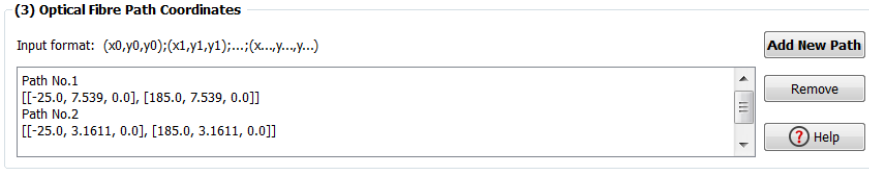
Figure P5.14: FBG virtual fibre paths.

4. Station (4): Because we want to analyse the crack growth, it is needed to extract all time increments. Select all time increments option;

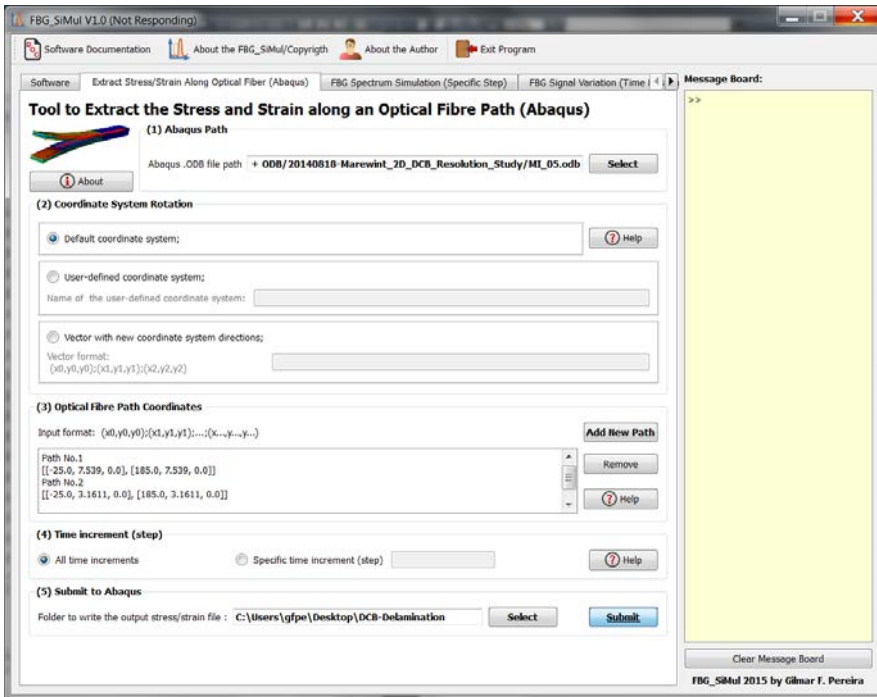5. Station (5): Select a folder to save the stress/strain files;

Figure P5.15: Tab 2: Stress and Strain along two optical fibre paths.

6. Press the push button **Submit**;

A temporary folder is created inside the selected output folder, containing an Abaqus post-processing script; Abaqus software should open and start to generate the stress/strain files. After Abaqus finish to extract the stress/strain files, close the software, and FBG_SiMul should delete the temporary folder and files, and show the following message:
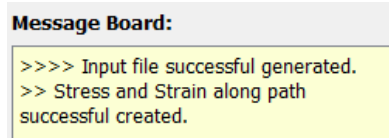
Figure P5.16: Extraction of Stress and Strain along a path completion message.

In the output folder, we can find the stress/strain files for the 2 paths and 3298 increments. The files are named as *Path**yy**_Step_**xxxx**.txt*, where **yy** is the path number and **xxxx** is the increment number.

Figure P5.17: Stress/Strain output files saved in the output folder.

4. Simulation of the Reflected Spectrum for a Specific Time Increment

In this section, we will simulate the reflected spectrum of the two FBG arrays for a specific time increment.
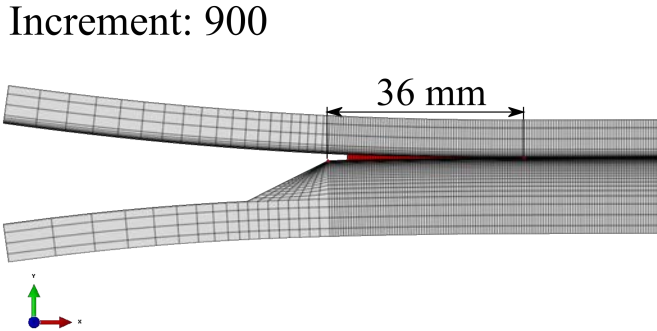
Figure P5.18: Crack tip position in the DCB specimen for the time increment 900.

At time increment **900** (see Fig. P5.18), the crack tip is located at 36 mm from the beginning of the optical fibre line. A 5 FBG array was defined as virtual measurement points, each with 10 mm of length and spaced 10 mm from each other. The first grating was defined 5 mm from the beginning of the optical fibre, as shown in Fig. P5.19.
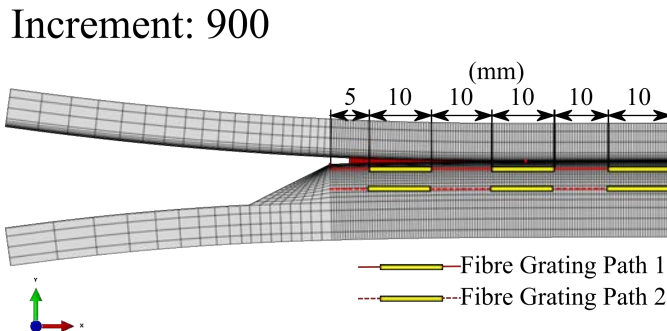
Figure P5.19: FBG array configuration in the DCB specimen.

Note that the FBG 2 is situated at the crack tip, where a large non-uniform strain field is expected, which creates a distortion on the reflected peak signal (non-uniform strain).

Reflected peak simulation tutorial (Tab 3):

1. Station (1): Insert the two files, *Path1_Step_0900.txt* and *Path2_Step_0900.txt*;

2. Select the file Path1_Step_0900.txt; it should become highlighted (see Fig. P5.20); set the skip row to **3**; toggle the input units to **mm** (units used in the FEM model).

(1) Select stress/strain files*

DCB-Delamination\Path1_Step_0900.txt	**Add Files**
DCB-Delamination\Path2_Step_0900.txt	Remove File
◄ ‖‖‖ ►	ⓘ File Format

Skip Row: 3

Input Units (Used in the fields with *)

○ SI (m)   ● SI (mm)
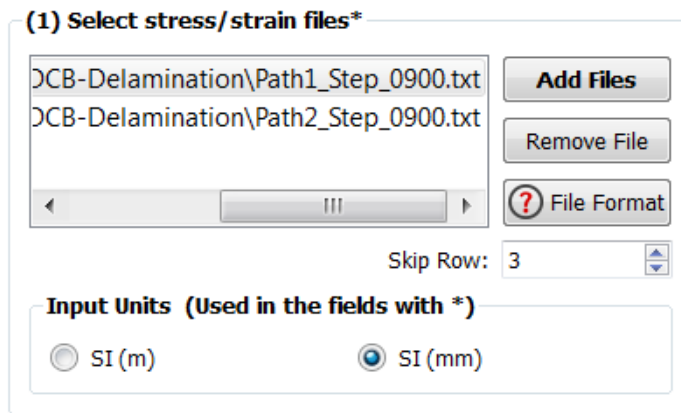
Figure P5.20: Select Stress/strain files for the time increment 900.

3. Station (2): We will analyse the three cases, but to start we will select **uniform strain**; leave the simulation resolution as the default value 0.05 nm;

4. Station (3): Leave the Optical Fibre Parameters as the default values;

5. Station (4): Set the number of FBGs per array to **5**; the FBG length to **10 mm**; the FBG longitudinal direction as **xx** (see axis of Fig. P5.19); and, leave the tolerance as the default value;

6. FBG position: Set the position of the FBG array as shown in Fig. P5.19; the distance is from the beginning of the line to the beginning of each grating; FBG position values (mm): 5; 25; 45; 65; 85;

7. Press the button **Auto** to distribute automatically the array of original wavelength (λ_b) along the available light bandwidth;

Figure P5.21: Fibre Bragg Grating Array Configuration.

8. Station (5): Toggle **"plot the undeformed FBG reflected signal"** and press the button **Simulate**;

9. If any error occurs it will be presented in the message board; then, when the loading bar reaches 100%, it means that the reflected spectrum was successfully simulated; press **Plot** to visualize it, or **Save as file** to save it as a .txt file;

10. Repeat this process to all type of simulations (uniform, non-uniform strain and transverse stress) and for both files: *Path1_Step_0900.txt* and *Path2_Step_0900.txt*;

Results: All different type of simulations for the path-1:

A screen-shoot of the plot window, containing the path-1 simulation for uniform and non-uniform strain contribution, is shown in Fig. P5.22. Then, to compare the three type of simulations, the FBG reflected spectrum data was saved as .txt file and plotted using an external software (see Fig. P5.23). The summarize FBG response for the three contributions is presented in table P5.4.
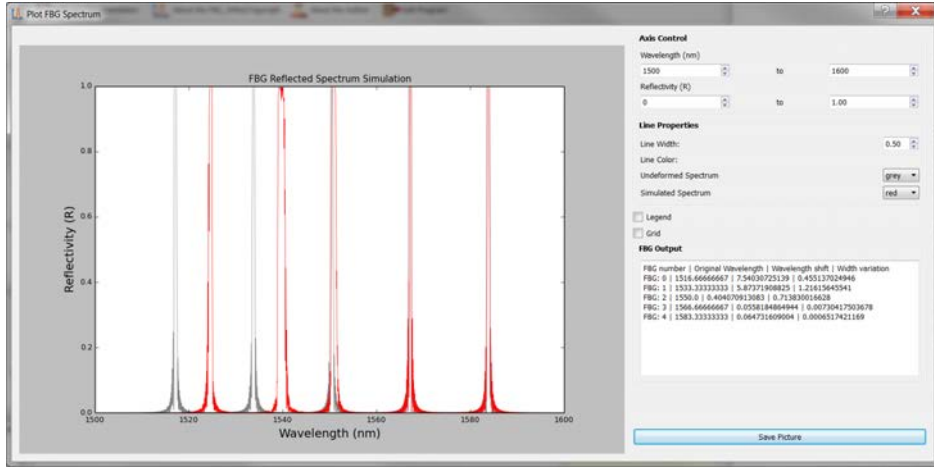
Figure P5.22: FBG_SiMul plot of the FBG simulation for non-uniform contribution.

Table P5.4: FBG array response for the time increment 900.

FBG Sensor Number	1	2	3	4	5
Original Wavelength (λ_b)	1516.66	1533.33	1550.0	1566.66	1583.33
Wavelength shift ($\Delta\lambda_b$)	7.54	5.87	0.41	0.06	0.06
Width variation ($\Delta\lambda_{wv}$)	0.45	1.21	0.71	0.01	0.01

By analysing the results of the three simulation methods, it becomes possible to determine the individual contribution of each simulation method to the sensor response. Thus, the strain field around the crack tip can be predicted and linked with the FBG response.

The uniform strain simulation describes the average longitudinal strain in each sensor. Thus, it is observed a large wavelength shift ($\Delta\lambda_b$) in the FBG 1 and 2, meaning that at this location the material is damaged and losing its compliance. In the non-uniform strain simulation, it is observed an increase of the FBG 1, 2 and 3 peak width. Particularly in FBG 2, the reflected peak is highly distorted, caused by the grating proximity with the crack tip, which causes a strain gradient (non-uniform strain). The transverse stress simulation does not show any peak splitting behaviour, as the magnitude of transverse stress is small. However, in other FEM models or loading configurations this can be different.

Based on this simulations, we can confidently say that it is the non-uniform strain field that will govern the sensor response near the crack tip;
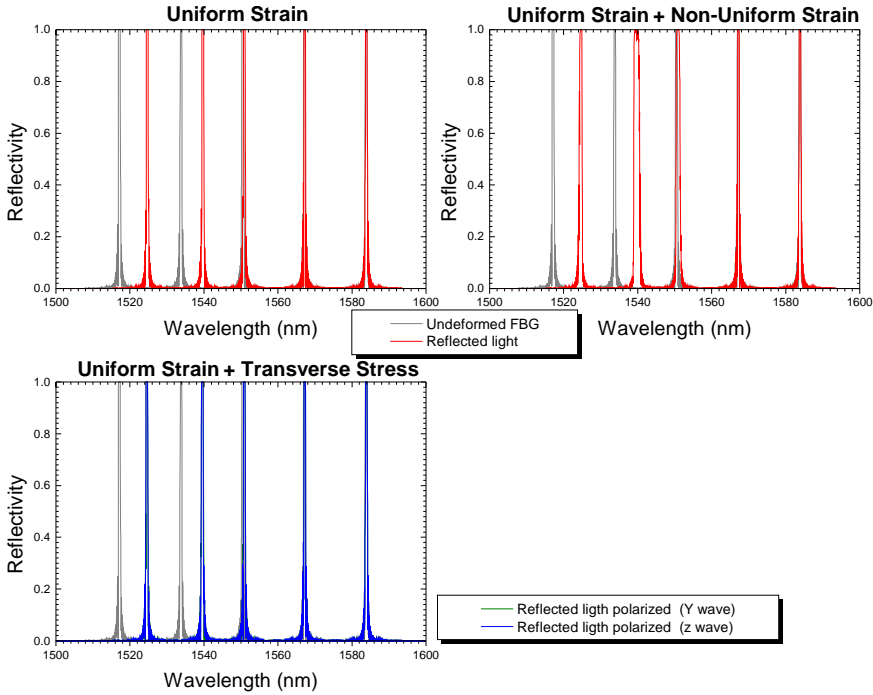
Figure P5.23: Simulate FBG reflected spectrum for the three simulation.

Results: Path-1 and Path-2 simulation comparison

Now lets focus on the FBG 2 (25 mm) and do an analyse of the two different fibre paths. The reflected peak simulation for the two FBG paths, considering non-uniform strain contribution, is shown in Fig. P5.24 and summarized in table P5.5. The shape of the reflected spectrum is similar for both paths; yet, in path-2, the wavelength shift is smaller as the path is more distant from the crack plane, resulting in a higher local compliance and less strain along the sensor. On the other hand, the strain gradient is larger in the path-2, resulting in a higher width variation ($\Delta\lambda_{wv}$).
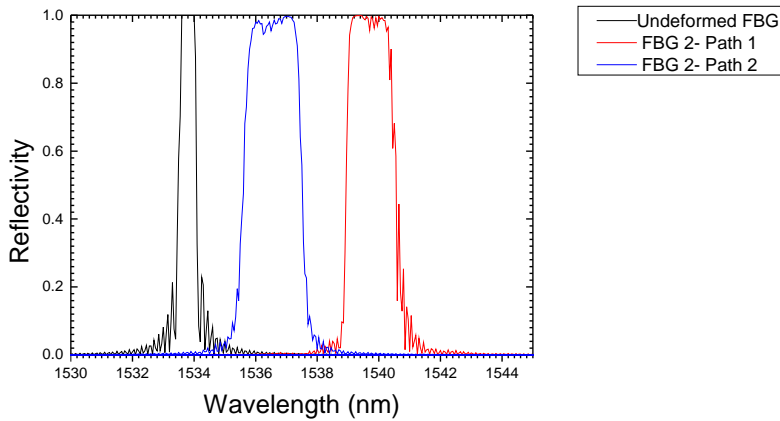
Figure P5.24: FBG 2 reflected peak simulation for the non-uniform strain contribution: path-1 and path-2 comparison.

Table P5.5: Summary of the FBG 2 reflected peak simulation for the non-uniform strain contribution: path-1 and path-2 comparison.

FBG Sensor N.2	Path-1	Path-2
Original Wavelength (λ_b)	1533.33	1533.33
Wavelength shift ($\Delta\lambda_b$)	5.87	2.80
Width variation ($\Delta\lambda_{wv}$)	1.21	1.56

Initially, the path-1 seemed more obvious to detect crack, however its proximity with the crack can promote the damage of the sensor. Thus, this simulation shows that a FBG array along the path-2 can also detect a crack successful, however it minimise the risk of damaging the sensor. Also, it can be concluded from this simulation result (similar conclusions as presented by Pereira, et al.[2], that the FBG output parameters, wavelength shift ($\Delta\lambda_b$) and width variation ($\Delta\lambda_{wv}$), can be used to determine the presence of the crack and to track its growth. The wavelength shift is a parameter connected to the strain level in the structure, in which a rapid increase of its magnitude is caused by a damage event that reduced the stiffness of the structure. In contrast, the width variation of the reflected peak is a parameter that only depends on the presence of the crack, independent of geometry and loading type. The width of the reflected peak increases when the crack is near the grating area, being low in

---

[2]G.F. Pereira, L.P. Mikkelsen, M. McGugan, Crack Detection in Fibre Reinforced Plastic Structures Using Embedded Fibre Bragg Grating Sensors: Theory, Model Development and Experimental Validation., PLoS One. 10 (2015) e0141495. doi:10.1371/journal.pone.0141495.

magnitude before and after the crack passes.

5. Simulation of the FBG Time Response

In this section, we will simulate the time response for the two FBG paths. The FBG array configuration is the same as presented in Fig. P5.25.

FBG Simulation tutorial (Tab 4):

1. Station (1): Insert all step files of the path-1 (later, repeat the tutorial for the path-2);

2. If the files are not sorted press the button **Sort**;

3. Station (2): Leave the optical fibre parameters as the default values;

4. Station (3): Set the number of FBG per array to **5**; the FBG length to **10 mm**; the FBG longitudinal direction as **xx**; and, leave the tolerance with the default value;

5. FBG position: Set the position of the FBG array as shown in Fig. P5.19; the distance is from the beginning of the line to the beginning of the grating; FBG position values (mm): 5; 25; 45; 65; 85;

6. Press the button **Auto** to distribute automatically the array original wavelength (λ_b) along the available light bandwidth;

Figure P5.25: Fibre Bragg Grating Array Configuration.

7. Station (4): Press the button **Generate**; this can take some time as the software have to load multiple files;

8. If any error occurs it will be presented in the message board; when the loading bar reaches 100% the FBG time response was successfully simulated; press **Plot** to visualize it or **Save as file** to save it as a .txt file;

9. Repeat this process for the path-2;
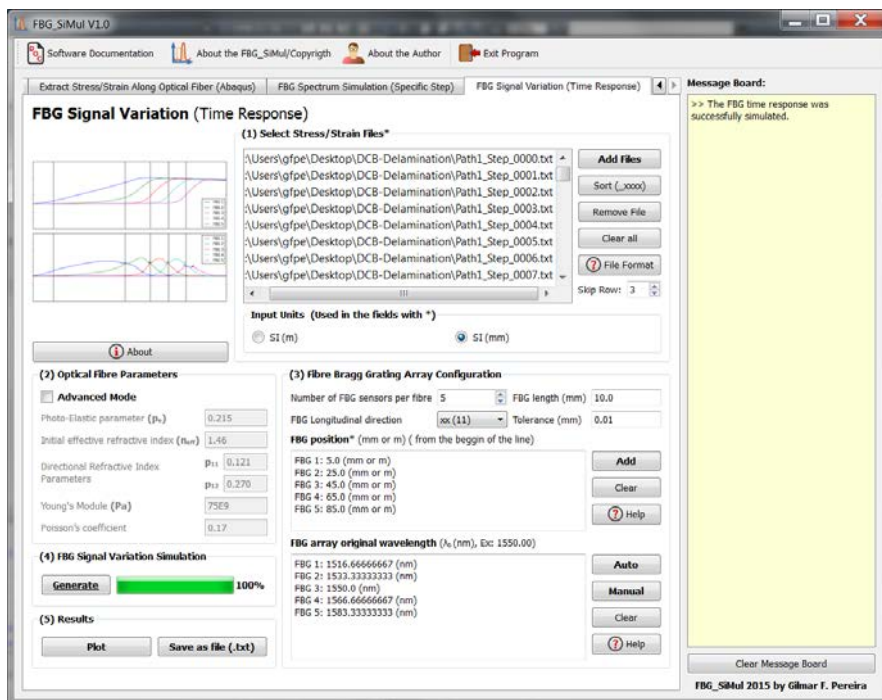
Figure P5.26: Tab 4: Time response simulation input.

Results: Paths comparison
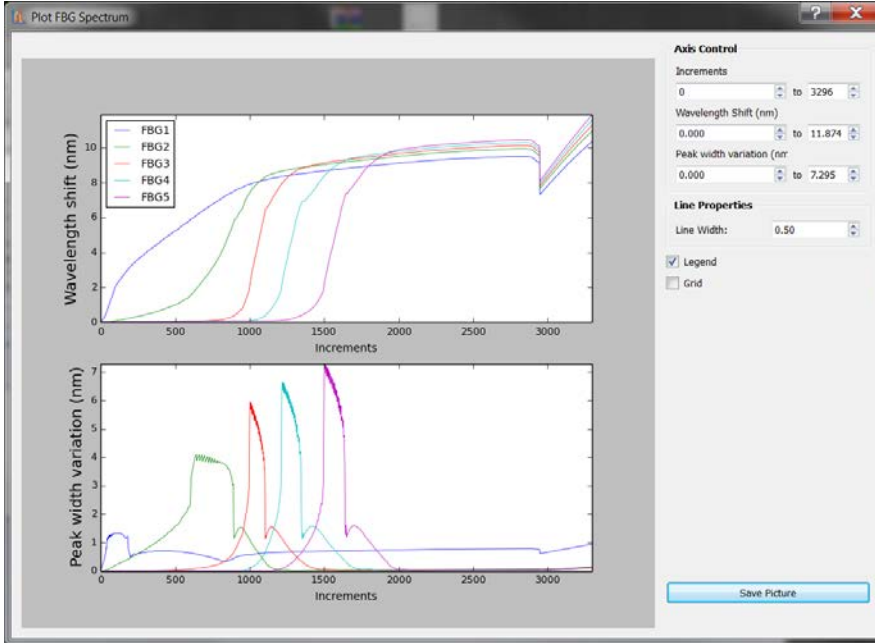
Figure P5.27: Path-1 FBG time response plot.

The FBG_SiMul plot window showing the FBG time response for the path-1 is shown in Fig. P5.27. The top plot shows the wavelength shift $\Delta\lambda_b$ caused by the longitudinal strain along the optical fibre, and the bottom plot shows the width variation of the reflected peak $\Delta\lambda_{wv}$ caused by the non-uniform strain and transverse stress.

A jump in the wavelength shift $\Delta\lambda_b$ can be observed when the crack passed the position of the grating. The damage/crack changes the material's local compliance and the load distribution, making the area that surrounds the sensor less stiff and more deformed; therefore, an increase in the strain was measured. However, it is possible to observe some differences in the evolution (shape) of the wavelength shift $\Delta\lambda_b$ from each FBG, because the sensor and the crack position related to the applied moments is different. It is also observed that a variation in the width of the reflected peak $\Delta\lambda_{wv}$ occurs when the crack is near the grating, and that the original peak width is restored after the crack passes the grating.

The FBG time response for the two fibre paths is shown in Fig. P5.28. As expected, both paths show the same type of response, however the magnitudes are lower for the path-2. Due to its proximity with the crack, the gratings in the path-1 measure larger variation of the reflected peak width. However, the path-2 can also detect cracks successful, minimizing the risk of damaging the sensor.
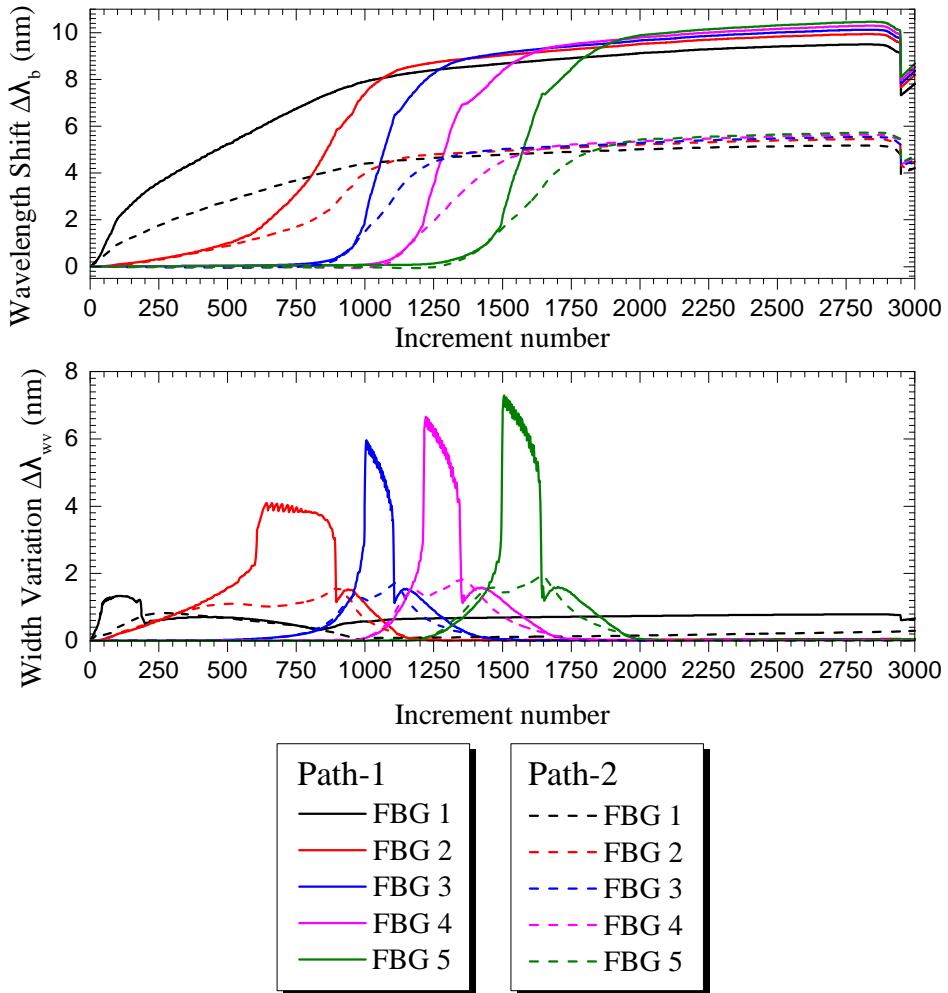
Figure P5.28: FBG time response plot: path-1 and path-2 comparison.

Cure-Induced Strains and Fatigue Performance of Unidirectional Glass Fibre Reinforced Epoxy

G. Pereira, J. Hüther, L.P. Mikkelsen, P. Brøndsted, *Cure-induced strains and fatigue performance of unidirectional glass fibre reinforced epoxy*, 2016
Draft Version, to be submitted later.

Draft

Abstract

During the curing process, an epoxy resin system undergoes a change in its chemical structure causing it to shrink. If this shrinkage happens in a liquid state, this will result in a volumetric dimension change without any mechanical/structural consequence; if it occurs in a non-liquid state, a permanent change in its structure is created, called residual strain, which can have an impact on the materials performance. Based on this, the article was divided in two parts to study the effect of the cure-induced residual strain on the fatigue and static performance of epoxy and FRP materials. In the first part of this article, it is demonstrated that the curing temperature have an impact on the total amount of residual strain; and in the second part, it is shown that the curing temperature have an impact on the materials fatigue performance. FBG sensors were used to measure the evolution of the residual strain during the curing process, and three different curing temperatures, 40^oC, 75^oC and 110^oC, were analysed.

P6.1   Introduction

The load carrying materials in modern wind turbine rotor blades are based on unidirectional glass fibre reinforced polymers (FRP) with fibres oriented along the main loading direction of the wind turbine rotor blade. As the FRP can be tailored to match the structure stress requirements, a high stiffness to weight ratio is obtained. The most common manufacturing procedure of large turbine rotor blades is based on vacuum assisted resin transfer moulding infusion technique, where the resin is infused in non-crimp unidirectional fabric containing a small amount of off-axis oriented fibres.

The fatigue performance and material stiffness are the key requirement, from a materials perspective, used to design large wind turbine rotor blades [1]. Even though, the unidirectional fibre bundles dominate the load carrying laminates, the off-axis oriented fibres bundles (backing bundles) are suspected to trigger the fatigue failure mechanism [2, 3], which can be intensified by the presence of residual stress. The residual stress or process-induced stress can be described as that stress present within a material in the absence of external loading or thermal gradients; and, in a thermoset polymer, the residual stress can be caused by a variety of reasons, but is generally connected with the manufacturing stage [4]. At this stage, the residual stress is caused by the chemical shrinkage of the polymer [5–7]. When the thermoset components are mixed, each molecule occupies a certain volume defined by their physical interactions and atomic motion; then, during the curing process these molecules will form covalent bonds resulting in a closer packing of the molecules, thereby decreasing the occupied volume by the so called curing shrinkage [6]. When the compliant matrix material shrinks between the stiff fibres, residual stresses are building up into the laminate.

Interaction between the residual stresses and the mechanical performance of FRP has been studied by a number of authors. Nakamura, et al. [8] show that the thermal residual stress have an effect on the matrix yielding and Huang, et al. [9] demonstrate that the ultimate strength of a fibre reinforced polymer material decreases as the residual stress increases. Devè [10] and Gascoigne [11] discuss in their work the phenomenon of matrix cracking induced by residual stress. Thus, the residual stress is a critical factor that should be taken into consideration during design of FRP structures, as it can influence the material mechanical performance.

Therefore, a full understanding of how the residual stress develops during the manufacturing process is becoming an emergent research topic. However, a direct link between the cure-induced residual stresses and its impact on the FRP fatigue performance is still missing. However, there is some evidences in literature showing that the residual stress can influence the materials properties; Warnet [12] observed a relation between transverse cracking and the level of residual stresses, and Asp, et al. [13] observed that the presence of residual stress creates a hydrostatic stress state around the fibres, which induces a more brittle crack growth. In this work, it is analysed a non-crimp unidirectional glass fibre fabric and an epoxy matrix, which represents a typical material system used in the wind turbine rotor blade industry. The focus is to study the influence of different curing cycles on the shrinkage of the matrix, and consequently its effect on the fatigue performance. The neat resin shrinkage is measured by two methods: a simple density measurement; and, by measuring the residual strain using a fibre Bragg grating. By combining these two measurement methods, it is possible to evaluate the shrinkage before the gel time, in a liquid state, and the shrinkage after the gel point, in a solid state. Then, following the same curing cycle profiles, specimens made of neat resin and FRP are tested in tensile and constant load fatigue.

P6.2   Experimental Procedure

P6.2.1   Residual Strain Measurement

During the curing process two different stages can be distinguished: shrinkage before the gel time, in a liquid state; and shrinkage after the gel point, in a non-liquid state. Before the gel point, the epoxy is in a liquid state, meaning that the reacting material can move freely and no permanent strain is created. However, after the gel point the material builds up permanent deformation, where its magnitude is defined by the material chemical shrinkage. Based on this, the total chemical shrinkage of an epoxy system can be quantified by performing volumetric variation measurements, before and after the cure; and, the amount of shrinkage that takes place after the gel point can be determined by performing residual strain measurements during the cure process.

Volumetric variation measurements

A variety of techniques have been applied to measure the volumetric change of a cross-linking resin. In mercury-based dilatometers [14–16], the resin specimen is cured submerged in an immiscible fluid and when the resin shrinks the fluid level change; in gas based pychometers the Boyle's law is used to measure the epoxy volumetric variation during the cure process [17]; or more recently, the rheometer technique [6, 17, 18] was used to measure real-time chemical shrinkage, by curing the resin between two rotating plates and measuring the gap variation between them. Real-time and in-situ measurements are the main advantage of these techniques, however these methods require expensive test equipments and skill operators.

$$\rho = \frac{m}{V} \tag{P6.1}$$

By considering that during the curing process any mass loss is so small that can be neglected and the conventional density formula given by Eq. (P6.1), then the density variation is inversely proportional to the volumetric variation. Thus, measuring the epoxy density before and after the curing process is the simplest and fastest method to obtain the total amount of chemical shrinkage [19, 20]. Although, it is not possible to evaluate the volumetric variation along the curing process (real-time measurement) with this method.

Density measurement procedure

The volumetric variation ($\Delta V = V_{final}/V_{initial}$) can be calculated, as shown in Eq. (P6.2), by measuring the epoxy density before ($\rho_{initial}$) and after the cure (ρ_{final}).

$$\Delta V = \frac{\rho_{initial}}{\rho_{final}} \tag{P6.2}$$

The initial density of the liquid epoxy can be calculated from the density of its constituents (the base and its hardener), by using the rule of mixture:

$$\rho_{initial} = \rho_{base}\nu_{base} + \rho_{hardener}(1 - \nu_{base}) \tag{P6.3}$$

where $\rho_{base} = 1.142\ g/cm^3$, $\rho_{hardener} = 0.9345\ g/cm^3$, and the volume fraction ν_{base} is given by Eq. P6.4.

$$\nu_{base} = \left(1 + \frac{\rho_{base}}{\rho_{hardener}} \left(\frac{1}{w_{base}}\right)\right)^{-1} \tag{P6.4}$$

Then, by considering a weight ratio $w_{base} = 100/34$, it is obtained an initial density of 1.081 g/cm^3. The final density (ρ_{final}) was measured using the Balance Mettler Toledo XS400 in buoyancy-mode.

Residual strain in non-liquid state

Different measurement techniques have been used to measure the evolution of the cure-induced residual strain during the curing process. In the X-ray diffraction technique [21], small metallic particles are added to the FRP specimen and the stress in these particles are measured by applying X-ray diffraction; in Raman spectroscopy [22], scattered light is used to measure the vibrational energy level of the chemical bonds; in the photo-elasticity method [23], the residual stress components are calculated by means of the stress-optic Brewster's Law; and in the acoustic wave method [24, 25], the residual stress is measured by evaluating the variation on the acoustic wave polarization and propagation speed. However, these methods have some limitations, for instance low measurement precision, expensive test equipment, or simply that they cannot be applied to real-time residual strain measurements.

Measurement systems based on optical fibre technology are a promising technique to evaluate the residual strain evolution during the curing process [26, 27]. Due to its small diameter, 125 μm, the sensor can be embedded in the resin without compromising its mechanical behaviour, and as the measured information is encoded as a light resonance wavelength the system have immunity to optical/power fluctuation, isolation and immunity to electromagnetic fields [28, 29]. Additionally, an embedded sensor can detect different phenomena occurring during the curing process, for example: the gel point, by evaluating the moment when the stress starts to build up; the vitrification point, when the sensor stops registering residual strain variations; and, the epoxy thermal contraction coefficient, by evaluating the cool-down stage [7].

An improved method to measure the residual strain using fibre Bragg grating sensors is presented in appendix-A of this article, where a new measurement methodology allows to decouple the temperature-strain cross sensitivity and to determine the gel point and residual strain with a high precision.

P6.2.2   Material System

The composite material investigated is based on the following 6 ply layup $[\pm 45/(b/0)2]_s$, where the b indicates the position of the backing layer. The following high modulus Ahistrom glass fibre fabric is used

- (b/$\pm$45): 600 g/m^2 non-crimp $\pm$45º direction 600 tex rowing stitched on a 100 g/m^2 random oriented chopped backing;

- (b/0): 1150 g/m^2 non-crimp 0º direction 2400 tex rowing stitched on a 100 g/m^2 $\pm$45º backing;

The plates were made by hand lay-up of dry fibre fabric, followed by vacuum infusion of an epoxy impregnation. The epoxy is composed by Aralide LY 1564SP and the hardener XB3486 from Huntsman mixed 100:34 parts by weight, followed by degassing under vacuum. The resulting thickness of the laminate is approximately

4.5 mm. In addition to the laminate, neat resin samples were manufactured based on the epoxy mixture, both in the shape of plates for mechanical testing and as tubes for residual strain and density measurements.

Three different curing cycles were performed, as shown in Fig. P6.1, which will be referred throughout the article as:

- Cure A 40°C - Two-stage curing at 40°C for min. 18 hours followed by a post-cure cycle at 75°C min. 5 hours;

- Cure B 75°C - Single-stage curing at 75°C for minimum 3 1/3 hour;

- Cure C 110°C - Single-stage curing at 110°C for minimum 3 1/3 hour;
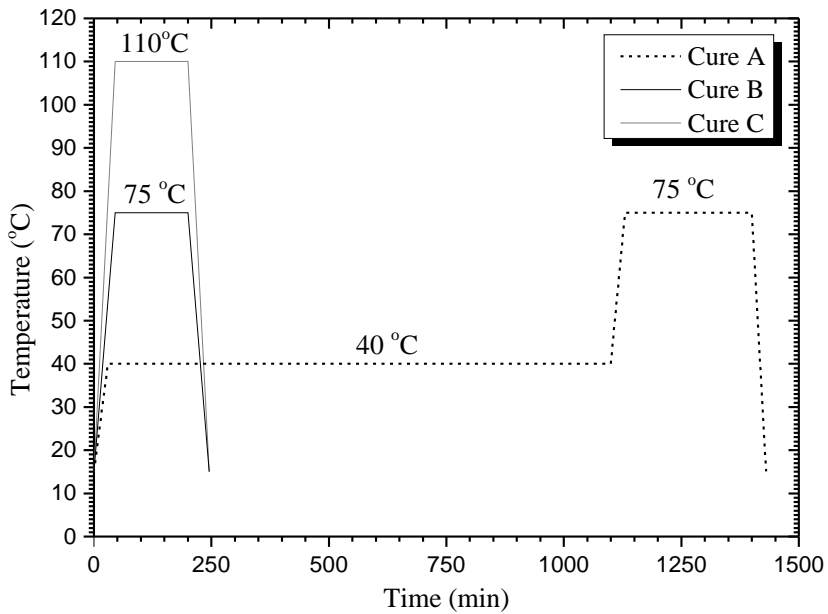
Figure P6.1: Epoxy curing profiles: temperature settings. The dashed line represents the cure profile A, the solid black line the cure profile B, and the grey line is the cure profile A.

P6.2.3   Curing of Neat Epoxy: Residual Strain

The experimental set-up used to measure the cure-induced residual strain is shown in Fig P6.2. Silicone shaped tubes, made of Elastosil M 4670 A/B from Wacker silicones, were used to hold the epoxy resin during the curing process. It was selected silicone due to its ability to follow the expansion/contraction of the epoxy, minimizing any displacement constrains.
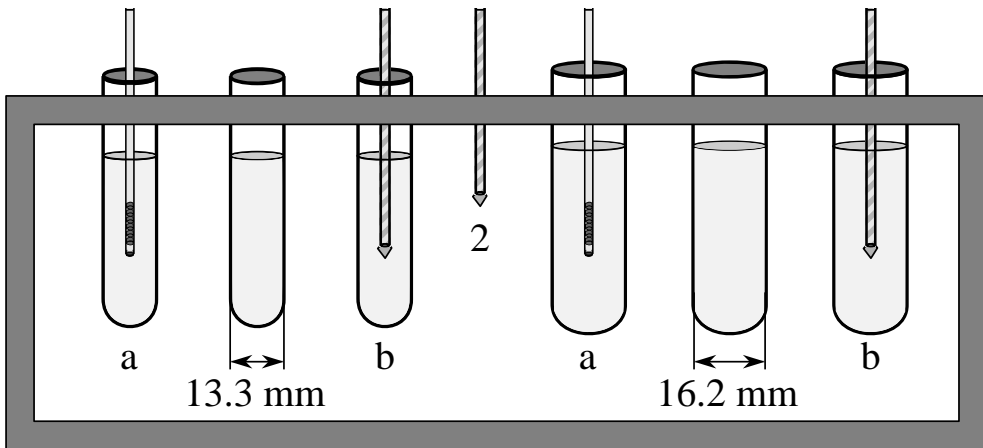
a: FBG sensor
b: Thermocouple

Figure P6.2: Experimental set-up for cure-induced residual strain measurement. Two sets of 3 silicon tubes with 13.3 mm and 16.2 mm of diameter; a-Silicon tube with embedded FBG sensor; b- Silicon tube with embedded thermocouple; 2- Thermocouple to monitor the furnace temperature.

Two sets of 3 silicon tubes, with a diameter of 13.3 mm and 16.2 mm, were used per curing cycle analysed. By increasing the tube diameter, and consequently the amount of resin, this will result in a more intense curing reaction with more heat being generated; thus, different exothermic peak magnitudes are obtained for the same cure temperature, allowing to study its effect on the residual strain. For each set of three tubes, one was instrumented with a thermocouple to measure the resin temperature, and other tube was instrumented with a FBG sensor. Both FBG sensor and thermocouple were aligned in the centre of the tube, and the temperature between tubes with the same diameter was considered similar, as the geometry, the resin quantities, and the sensor position were the same. In the third tube, no sensors were

installed (pure resin only), which later was used for the density measurements. The temperature in the furnace was measured at two different locations, by thermocouples, to ensure that the heat was distributed homogeneously. Uncoated single mode FBG sensors with a grating length of 10 mm were used to perform the measurements. Each sensor was cut to an appropriate length, cleaned and seized to increase the adhesion to the resin. The FBG sensor signal was acquired at a rate of 1HZ using a FS2200-Industrial BraggMeter supplied by HBM-FiberSensing^{TM}. The optical fibre parameters used in the measurements are shown in table P6.1.

Table P6.1: Fibre Bragg Grating: optic and mechanical parameters.

Fibre Bragg Grating Parameters	
Photo-elastic coefficient (p_e) [30]	0.22
Thermo-optic coefficient (ξ) [30]	8.3E-6
Thermal expansion coefficient (α_f) [30]	$0.55\times 10^{-6} \ \varepsilon/K$
Wavelength peak (λ)	1517.20; 1532.20; 1548.05; 1562.38 (nm)

P6.2.4   Specimens Configuration

Neat Resin Specimens: for Static Test

Neat resin specimens for static test were produced using the same epoxy system, Aralide LY 1564SP/ XB3486 Huntsman epoxy system, and cut following the international standard ISO 527-2 (standard 1993), as shown in Fig. P6.3. For each cure profile, 5 (five) specimens were produced and tested.
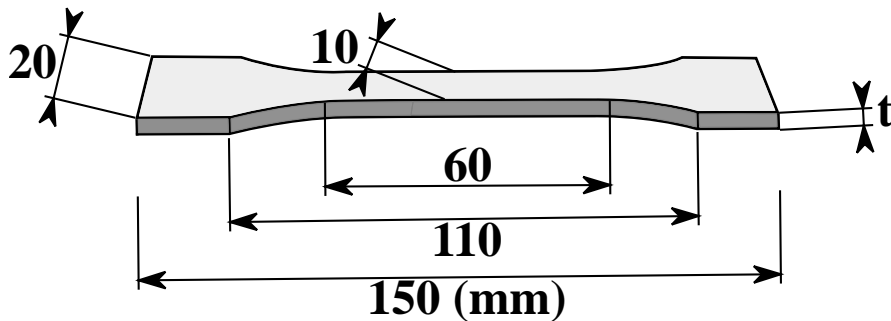
Figure P6.3: Neat resin specimen geometry, based on the international standard ISO 527-2.

Fibre Reinforced Epoxy Specimens: for Static and Fatigue Test

The fibre reinforced polymer (FRP) specimens were cut from the laminate plate into butterfly shaped specimens, as shown in Fig. P6.4. This geometry was developed by DTU Wind Energy [2] and it is optimised for testing UD composite materials, as standard plane specimen geometries tend to fail outside the gauge area. A total number of 12 specimens were manufacture for each cure profile, where 3 were used for the tensile testing and 9 for the fatigue testing.
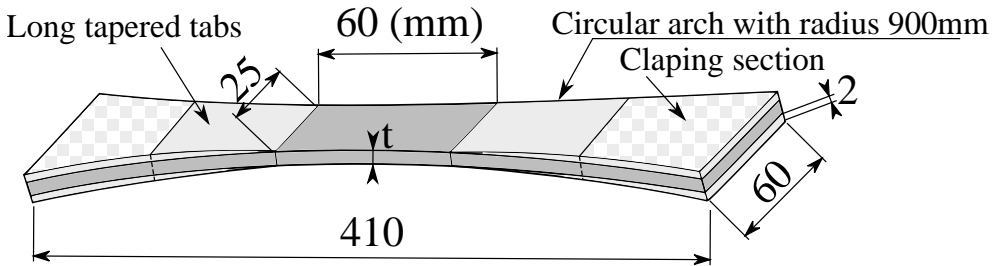
Figure P6.4: Fibre reinforced polymer specimen geometry.

P6.2.5   Tensile and Fatigue Test Procedure

The tensile (quasi-static) and fatigue test procedure are based on the standardized method ISO 527, and its different testing parameters are summarised in table P6.2.

Table P6.2: Tensile and Fatigue Test Procedure based on the standardized method ISO 527.

	Tensile (Quasi-static) Test	Fatigue Test
Specimen tested	Neat resin & FRP	FRP
Test machine	Servo hydraulic Instron	Servo hydraulic Instron
Load cell	5 kN	100 kN
Monitoring	Extensometers $50/\pm2.5$ mm	Extensometers $50/\pm2.5$ mm
Control mode	Stress	Stress
Speed Rate	2 mm/s	-
Frequency	-	5 Hz
Stress waveform	-	Sinusoidal
Stress ratio R	-	0.1
Max. initial strain	-	Varying

P6.3 Experimental Results

P6.3.1 Density Measurements

The density of the cured specimens (ρ_{final}) measured by the buoyancy method are shown in table P6.3. All the curing cases show similar density values, leading to a total volume variation ratio of 0.94 ($V_{final}/V_{initial}$), as shown in Eq. (P6.5). Thus, it can be concluded that the variation of density and consequently the total variation of volume (total shrinkage) are not affected by the curing temperature.

$$\frac{V_{final}}{V_{initial}} = \frac{\rho_{initial}}{\rho_{final}} = \frac{1.08 \ g/cm^3}{1.15 \ g/cm^3} = 0.94 \qquad (P6.5)$$

Table P6.3: Density measurements for the 3 curing cycles.

Curing Cycle	Tube Diameter	Density g/cm^3	Deviation g/cm^3
A: 40° C	13.3 mm	1.149	0.001
	16.2 mm	1.150	0.001
B: 75° C	13.3 mm	1.150	0.001
	16.2 mm	1.150	0.001
C: 110° C	13.3 mm	1.149	0.001
	16.2 mm	1.150	0.001

P6.3.2 Residual Strain (non-liquid state)

The strain and temperature evolution during the curing process for the profile A and B are presented in Fig. P6.5. The strain was calculated by applying the Eq. (P6.14) and (P6.15) (presented in appendix A) to the wavelength shift measured by the embedded FBG sensor and the temperature from the embedded thermocouple. The solid line represents the temperature measured by the thermocouple embedded in the resin, and the dashed line the temperature in the furnace.

To describe and quantify the strain and temperature evolution in all the tested cases, key parameters (a, b, c, d and e) were identified from the measurements, as shown in Fig. P6.5. The parameter a is the gel point time (in min); b is the final residual strain (ε in %); c is the chemical shrinkage (ε in %), i.e., the residual strain that is formed at a constant furnace temperature; d is the thermal contraction strain (ε in %), caused by the cooling of the material after the curing process; e is the exothermic peak (in ^{o}C) measured inside the resin.

Cure profile C: 75°C

Cure profile B: 40-75°C
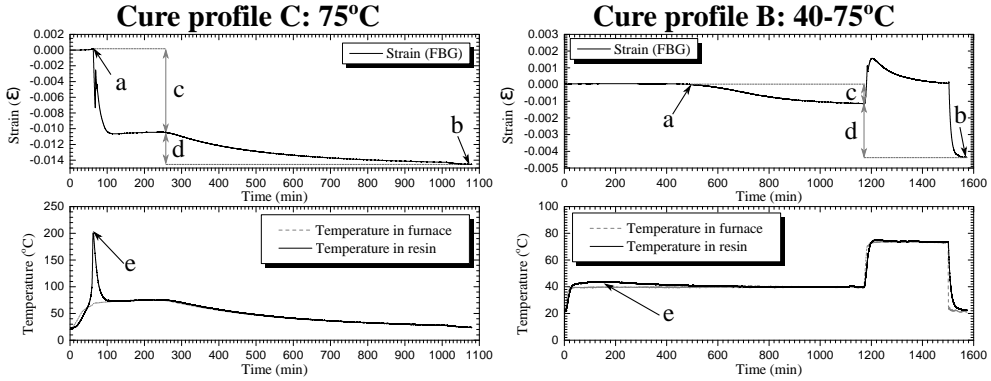
Figure P6.5: Strain and temperature measurements during the curing process: Cure profile B (75°C) and cure profile B (40-75°C). a- gel point; b- final residual strain; c- chemical shrinkage as strain; d- thermal contraction as strain; e- exothermic peak, maximum temperature measure in the resin.

The residual strain and temperature key parameters measured during the three curing cycles are presented in table P6.4.

Table P6.4: Residual strain and temperature measurements during curing process: Cure cycle A, B and C.

Curing cycle	Tube Diameter	a: Gel point (min)	b: Residual strain $\varepsilon(\%)$	c: Chemical Shrinkage $\varepsilon(\%)$	d: Thermal contraction $\varepsilon(\%)$	e: Exoth. peak (°C)
A: 40°C	13.3 mm	496.9	0.44	0.11	0.33	44.0
	16.2 mm	457.2	0.44	0.12	0.32	45.4
B: 75°C	13.3 mm	31.5	1.31	0.89	0.42	192.3
	16.2 mm	31.9	1.44	1.04	0.40	200.9
C: 110°C	13.3 mm	19.6	1.24	0.518	0.722	251.3
	16.2 mm	19.4	0.82	0.215	0.605	264.7

P6.3.3   Quasi-static Tensile Test

The tensile properties of the neat resin specimens, presented in Fig. P6.6 and table P6.5, show similar Young's modulus for all the curing temperatures and rather similar maximum stress. Thus, no relation between the curing temperature and the static properties was found.
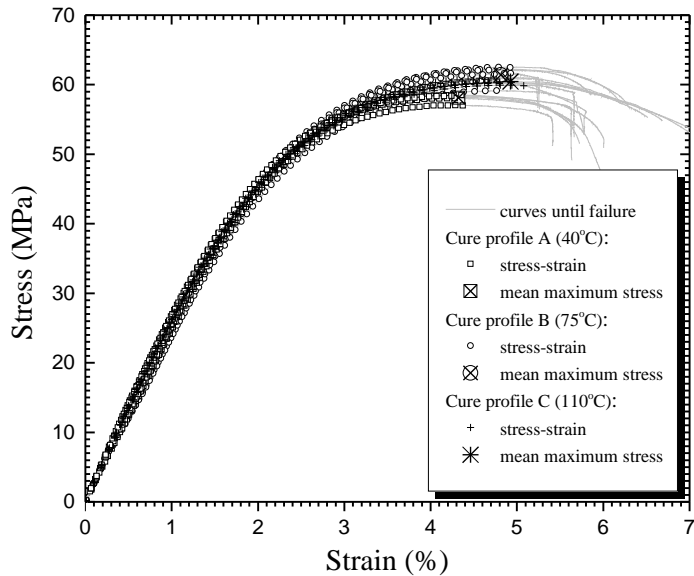
Figure P6.6: Experimental tensile test stress-strain curve of neat resin specimens produced by the cure profile A, B and C. The grey curves represent the stress-strain until failure and the symbols the stress-strain curve until the maximum stress. The large symbols represent the mean value of the maximum stress obtain in each set.

Table P6.5: Static test properties: Neat resin and FRP specimens..

	Neat Resin Specimens		**FRP Specimens**	
Curing cycle	Young's modulus (GPa)	Max. Stress (MPa)	Young's modulus (GPa)	Max. Stress (MPa)
A: 40°C	2.76 (S=0.1)	58.1 (S=0.5)	37.5 (S=0.2)	1009 (S=7)
B: 75°C	2.71 (S=0.1)	61.4 (S=1.2)	38.4 (S=0.6)	987 (S=26)
C: 110°C	2.79 (S=0.1)	60.5 (S=0.4)	36.5 (S=0.34)	968 (S=11)

The FRP specimen tensile test results are shown in Fig. P6.7 and summarised in table P6.5. It can be observed a small variation on the Young's modulus and maximum stress, when compared with the neat resin specimen. Yet, this can be justified by small variations on the fibre fraction ratio caused by manufacturing uncertainties, as the Young's modulus and maximum stress properties of a FRP specimen are driven by the fibre/reinforcement properties.
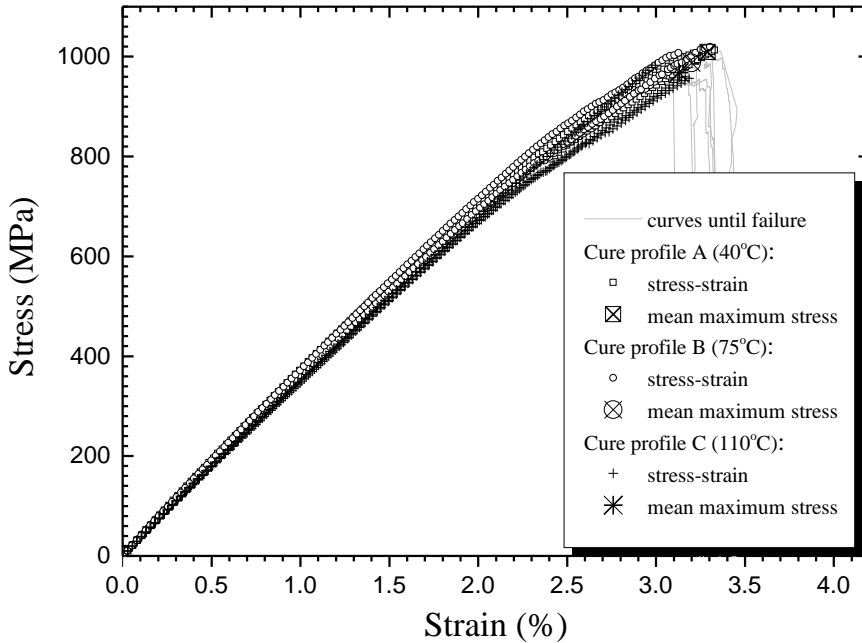

Figure P6.7: Experimental tensile test stress-strain curve of neat resin specimens produced by the cure profile A, B and C. The grey curves represent the stress-strain until failure and the symbols the stress-strain curve until the maximum stress. The large symbols represent the mean value of the maximum stress obtain in each set.

P6.3.4   Fatigue Test

The Wöhler curves (fatigue SN curves) of the FRP specimens produced by the cure profile A, B and C are shown in Fig. P6.8, where the points represent the number of cycles that the specimen experienced before failing. Each curve series was fitted with the Basquin Eq. (P6.6), obtained by following the guidelines provided in ASTM E739-10.

$$\varepsilon(N) = aN^{(1/m)} \tag{P6.6}$$

The parameter N is the number of cycles, ε represents the maximum initial strain in the first undamaged fatigue cycle, a and m are the Basquin constants. The fatigue results, presented in Fig. P6.8 and table P6.6, show that the fatigue performance of FRP decreases for specimens produced with higher curing temperature. This suggests that the fatigue performance of a structure produced by an epoxy system strongly depends on the amount of cure-induced residual stress.
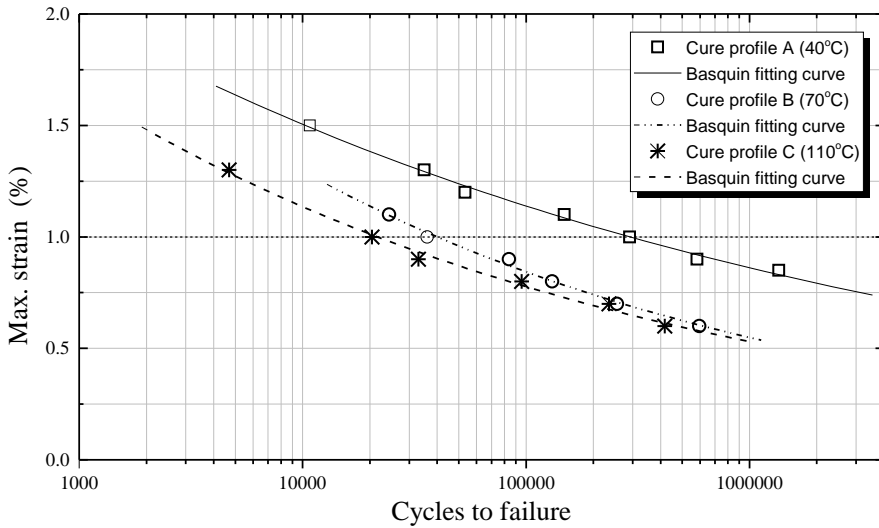
Figure P6.8: Experimental Wöhler curves of the FRP specimens manufacture with different curing temperatures. The symbols represent the number of cycles that the specimen experienced before failure for a certain level of strain; the lines represent the Basquin fitting curve.

Table P6.6: Normalised Basquin constants for the FRP fatigue test.

FRP Specimens	
Curing cycle	Basquin fitting parameters
A: 40°C	a=293 311; m=8.29
B: 75°C	a=40 535; m=5.27
C: 110°C	a=21 441; m=6.70

P6.4 Discussion and Conclusions

The epoxy volumetric variation before and after the curing (density measurment) corresponds to the material total shrinkage that occurs in the liquid and non-liquid state. To compare the total shrinkage with the residual strain, the volumetric variation was converted to a one dimension strain (ε_{TS}) using Eq. (P6.7).

$$V_{final} = V_{initial}(1 + \varepsilon_{TS})^3 \tag{P6.7}$$

A total shrinkage ε_{TS} of 2.04% was obtained for all tested cases (see Eq. P6.8), meaning that the epoxy contracts 2.04% in each direction independently of the curing temperature. This value of total shrinkage represents the maximum magnitude that the residual strain (non-liquid) can reach.

$$\varepsilon_{TS} = \sqrt[3]{\frac{V_{final}}{V_{initial}}} - 1 = -2.04 \ \% \tag{P6.8}$$

By analysing the residual strain measured by the FBG sensors, as presented in table P6.4, it can be concluded that the final residual strain (b) increases as the curing temperature increase, which is caused by the increase on the chemical shrinkage and thermal contraction.

However, for the cure profile C: 110°C, the final residual strain decreased comparatively with the cure profile B: 75°C. This was caused by the fact that the epoxy was cured with a temperature higher than the glass transition temperature (TG $\approx$ 85°C) as suggested by the manufacturer. In Fig. P6.9, it is shown the residual strain and temperature measured during the cure profile C: 110°C, where it can be observed jumps on the residual strain value during the exothermic peak. At high temperatures the epoxy starts to change its behaviour and even degraded, which leads to a not perfect strain transfer to the FBG sensor, creating this behaviour.

The chemical shrinkage (c) strongly depends on the magnitude of the exothermic peak temperature, but the thermal contraction (d), resulting from the cooling process, is only affected by the curing temperature. Thus, the amount of heat generated by the curing process directly influences the chemical shrinkage and consequently the residual strain.

On the other hand, the exothermic peak increases with the rate of the curing reaction (catalyse), i.e., more thermal energy is generated per time increment, when the curing temperature is higher and/or the quantity of reactants is higher. These
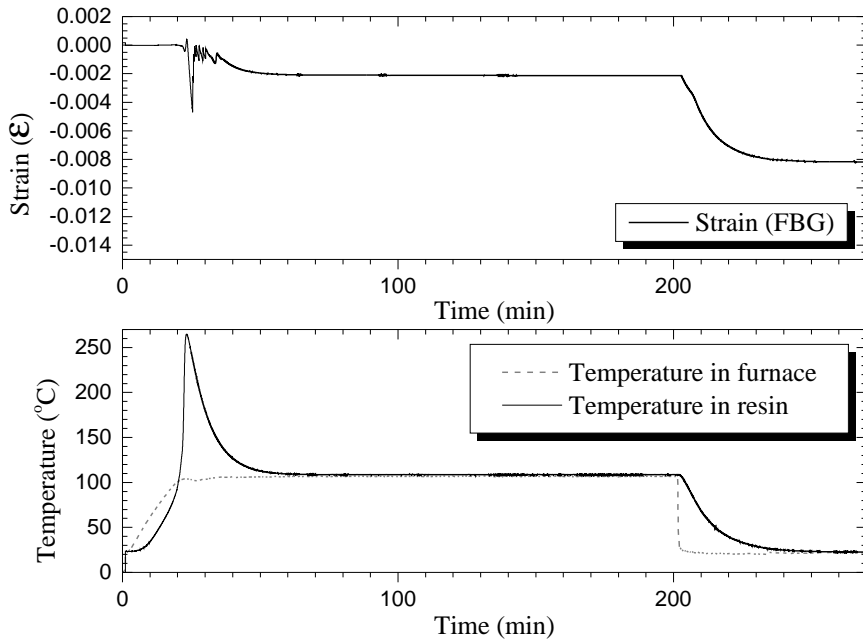
Figure P6.9: Strain and temperature measurments during the curing process: Cure profile C-110°C.

results show that different components can present different residual strains, even if they were produced with the same curing temperature; and, in order to reduce the final residual strain the curing temperature should be as low as possible, and the overshoot of the exothermic peak has to be minimized.

The quasi-static tensile tests performed show that the curing temperature, and consequently the residual strain, does not influence the neat resin or the FRP specimens performance. Although, the fatigue tests show that the FRP failure performance is decreased as the curing temperature increases, suggesting that there is a direct link between the fatigue performance and the cure-induced residual strain.

Summary of conclusion:

- The total volumetric variation that an epoxy can undergoes is defined by its chemical structure, and it is not influenced by the curing temperature;

- The total volumetric variation (total shrinkage ε_{TS}) can be evaluated by performing density measurements before and after the cure;

- The total shrinkage represents the maximum magnitude that the residual strain can reach;

- The residual strain ($\varepsilon_{residual}$) strongly depends on the curing temperature and the exothermic peak;

- Different components produced with the same curing temperature can experience different exothermic peaks (especially if the quantity of epoxy is different), which will result in different values of residual strain ($\varepsilon_{residual}$);

- The curing temperature does not have any impact on the tensile performance of epoxy and FRP specimens;

- The FRP fatigue performance is decreased when the curing temperature increases;

Acknowledgement

References

[1] R. Nijssen and P. Brøndsted, *Advances in Wind Turbine Blade Design and Materials.* Elsevier, 2013, pages 175–209, ISBN: 9780857094261. DOI: `10.1533/9780857097286.2.175`.

[2] J. Z. Hansen, "The effects of fibre architecture on fatigue life-time of composite materials," PhD thesis, 2013.

[3] K. Jespersen and et al., "Fatigue damage assessment of glass / polyester composite using x-ray computed tomography," *Submitted*, 2016.

[4] M. Shokrieh and A. Ghanei Mohammadi, *Residual Stresses in Composite Materials.* Elsevier, 2014, pages 3–14, ISBN: 9780857092700. DOI: `10.1533/9780857098597.1.3`.

[5] J. Barnes and G. Byerly, "The formation of residual stresses in laminated thermoplastic composites," *Composites Science and Technology*, volume 51, number 4, pages 479–494, January 1994, ISSN: 02663538. DOI: 10.1016/0266-3538(94)90081-7.

[6] D. U. Shah and P. J. Schubel, "Evaluation of cure shrinkage measurement techniques for thermosetting resins," *Polymer Testing*, volume 29, number 6, pages 629–639, 2010, ISSN: 01429418. DOI: 10.1016/j.polymertesting.2010.05.001.

[7] P. P. Parlevliet, H. E. Bersee, and A. Beukers, "Measurement of (post-)curing strain development with fibre bragg gratings," *Polymer Testing*, volume 29, number 3, pages 291–301, May 2010, ISSN: 01429418. DOI: 10.1016/j.polymertesting.2009.12.002.

[8] T. Nakamura and S. Suresh, "Effects of thermal residual stresses and fiber packing on deformation of metal-matrix composites," *Acta Metallurgica et Materialia*, volume 41, number 6, pages 1665–1681, 1993, ISSN: 09567151. DOI: 10.1016/0956-7151(93)90186-V.

[9] "Strength formulae of unidirectional composites including thermal residual stresses," *Materials Letters*, volume 43, number 1-2, pages 36–42, 2000, ISSN: 0167577X. DOI: 10.1016/S0167-577X(99)00227-X.

[10] H. Dève and M. Maloney, "On the toughening of intermetallics with ductile fibers: role of interfaces," *Acta Metallurgica et Materialia*, volume 39, number 10, pages 2275–2284, 1991, ISSN: 09567151. DOI: 10.1016/0956-7151(91)90010-X.

[11] H. E. Gascoigne, "Residual surface stresses in laminated cross-ply fiber-epoxy composite materials," *Experimental Mechanics*, volume 34, number 1, pages 27–36, 1994, ISSN: 0014-4851. DOI: 10.1007/BF02328439.

[12] L. Warnet, R. Akkerman, and P. Reed, "The effect of residual stress on transverse cracking in cross-ply carbon-polyetherimide laminates under bending," in *European Structural Integrity Society*, volume 32, 2003, pages 465–476, ISBN: 9780080441955. DOI: 10.1016/S1566-1369(03)80117-6.

[13] L. Asp, L. Berglund, and R. Talreja, "Prediction of matrix-initiated transverse failure in polymer composites," *Composites Science and Technology*, volume 56, number 9, pages 1089–1097, January 1996, ISSN: 02663538. DOI: 10.1016/0266-3538(96)00074-7.

[14] R. W. Penn, "A recording dilatometer for measuring polymerization shrinkage.," *Dental materials : Official publication of the Academy of Dental Materials*, volume 2, number 2, pages 78–9, 1986, ISSN: 0109-5641. DOI: 10.1016/S0109-5641(86)80056-2.

[15] K. F. Schoch, P. A. Panackal, and P. P. Frank, "Real-time measurement of resin shrinkage during cure," *Thermochimica Acta*, volume 417, number 1, pages 115–118, 2004, ISSN: 00406031. DOI: 10.1016/j.tca.2003.12.027.

[16]   "A viscoelastic model for predicting isotropic residual stresses in thermosetting materials: effects of processing parameters," *Journal of Composite Materials*, volume 35, number 10, pages 826–848, 2001, ISSN: 00219983. DOI: 10.1177/0021998001772662424.

[17]   *Measuring polymerization shrinkage of composites utilizing a gas pycnometer*, August 2010. DOI: 10.14295/bds.2003.v6i3.595.

[18]   M. Haider, P. Hubert, and L. Lessard, "Cure shrinkage characterization and modeling of a polyester resin containing low profile additives," *Composites Part A: Applied Science and Manufacturing*, volume 38, number 3, pages 994–1009, 2007, ISSN: 1359835X. DOI: 10.1016/j.compositesa.2006.06.020.

[19]   K. P. Pang and J. K. Gillham, "Anomalous behavior of cured epoxy resins: density at room temperature versus time and temperature of cure," *Journal of Applied Polymer Science*, volume 37, number 7, pages 1969–1991, 1989, ISSN: 00218995. DOI: 10.1002/app.1989.070370718.

[20]   R. A. Fischbein, "Method for the determination of the cure shrinkage of epoxy formulations," *Journal of Scientific Instruments*, volume 43, number 7, pages 480–480, 1966, ISSN: 0950-7671. DOI: 10.1088/0950-7671/43/7/415.

[21]   G. Albertini, G. Bruno, A. Carradò, F. Fiori, M. Rogante, and F. Rustichelli, "Determination of residual stresses in materials and industrial components by neutron diffraction," *Measurement Science and Technology*, volume 10, number 3, R56–R73, 1999, ISSN: 0957-0233. DOI: 10.1088/0957-0233/10/3/006.

[22]   A. Nielsen and R. Pyrz, "A novel approach to measure local strains in polymer matrix systems using polarised raman microscopy," *Composites Science and Technology*, volume 62, number 16, pages 2219–2227, December 2002, ISSN: 02663538. DOI: 10.1016/S0266-3538(02)00174-4.

[23]   B. Andersson, A. Sjögren, and L. Berglund, "Micro- and meso-level residual stresses in glass-fiber/vinyl-ester composites," *Composites Science and Technology*, volume 60, number 10, pages 2011–2028, August 2000, ISSN: 02663538. DOI: 10.1016/S0266-3538(00)00099-3.

[24]   C. P. Ostertag and E. Drescher-Krasicka, "Novel residual stress measurement techniques to measure residual stresses in fiber reinforced composites," *Journal of Materials Science*, volume 34, number 3, pages 557–563, ISSN: 1573-4803. DOI: 10.1023/A:1004598729771.

[25]   R. G. Reid, "The measurement of longitudinal residual stresses in unidirectional glass fibre reinforced plastic," PhD thesis, March 2010.

[26]   M. Harsch, J. Karger-Kocsis, and F. Herzog, "Strain development in a filled epoxy resin curing under constrained and unconstrained conditions as assessed by fibre bragg grating sensors," *Express Polymer Letters*, volume 1, number 4, pages 226–231, 2007, ISSN: 1788618X. DOI: 10.3144/expresspolymlett.2007.34.

[27] T. Kosaka, K. Osaka, and Y. Sawada, "Evaluation of residual strain of fibres in matrix resin during cure process by optical fibre sensors," in *ICCM17- 17TH INTERNATIONAL CONFERENCE ON COMPOSITE MATERIALS*, Edinburgh, UK, 2009.

[28] G. Luyckx, E. Voet, N. Lammens, and J. Degrieck, "Strain measurements of composite laminates with embedded fibre bragg gratings: criticism and opportunities for research.," volume 11, number 1, pages 384–408, 2011, ISSN: 1424-8220. DOI: 10.3390/s110100384.

[29] O. Frazão, L. a. Ferreira, F. M. Araújo, and J. L. Santos, "Applications of fiber optic grating technology to multi-parameter measurement," *Fiber and Integrated Optics*, volume 24, number 3-4, pages 227–244, 2005, ISSN: 0146-8030. DOI: 10.1080/01468030590922966.

[30] K. O. Hill, Y. Fujii, D. C. Johnson, and B. S. Kawasaki, "Photosensitivity in optical fiber waveguides: application to reflection filter fabrication," *Applied Physics Letters*, volume 32, number 10, page 647, 1978, ISSN: 00036951. DOI: 10.1063/1.89881.

[31] F. T. S. Yu, *Fiber optic sensors*, First Edit, F. T. YU and S. Yin, Eds. Marcel Dekker, 2002, 494 S, ISBN: 9780824744571.

[32] K. Hill and G. Meltz, "Fiber bragg grating technology fundamentals and overview," *Journal of lightwave technology*, volume 15, number 8, pages 1263–1276, 1997.

[33] G. F. Pereira, L. P. Mikkelsen, and M. McGugan, "Crack detection in fibre reinforced plastic structures using embedded fibre bragg grating sensors: theory, model development and experimental validation.," *PloS one*, volume 10, number 10, e0141495, 2015, ISSN: 1932-6203. DOI: 10.1371/journal.pone.0141495.

[34] "Temperature-compensating multiple fiber bragg grating strain sensors with a metrological grating," *Optics and Lasers in Engineering*, volume 41, number 1, pages 205–216, January 2004, ISSN: 01438166.

[35] W. W. Morey, G. Meltz, and W. H. Glenn, "Fiber optic bragg grating sensors," in *Proc. SPIE, Fiber Optic and Laser Sensors VII*, February 1990, pages 98–107. DOI: 10.1117/12.963022.

[36] M. Caponero, D. Colonna, R. Montanini, and S. Pirrotta, "Development of a fibre-optic sensor for position monitoring of vertex detectors in high energy physics experiments," *Measurement Science and Technology*, volume 17, pages 1601–1608, 2006, ISSN: 0957-0233. DOI: 10.1088/0957-0233/17/6/043.

P6 Appendix-A: Cure-induced residual strain measured by embedded Fibre Bragg Grating

A fibre Bragg grating (FBG) is a periodic modulation of the refractive index along a section of an optical fibre, that when illuminated by a broadband light source reflects a narrow band of light. The grating is created by exposing the optical fibre core to an intense ultraviolet light interference pattern, which increases the photo-sensitivity of the silica [31]. The spectral response of a homogeneous FBG is a single peak centred at the wavelength λ_b, described by the Bragg condition,

$$\lambda_b = 2n_{eff}\Lambda \tag{P6.9}$$

where the parameter n_{eff} is the effective refractive index at the location of the grating, and Λ is the constant nominal period of the refractive index modulation [32]. Any external load or temperature variation affecting the grating region will change its refractive index and its period of modulation, which causes a shift in the wavelength of the reflected peak ($\Delta\lambda_b$) [33], as shown in Fig. P6.10.

In a free FBG sensor the wavelength shift $\Delta\lambda_b$ caused by deformation (ε_x) or temperature change (ΔT) is describe by Eq. (P6.10).

$$\frac{\Delta\lambda_b}{\lambda_b} = (1 - p_e)\varepsilon_x[(1 - p_e)\alpha_f + \xi]\Delta T \tag{P6.10}$$

The parameter p_e is the optical fibre photo-elastic coefficient, α_f is the thermal expansion coefficients of the optical fibre, and ξ is the thermo-optic coefficient [30, 34–36]. Based on this, the FBG sensor response during the curing process can be divided in two parts:

- The FBG response before the gel point. At this stage, the epoxy is in a liquid state that makes it unable to transfer strain to the FBG sensor; consequently, the sensor only experiences temperature variation caused by the heating of the furnace and/or the heat generated by the exothermic cure reaction. Thus, the FBG wavelength shift is governed by the optical fibre thermal expansion (α_f) and the thermo-optic coefficient (ξ), as described in Eq. (P6.11).

$$\frac{\Delta\lambda_b}{\lambda_b} = [(1 - p_e)\alpha_f + \xi]\Delta T \tag{P6.11}$$

- The FBG response after the gel point. When reaching gelation (or gel point), the physical bond between the FBG and the epoxy gets strong enough to transfer strain. Then, the effect of the optical fibre thermal expansion in the overall thermal expansion can be neglected, as the FBG cross section is much smaller than the specimen cross section. This makes the FBG wavelength shift governed by the epoxy thermal expansion (α_{epoxy}) and by the chemical shrinkage (ε_{ch}) that occurs in this non-liquid state, as described by Eq. (P6.12).
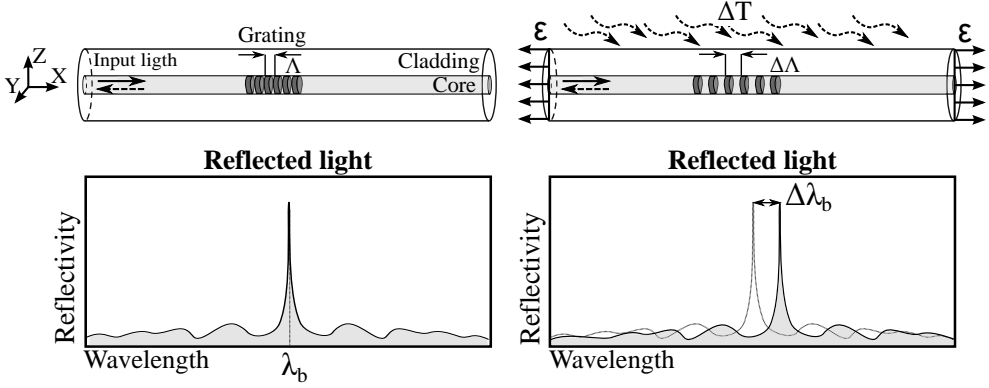
Figure P6.10: Fibre Bragg Grating working principle: spectral response of a homogeneous FBG. The parameter λ_b is the wavelength of the reflected peak, and Λ is the constant nominal period of the refractive index modulation.

$$\frac{\Delta \lambda_b}{\lambda_b} = (1 - p_e)\varepsilon_{ch}[(1 - p_e)\alpha_{epoxy} + \xi]\Delta T \qquad \text{(P6.12)}$$

Then, the epoxy residual strain ($\varepsilon_{residual}$) is obtained by adding the thermal expansion strain ($\alpha_{epoxy}\Delta T$) to the chemical shrinkage (ε_{ch}), as described in Eq. (P6.13). Note that it is easier to analyse the residual strain as a single component ($\varepsilon_{residual}$), as the epoxy thermal expansion varies along the curing process, which makes the thermal expansion-chemical shrinkage decoupling impossible.

$$\frac{\Delta \lambda_b}{\lambda_b} = (1 - p_e)\varepsilon_{residual} + \xi\Delta T \qquad \text{(P6.13)}$$

The measurement methodology developed to determine the gel point and the residual strain variation during the curing process is schematically shown in Fig. P6.11. The $\Delta \lambda_b$ is the wavelength shift measured by the embedded FBG sensor, and the ΔT is the temperature measured by the embedded thermocouple, which is used to decouple the FBG thermal-optical cross sensitivity ($\xi\Delta T$). As no strain is transferred from the epoxy to the FBG sensor before the gel point, the Equation/condition (P6.14) can be used to describe this stage.

$$\varepsilon_{residual} = \frac{\left[\dfrac{\Delta \lambda_b}{\lambda_b} - [(1 - p_e)\alpha_f + \xi]\Delta T\right]}{(1 - p_e)} = 0 + tolerance \qquad \text{(P6.14)}$$

The point (in min) when the Equation/condition (P6.14) fails determines the gel point. Then, the evolution of the cure-induced residual strain is described by the Equation (P6.15).

$$\varepsilon_{residual} = \frac{\left[\dfrac{\Delta\lambda_b}{\lambda_b} - \xi\Delta T\right]}{(1 - p_e)} \tag{P6.15}$$
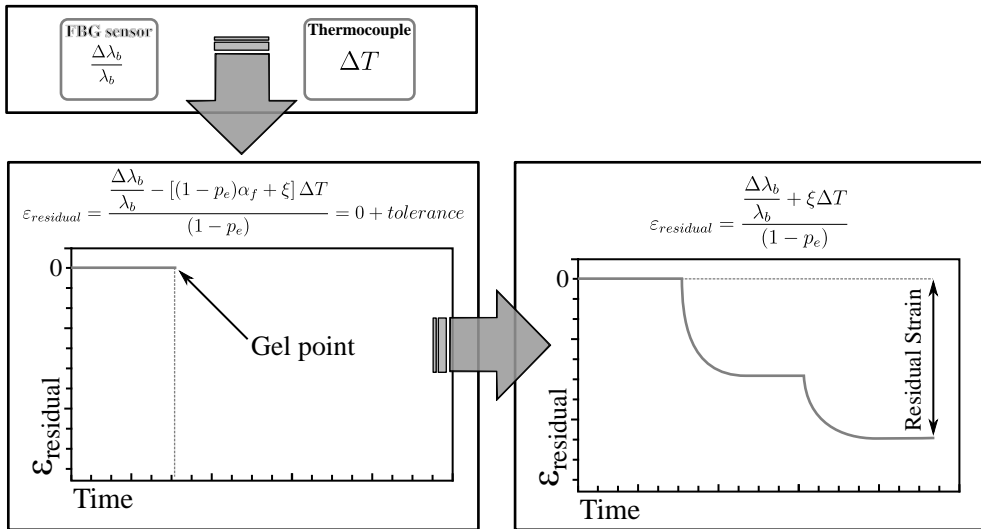
Figure P6.11: Cure-induced residual strain measurement methodology, using a FBG sensor and a thermocouple. The parameter $\Delta\lambda_b$ is the wavelength shift measured by the FBG sensor, and ΔT is the temperature measured by the thermocouple inside the epoxy.

Double Cantilever Beam Fracture Process Zone Length: Analytical and Numerical Analysis

G. Pereira, B.F. Sørensen, L.P. Mikkelsen, *Double Cantilever Beam Fracture Process Zone Length: Analytical and Numerical Analysis*, 2016
Draft Version, to be submitted later.

Draft

Abstract

An analytical equation that describes the fracture process zone length in function of the double cantilever beam specimen geometry, the loading mixed mode (moments ratio), and the material cohesive-law parameters, is presented in this article. This equation is used to tune the specimen length to the fracture test procedure, and to analyse how a change in one testing/specimen parameter can influence the fracture process zone length. Scaling relations that describe how the fracture process zone length scales with the beams height, cohesive-law parameters, and side-groove geometry are derived from the analytical equations, and validated by a finite element method model. It is found that the fracture process zone length is strongly influenced by the ductility of the cohesive-law, and the ratio of the crack front width/specimen width.
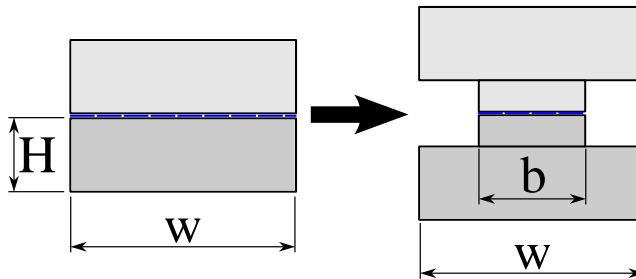
Notation

|	
DCB	double cantilever beam;
H	beam height (mm);
w	beam width (mm);
b	crack front width (mm);
l_{fpz}	fracture process zone length (mm);
M	moment applied to the beam elastic center (N.mm);
N	axial force applied to the beam elastic center (N);
E	Young's modulus (MPa);
I	bending moment inertia (mm^4);
A	cross section area (mm^2);
$index_1$	DCB top beam;
$index_2$	DCB bottom beam;
$index_3$	undamaged DCB;
σ_c	critical traction stress (MPa);
δ_c	critical opening (mm);
$\delta_{1,2}$	opening in the global coordinate system (mm);
$\delta_{t,n}$	opening in the local coordinate system (mm);
$\theta_{1,2}$	beams rotation (rad);
$na_{1,2}$	elastic center position (mm);
c_{shape}	parameter that describes the shape of the cohesive-law;
ξ	moments ratio (M_2/M_1);
gH	side-groove height (mm);
α, C_1, C_2	auxiliary variables;

P7.1   Introduction

Structures made of fibre reinforced materials can fail along weak interfaces; however, one complication of interface fracture is that the fracture energy depends on the ratio between shear and normal stress, also called mode mixity [1, 2]. Thus, it is necessary to develop experimental methods that can measure the crack-growth resistance of these materials for all the different fracture modes. Several test configurations have been developed by several authors, such as the asymmetric DCB-specimen [3], end-notched-flexure [4], cracked lap shear [5], and mixed mode bending [6]. And more recently, Sørensen, et al. [7] developed a double cantilever beam with uneven bending moments (DCB-UBM) test procedure, which can measure the material's energy release rate from pure mode-I to pure mode-II, with the same specimen geometry and a stable crack growth.

However, in some cases, if the material is too stiff or have a high fracture toughness the machine loading limit is reached, becoming impossible to perform a valid fracture test. A possible solution to overcome this is by testing the DCB specimens with side-grooves, as shown in Fig.P7.1, where the energy, and consequently the loading required to growth the crack, decreases as the ratio side-groove width/specimen width (b/w) decreases.

The conventional J-integral [8, 9] is limited to symmetric DCB specimen cases, without side-grooves, and it requires that the crack plane is located at the specimen middle (symmetric) plane. Thus, Toftegaard, et al. [10] developed a general 3D J-integral that can be applied to any DCB configuration, allowing the experimental measurement of the material fracture energy release rate, and consequently the interface cohesive-law. Additionally, this general 3D J-integral can be applied to DCB specimens with side-grooves, cracks running in a non-symmetric plane, and it can even handle material variation, as a DCB with each beam composed of a different material.

Figure P7.1: Schematic representation of double cantilever beam with and without side-grooves; H is the beam height, w is the beam width, and b represents the crack front width.
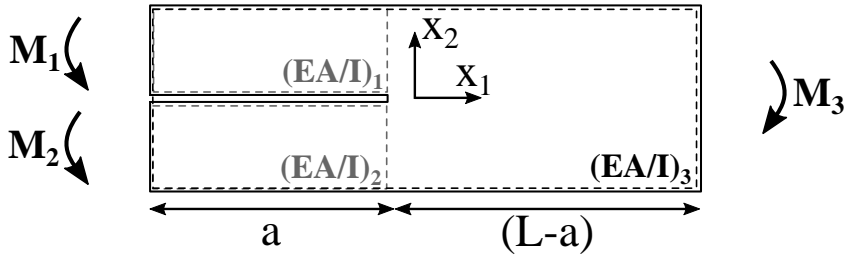
Figure P7.2: J-integral developed by Toftegaard, et al. [10] evaluated around a notch; M is the bending moment applied to the elastic center, the index's $_{1,2}$ represent the top and bottom beam before the crack tip and the index $_3$ the undamaged beam (after the crack tip), A is the cross section area, I is the bending moment of inertia, and E represents the material Young's modulus.

The general 3D J-integral integrated around a notch in a DCB-like specimen (see Fig. P7.2), is described by:

$$J = \frac{M_1^2}{2b(EI)_1} + \frac{M_2^2}{2b(EI)_2} - \frac{M_3^2}{2b(EI)_3} \qquad \text{(P7.1)}$$

where, M is the moments applied to the elastic center, the index's $_{1,2}$ represent the top and bottom beam before the crack tip and the index $_3$ represents the undamaged beam (after the crack tip), b is the crack tip width, A is the cross section area, I is the bending moment of inertia, and E represents the material Young's modulus. For a DCB specimen loaded with moments (as in the fracture test apparatus developed by Sørensen [7]), the general 3D J-integral can be simplified as:

$$J = \frac{M_1^2}{2b(EI)_1} + \frac{M_2^2}{2b(EI)_2} - \frac{(M_1 + M_2)^2}{2b(EI)_3} \qquad \text{(P7.2)}$$

where M_1 and M_2 represent the moments applied to the top and bottom beam, respectively.

Numerical models demonstrated that the general 3D J-integral is consistent with the previous theories, and it can be applied to any DCB geometry, material configuration, or side-groove dimension; however, it was also observed that the fracture process zone is strongly influenced by the specimen geometry and by the material fracture properties, as also described by some authors [11–13]. More specifically in DCB specimens, Bao [14] and Suo [15] observed that the fracture process zone length (l_{fpz}) scales with the specimen geometry, $l_{fpz} \propto H^{3/4}$, and the material cohesive-law parameters, $l_{fpz} \propto \sigma_c^{-1/4}$ and $l_{fpz} \propto \delta_c^{1/4}$.

The fracture process zone is defined as the zone near a crack tip where the material developed damage. In a DCB specimen, where the delamination is followed by fibre bridging (see Fig. P7.3), the fracture process zone length is defined as the distance between the position where there is no physical connection among the crack faces, and the position where the stress reaches the material cohesive stress (σ_c).

The l_{fpz} dependency on geometry and fracture properties can have implications on the fracture test procedure, and lead to errors in the experimental results. In other words, to obtain a valid energy release rate measurement, by using the J-integral method, it is required that a steady state crack growth (fully developed fracture process zone) developed within the specimen length; thus, $l_{fpz} < DCB\ length$ is a fracture test requirement.
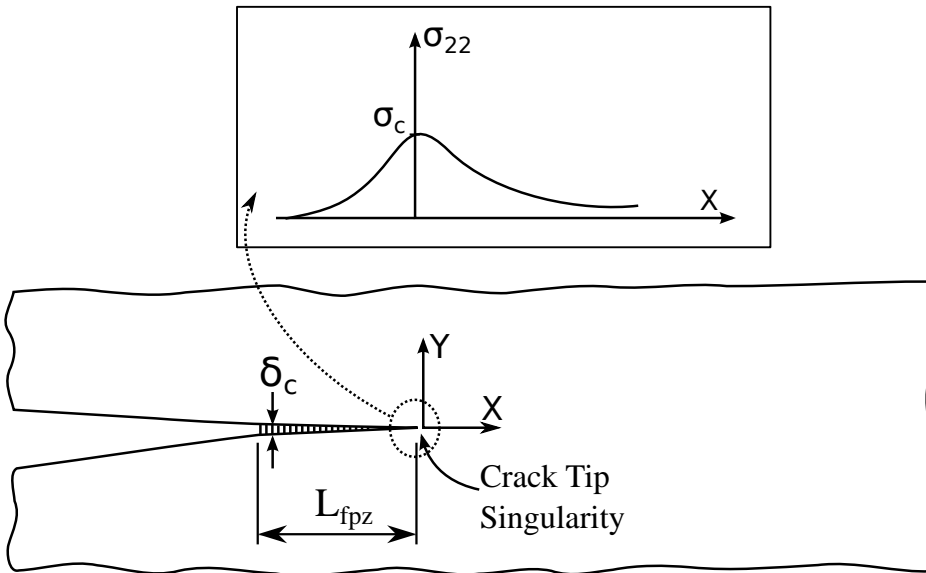
Figure P7.3: Schematic representation of the fracture process zone; l_{fpz} is the fracture process zone length, δ_c represents the critical opening, and σ_c is the critical traction stress.
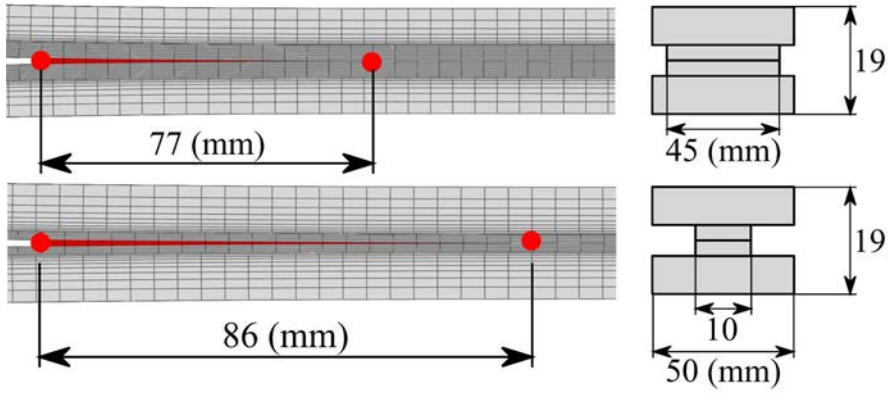
Figure P7.4: Finite element method model of the fracture process zone length (l_{fpz}) in a DCB with different side-grooves dimensions, loaded in mode-I. Interface cohesive-law: $\sigma_c = 1.1$ (MPa); $\delta_c = 1.1$ (mm).

Returning to the use of side-grooves in DCB specimens, Fig. P7.4 shows that the l_{fpz} increases as the side-groove/specimen width ratio (b/w) decreases, which makes this fracture process zone dependency a relevant issue within the fracture testing field. Thus, the main objective of this article is to developed tool/equation to describe the l_{fpz}, which can be used to tune the fracture test procedure and the DCB specimen dimensions.

P7.2   Fracture Process Zone Length: Analytical Equation

The general equation that describe l_{fpz} in function of the DCB specimen geometry, mixed-mode ratio, and the material cohesive-law parameters, is presented in Appendix A. This equation is based on the general 3D J-integral developed by Tofte-gaard [10], and the beam displacement equations presented in Sørensen work [8] (Appendix-A). This equation can describe the l_{fpz} for any 3D DCB specimen configuration, and for a crack developing in the specimen middle plane (symmetric) or outside (non-symmetric).

However, this Eq. (P7.31) is too long, making it not practical to study the influence of each parameter in the l_{fpz}. Thus, in the following sections only pure mode-I and mode-II are addressed, as it correspond to the extreme cases and the l_{fpz} for any mixed-mode combination will lay between this two behaviours.

P7.2.1 DCB Without Side-Grooves and Symmetric Crack-Plane

For a DCB specimen with both beams composed by the same material, without side-grooves (see Fig. P7.13), and where the crack develops in the specimen middle plane (symmetric), the following simplifications can be made:

- the bending neutral axis is equal to the geometric neutral axis, i.e. $na_{1,2} = H_{1,2}/2$;

- the crack front width is equal to the beam width, $(w = b)$;

- symmetric crack-plane and beams composed by the same material:

    - $EI_1 = EI_2 = E(bH_{1,2}^3)/12$;
    - $EI_3 = E(2bH_{1,2}^3)/12$;

For a pure mode-I fracture, ξ=-1, the parameter α described by Eq. (P7.23) can be rewritten as:

$$\alpha = \frac{24}{EbH^3} \tag{P7.3}$$

and, the fracture process zone length for mode-I $l_{fpz(I)}$ is defined by:

$$l_{fpz(I)} = \frac{1}{12} \frac{\arccos\left(\dfrac{6H\sqrt{\dfrac{c_{shape}\sigma_c\delta_c}{EH^3}} + 6\delta_c\sqrt{\dfrac{c_{shape}\sigma_c\delta_c}{EH^3}} - \sqrt{12}}{6H\sqrt{\dfrac{c_{shape}\sigma_c\delta_c}{EH^3}} - \sqrt{12}}\right)\sqrt{12}}{\sqrt{\dfrac{c_{shape}\sigma_c\delta_c}{EH^3}}} \tag{P7.4}$$

The parameter σ_c is the critical stress, δ_c the critical opening, and c_{shape} describes the shape of the cohesive law (see Appendix-A). For a pure mode-II fracture, ξ=1, the parameter α described by Eq. (P7.23) can be rewritten as:

$$\alpha = \frac{18}{EbH^3} \tag{P7.5}$$

and, the fracture process zone length for mode-II $l_{fpz(II)}$ is defined by:

$$l_{fpz(II)} = \frac{1}{4} \frac{\arccos\left(\dfrac{1}{2}\dfrac{2H^2 - \delta_c^2}{H^2}\right)}{\sqrt{\dfrac{c_{shape}\sigma_c\delta_c}{EH^3}}} \tag{P7.6}$$

Fracture Process Zone Length Scaling: Parametric Analysis

The knowledge of how the l_{fpz} scales with the different parameters can be used as a tool to analyse and design the best specimen configuration/dimension. Some authors already demonstrated that the l_{fpz} of a DCB specimen loaded in mode-I scales with the specimen geometry and the cohesive-law parameters. Suo, et al. [15] observed experientially that l_{fpz} have a strong thickness dependence, scaled as $l_{fpz} \propto H^{3/4}$; and, Bao, et al. [14] expanded this study to the cohesive-law parameters, where they observed $l_{fpz} \propto \sigma_c^{-1/4}$ and $l_{fpz} \propto \delta_c^{1/4}$. However, to the author's knowledge, no research papers dealt with this scaling in mode-II or with the effect of side-grooves.

Thus, the different l_{fpz} scaling relations were calculated from Eq. (P7.4) using Taylor series, and for mode-I loading are described as:

$$
\begin{aligned}
l_{fpz(I)} &\propto H^{3/4} \\
&\propto \sigma_c^{-1/4} \\
&\propto \delta_c^{1/4}
\end{aligned}
\tag{P7.7}
$$

and for mode-II loading:

$$
\begin{aligned}
l_{fpz(II)} &\propto H^{1/2} \\
&\propto \sigma_c^{-1/2} \\
&\propto \delta_c^{1/2} \; for \; \delta_c < H/2
\end{aligned}
\tag{P7.8}
$$

These l_{fpz} scaling relations agree with the values described by *Suo* and *Bao*. A comparison between the analytical equation and the different l_{fpz} scaling, obtained by varying one parameter and maintaining the remaining constant, is shown in Fig. P7.5 and P7.6. The default parameters used in this comparison are: $E = 44.33 \, GPa$; $\delta_c = 1.1 \, mm$; $\sigma = 1.1 \, MPa$; $H = 9.5 \, mm$; $w = 50 \, mm$; $c_{shape} = 1/2$;

It is observed that the l_{fpz} scaling follows the same trend in both fracture modes, however it is much more pronounced in mode-II loading. An increase in the specimen height, H, leads to an increase in l_{fpz}; however, for standard specimen height values, it does not have a big contribution to the increase of the fracture process zone. In terms of cohesive-law parameters, l_{fpz} increases as the critical opening (δ_c) increase and/or the critical stress (σ_c) decreases. This means that a ductile interface creates a larger fracture process zone, specially in mode-II fracture. Thus, even if the DCB length is long enough to hold the fracture process zone in mode-I fracture, it may not be long enough for a mode-II fracture.
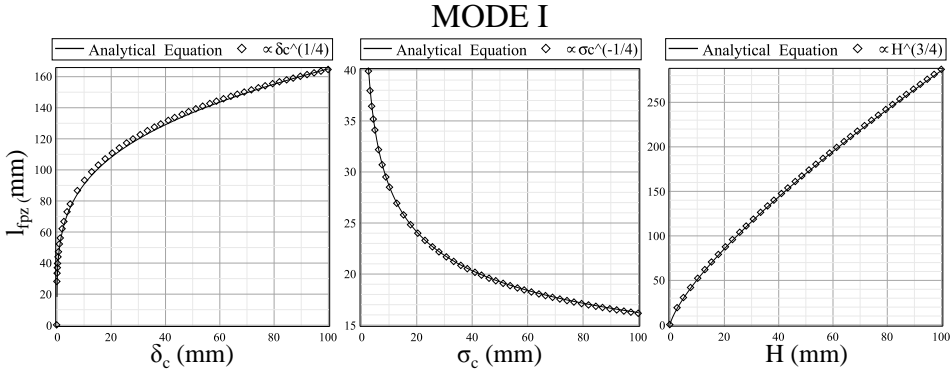
MODE I

Figure P7.5: Fracture process zone length scaling: Mode-I.
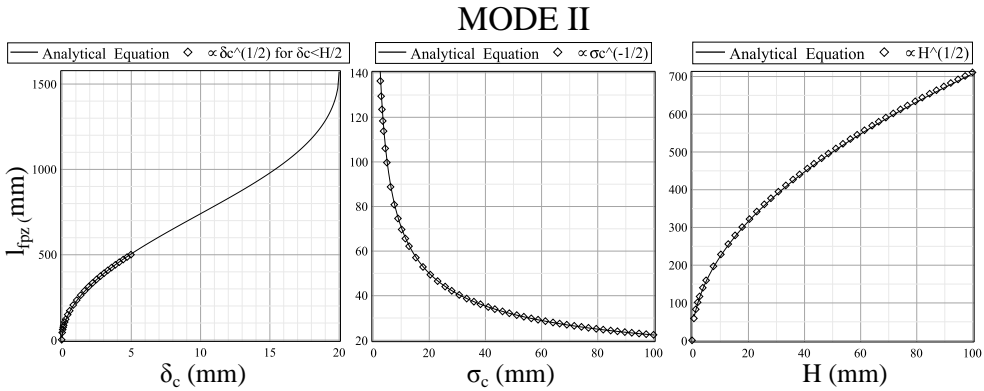
MODE II

Figure P7.6: Fracture process zone length scaling: Mode-II.

P7.2.2　Crack Front Width Effect

Another parameter analysed is the effect of the crack front width in the l_{fpz}, as varying the crack front width can be considered a zero height side-groove. This is relevant, as the moment required to propagate a crack can be reduced by decreasing the crack front width, as shown in Eq. (P7.22). I.e., for the same energy release rate, J, a decrease in the crack front width, b, represents a decrease in the moment by $M \propto \sqrt{b}$. A smaller crack front width can be achieved by placing slip foils at the crack plane.

The l_{fpz} of a DCB specimen with a varying crack front width, for mode-I and mode-II, are described by:

$$l_{fpz(I)} = \frac{1}{12} \frac{\arccos\left(\dfrac{6H\sqrt{\dfrac{c_{shape}\sigma_c\delta_c\mathbf{b}}{EH^3\mathbf{w}}} + 6\delta_c\sqrt{\dfrac{c_{shape}\sigma_c\delta_c\mathbf{b}}{EH^3\mathbf{w}}} - \sqrt{12}}{6H\sqrt{\dfrac{c_{shape}\sigma_c\delta_c\mathbf{b}}{EH^3\mathbf{w}}} - \sqrt{12}}\right)\sqrt{12}}{\sqrt{\dfrac{c_{shape}\sigma_c\delta_c\mathbf{b}}{EH^3\mathbf{w}}}} \qquad (P7.9)$$

$$l_{fpz(II)} = \frac{1}{4} \frac{\arccos\left(\dfrac{1}{2}\dfrac{2H^2 - \delta_c^2}{H^2}\right)}{\sqrt{\dfrac{c_{shape}\sigma_c\delta_c\mathbf{b}}{EH^3\mathbf{w}}}} \qquad (P7.10)$$

The ratio between the DCB width and the crack front width, defined by b/w, have a big impact on the l_{fpz}, as it can be observed in the l_{fpz} scaling equations:

$$l_{fpz(I)} \propto \left(\frac{b}{w}\right)^{-1/4} \quad for\ ModeI \qquad (P7.11)$$

$$l_{fpz(II)} \propto \left(\frac{b}{w}\right)^{-1/2} \quad for\ ModeII \qquad (P7.12)$$

The comparison between the analytical equation and the l_{fpz} scaling to different b/w ratios is shown in Fig. P7.7 (the same default parameters were used to perform the comparison). These results show that the ratio between the crack front width/specimen width have a big impact on the l_{fpz}, specially in mode-II loading; and, that the minimum DCB specimen length increases as the ratio b/w decreases.
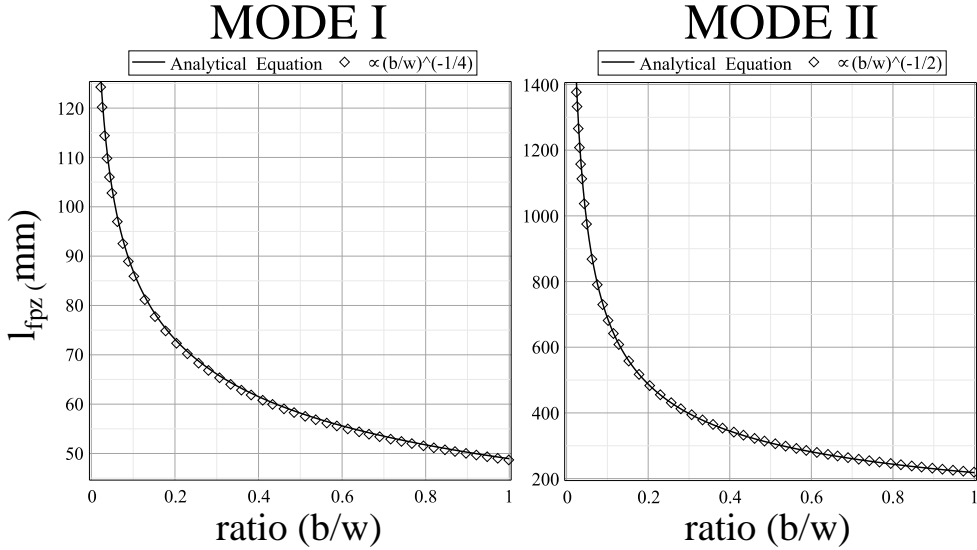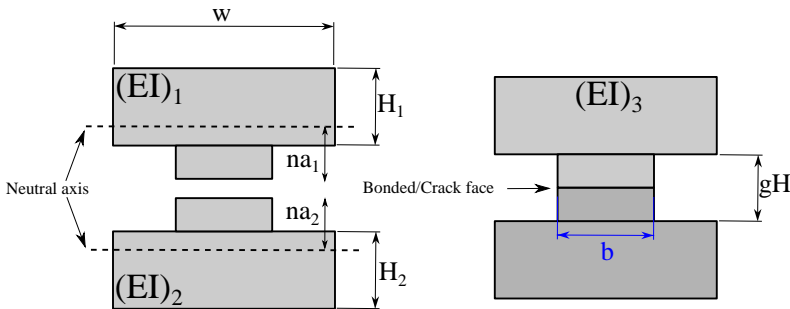
Figure P7.7: Effect of the ratio between the DCB width and the crack front width, b/w, on the fracture process zone length.
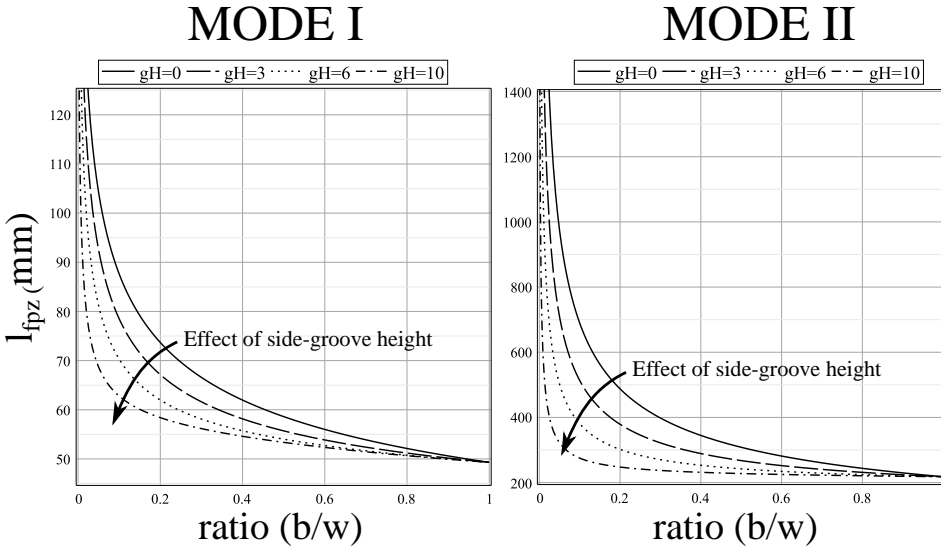
P7.2.3   Side-Groove Geometry Effect

As previously observed, a zero height side-groove have a big impact on the l_{fpz}. Thus, following this, the effect of the side-groove height is analysed in this section.

Considering the geometry of a DCB specimen with square side-grooves as presented in Fig. P7.8, for a fix groove height (gH), a decrease on the crack front width (b) have a big impact on the bending inertia (EI) and on the neutral axis position (na).

Figure P7.8: Cross-section of a DCB specimen with square side-grooves.

MODE I

MODE II

Legend: gH=0, gH=3, gH=6, gH=10

Mode I plot: y-axis l_{fpz} (mm) from 50 to 120+, x-axis ratio (b/w) from 0 to 1. Annotation: "Effect of side-groove height".

Mode II plot: y-axis from 200 to 1400, x-axis ratio (b/w) from 0 to 1. Annotation: "Effect of side-groove height".

Figure P7.9: Effect of the side-groove height (gH) in the fracture process zone length and in the b/w effect.

This EI/na and gH cross-dependency makes impossible to simplified the expression that describes the l_{fpz}, Eq. (P7.31), leading to an analytical solution that is too long to be presented in this article. Nevertheless, the effect of the side-groove height in the l_{fpz} is graphically represented in Fig. P7.9. The same default parameters were used, and the total DCB height was hold constant, 19 mm. (as the gH increases the $H_{1,2}$ have to decrease). It is observed that an increase on the grove height causes a decrease on scaling effect, $l_{fpz(I)} \propto (b/w)^{-1/4}$ (mode-I) and $l_{fpz(II)} \propto (b/w)^{-1/2}$ (mode-II), as observed in the zero height side-groove case.
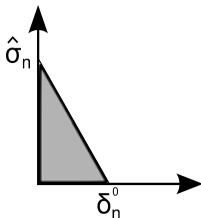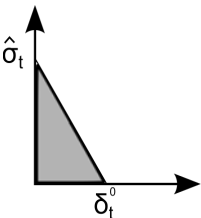
P7.3   Numerical Validation

A numerical model of a 3D DCB specimen was developed to validate the equation that describes l_{fpz} in function of the different geometric, fracture mode, and cohesive-law parameters. It was used the same cross-section geometry ($H = 9.5mm$; $w = 50mm$), however, the specimen length was set to 2000 mm, in order to hold the fracture process zone within the specimen length limits. The beams were modelled using 8-node linear elements with incompatible modes, and the delamination/fibre bridging was modelled using 8-node linear cohesive elements along the delamination plane [16, 17]. The cohesive elements express the cohesive law (traction-separation), meaning a progressive loss of the cohesion between the two crack faces with the local crack

opening δ_c. In an undamaged state, the cohesive elements follow a linear-elastic behaviour, defined as the penalty stiffness K, which relates the nominal stress to the nominal opening. The penalty stiffness K was set to *1000* (MPa), meaning a stiff linear-elastic behaviour. The damage initiation was calculated using a *Maximum Stress* criterion, as described by Eq. (P7.13) [18].

$$f = Max \left\{ \frac{\sigma_n}{N_{max}}; \frac{\sigma_t}{T_{max}}; \frac{\sigma_s}{S_{max}} \right\} = 1 \qquad \text{(P7.13)}$$

The parameter f is the damage criterion, and it is fulfilled when it reaches the value $f = 1$. The parameters $\sigma_{n,s,t}$ are the nominal stress in the normal, first shear and second shear directions, respectively, and N_{max}, S_{max}, and T_{max} are cohesive-law parameters; the parameters δ_0^* and δ_c^* are the crack opening displacement to the local crack plane for damage initiation and critical damage. When the initiation criterion is full-filled, a damage evolution law describes the material stiffness degradation, and in this DCB model it was used a linear softening displacement criterion, defined by the opening at damage initiation (δ_0^*) and the opening at failure (δ_c^*). The mixed-mode behaviour was set as mode-independent, meaning that no fracture coupling behaviour is modelled. The material properties and cohesive-law parameters used are described in table P7.1.

Table P7.1: DCB material properties and cohesive-law parameters.

UD mechanical properties	
Young's modulus in Fiber direction E_1	44.33 GPa
Young's modulus transv. Fiber dir. E_2	12.94 GPa
Shear modulus G_{12}	4.39 GPa
Poisson's ratio ν_{12}	0.23
Shear modulus $G_{13} = G_{23}$	4.39 GPa

Interface damage properties			
Mode I		**Mode II**	

Traction-separation law			
$\hat{\sigma}_n$	1.1 (MPa)	$\hat{\sigma}_t$	1.1 (MPa)
$\delta_n^0 (mm)$	1.1 (mm)	$\delta_t^0 (mm)$	1.1 (mm)
Energy Release Rate (steady state)			
J_n^{ss}	0.605 kJ/m^2	J_t^{ss}	0.605 kJ/m^2

Some authors suggest a minimum of 10 cohesive elements within the fracture process zone to represent accurately the fracture process [19, 20]; however, a mesh size of 1 mm was used to modelled the delamination/crack, which gives a minimum of 70 elements within the fracture process zone and increases the measurement resolution of the l_{fpz}. The l_{fpz} was obtained by evaluating the maximum distance between the first element where the damage criterion (Eq. (P7.13)) is fulfilled, and the first element where the damage propagation is over.

The comparison between the l_{fpz} prediction by the numerical models and the analytical equations, Eq. (P7.9) and (P7.10), is shown in Fig. P7.10. It is observed that the analytical equations underestimate the l_{fpz} values. This is due the fact that the analytical equations were developed based on Kirchoffs assumptions, where only deformation duo to bending moments are accounted, and in the reality/numerical model, the traction force due to the fibre bridging creates an opposite moment, reducing the beam curvature and opening, as shown in Fig. P7.11. The parameter τ represents the fibre bridging contribution to the opposite moment.

However, the scaling behaviour observed in the numerical models is the same as the one predicted by the analytical equations. Thus, it is possible to predict the l_{fpz} by only performing one numerical model, and then scaling it by using the l_{fpz} scaling equations, as shown in Fig. P7.12.
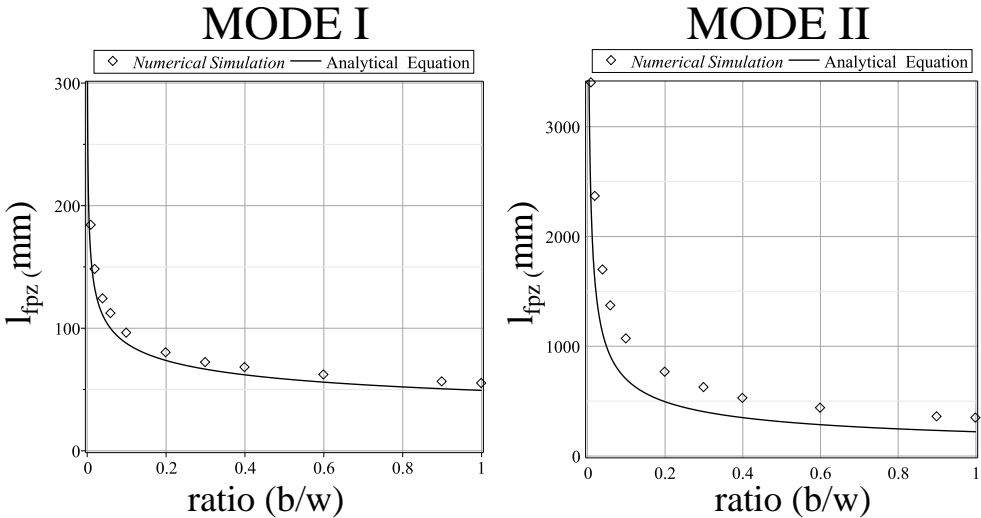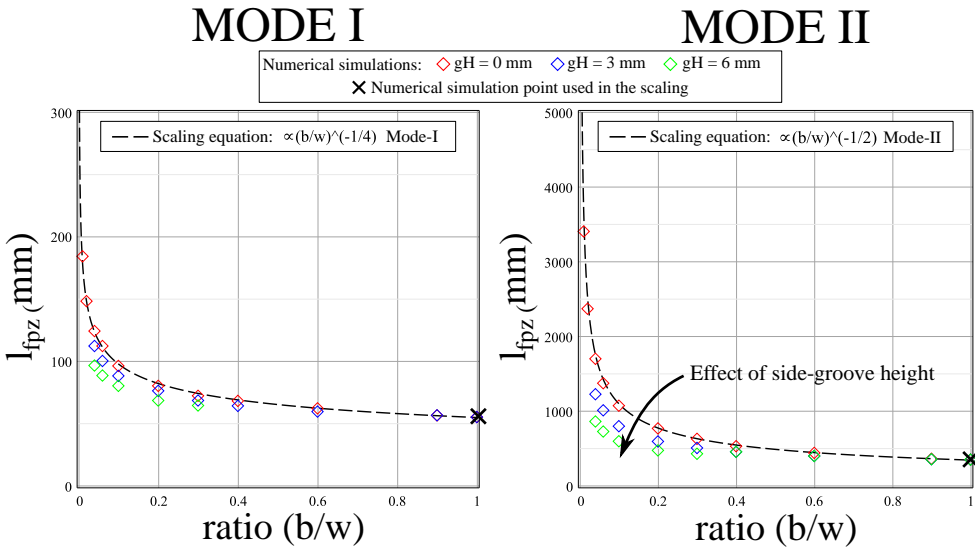

Figure P7.10: l_{fpz} prediction in function of b/w ratio: numerical model and analytical equation comparison.
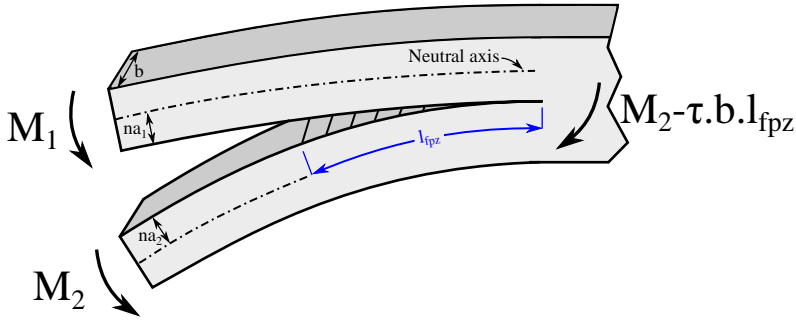
Figure P7.11: Fibre bridging contribution to the moments applied to the DCB.

The l_{fpz} is predicted accurately by the scaling equations, Eq. (P7.11) and (P7.12), using as reference the l_{fpz} given by the numerical model without side-grooves. The side-groove height effect on decreasing the *(b/w)* scaling, $l_{fpz(I)} \propto (b/w)^{-1/4}$ (mode-I) and $l_{fpz(II)} \propto (b/w)^{-1/2}$ (mode-II), is also visible in the numerical simulation.

Figure P7.12: l_{fpz} prediction in function of b/w ratio and side-groove height: numerical model and scaling equation comparison.

P7.4   Discussion and Conclusion

An analytical equation that describes the fracture process zone length, l_{fpz}, in function of the DCB geometry, moments ratio, and cohesive-law parameters, was developed in this article. To obtain a valid energy release rate measurement, using the J-integral method applied to a DCB specimen, it is required that a steady state growth (fully developed damage) develops within the specimen length. Thus, this equation can be used to tune the specimen to the fracture testing, and to analyse how a change in one parameter can influence the fracture process zone and consequently the experimental results.

Two "short" equations describing the l_{fpz} for the pure mode-I and mode-II were deducted from the analytical equation, which allow a direct prediction of the l_{fpz} without the need of a dedicate software to solve the large analytical equation. Even more direct, scaling relations that describe how l_{fpz} scales with the beams height, cohesive-law parameters, and side-groove geometry, were derived from the analytical equation using Taylor series.

The l_{fpz} scaling follows the same trend in both fracture modes, however it is much more pronounced in mode-II. Thus, the reader should be aware that the minimum specimen length required for a valid fracture test can change with the different moments ratio. Globally, the l_{fpz} gets larger as the critical opening (δ_c) increases and/or the critical stress (σ_c) decrease, which means that a more ductile interface creates larger fracture process zone. In terms of side-grooves, the ratio between the crack front width/specimen width (b/w) have a big impact on the l_{fpz}, increasing it rapidly as the ratio b/w decreases. However, this behaviour can be softened by using side-grooves with larger heights; i.e., for the same total DCB heigh, an increase on the side-groove height (gH) decreases the b/w scaling effect.

Finite element method simulations of the DCB specimen show that the analytical equation underestimates the l_{fpz}, as the traction force due to fibre bridging is not accounted in the analytical equation. However, the l_{fpz} values obtained from the analytical equation can still be used as an estimative, as the error obtain is less than 20%. Also, the numerical simulations showed that the l_{fpz} is predicted accurately by the scaling equations, when using as reference the l_{fpz} given by the numerical model of a DCB without side-grooves. This numerical model can be developed in 2D, as no 3D features (side-grooves) are required, making this approach fast. (Also, values from experiments can be used as reference for the scaling analysis)

Acknowledgement

References

[1] J. Hutchinson and Z. Suo, *Advances in Applied Mechanics Volume 29*, series Advances in Applied Mechanics. Elsevier, 1991, volume 29, pages 63–191, ISBN: 9780120020294. DOI: `10.1016/S0065-2156(08)70164-9`.

[2] M. Benzeggagh and M. Kenane, "Measurement of mixed-mode delamination fracture toughness of unidirectional glass/epoxy composites with mixed-mode bending apparatus," *Composites Science and Technology*, volume 56, number 4, pages 439–449, January 1996, ISSN: 02663538. DOI: `10.1016/0266-3538(96)00005-X`.

[3] V. Mollón, J. Bonhomme, J. Viña, and A. Argüelles, "Mixed mode fracture toughness: an empirical formulation for determination in asymmetric dcb specimens," *Engineering Structures*, volume 32, number 11, pages 3699–3703, 2010, ISSN: 01410296. DOI: `10.1016/j.engstruct.2010.08.014`.

[4] S. Hashemi, A. J. Kinloch, and J. G. Williams, "The analysis of interlaminar fracture in uniaxial fibre-polymer composites," *Proceedings of the Royal Society A: Mathematical, Physical and Engineering Sciences*, volume 427, number 1872, pages 173–199, 1990, ISSN: 1364-5021. DOI: `10.1098/rspa.1990.0007`.

[5] Y.-H. Lai, M. Dwayne Rakestraw, and D. A. Dillard, "The cracked lap shear specimen revisited—a closed form solution," *International Journal of Solids and Structures*, volume 33, number 12, pages 1725–1743, 1996, ISSN: 00207683. DOI: `10.1016/0020-7683(95)00124-7`.

[6] G. Fernlund and J. Spelt, "Mixed-mode fracture characterization of adhesive joints," *Composites Science and Technology*, volume 50, number 4, pages 441–449, January 1994, ISSN: 02663538. DOI: `10.1016/0266-3538(94)90052-3`.

[7] B. F. Sørensen, K. Jørgensen, T. K. Jacobsen, and R. C. Østergaard, "Dcb-specimen loaded with uneven bending moments," *International Journal of Fracture*, volume 141, number 1-2, pages 163–176, 2006, ISSN: 0376-9429. DOI: `10.1007/s10704-006-0071-x`.

[8] B. F. Sørensen and T. K. Jacobsen, "Characterizing delamination of fibre composites by mixed mode cohesive laws," *Composites Science and Technology*, volume 69, number 3-4, pages 445–456, March 2009, ISSN: 02663538. DOI: `10.1016/j.compscitech.2008.11.025`.

[9] B. F. Sørensen, "Cohesive law and notch sensitivity of adhesive joints," *Acta Materialia*, volume 50, number 5, pages 1053–1061, 2002, ISSN: 13596454. DOI: `10.1016/S1359-6454(01)00404-9`.

[10] H. Toftegaard, G. Pereira, and B. F. Sørensen, "Three-dimensional J integral solution for layered or graded DCB specimens with non-rectangular cross-section – J in terms of stiffness," *To be submitted in 2016*,

[11]   K. Ha, H. Baek, and K. Park, "Convergence of fracture process zone size in cohesive zone modeling," *Applied Mathematical Modelling*, volume 39, number 19, pages 5828–5836, 2015, ISSN: 0307904X. DOI: 10.1016/j.apm.2015.03.030.

[12]   C.-. Y. Hui, J. A., S. J. Bennison, and J. D. Londono, "Crack blunting and the strength of soft elastic solids," *Proceedings of the Royal Society A: Mathematical, Physical and Engineering Sciences*, volume 459, number 2034, pages 1489–1516, 2003, ISSN: 1364-5021. DOI: 10.1098/rspa.2002.1057.

[13]   W. Yao and K. R. Wu, "Fracture process zone of composite materials as concrete," in *Fracture Mechanics of Concrete Structures*, Freiburg, Germany, 1998, pages 421–430.

[14]   G. Bao and Z. Suo, "Remarks on crack-bridging concepts," *Applied Mechanics Reviews*, volume 45, number 8, page 355, 1992, ISSN: 00036900. DOI: 10.1115/1.3119764.

[15]   Z. Suo, G. Bao, and B. Fan, "Delamination r-curve phenomena due to damage," *Journal of the Mechanics and Physics of Solids*, volume 40, number 1, pages 1–16, 1992, ISSN: 00225096. DOI: 10.1016/0022-5096(92)90198-B.

[16]   G. Alfano and M. A. Crisÿeld, "Finite element interface models for the delamination analysis of laminated composites : mechanical and computational issues," *International Journal For Numerical Methods In Engineering*, volume 50, number March 2000, pages 1701–1736, 2001.

[17]   V. N. Burlayenko and T. Sadowski, "FE modeling of delamination growth in interlaminar fracture specimens," volume 2, pages 95–109, 2008.

[18]   ABAQUS™, *User Manual. Version 6.13, ABAQUS Inc., Pawtucket, Rhode Island, USA*. USA, 2013.

[19]   D. Álvarez, B. Blackman, F. Guild, and a.J. Kinloch, "Mode i fracture in adhesively-bonded joints: a mesh-size independent modelling approach using cohesive elements," *Engineering Fracture Mechanics*, 2013, ISSN: 00137944. DOI: 10.1016/j.engfracmech.2013.10.005.

[20]   a. Turon, C. Dávila, P. Camanho, and J. Costa, "An engineering solution for mesh size effects in the simulation of delamination using cohesive zone models," *Engineering Fracture Mechanics*, volume 74, number 10, pages 1665–1682, 2007, ISSN: 00137944. DOI: 10.1016/j.engfracmech.2006.08.025.

P7 Appendix-A: Fracture Process Zone Length - General Analytical Equation

A general equation that describes l_{fpz} in function of the DCB specimen geometry, fracture modes, and the material cohesive-law is presented in this appendix. This equation is based on the general 3D J-integral developed by Toftegaard, et al. [10], and the beam displacement equations presented in Appendix A of Sørensen work [8], which were modified to represented a 3D specimen.

    The displacement and rotation of the beams, due to the loading by moments, are calculated using Kirchoffs assumptions; thus, only deformation due to bending moments are accounted, and the traction in the beams from the fibre bridging phenomena is neglected.

Beams Displacement and Rotation

For a DCB specimen with a crack growing in a non-symmetric plane and loaded with moments at the beams ends, as shown in Fig. P7.13, the displacement between the two end point of the cohesive zone in the global coordinate system (x_1, x_2) is given by [8]:

$$\delta_1 = \left(\frac{EI_2}{M_2} + na_2\right)\sin(\theta_2) - \left(\frac{EI_1}{M_1} - na_1\right)\sin(\theta_1) \qquad \text{(P7.14)}$$

$$\delta_2 = \left(\frac{EI_2}{M_2} + na_2\right)(1 - \cos(\theta_2)) - \left(\frac{EI_1}{M_1} - na_1\right)(1 - \cos(\theta_2)) \qquad \text{(P7.15)}$$

where δ represents the opening in the global reference, E is the Young's modulus, I is the bending moment of inertia, θ is the rotation of the beam (see figure P7.14), M represents the moments applied, and na the bending neutral axis.
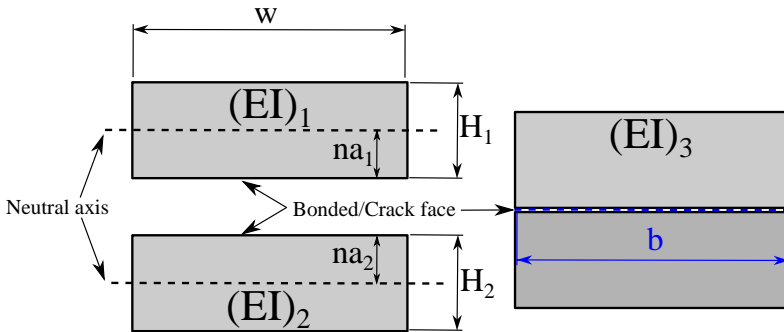
**Figure P7.13:** DCB cross-section geometry: specimen without side-groves.

The index $_1$ and $_2$ represent the top and bottom beam, respectively. (**Note:** For a DCB specimen where the crack grows in the middle plane, symmetric case, the neutral axis, na_1 and na_2, are equal to half of the beam height, $\frac{1}{2}H$)

The rotation angles $\theta_{1,2}$ at the end of the fracture process zone, as presented in Fig. P7.14, are described by:

$$\theta_1 = \frac{M_1 l_{fpz}}{EI_1} \tag{P7.16}$$

$$\theta_2 = \frac{M_2 l_{fpz}}{EI_2} \tag{P7.17}$$

The parameter l_{fpz} is fracture process zone length along the neutral axis, measured from the crack tip to the point where the end-openings are determined.
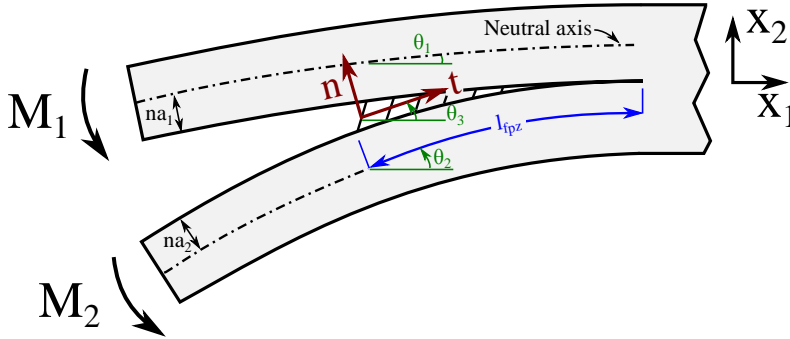
Figure P7.14: DCB specimen loaded with moments: beam rotation angles (θ_i), fracture process zone (l_{fpz}), and coordinate systems.

Critical Opening: Local and Global Coordinate System

To describe correctly the traction-opening cohesive-law, the end opening needs to be represented in the local coordinate system (n, t). Thus, the local openings $\delta_{1,2}$ as function of the beam rotation angle and global openings $\delta_{1,2}$ (global coordinates $x_1; x_2$), are given by:

$$\delta_t = \delta_1 \cos(\theta_3) + \delta_2 \sin(\theta_3) \tag{P7.18}$$

$$\delta_n = -\delta_1 \sin(\theta_3) + \delta_2 \cos(\theta_3) \tag{P7.19}$$

$$\theta_3 = \frac{\theta_1 + \theta_2}{2} \tag{P7.20}$$

Then, the total opening δ_c (critical opening) can be calculated by the law of Pythagoras, as described by Eq. (P7.21).

$$\delta_c = \sqrt{\delta_t^2 + \delta_n^2} \tag{P7.21}$$

P7.4.1   Cohesive-Law: General 3D J-Integral

The general 3D J-Integral (described by Eq. (P7.2)) was used to link the moments applied to the DCB, and consequently the l_{fpz}, to the material's cohesive-law. The general 3D J-integral was re-written as:

$$J = \frac{1}{2}\frac{M_1^2 \alpha}{b} \tag{P7.22}$$

$$\alpha = \frac{1}{EI_1} + \frac{\xi}{EI_2} - \frac{(1+\xi)^2}{EI_3} \tag{P7.23}$$

where the parameter ξ represents the mixed mode ratio, as described by Eq. (P7.24).

$$\xi = \frac{M_2}{M_1} \tag{P7.24}$$

The material energy release rate (J) is the area under the traction-separation curve, as shown in figure P7.15, and it can present different shapes. Thus, to represent this different shapes, the energy release rate J is defined as:

$$J = c_{shape}\sigma_c \delta_c \tag{P7.25}$$

where σ_c is the critical stress, δ_c the critical opening, and c_{shape} is a parameter that describes the shape of the cohesive-law, which can vary $0 < c_{shape} \leq 1$.
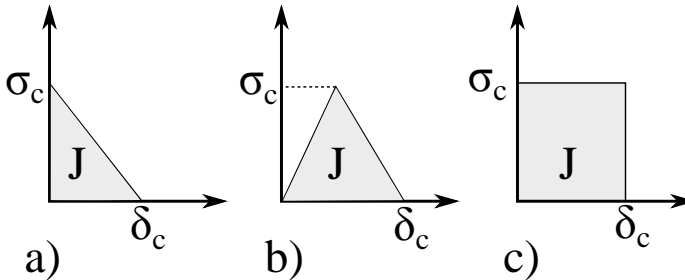
Figure P7.15: Representation of the different shapes that the cohesive-law can present.

The bending moment defined in Eq. (P7.22) can be re-written in function of the cohesive-law parameters as:

$$M_1 = \pm \frac{\sqrt{2\alpha c_{shape}\sigma_c \delta_c b}}{\alpha} \qquad (P7.26)$$

l_{fpz} Represented in the Global Coordinate System $(x_1; x_2)$

The opening in the global coordinate system $(\delta_1; \delta_2)$ as function of the cohesive-law parameters, DCB geometry, and l_{fpz}, is obtained by combining Eq. (P7.14), (P7.15), (P7.16), (P7.17), and (P7.26):

$$\delta_1 = \left(\frac{\sqrt{2}}{2}C_2 + na_2\right) sin\left(\sqrt{2}\frac{l_{fpz}}{C_2}\right) - \left(\frac{\sqrt{2}}{2}C_1 - na_1\right) sin\left(\sqrt{2}\frac{l_{fpz}}{C_1}\right) \qquad (P7.27)$$

$$\delta_2 = \left(\frac{\sqrt{2}}{2}C_2 + na_2\right)\left(1 - cos\left(\sqrt{2}\frac{l_{fpz}}{C_2}\right)\right) - \left(\frac{\sqrt{2}}{2}C_1 - na_1\right)\left(1 - cos\left(\sqrt{2}\frac{l_{fpz}}{C_1}\right)\right) \qquad (P7.28)$$

The coefficients C_1 and C_2 are defined as:

$$C_1 = \frac{EI_1}{\xi\sqrt{\alpha c_{shape}\sigma_c \delta_c b}} \qquad (P7.29)$$

$$C_2 = \frac{EI_2}{\xi\sqrt{\alpha c_{shape}\sigma_c \delta_c b}} \qquad (P7.30)$$

Note that δ_1 and δ_2 do not represent the cohesive-law parameter, critical opening δ_c. To obtained an equation that represents the l_{fpz} exclusively in function of the DCB geometry, mixed-mode ratio, and the cohesive-law parameters, the opening have to be represented in the local coordinate system, δ_c.

l_{fpz} Represented in the Local Coordinate System $(x_1; x_2)$

The general equation that describes the l_{fpz} in function of the DCB geometry, mixed-mode ratio, and the cohesive-law parameters is obtained by combining Eq. (P7.18), (P7.19), (P7.20), (P7.21), (P7.27), and (P7.28):

$$
\begin{aligned}
\delta_c^2 = &\left[-\left(\left(\frac{\sqrt{2}}{2}C_2 + na_2 \right) \sin\left(\sqrt{2}\frac{l_{fpz}}{C_2} \right) - \left(\frac{\sqrt{2}}{2}C_1\,\xi - na_1 \right) \sin\left(\sqrt{2}\frac{l_{fpz}}{C_1\,\xi} \right) \right) \right. \\
&\sin\left(\frac{\sqrt{2}}{2}\left(\frac{l_{fpz}}{C_1\,\xi} + \frac{l_{fpz}}{C_2} \right) \right) + \left(\left(\frac{\sqrt{2}}{2}C_2 + na_2 \right)\left(1 - \cos\left(\sqrt{2}\frac{l_{fpz}}{C_2} \right) \right) \right. \\
&\left. \left. - \left(\frac{\sqrt{2}}{2}C_1\,\xi - na_1 \right)\left(1 - \cos\left(\sqrt{2}\frac{l_{fpz}}{C_1\,\xi} \right) \right) \right) \cos\left(\frac{\sqrt{2}}{2}\left(\frac{l_{fpz}}{C_1\,\xi} + \frac{l_{fpz}}{C_2} \right) \right) \right]^2 \\
&+ \left[\left(\left(\frac{\sqrt{2}}{2}C_2 + na_2 \right)\sin\left(\sqrt{2}\frac{l_{fpz}}{C_2} \right) - \left(\frac{\sqrt{2}}{2}C_1\,\xi - na_1 \right)\sin\left(\sqrt{2}\frac{l_{fpz}}{C_1\,\xi} \right) \right) \right. \\
&\cos\left(\frac{\sqrt{2}}{2}\left(\frac{l_{fpz}}{C_1\,\xi} + \frac{l_{fpz}}{C_2} \right) \right) + \left(\left(\frac{\sqrt{2}}{2}C_2 + na_2 \right)\left(1 - \cos\left(\sqrt{2}\frac{l_{fpz}}{C_2} \right) \right) \right. \\
&\left. \left. - \left(\frac{\sqrt{2}}{2}C_1\,\xi - na_1 \right)\left(1 - \cos\left(\sqrt{2}\frac{l_{fpz}}{C_1\,\xi} \right) \right) \right) \sin\left(\frac{\sqrt{2}}{2}\left(\frac{l_{fpz}}{C_1\,\xi} + \frac{l_{fpz}}{C_2} \right) \right) \right]^2
\end{aligned}
$$

$$\text{(P7.31)}$$

DTU Wind Energy is a department of the Technical University of Denmark with a unique integration of research, education, innovation and public/private sector consulting in the field of wind energy. Our activities develop new opportunities and technology for the global and Danish exploitation of wind energy. Research focuses on key technical-scientific fields, which are central for the development, innovation and use of wind energy and provides the basis for advanced education at the university.